Dermatologie der
Universitätsmedizin Mainz

Max-Planck-Institut für
Polymerforschung

Sonderforschungsbereich 1066

Modulation of Pharmacokinetics of Nanodimensional Drug Carriers

Dissertation

Zur Erlangung des Grades
Doktor der Naturwissenschaften

Am Fachbereich Biologie
der Johannes Gutenberg-Universität Mainz

Adelina Haller
geb. am 13.03.1992 in Ludwigsburg

Mainz, 2021

Amtierender Dekan:	Prof. Dr. rer. nat. Hans Zischler	Institut für Anthropologie, Johannes Gutenberg-Universität Mainz
1. Berichterstatter:	Prof. Dr. med. Volker Mailänder	Dermatologie, Universtitätsmedizin Mainz und Physikalische Chemie der Polymere, Max-Planck-Institut für Polymerforschung
2. Berichterstatterin:	[redacted]	Institut für Entwicklungsbiologie und Neurobiologie, Johannes Gutenberg Universität Mainz
3. Prüferin:	[redacted]	Physikalische Chemie der Polymere, Max-Planck-Institut für Polymerforschung

Tag der mündlichen Prüfung:

„Eine Investition in Wissen bringt immer noch die besten Zinsen“

Benjamin Franklin

[redacted]

I. Eidesstattliche Erklärung

Hiermit versichere ich,

i. dass die wissenschaftliche Arbeit selbstständig verfasst und ausschließlich die angegebenen Quellen und Hilfsmittel verwendet wurden.
ii. dass keine entgeltliche Hilfe Dritter, insbesondere Promotionsberatung oder -vermittlung in Anspruch genommen wurde.
iii. dass die eingereichte wissenschaftliche Arbeit noch an keiner anderen deutschen oder ausländischen Hochschule oder vergleichbaren Einrichtung zur Erlangung eines akademischen Grades eingereicht worden ist.
iv. noch kein Promotions-, Ph.D.- oder ein vergleichbares Graduierungsverfahren im Promotionsfach erfolglos beendet zu haben.
v. noch kein Promotions-, Ph.D.- oder ein vergleichbares Graduierungsverfahren im Fachgebiet der Promotion erfolgreich abgeschlossen habe.
vi. bereits publizierte Auszüge oder Arbeiten kenntlich zu machen.

Adelina Haller

……

Mainz, ……

II. Table of content

III. Abstract (english)

The principle of nanocarriers enables targeted transport of the drug to the cell. This novel drug delivery systems allow to better control side effects and increase the effectiveness of the packaged drug. Pharmacokinetics were studied in more detail for different nanocarrier systems in terms of nonspecific and targeted uptake by the reticuloendothelial system (RES). Predominantly flow cytometry and *In vivo* imaging (IVIS) were used. These studies allowed us to make assumptions about the effectiveness of the here investigated nanotherapeutics.

The main objective of this work was to examine the effect of the co-medication of heparin on the pharmacokinetics of nanocarriers. The first chapter describes the influence of heparin on the nonspecific uptake of clinically relevant liposomal formulations into the phagocytosing cells of the RES. *In vivo*, high-dose intravenous heparinization promoted accumulation of Doxil®-like liposomes in the liver and spleen to a small extent. These weak changes do not suggest that a concomitant heparinization could affect liposomal therapy. In the second chapter, it was shown that heparin modulates the uptake of the proteinbased antigen shell nanovaccine, ovalbumine nanocapsule, in favor of the dendritic cells. The effect of ‘passive targeting’ could not be induced *in vivo* by a high-dose heparinization. The cellular biodistribution of this novel nanovaccine was described in detail for the first time.

The second objective of this work was to investigate pharmacokinetics of novel designs and compositions of nanocarrier systems. The third chapter, a collaboration with the Max Planck Institute for Polymer Research, describes the biodistribution and preferential cellular uptake by Kupffer cells of the mesoporpous polydexamethason-loaded silica nanocapsule - a capsule loaded with a polymerized anti-inflammatory drug against inflammatory liver disease combining the benefits of targeting and controlled drug release. The fourth chapter, a collaboration with members of the SFB 1066, describes the establishment of a method to characterize the intracellular release of doxorubicin from *de novo* liposomal formulations using the Amnis® ImageStream® X Mark II.

This work contributes to a better understanding of the complexity of the pharmacological properties of different nanocarrier systems.

IV. Zusammenfassung (deutsch)

Das Prinzip der *Nanocarrier* ermöglicht einen gezielten Transport des Wirkstoffs in nanodimensionalen Verpackungen zur Zelle. Dieses neuartige System der Wirkstoff Verabreichung ermöglicht es Nebenwirkungen besser zu kontrollieren und die Effektivität des verpackten Medikaments zu steigern. Die Pharmakokinetik wurde für verschiedene Nanocarriersysteme in Hinblick auf die unspezifische und gezielte Aufnahme durch das retikuloendotheliale System (RES) genauer untersucht. Hierbei wurden vorwiegend druchflusszytometrische Verfahren eingesetzt, sowie *In vivo* Bildgebung (IVIS) der Fluoreszenz. Diese Untersuchungen ermöglichten uns Annahmen über die Effektivität des Nanotherapeutikums zu treffen.

Das Hauptziel dieser Arbeit war es, den Einfluss der Co-Medikation von Heparin auf die Pharmakokinetik von Nanocarriern zu untersuchen. Das erste Kapitel beschreibt den Einfluss von Heparin auf die unspezifische Aufnahme von klinisch relevanten liposomalen Formulierungen in phagozytierende Zellen des RES. *In vivo*, konnte gezeigt werden, dass eine hoch dosierte intravenöse Heparinisierung die Akkumulation in Leber und Milz in statistisch signifikantem, aber insgesamt geringem Umfang fördert. Diese schwach ausgeprägten Veränderungen, deuten nicht darauf hin, dass eine einhergehende Heparinisierung die Therapie mit Liposomen beeinflussen könnte. Im zweiten Kapitel wurde gezeigt, dass Heparin die Aufnahme des proteinbasierten Antigenhüllen-Nanovakzins, der Ovalbumin-Nanokapsel, zu Gunsten der dendritischen Zellen moduliert. Der Effekt der ‚passiven Adressierung' konnte *in vivo* durch eine hochdosierte Heparinisierung nicht hervorgerufen werden. Die zelluläre Bioverteilung dieses neuartigen Nanovakzins wurde zum ersten Mal detailliert beschrieben.

Das zweite Ziel dieser Arbeit war die Untersuchung der Pharmakokinetik von neuartigen Designs und Zusammensetzungen von Nanocarrier-Systemen. Das dritte Kapitel, eine Zusammenarbeit mit dem Max-Planck-Institut für Polymerforschung, beschreibt die Biodistribution und die bevorzugte zelluläre Aufnahme durch Kupffer-Zellen der mit mesoporösem Polydexamethason beladenen Siliziumdioxid-Nanokapsel - einer Kapsel, die mit einem polymerisierten entzündungshemmenden Medikament gegen entzündliche Lebererkrankungen beladen ist und die Vorteile von Targeting und kontrollierter Wirkstofffreisetzung kombiniert. Das vierte Kapitel, eine Kollaboration innerhalb des SFB 1066, handelt von der Etablierung einer Methode zur Charakterisierung der intrazellulären Freisetzung von Doxorubicin aus *de novo* liposomalen Formulierungen unter Verwendung des Amnis® ImageStream® X Mark II.

Diese Arbeit leistet einen Beitrag um die Komplexität der pharmakologischen Eigenschaften von verschiedenen Nanocarriersystemen besser zu verstehen.

1 Introduction

The introduction serves to familiarize the reader with various nanocarrier systems. Furthermore, the pharmacokinetics of nanocarriers are explained with a focus on the reticulo endothelial system (RES). In the third part, the main molecule considered in this context, heparin, is discussed in more detail.

1.1 Nanodimensional therapeutics

"The new concept of nanomedicine arose from merging nanoscience and nanotechnology with medicine."[1] The nanodimensional systems applied for medical purposes can be carriers for active substances or therapeutic agents themselves [1]. The International Union of Pure and Applied Chemistry (IUPAC) defines the term 'nanoparticles' as particles ranging of a size from 10 – 100 nm [2]. In contrast, the U.S. Food and Drug Administration (FDA) considers a more comprehensive title for 'nanotechnology':

> "Nanotechnology allows scientists to work on the scale of molecules to create, explore, and manipulate the biological and material worlds measured in nanometers, one-billionth of a meter. […] The Task Force has not adopted a precise definition for 'nanoscale materials,' 'nanotechnology,' or related terms to define the scope of its work. The Task Force concluded that it would be most productive to take a broadly inclusive approach in identifying potentially relevant studies, data, and other information. The Task Force believes FDA should continue to pursue regulatory approaches that take into account the potential importance of material size and the evolving state of the science. Moreover, while one definition for 'nanotechnology,' 'nanoscale material,' or a related term or concept may offer meaningful guidance in one context, that definition may be too narrow or broad to be of use in another. Accordingly, the Task Force does not recommend attempting to adopt formal, fixed definitions for such terms for regulatory purposes at this time. As FDA learns more about the interaction of nanoscale materials with biological systems and generalizable concepts that can inform the agency's judgment, it may be productive to develop formal, fixed definitions, appropriately tailored to the regulation of nanoscale materials in FDA-regulated products." [3]

1.1.1 Liposomal formulations in clinical use

Liposomes are the first clinically and most frequently used nanodimensional therapeutics since the approval of Doxil® in 1995 [4]. Nowadays liposomes with different ingredients are used not only for cancer therapy but also for fungal infections, pain therapy and vaccinations [5] (see Table 1). Last but not least, liposomal RNA-based nanovaccines offer an outstandingly promising approach for finding an effective and tolerable vaccine against Sars-CoV-2 [6].

Table 1: Overview on marketed liposomal formulations with clinical use.

Marketed liposomes (2017)

Cancer Therapy	Fungal Diseases	Analgetics	Viral Vaccines
DaunoXome® Doxil® Depocyt® Marqibo® Myocet® Onivyde™	Abelcet® Ambisome® Amphotec®	DepoDur™ Exparel®	Epaxal® Inflexal®V

[1]

Alike physiological occurring vesicles, the formulation of liposomes base on phospholipids and cholesterol forming a lipid bilayer with aqueous core [8]. Hydrophyl pharmaceutical agents can be loaded into the aqueous cavity. By delivering the chemotherapeutic substance DXR within the hydrophilic core of liposomes [9], side effects of DXR can be reduced dramatically [10]. Doxil® is a liposomal formulation for delivering the chemotherapeutic DXR and was approved in 1995 for the treatment of Karposi's sarcoma [4]. Doxil® is further used for the treatment of breast cancer and ovarian cancer [11]. By liposomal delivery, the clearance of DXR is reduced, pharmaceutical half live prolonged, what leads to a higher DXR accumulation in the tumor, about 4 - 16 times higher than treatment with pure DXR [12]. The enhanced permeability and retention (EPR) effect is taken advantage of for passively targeting liposomal anti-tumor therapeutics towards tumor tissue [13].The permeability of the endothelium is increased in case of local inflammations [14] and therefore in several tumors. The liposomal composition of Doxil® consists of hydrogenated soy phosphatidylcholine (HSPC), cholesterol (CHOL) and N-(carbonyl-methoxypolyethylene glycol 2000)-1,2-distearoyl-sn-glycero-3-phosphoethanol-amine sodium salt (PEG2000-DSPE) in a molar ratio of 56 : 39 : 5 (mol-%) [7]. Thus Doxil® is a PEGylated nanocarrier system. The size of Doxil® ranges from 80 to 100 nm (diameter) [9]. (Table 2)

Myocet® is another formulation loaded with DXR. The liposomal composition of Myocet® consists of CHOL and egg phosphatidylcholine (EPC) in a molar ratio of 45 : 55 (mol-%). In contrast to Doxil®, Myocet® is non-PEGylated formulation and therefore exhibits different pharmacokinetics than Doxil® [5]. Myocet® was approved for treatment of breast cancer in 2000 [15]. The liposomes hydrodynamic diameter ranges from 150 - 250 nm. The larger size causes a higher recognition and uptake by the RES but reduces cardiotoxicity of DXR and gastrointestinal adverse effects [7]. The anti-tumor efficacy of Myocet® is similar to DXR while exhibiting lower toxicity [16] (Table 2). In Figure 1 it is shown how the biodistribution of DXR

[1] Table adapted from Bulbake et al. 7. Bulbake, U., et al., *Liposomal formulations in clinical use: an updated review.* Pharmaceutics, 2017. **9**(2): p. 12., pharmaceutics 2017, fig 2. (Open access article distributed under the Creative Commons Attribution License).

depends on the liposomal formulations. Especially Doxil® exhibits a longer blood circulation time compared to Myocet® and pure DXR. The formulation Myocet® leads to a strong accumulation of DXR in the spleen.

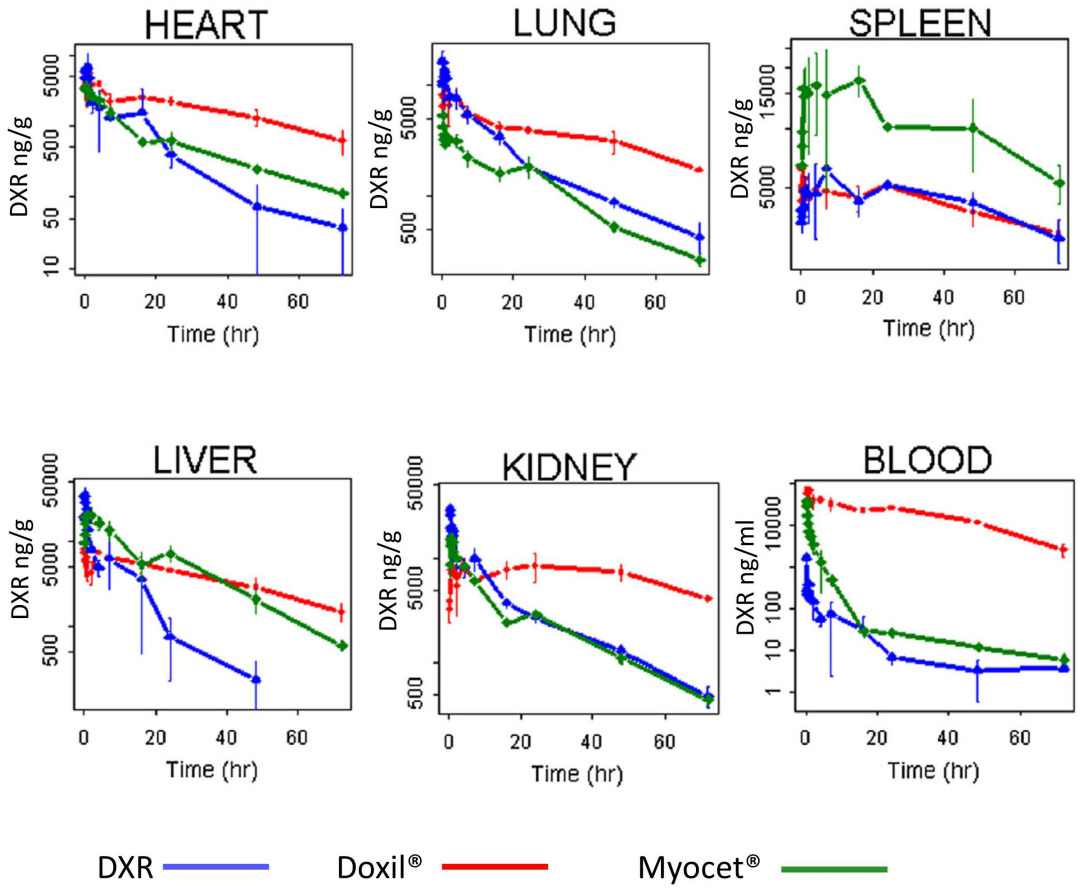

Figure 1: "Total doxorubicin concentration to time profile in tissues and blood" [5].

The graph shows mean and SD of DXR concentration in organs, n = 3. Mice were treated with either of the three delivery forms of DXR: DXR (blue), Doxil® (red), Myocet® (green).[2]

Ambisome® transports the active substance, amphotericin B, which is included into the liposomal bilayer in contrast to Myocet® and Doxil®, which encapsulate the pharmaceutical agent (see Table 2). The liposomal formulation of Ambisome® is constituted of HSPC, CHOL, distearoylphosphatidylglycerol (DSPG) and amphotericin B in a molar ratio of (48 : 10 : 23 : 9). The hydrodynamic diameter is around ~100 nm [17]. Liposomal amphotericin B is used for treatment of severe fungal infections in clinic [18, 19]. Application of amphotericin B in form of liposomes is more compatible with kidney restrictions than the free pharmaceutical compound [18]. Ambisome® is tolerated at higher doses than conventional amphotericin B and has a

[2] Adapted with permission of the publisher from 5. Luo, R., et al., *Distinct biodistribution of doxorubicin and the altered dispositions mediated by different liposomal formulations.* International journal of pharmaceutics, 2017. **519**(1-2): p. 1-10. Copyright (2017) International Journal of Pharmaceutics.

wider therapeutic window while retaining its pharmacological properties [17]. However, the lipid complexes are rapidly cleared. Mainly, Ambisome® accumulates in the liver and spleen [20, 21]. (Table 2)

Also, liposomes are suitable for delivery of enzymes, virus particles [7] and RNA molecules to target cells. The Latter have not only received greater attention in the research for personalized cancer therapeutics, but most recently also in the development of the corona vaccine [6, 22].

Table 2: Overview on three clinically relevant liposomal formulations: Doxil®, Myocet® and Ambisome®.

Drug (brand name)		
Doxil®	**Myocet®**	**Ambisome®**
Scetch		
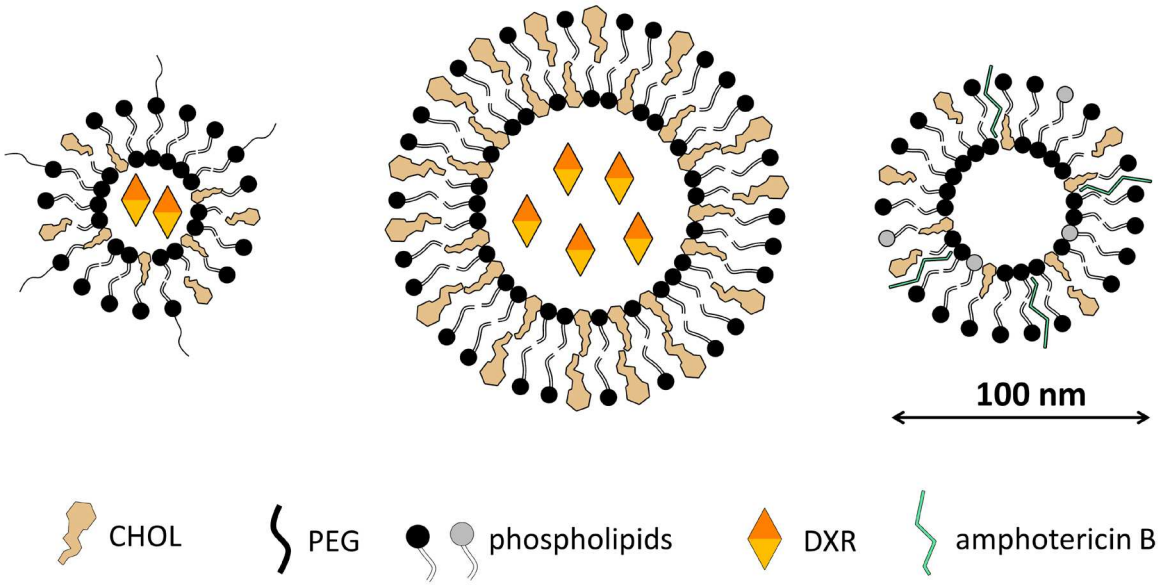		
Diameter		
80 - 100 nm	150 - 250 nm	~100 nm
Lipid constitution (molar ratio, mol-%)		
HSPC : CHOL : PEG 2000-DSPE (56 : 39 : 5)	EPC : CHOL (55 : 45)	HSPC : DSPG : CHOL : amphotericin B (48 : 10 : 23 : 9)
Indication		
Kaposi's sarcoma, ovarian cancer, breast cancer	breast cancer	fungal infections

Summary of section 1.1.1: Liposomal formulations in clinical use

1.1.2 The antigen shell nanovaccine, ovalbumine nanocapsule (OVA-NC)

As already mentioned, nanovaccines are another therapeutic application of nanocarriers (see 1.1.1). Nanovaccines transport antigens or antigen-coding mRNA to dendritic cells (DCs) in order to evoke an adaptive immune response (see Figure 2) [23].

Dendritic cells (DCs) form a bridge from the innate immune system to the adaptive immune system. The function of dendritic cells is to recognize pathogens, ingest them, and process them to present pathogen-specific antigens to T-cells. The dendrites of immature DC increase the cell surface area and thus the probability of encountering pathogens. Upon activation, dendrites recede (see Figure 2) and the cells migrate to secondary lymphoid organs where they simulate specific T-cells. DCs play a crucial role in adaptive immunization against various pathogens such as viruses and bacteria and vaccinated antigens. [24, 25]

In contrast to conventional vaccine, ‘antigen + adjuvants’, nanovaccines bear following advantages. The nanodimensional size and structure mimics natural pathogens what causes a preferential uptake by DCs of the drug [26]. Adjuvants are immune-stimulatory substances which enhance the process of immunization [27] but also cause side effects of vaccination [28]. The encapsulation of the stimulatory agents has potential to reduce the side effects and to enhance efficacy; The adjuvants effect primarily in cells, which engulfed antigens.

Piradashvili et al. [29] succeeded in generating a hydrous core capsule consisting of a protein envelope that can be degraded intracellularly. The envelope of this capsule consists of anantigen and the hydrous core can be loaded with adjuvants [30]. When the capsule becomes digested in the lysosome, adjuvants are released in order to activate the DC (Figure 2). Passlick et al. [30] proofed *in vitro,* that a specific immune response against ovalbumin (OVA) can be induced by capsules consisting of an OVA antigen shell. OVA is an excellent model antigen to evaluate the immune response as there exist established read-outs for the specific T-cell induced immune response [31]. Therefore, OVA frequently acts as a model antigen for the examination of novel vaccines [32, 33].

In chapter 2, we will examine the biodistribution and cellular uptake of OVA-NCs in more detail with the overarching question of how the anticoagulant heparin regulates the uptake into DCs and competing macrophages.

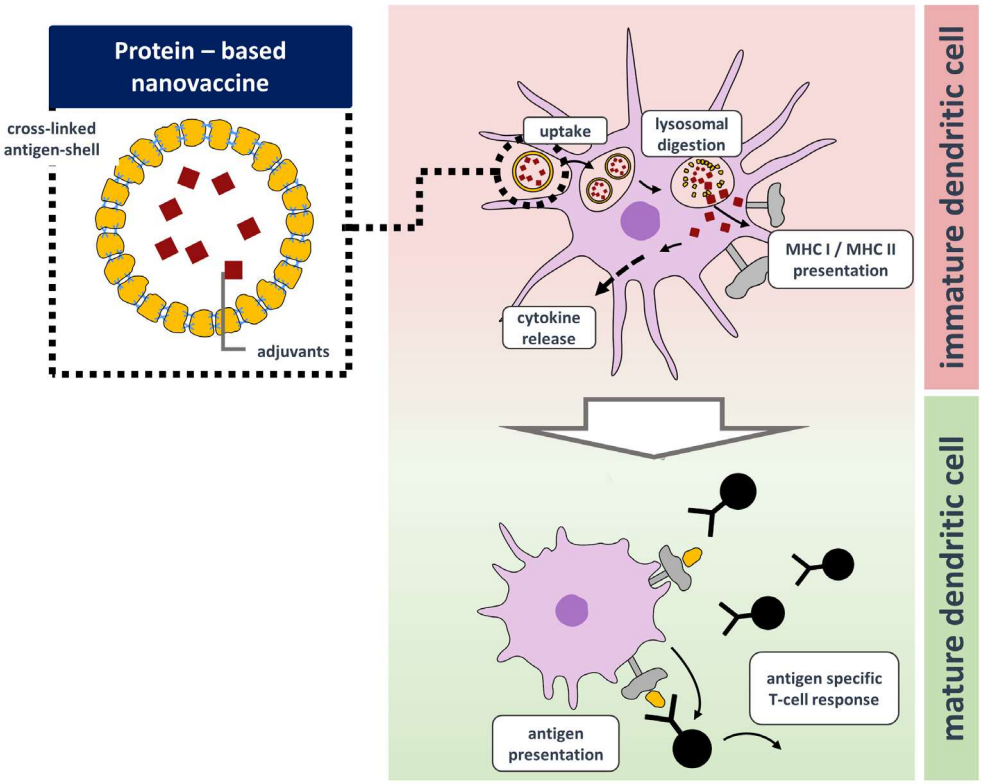

Figure 2: Schema of immunization with a cross-linked protein-based antigen-shell nanovaccine.

The shell of the nanovaccine consists of cross-linked antigens and the core is loaded with adjuvants. When the capsule is engulfed by immature dendritic cells, the protein-shell is digested inside the lysosome and adjuvants are released. This causes an activation of the dendritic cell, leading to crosspresentation of the antigenic protein shell fragments *via* MHC molecules in secondary lymphoid organs. Cytokine release lures and stimulates antigen-reactive T-cells.

1.1.3 Polydexamethason loaded mesoporous silica nanocapsule (SiO_2 NC-PDXM)

The SiO_2 NC-PDXM is described in section 5 (Chapter 3: Characterization of the Polydexamethason Silica Nanocapsule).

1.1.4 Summary of relevant nanocarrier systems in the scope of this work

In this work, three nanocarrier systems were investigated, which are summarized in Table 3. All three systems differ in terms of their therapeutic use, structure and their principle. Liposomal formulations are mainly used for carrying hydrophilic substances as the chemotherapeutic DXR. The EPR effect favors accumulation of the drug carriers in tumors and altered clearance mechanisms improve the profile of side effects. The OVA-NC represents a model for an antigen shell nanovaccine. The pathogenlike size of the drug, favors uptake by DCs, which initiate an adaptive immune response. The SiO_2 NC-PDXM, a mesoporous silica nanocapsule, enables constant release of small monomers but not large polymers. PDXM is a pH-responsive polymer, which degrades into the active substance inside distinct cell-compartments. (see 1.1)

Table 3: Summary on relevant nanocarrier systems

Therapy	**Anti-tumor**	**Nanovaccine** (Anti-tumor)	**Anti-inflammatory** (for hepatic inflammations)
Example (develop-mental stage)	**Doxil®** (FDA-approved) 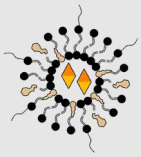	**OVA-NC** *(in vitro)* 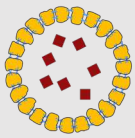	**SiO_2 NC-PDXM** *(in vitro)* 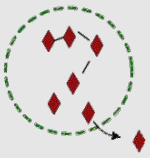
Principle	Encapsulation of highly effective substances (e.g. DXR)	Packing adjuvants and antigen together	Targeted delivery of Nf-κB inhibitor to inflammation-enhancing macrophages
Advantage towards free drug	Reduced side-effects, higher efficacy	The immune stimmulatory adjuvants acts only in cells with antigens	Targeted release of substance
Target site	**Tumor** 	**Spleen** 	**Liver** 
Target cell	**Tumor cell** 	**Dendritic cell** 	**Macrophage** 
Targeting property	EPR effect (see 1.1.1)	Preferential uptake by DCs because of pathogen-like size	Blood clearance of „foreign“ bodies by liver macrophages (see 1.2.5.2)

The summarises relevant nanocarrier systems of this work which are described in section 1.1 and the respective chapters (1-4).

1.2 Pharmacokinetic of nanodimensional therapeutics

1.2.1 Terms of pharmacology

The **pharmacodynamics** describe the drug profile: The dose-response relationship, mechanisms of action and interactions of a drug with other molecules [34]. The **pharmacokinetic** describes the processes, which influence the final drug concentration at the target site (**biophase**). The **bioavailability** is the extent of availability of the applied drug at the target site [35]. Pharmacodynamics and thus therapeutic success are substantially influenced by pharmacokinetics (Figure 3).

The **therapeutic index** is calculated from values of the dose-response curve in relation to values of the dose-lethality curve. The **therapeutic window** is the range of dose, which causes an effective treatment without toxicity. The wider the therapeutic window, the higher the safety of the drug. The **pharmacovigilance** describes the observation and documentation of drug-related adverse effects.

Figure 3: Therapy outcome is dependent on the pharmacokinetics.

1.2.2 Pharmacokinetic processes of nanocarriers

The factors influencing the pharmacokinetics and ultimately the pharmacological effect of intravenous (i.v.) applied nanodimensional drugs are outlined in Figure 4 and Figure 5. Small sized (< 6nm) nanocarriers are removed from the blood by the kidney and secreted with the urine. Larger sized (> 6nm) are secreted by the liver with the bile from hepatocytes (the process is described in 1.2.5) [36-38]. The reticulo endothelial system (RES), consisting of mononuclear phagocytes which are predominantly located in liver and spleen, take up the particles for long term retention and digestion [39]. Metabolites can be released from these cells and cleared from the organism by the other mechanisms. (Figure 4)

The chance that a nanodimensional drug reaches the target site depends on the circulation time of the nanocarriers and its targeting ability. A nanodimensional drug is more efficient the more particles reach the target siteand are taken up by the target cells. Taken up by the target cells, the intracellular trafficking and the release speed of the pharmaceutical agent are decisive for the bioavailability and effect of the drug as well. (Figure 5) The circulation time of most nanocarriers is influenced by the unspecific uptake of the RES, the components of which are discussed in more detail in the following sections. Thus, the clearance by the RES has a major impact on the extend of the pharmacological effect and ultimately therapy outcome [40, 41]. (Figure 5)

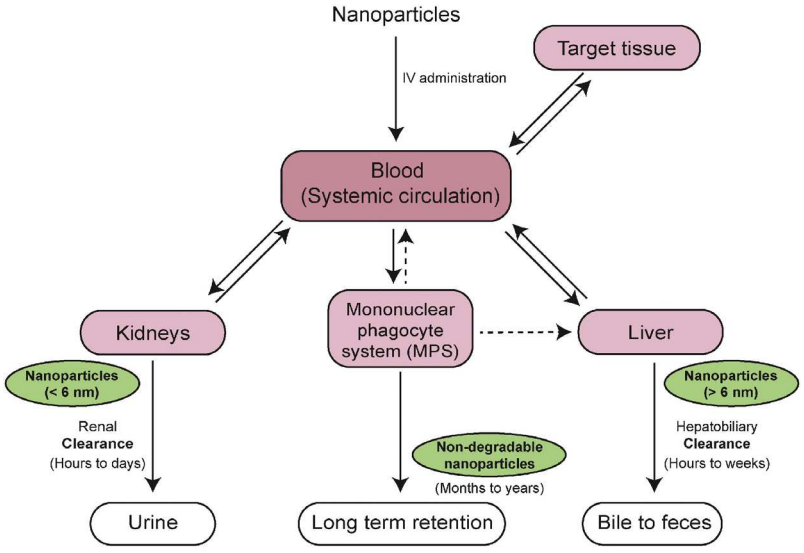

Figure 4: “Schematic of nanoparticle clearance pathways” [39].

Nanoparticles which are injected into the blood, are cleared by the kidney (< 6nm) [38] and liver (> 6nm) [36] and secreted with the urine or bile. Nanoparticles taken up by the RES (here named mononuclear phagocyte system (MPS)) can be retained for long term retention.[3]

[3] Reproduced with the permission of the publisher from 39. Zhang, Y.-N., et al., *Nanoparticle–liver interactions: cellular uptake and hepatobiliary elimination.* Journal of controlled release, 2016. **240**: p. 332-348. – Copyright (2016) Journal of Controlled Release. The authors adapted the figure 36. Yu, M. and J. Zheng, *Clearance Pathways and Tumor Targeting of Imaging Nanoparticles.* ACS nano, 2015. **9**(7): p. 6655-6674.

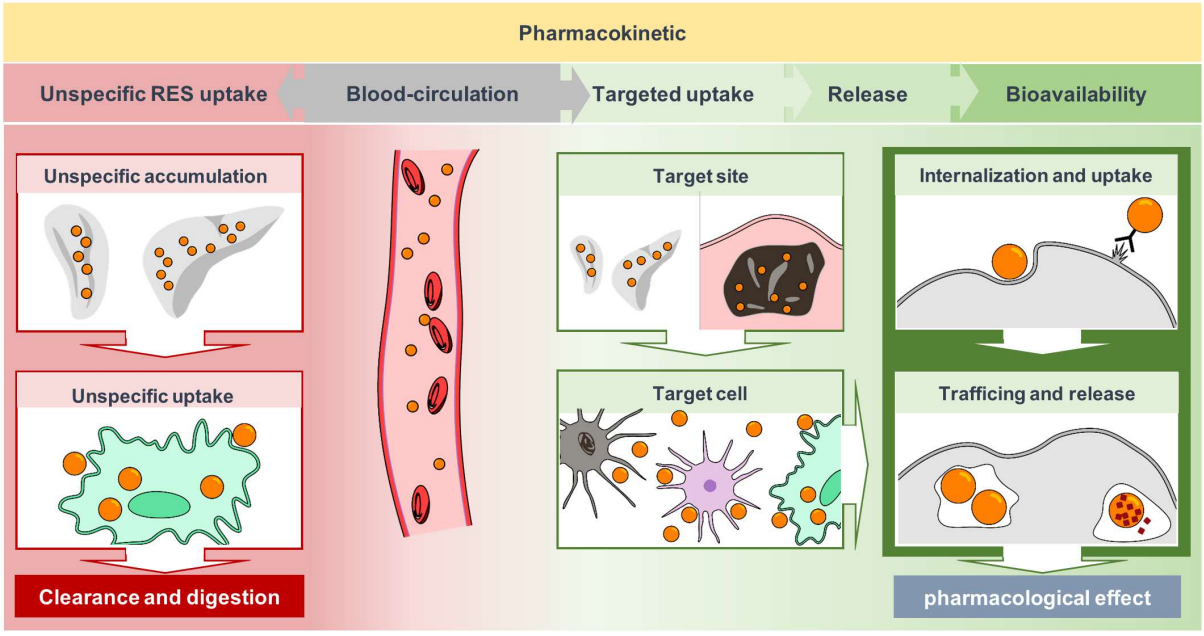

Figure 5: Overview on pharmacokinetic processes of nanocarriers investigated in this work.

Blood circulation time of nanocarriers (orange balls) > 6nm, is negatively influenced (red shaded) by the uptake of the RES. A prolonged circulation time favors (green shaded) the accumulation of nanocarriers at the target site and the uptake into the target cell. Intracellular trafficking and release influence bioavailability and therefore the pharmacological effect of the loaded pharmaceutical agent.

1.2.3 Events causing blood elimination of nanocarriers

When nanocarriers are administered i.v., there are events that decide the fate of these and can prevent them from reaching the target cell.

Some of the events after i.v. administration deciding the fate of nanocarriers, are outlined in Figure 6: When nanocarriers are administered into the blood, components of the blood adsorb on the surface [42] forming the corona (see Figure 6, (1.)). The protein composition of the corona, is dependent on the shape [43], physicochemical surface characteristics of nanocarriers [44, 45] and the surrounding biological fluid [46, 47]. The composition of the corona influences cellular uptake [48] and biodistribution [47, 49]. Adsorption of opsonizing proteins, including complement factors and Immuneglobuline G (IgG) molecules, makes nanocarriers susceptible to uptake by immune cells [50] (see Figure 6, (6.)), what causes a faster clearance by macrophages (see Figure 6, (7.)). The relevance of corona formation for pharmacokinetics is evident. As described before within the examples of Doxil® and Myocet®, PEGylated nanocarriers exhibit a longer circulation time [51]. The PEG-chains reduce protein adsorption, by forming a shed of H_2O molecules, leading to reduced opsonation and uptake by the cells of the RES [51]. As an alternative the specific adsorption of proteins has been proposed [52]. But not only specific proteins cause an opsonation, also adsorbing proteins can change their natural conformation and signal to the immune system ‘a foreign body’ [53]. Furthermore, the adsorption of plasma components can cause aggregations [54] (see Figure

6, (2.)). Larger aggregates of nanocarriers are retained in the first capillaries immediately after peripheral vein injection - the lung capillaries [54] (see Figure 6, (3.)).

In addition, depending on their size (< 150 nm), particles can be filtered through the microanatomical structures, sinusoids, in the liver (see below) and spleen (see below) exhibiting a high permeability. Smaller particles (< 6 nm) can be filtered inside the glomeruli of the kidney [55] (see Figure 6, (5.)).

Macrophages in the vascular system of liver and spleen are prone to internalize and take up nanocarriers [56, 57] (see Figure 6, (7.)). Taken together the RES, to which mainly the phagocytes of liver and spleen contribute, mainly influences pharmacokinetics of nanocarriers and thereby influences the pharmacodynamics of nanodimensional drugs. The following chapters will take a closer look at the two organs, which harbor the largest part of the RES and outline their role for the pharmacokinetics of nanocarriers.

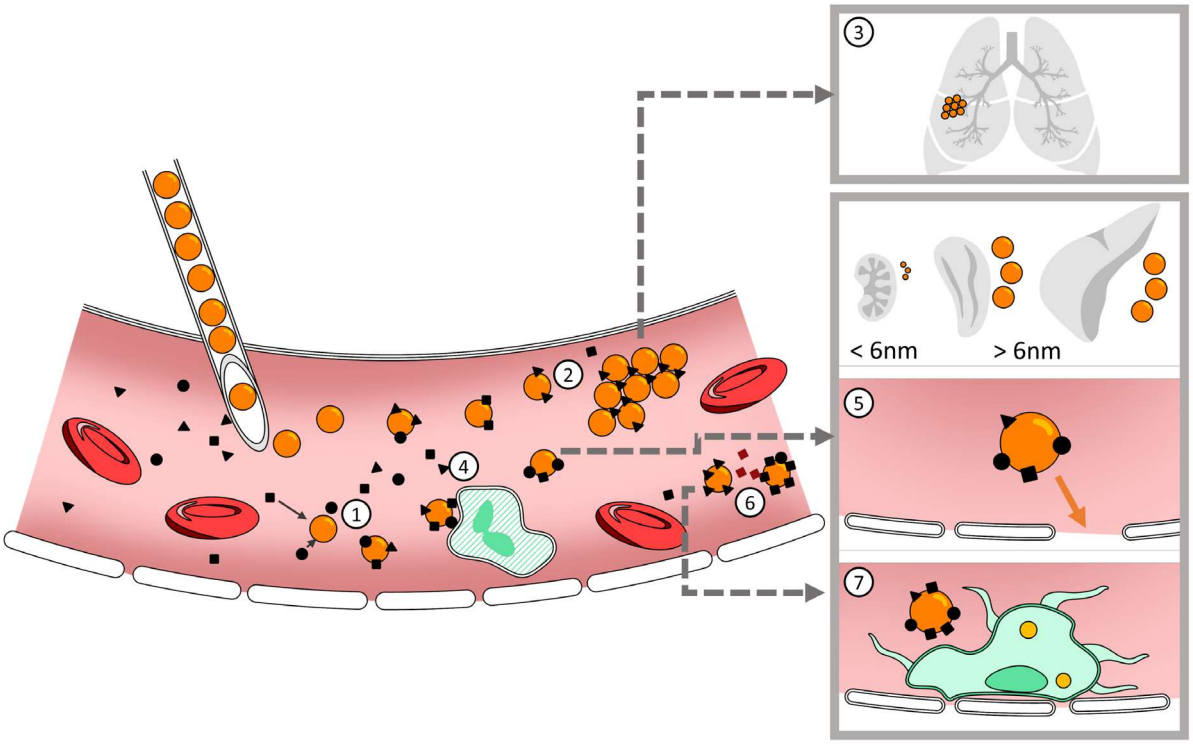

Figure 6: Events of blood elimination of i.v. injected nanocarriers *in vivo*.

The image shows a blood vessel into which nanocarriers (orange balls) are injected. In the blood vessel reside blood protein components (black symbols) and a phagocyte blood cell (grey). Events of blood elimination: (1.) Formation of the corona upon contact with blood. (2.) Aggregation of nanocarriers caused by plasma components. (3.) Sticking of aggregates in the first capillaries (lung), if aggregation occured. (4.) Interaction and uptake by blood cells (granulocytes). (5.) Extravasation through epithelial slits in liver and spleen. (6.) Opsonization of particles. (7.) Internalization by macrophages in blood vessels. While small particles (<6 nm) are secreted by the kidney [38], larger particles are filtered in the liver and spleen by the microanatomical endothelial constitution.

1.2.4 The role of the spleen

1.2.4.1 The structure and functional anatomy of the spleen

As the most perfused organ in the body, related to its weight [58], the spleen is predestined to filter blood cells and blood-born organisms. The micro-anatomical structures, the sinusoids filter old and broken blood cells like a sieve [59]. Foreign bodies such as blood germs are internalized by the scavenger receptors of the macrophages in the marginal zone [60]. From a pharmacological point of view, it appears that the spleen is a relevant organ for the blood clearance of nanodimensional therapeutics and thus for their pharmacokinetics [61].

The anatomy of the spleen is outlined in Figure 7 A. Blood enters the spleen by the splenic artery and reduces flow speed when entering the central arterioles of the lymphoid tissue. The continuous sheath of T- and B-cell areas, which is perfused by smaller arterioles is defined as the white pulp. Most of the blood volume passes the anatomical border of the white pulp which is an area called the marginal zone. The marginal zone separates the white pulp from the red pulp and the vessels are lined out by macrophages expressing a wide set of scavenger receptors [62]. Also, B-cells, fibroblasts and in humans T-cells, glide out this zone [62]. Through the marginal zone the blood is directed to the red pulp, passing the cords and venous sinuses [63]. By passing from the cords into sinuses at low flow speed, damaged and old red blood cells are withheld by sinuses formed of stress fibers and parallel endothelial cells [64] (Figure 7 B). The filtered particles are phagocytized by the local macrophages of the red pulp [55, 65].

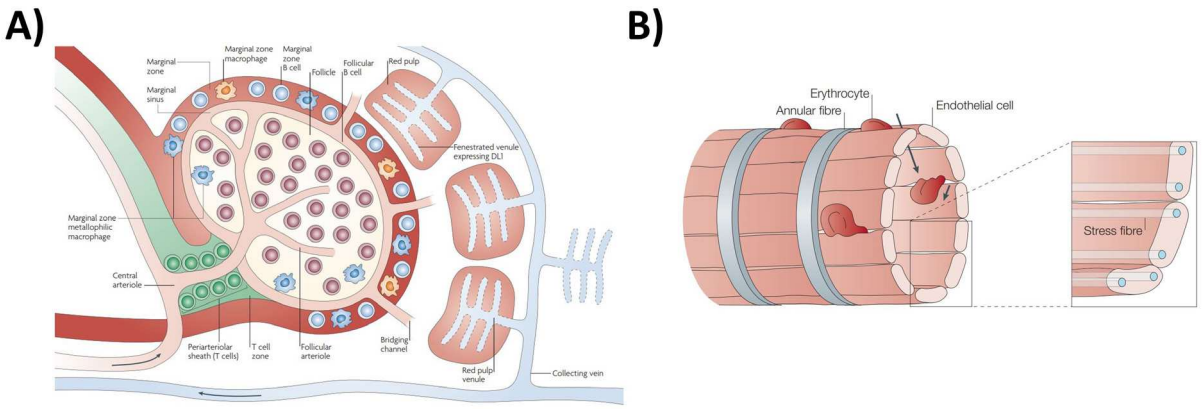

Figure 7: Microanatomical overview and structure of the spleen.

A: Schematic view of the anatomy of the spleen.[4] **B:** Microanatomical structure of venous sinuses located in the chord of the red pulp.[5]

[4] Reproduced with permission of the publisher. 66. Pillai, S. and A. Cariappa, *The follicular versus marginal zone B lymphocyte cell fate decision.* Nature Reviews Immunology, 2009. **9**(11): p. 767-777.. Copyright (2009) Nature Reviews Immunology.

[5] Adapted with permission of the publisher. 64. Mebius, R.E. and G. Kraal, *Structure and function of the spleen.* Ibid.2005. **5**: p. 606. Copyright (2005) Nature Reviews Immunology.

1.2.4.2 The four macrophage subtypes of the spleen

The unique anatomical structure of the spleen and the different and specialized functions of the tissue evoke four subtypes of macrophages that can be crystallized in the organ [62] (see Table 4). The white pulp macrophages (WPM) are supposed to exhibit similar functions as the macrophages located in other, secondary lymphatic organs [62]. These macrophages in the T-cell area lack expression of F4/80 in the mouse [62, 67]. The red pulp macrophages (RPM) in mice mostly express F4/80 [68]. There are two types of macrophages in the marginal zone: SIGN-R1 (CD209b) positive marginal zone macrophages (MZM) and the Sialic acid-binding immunoglobulin-type lectin 1 (Siglec-1) (CD169) expressing marginal metallophilic macrophages (MMM). SIGN-R1 is a C-type lectin mediating recognition of saccharides of bacteria and Siglec-1 acts as a receptor responsible for uptake of germs. The macrophages of the marginal zone show a high capacity to clear and degrade various bacterial organisms and viruses. [62]

Table 4: Summary on the four splenic murine macrophage populations.

Abb.	Macrophages	Physiological function	Marker expression
WPM	White pulp macrophages	Uptake and digestion of apoptotic cells in the germinal center	F4/80$^-$, CD68$^+$, CD11b$^-$
RPM	Red pulp macrophages	Uptake and and digestion of erythrocytes	F4/80$^+$, CD68$^+$, CD11b$^+$
MZM	Marginal zone macrophages	Internalization, phagocytosis and degradation of bacteria, viruses and parasites	CD209b$^+$
MMM	Marginal metallophillic macrophages	Mediation of antigens to dendritic cells, internalization, phagocytosis and degradation of bacteria, viruses and parasites	CD169$^+$

Source of content: [67, 69].

1.2.4.3 The (‘undesired’) cellular uptake of nanocarriers in the spleen

Due to the favorable position in the marginal zone and the predisposition in pathogen clearance, especially the macrophages of the marginal zone are prone to internalize nanocarriers [57]. Larger particles are filtered in the chords of the red pulp [65], what leads to subsequent phagocytosis by the RPM macrophages [61]. Especially non-PEGylated liposomes, accumulate in the spleen [5] and thereby the spleen can influence the pharmacological effect of the drug. Nevertheless, the spleen is a target organ for certain applications.

Nanovaccines, as the protein-based antigen shell capsule (see 1.1.2), transport antigens and adjuvants to dendritic cells and effectively mediate an immune response through them. Anti-tumor nano-vaccinations have shown the be more effective via i.v. administration compared to subcutaneous injection [70]. Intravenous administration of nanovaccines induces a strong anti-tumor immune response mediated in the spleen [21, 32, 71, 72]. The high density of DCs and the large T-cell areas are favorable to successfully evoke an adaptive immune response. (Figure 8).

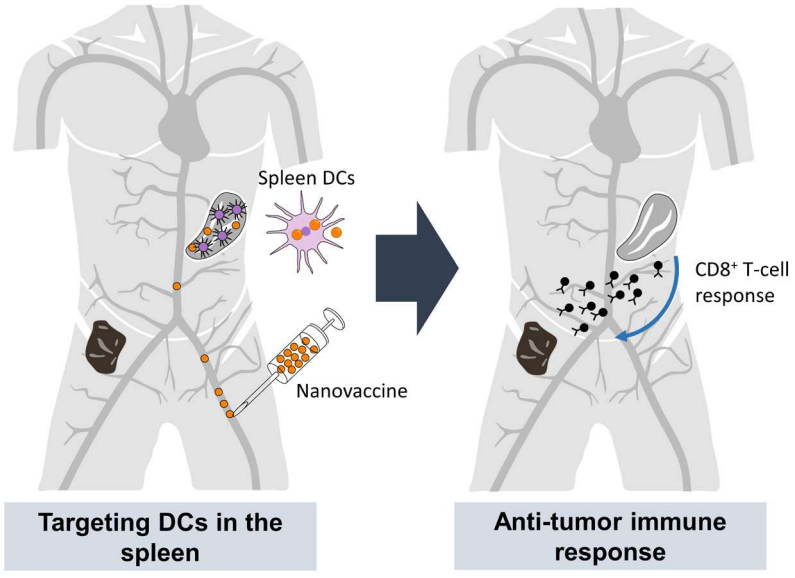

Figure 8: I.v. administered nanovaccine evokes the anti-tumor response *via* the spleen.

1.2.4.4 The spleen mediating the immune response

In addition to its ability to purify the blood, the spleen is an important immunological organ. The whole lymphatic system flows there together. In the white marrow of the spleen, T- and B-cell areas are located, which contribute to the adaptive immune responses [64]. Guilliams et al. [73] defines four dendritic cell subtypes, which occur in the spleen (Table 5): Conventional

dendritic cells type 1 (cDC1), conventional dendritic cells type 2 (cDC2), plasmacytoid dendritic cells (pDC) and monocyte derived dendritic cells (mDC). cDC1 and cDC2 are cross-presenting the antigen to $CD8^+$ and $CD4^+$ T-cells respectively and thereby mediate the specific immune response against antigens [74-76]. mDCs express MHCII and are able to cross-present antigens to CD4+ T-cells [77-79]. Mainly the conventional type 1 dendritic cells (cDC1) mediate a $CD8^+$ T-cell (cytotoxic T-cell) response, which in the end selectively eliminate the tumor cell [80]. pDCs mediate interferon 1 dependent downstream processes [81]. A shematic representation of immune response evocation *via* dendritic cells by a nanovaccine was already shown in Figure 2 (see 1.1.2).

Table 5: Overview on the four splenic murine dendritic cell populations.

Abb.	Dendritic cells	Function	Marker expression
cDC1	Conventional dendritic cell type 1	Cross-presenting the antigen to $CD8^+$ T-cells	$CD11c^+$, $MHCII^+$, $CD8^+$
cDC2	Conventional dendritic cell type 2	Cross-presenting the antigen to $CD4^+$ T-cells	$CD11c^+$, $MHCII^+$
pDC	Plasmacytoid dendritic cell	Interferon 1 dependent downstream processes	Siglec H^+
mDC	Monocyte derived dendritic cell	Cross-present antigens to $CD4^+$ T-cells	$MHCII^+$, $CD11b^+$

Source of content: [73].

1.2.5 The role of the liver

1.2.5.1 Function and anatomy of the liver

The liver is the largest gland within the organism and fulfilling multiple functions. The liver parenchymal cells, hepatocytes, secrete the bile, which is transported by the bile duct into the duodenum. Hepatocytes in addition store vitamins, glycogen and iron. Further the organ is regulating hormones and metabolizes waste products for renal and hepatobilar elimination. [82] As an organ highly supplied with blood and connected to the arterial circulation, it filters blood from blood-born organisms and foreign bodies - alike the spleen [83]. From an immunological point of view, the liver is an important organ in the fight against pathogens [84] but also for mediating immune tolerance [85].

The parenchymal cells, the so-called hepatocytes, make up the majority of the liver cells. The non-parenchymal liver cells (NPCs) consist of about 66-75 % liver sinusoidal endothelial cells and 25-33 % Kupffer cells (Kupf) [86, 87]. In addition, hepatic stellate cells, cholangiocytes, migrated and resident immune cells contribute to the non-parenchymal cells [88].

There are also microanatomical peculiarities in this organ, which are particularly relevant for the non-specific uptake of nanocarriers [89]. Sinusoids connect the portal triads and central veins, where the arterial blood and of the portal vein tile together [90]. The sinusoids are lined by specific endothelial cells, the liver sinusoidal endothelial cells (LSECs). The Kupf reside inside the blood vessel (Figure 9) [91]. The LSECs form the fenestrae, which allow a direct interaction of plasm components and parenchymal cells in the space of Disse. Particles of up to 150 nm can extravasate these vascular slits [89, 92]. (Figure 9)

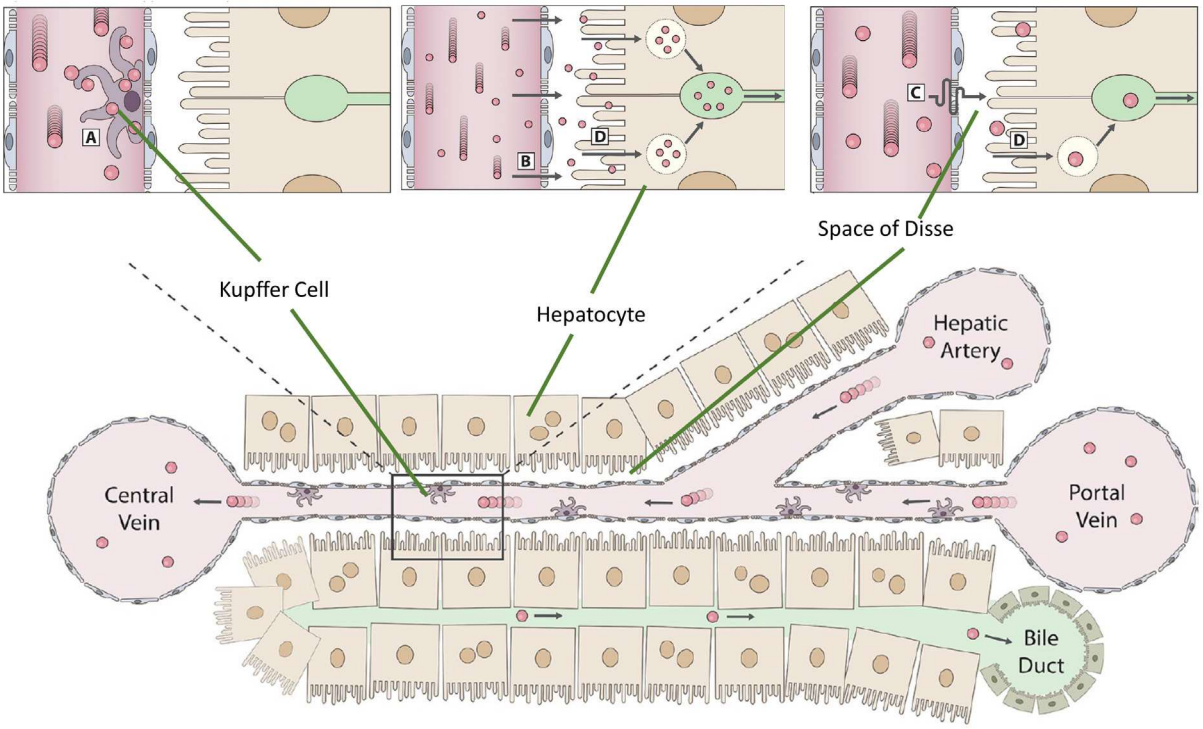

Figure 9: Schematic illustration oft the blood clearance of nanoparticles by the liver.

Top left: Kupf internalize and take up nanocarriers. *Top middle:* Small nanocarriers (< 150 nm) evade through the fenestrae into the space of Disse. *Top right:* Larger particles (> 150 nm) have difficulties passing the fenestrae of the LSECs.[6]

1.2.5.2 The (‘undesired’) cellular uptake in the liver

Kupf make up 80-90% of the total macrophages in the body and thus represent an essential part of the primary immune response [93, 94]. Equipped with various scavenger receptors, Kupf are able to recognize and internalize foreign particles and absorb them through various mechanisms [95]. At already 2 nm, Kupfs take up particles [96]. “Larger particles may display

[6] Adapted with the of the publisher permission from 89. Poon, W., et al., *Elimination pathways of nanoparticles.* Acs Nano, 2019. **13**(5): p. 5785-5798. - Copyright (2019) American Chemical Society.

increased avidity due to their greater surface area for interaction with the cell membrane and adjacent receptors", Zhang et al. [39] concludes.

The non-specific uptake by Kupfs is a major challenge in nanomedicine delivering nanocarriers to the desired therapeutic site [56]. Nevertheless, this circumstance can be used for targeted delivery of inflammatory drugs in hepatite; Kupfs significantly contribute to the development of hepatitis through the release of inflammatory signaling molecules [97]. In chapter 3 we present a capsule, loaded with an anti-inflammatory polydrug (poly-dexamethasone), regulating the inflammatory activity of NPCs. In Table 6 the cells of the liver, which have significant effect on pharmacokinetics of nanocarriers are outlined.

Table 6: Overview on liver cells relevant for this work.

	Abb.	Cell	Function
Parenchymal cells	-	**Hepatocytes**	Parenchymal cells of the liver. • Metabolism of waste products. • Hepatobilar elimination. • Storage of vitamins, glycogen and iron.
Non-parenchymal cells (NPCs)	**LSEC**	Liver sinusoidal endothelial cells	Endothelial cell • Immune tolerance • Formation of fenestrae
	Kupf	Kupffer cells	Resident liver macrophages • Clearance of blood • Primary immunity
	DC	Dendritic cells	Induction of the adaptive immunity
	Mono, MO	Bone marrow derived immune cells (macrophages, monocytes)	Primary immunity

The table summarizes (1.2.5).

1.3 Heparin

1.3.1 The background of heparin

The high negatively charged bio-molecule heparin, which occurs in various tissues [98], is produced in the mast cells of Ehrlich [99]. The linear polysaccharide heparin consists of repeating disaccharide subunits of uronic acid-(1,4)-D-glucosamine. Complex sequences emerge from additional substitution of subunits with N-sulfate, O-sulfate and N-acetyl-groups [100]. The molecular weight of the unfractionated heparin (UFH) is around 10 - 20 kDa [101]. Today, UFH is still derived from animal tissue and therefore not a standardized molecule with a defined length and sequence. In 1940 – 1960, bovine lung material served for obtaining the anticoagulant with an activity of 140 U/mg. Later heparin has been gained from the mucosa of the swine or bovine reaching an activity of 180 - 200 U/mg [101].

Heparin was discovered in 1916 by McLean et al. [102] and the anticoagulant effect was described two years later by Howell et al. [103]. Due to the simple preparation of the initially-called ‘heparphosphatide’ from the liver, the name ‘heparin’ was derived later [102]. One must correct, heparin does not belong to the phosphatides because of absence of phosphor groups [104].

The anticoagulant effect of heparin [103], is caused by the activation of antithrombin III (ATIII). By binding of the serpin, ATIII, to a specific pentasaccharide sequence (Figure 10) [100, 105], which occurs in heparin but also in heparans of the vascular surface, a conformational change of the molecule activates its protease inhibiting activity [106] downregulating the function of the coagulation factor Xa. The UFH possesses also capacity to bind thrombin, forming a complex of heparin, ATIII and thrombin, impairing the activity of the coagulation factor IIa (thrombin) [107]. The activated serin protease (factor IIa) catalyzes various reactions of the coagulation cascade. Approximately one-third of the length of the disaccharide sequence have anticoagulant activity [108].

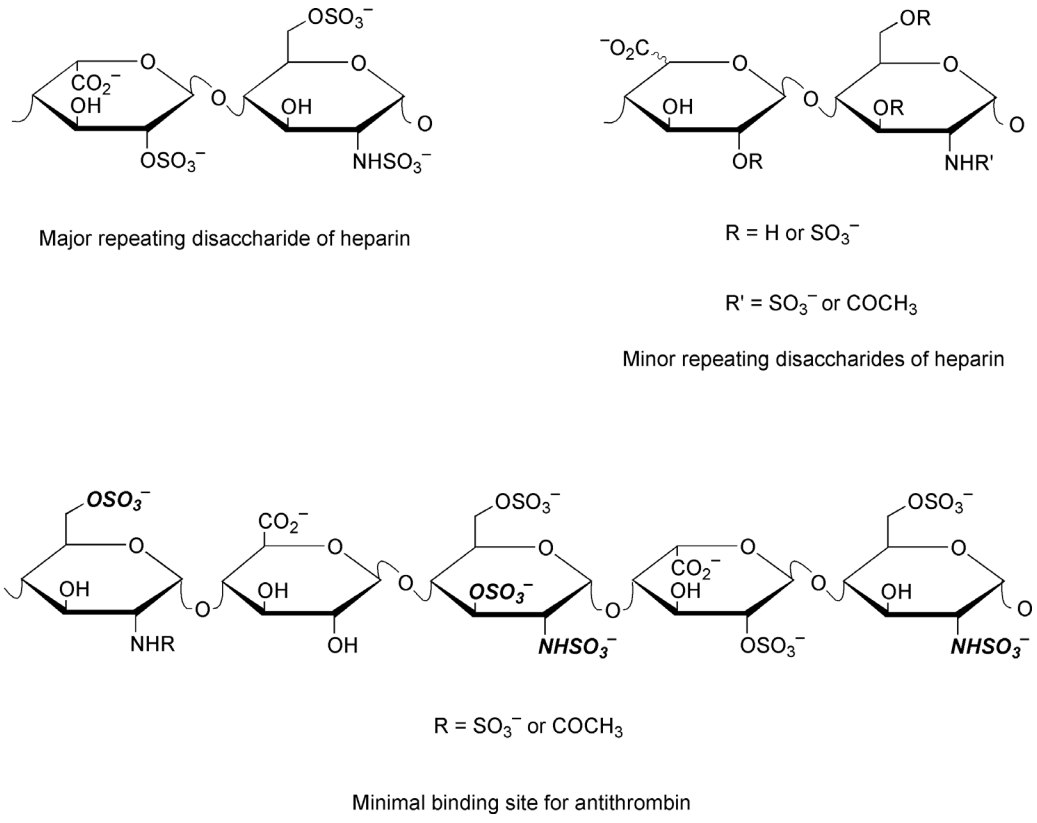

Figure 10: The chemical structure of heparin

Top left: Major repeating disaccharide sequence of heparin. *Top right:* Minor repeating disaccharide sequence of heparin. *Bottom:* Minimal binding side for AT III.[7]

1.3.2 The clinical use of heparin

Heparin is a broadly used anticoagulant applied both prophylactically and therapeutically [109]. UFH is applied i.v. in following clinical situations: During cardiovascular interventions, heparin is given i.v. at a high dose to evoke anti-coagulation for a defined period. Furthermore, heparin is administered i.v. over a period of days for treatment of thromboembolisms, pulmonary embolism and to prevent further cardiovascular events during a heart attack [110]. For prophylaxis of thrombosis, heparin is injected subcutaneously [110], what causes a continuous release into the blood and lower plasma concentrations of heparin [111]. While UFH still plays a role in the clinic, the low molecular weight heparins (LMWHs) now prevail for thrombosis prophylaxis and treatments of thromboembolisms [110] (see below).

The route of application influences pharmacokinetics. While i.v. injection causes a strong increase of serum concentration, the half-life is short. To keep a constant blood level, recurring boluses are required. Predicting pharmacokinetics of heparin is difficult because of the

[7] Reproduced with the permission of the publisher from 100. Rabenstein, D.L., *Heparin and heparan sulfate: structure and function.* Natural product reports, 2002. **19**(3): p. 312-331. Copyright (2002) Royal Society of Chemistry.

heterogeneity of molecular weights. For a long time there has been no conventional method available to determine the concentration of heparin directly. Maurer et al. established an approach to determine heparin directly, forming by titration of protamine nanoparticles which formation is measured by dynamic light scattering [112]. For monitoring heparin concentration in the blood directly, as necessary during cardiac surgery, the activated clotting time (ACT), which was established in 1966 [113], is the method of choice. However, this indirect method is influenced by temperature and individual coagulation parameters of the patient [112]. It is difficult to find a specific antibody on the market, to detect heparin by an immunoassay. The reason for this is most likely the heterogeneity of the molecule and its wide distribution in animals and humans.

1.3.3 The pharmacocinektics of heparin

Boneau et al. [114] described the pharmacokinetic behaviors of heparins in rabbits (Figure 11). Basically, there are two mechanism removing heparin from the blood: a saturable mechanism, which is dose dependent, and a mechanism correlating to the dose linearly [111]. Boneau et al. [114], with regard to the evidence of the literature, assumes behind the saturable mechanism, the RES and endothelial cells. Dawnes et al. [115] analyzed the biodistribution of heparin and showed a strong accumulation in liver and weaker accumulation in the spleen, lungs and kidneys using iodinated heparin. Histochemically it was shown, that heparin is adsorbed by cells of the endothelium [116]. RES cells (The RES is described in 1.2.2 - 1.2.5) take up and store the polysaminoglycane [117]. The meaning of phagocytosis of macrophages for the pharmacokinetics of heparin was shown by blocking the RES [118]. The affinity of binding endothelium is dependent on the molecular weight [119] and is lower for LMWHs [114, 120]. The linear elimination process of heparins (Figure 11) is evoked by the renal clearance and predominantly active at high doses, whereas at low doses the saturable mechanism takes over the major part of clearance [114]. At high initial concentrations of heparin (> 200 U/kg), the elimination curve was reported having a concave-convex shape. At low doses (< 100 U/kg) the elimination behaved in an exponential manner [111, 121]. Following at higher doses the half-life is prolonged. When heparin is applied subcutaneously, the plasma concentrations depending on dose are 12 - 40 times lower than applied intravenously. The clearance then is mainly caused by the saturated cellular mechanism and the polysaminoglycane has to diffund from the interstitium into the blood [114].

An initial bolus in cardio vascular surgery ranges to 300 - 400 U/kg body weight, other boluses of 5,000 U follow to keep a high anticoagulant level [122, 123]. Assuming a blood volume of 5 liters for a person of 70 kg, the initial blood concentration of heparin is around 4,200 U/l (4.2

U/ml). For this dose half-lifes were estimated around 107 minutes [122] and 153 minutes [123] in literature.

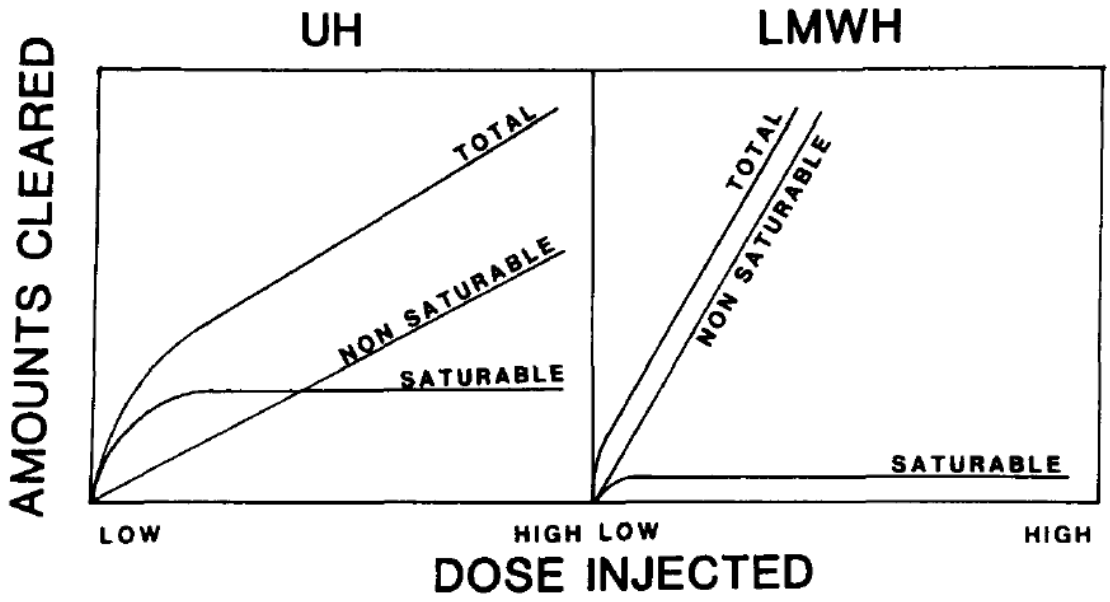

Figure 11: Schematic representation of heparin clearnce after i.v. injection.[8]

1.3.4 Excurse: Low molecular weight heparins (LMWHs)

LMWHs are fractions of heparin generated by controlled enzymatic or chemical processes. LMWHs differ from UFH by their molecular weight, which is around 5 kDa and the pharmacokinetics, which are more predictable for LMWHs [124]. LMWHs have fewer binding abilities to endothelial cells and RES-cells (saturated mechanism of clearance) leading to a longer half-life than UFH [125] (see Table 7). In contrast to UFH, LMWHs are predominantly removed from the blood by the kidney and therefore exhibit more predictable pharmacokinetics. Examples of enzymatic cleaved LMWHs are Enoxaparin and Tinzaparin. Fondaparinux, is a synthetic heparin, consisting only of the ATIII-binding sequence and therefore exhibits a high anti-Xa activity towards anti-factor IIa acticity [126] (see Table 7).

According to the Analysis of Credence Research, the market share by product in 2016, for UFH was around 15%, for LMWH around 60 % and for ultra-low molecular weight heparins (e.g. Fondaparinux) around 25% [127].

[8] Reproduced with the permission of the publisher from 114. Boneu, B., C. Caranobe, and P. Sie, *3 Pharmacokinetics of heparin and low molecular weight heparin.* Bailliere's clinical haematology, 1990. **3**(3): p. 531-544. Copyright (1990) Elsevier.

Table 7: Comparision of UFH and a selection of LMWHs.

	Heparin (UFH)	Enoxaparin	Tinzaparin	Fondaparinux
Brand name		Clexane®	Innohep®	Arixtra®
Molecular weight	10-30 kDa	4.6 kDa	6.5 kDa	1.7 kDa
Plasm elimination half-life (h)	0.5-2	4.5	3.4	17
Anti-Xa activity	180 - 200 U/mg	100 U/mg	100 U/mg	NA
Anti-Xa/IIa ratio	NA	3.8	2.8	selective anti-Xa

Source of content: [126] and [128].

1.3.5 Heparin and its effect on cellular uptake of nanocarriers

The constitution of the nanocarriers' protein corona decisively influences cellular uptake *in vitro* and *in vivo*. Implementation of opsonin, like complement factors can trigger uptake by macrophages. The composition of the protein corona is defined by the surrounding medium of the nanocarriers. Schöttler et al. [45] have shown that adding of heparin into the process of protein corona formation causes a reduction of uptake of amino-functionalized polystyrene particles in HeLa cells. Schöttler et al. [45] for their study applied a heparin concentration of 17 U/ml, which is present in plasma after blood has been drawn into heparin blood collecting vials. Champanhac et al. [129] investigated the effect of heparin implementation into the protein corona of amino-functionalized polystyrene particles at clinically relevant heparin concentrations (0 – 4 U/ml). In this study, human plasma was used for formation of the heparin-protein corona. Champanhac et al. [129] observed significantly reduced uptake of coated particles into HeLa cells with a heparin concentration at 0.25 U/ml. For formation of the corona either human citrate plasma was supplemented with heparin before adding to the polystyrene particles or particles were coated with plasma first and subsequently incubated with heparin (Figure 12). While Champanhac et al. [129] have observed a reduction in HeLa cells the uptake increased in RAW 264.7 cells. Primary human monocytes from blood, alike HeLa cells, reduced the uptake of heparin-plasma coated polystyrene particles, while primary derived macrophages increased the uptake of particles coated with heparin.

There have no studies occurred on the effect of heparin on the uptake of nanocarriers *in vivo* yet*;* Despite the fact that heparins have a fairly broad application and nanodimensional therapies have become more frequent.

Still, we have found one study from the year 1986 on the effect of heparin-modified LDL (low density lipoproteins) on the uptake into the aortic vessel. LDL are complexes of CHOL and proteins of the lipid transport (22 nm) [130]. Srinivasan et al. [131] observed: "The intravascular

clearance of native and heparin-complexed LDL remained essentially the same, … but the aortic uptake of heparin bound LDL was 30% less than the native LDL." [131]. The group suggested a reduced binding of the heparin-complexed LDL to proteoglycans of the tissue.

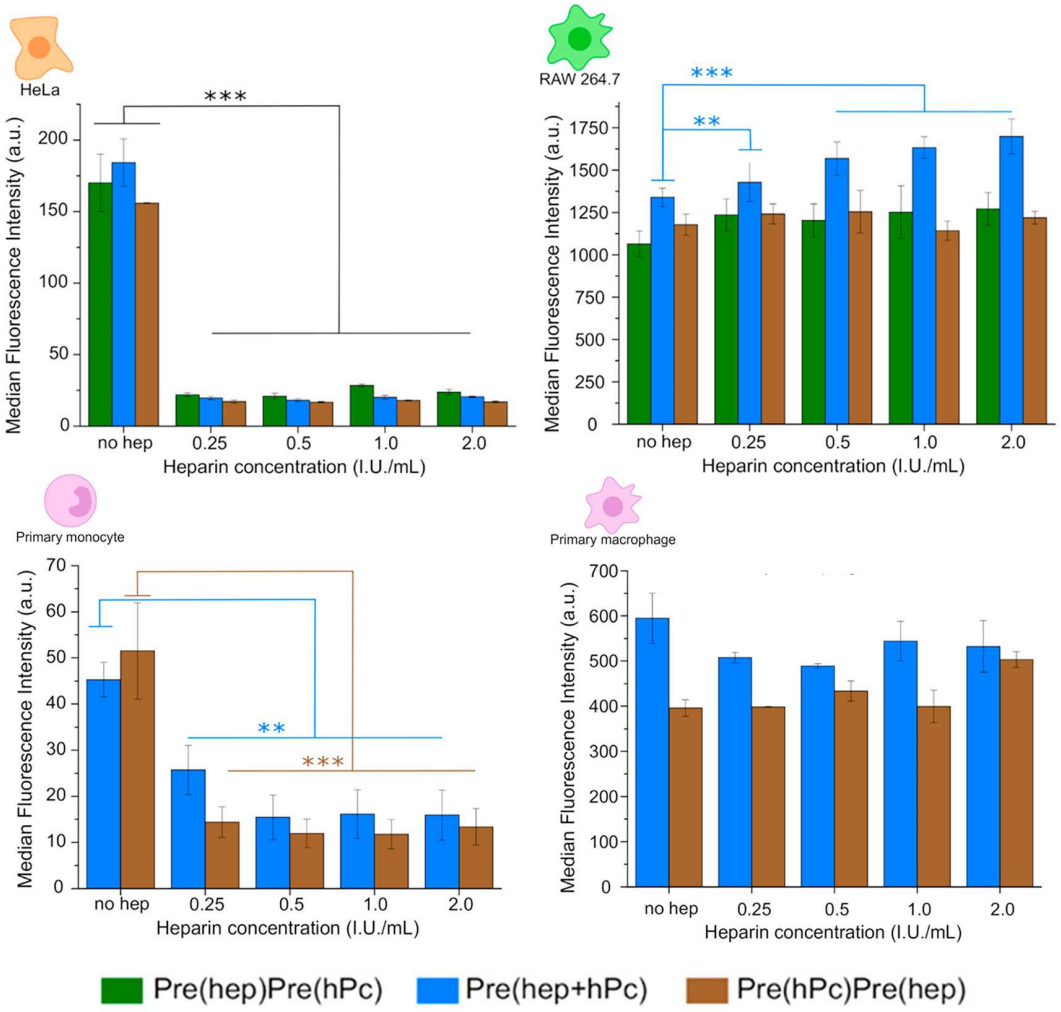

Figure 12: Adding of heparin into the process of corona formation of nanocarriers changes uptake.

Amino-functionalized polystyrene particles were incubated with human citrate plasma (hPC) and heparin (hep) in different order (see legend below). *Green:* 1. hep 2. hPc, *blue: 1.* hep + hPc, *brown:* 1. hPc 2. hep. The uptake into the HeLa, RAW264.7, primary monocytes and primary differentiated macrophages was investigated by flow cytometry.[9]

[9] Adapted with permission of the publisher from 129. Champanhac, C., et al., *Timing of Heparin Addition to the Biomolecular Corona Influences the Cellular Uptake of Nanocarriers.* Biomacromolecules, 2019. **20**(10): p. 3724-3732. Copyright (2019) American Chemical Society.

2 Aims

Nanocarriers are drug containers that significantly influence the pharmacokinetics of the loaded substance. When nanocarriers are applied intravenously, there are several factors that influence the bioavailability of the drug. Nonspecific uptake by the phagocytosing cells of the RES reduces the blood circulation time and thus the likelihood of uptake into the target cell. Once at the target site, the ability of the particulate system to release the loaded compound intracellularly determines bioavailability and thus pharmacological effect. Ultimately, pharmacokinetics influences the therapeutic outcome of nanotherapies. (Figure 13)

The goal of this work was to investigate effects that alter the pharmacokinetics of nanocarriers and thus have the potential to change therapeutic outcomes.

The main objective was to investigate the effect of a concomitant heparinization on the pharmacokinetics of nanodimensional drugs. The findings on the polysaminoglycan heparin, revealed a modulatory ability for nanoparticle uptake of the molecule into phagocytes. Phagocytes of the RES significantly influence the pharmacokinetics of the nanocarrier (see 1.2), and heparin at the same time is a widely used and established drug (see 1.3). No studies exist on the influence of heparin on nanotherapies, although heparin is a commonly co-administered drug. The first objective was to investigate the manner in which heparinization alters the nonspecific uptake of clinically relevant liposomal formulations into the RES. (see 3, chapter 1) Second, the potential of heparin to modulate the unspecific cellular uptake by macrophages and the favorable uptake by DCs of the protein-based nanovaccine, OVA-NC, should be unraveled. Targeting of nanovaccines towards DCs, based on surface modification with sugars or antibodies, has been already investigated [132]. The use of a co-applied molecule to enhance targeting is innovative. In addition, the cellular- and biodistribution of the novel protein-based nanovaccine. (see 4, chapter 2)

Further, we tailor how the design and composition of nanocarrier systems can influence pharmacokinetics. We present a novel system combining the benefits of targeted uptake and controlled release: The polydexamethasone (PDXM)-loaded mesoporous silica nanocapsule (SiO2 NC-PDXM) as a model for a capsule containing a pH-sensitive polymerized drug. The aim was to investigate biodisitrbiution to confirm the targeted uptake into Kupffer cells and the higher efficacy of SiO2 NC-PDXM compared to dexamethasone (DXM) or PDXM alone. (see 5, chapter 3) Destabilized liposomal *de novo* formulations should be analyzed for the intracellular release of DXR. Combining flow cytometry and microscopy an approach with high statistical validity with the Amnis® Imagestream®XMark II, was established. (see 6, chapter 4)

The versatility of nanocarriers in terms of structure and application, as well as their complex pharmacokinetics, require a high level of understanding for further development and clinical

applications. This work is intended to provide insights that contribute to the overall understanding of the pharmacokinetics of nanodimensional therapeutics.

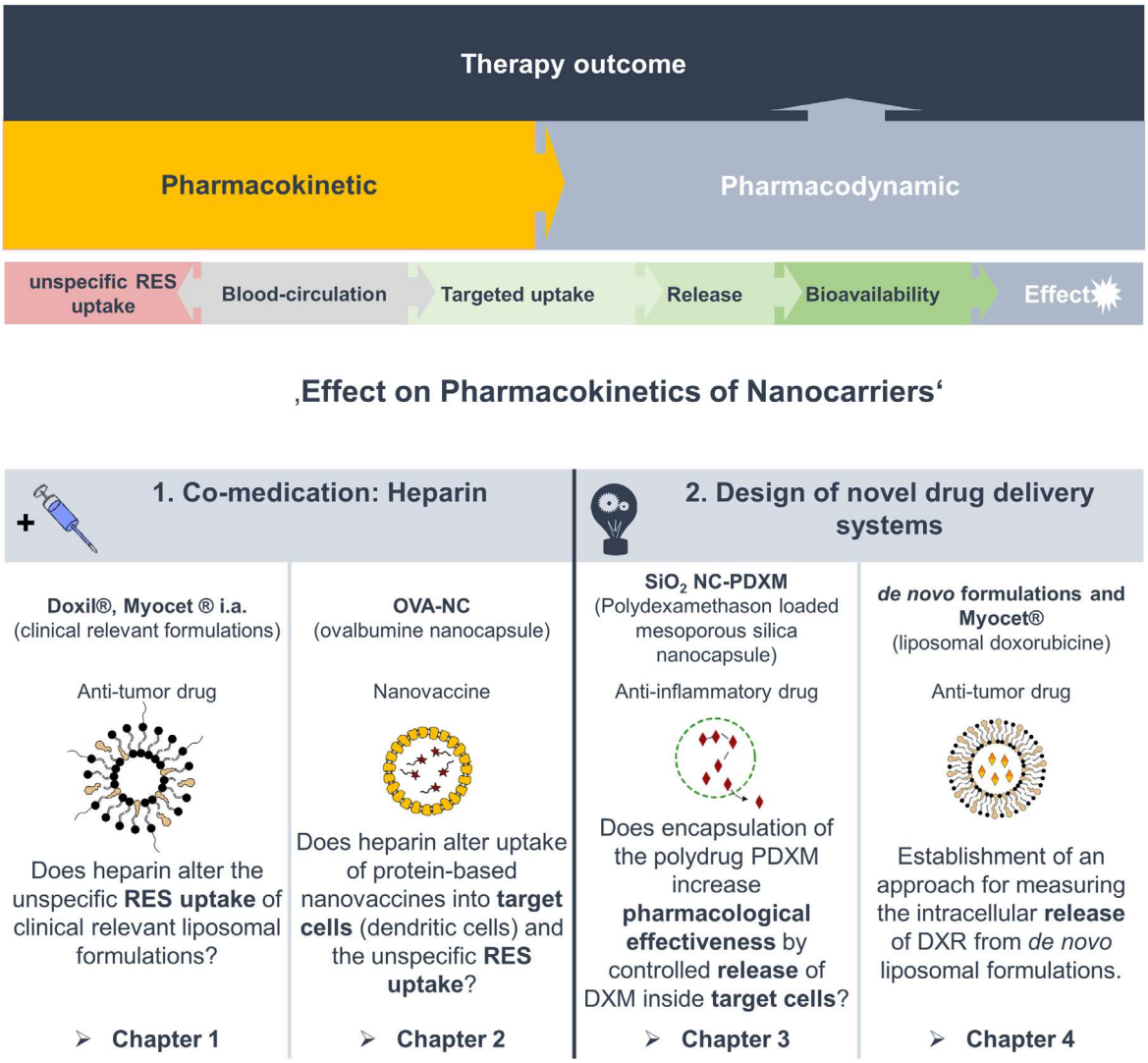

Figure 13: Summary: Background and objectives of the thesis.

3 Chapter 1: Heparin and Liposomes

This chapter, in form of a scientific paper, represents the first part of the main project of the thesis (co-medication of heparin). The manuscript is planned to publish in 2021. The work was a collaboration with the group of [redacted], Institute of Pharmaceutical and Biomedical Sciences at the Johannes Gutenberg-University Mainz. [redacted] kindly provided all liposomes. Further group members assisted when carrying out the animal experiments.

High dose Heparinization has the Potential to modulate the Uptake by RES-cells *in vitro* and to alter Biodistribution of Liposomes *in vivo*

[redacted]

[a] Department of Dermatology, University Medical Center of the Johannes Gutenberg-University Mainz, Langenbeckstrasse 1, 55131 Mainz, Germany

[b] Max Planck Institute for Polymer Research, Ackermannweg 10, 55128 Mainz, Germany

[c] Institute of Pharmaceutical and Biomedical Sciences, Johannes Gutenberg University, Staudingerweg 5, 55126 Mainz, Germany

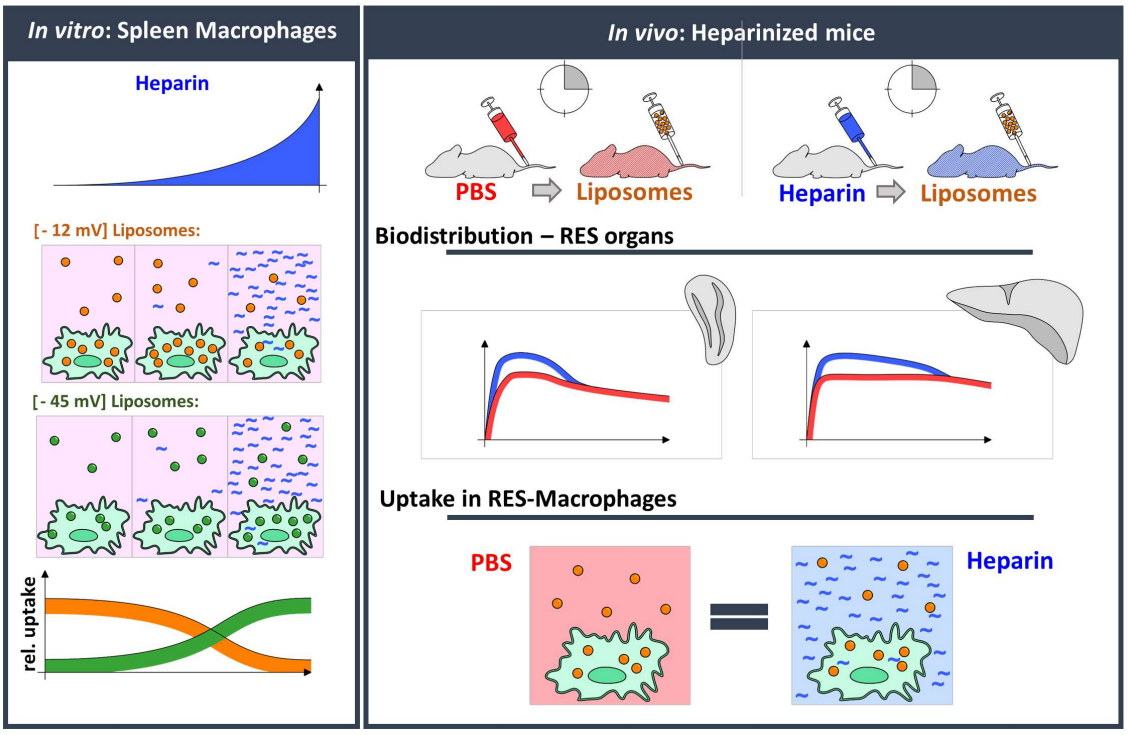

Figure 14: Graphical abstract chapter 1 - Heparin and Liposomes.

3.1 Abstract

The field of nanodimensional therapeutics is constantly growing, with the use of liposomes becoming more frequent in clinic. During liposomal therapy patients can be co-treated with heparin e.g. in the course of cardiovascular events. If heparin effects pharmacokinetics of liposomal therapies, the design of several medications in clinic has to be reconsidered.

The uptake of clinically relevant liposomal formulations into RES-cells cultured under physiological concentrations of heparin (0 - 4 U/ml) was quantified by flow cytometry. Considerable changes were observed at the highest concentration of 4 U/ml heparin. The formulation of Doxil® exhibited a significant decrease of the uptake in the red pulp macrophages.

Moreover, we studied the effect of a high-dosed intravenous (i.v.) heparinization on the biodistribution and cellular uptake of liposomes (Doxil® formulation) in mice for the timepoints 30, 120, and 360 minutes. The *In Vivo* Imaging Spectrum (IVIS) analysis of the organs revealed a significant increase of uptake in the liver at 30 and 120 minutes, and for the spleen at 120 minutes. At 360 minutes the differences of biodistribution of Lip-Dox equalized.

The study shows that an i.v. high dose heparinization causes a slight, but significant effect on the pharmacokinetic of liposomes *in vivo*. Therefore, we conclude that heparinization of patients may not affect strongly the pharmacokinetics and therapy outcome of liposomal treatment.

3.2 Introduction

The anticoagulant heparin, which is administered in the course of thrombosis preventive measurements and cardiovascular events, often is applicated in conjunction with other medications. It is very likely, that some patients undergoing liposomal therapies also obtain a heparinization. The interaction between nanoparticles and heparin from a clinical point of view has not been investigated yet.

Heparin is a negatively charged biomolecule containing sulfonic groups and belongs to the family of glycosaminoglycans [1-3]. Schöttler et al. [11] and Champanhac et al. [12] showed the potential of heparin to modify the uptake of polystyrene nanoparticles into specific cell types, especially in phagocytes. The incorporation of heparin into the protein corona of amino-functionalized polystyrene nanoparticles led to a significant decrease of uptake into HeLa cells and human primary monocytes [12]. It was observed, that this effect is dependent on the cell type, the concentration of heparin and the surface modification of the nanoparticle. The exact mechanism of this observation has not been clarified.

Doxorubicin (DXR) loaded liposomal nanocarriers are one of the most commonly applied nanotherapeutics since the FDA approval of Doxil® in 1995 [4-6]. The main function of those drugs is to transport effectively small molecular substances to target cells (e.g. tumor cells) and to reduce the adverse effects of the active ingredient [7]. The anti-tumor drugs Doxil® and Myocet® encapsulate both DXR but differ in surface characteristics: whereas the formulation of Doxil® is decorated with PEG-chains [8], Myocet® is not [9]. This results in an altered biodistribution and lower circulation time for Myocet® compared to Doxil® [10]. Ambisome® carrying the active substance, amphotericin B, within the lipid layer and is applied in clinical therapy for severe fungal infections [9].

The interactions of nanodimensional therapeutics with the reticulo endothelial system (RES) plays a major role for the blood clearance and pharmacokinetics. Sequestration of nanocarriers in the phagocytes of the RES shortens the circulation time of the nanodimensional drugs and thereby negatively influences the efficiency of the medication [13, 14]. A large proportion of nanocarriers is filtered in the liver and spleen where local phagocytes take up the nanocarriers [15, 16]. From a physiological point of view, the RES is responsible for sequestration, clearance and digestion of larger particles such as pathogens, damaged blood cells and other exogenous larger particles [19, 22, 23]. The special microvascular structure in liver and spleen creates conditions for the effective interception of nanocarriers [18, 24, 25]. Doxil®, Myocet® and Ambisome® are mainly captured by the liver [10, 26]. Taking into account the organ size of liver and spleen, a higher density of liposomes must accumulate in the spleen, pointing out the ‘emerging role of the spleen’ [16] for the liposomal drugs.

Based on the findings of Champanhac et al. [12], we want to investigate if a heparinization can influence the pharmacokinetics of liposomal nanocarriers. We focused on the non-specific uptake into the RES because of its important role for the outcome of liposomal therapies [13, 14] and because of the *in vitro* results on phagocyte cell lines obtained before [12]. Changes of pharmacokinetics of liposomes caused by the presence of heparin would be a caveat for the co-administration of anti-coagulants with liposomal therapies.

3.3 Results

Studying the cellular uptake and biodistribution of clinically relevant liposomal formulations, liposomes were labelled with the lipophilic dyes DiD and DiR, which were incorporated in the lipid layers (see 8.1.2). We prepared liposomes with the known lipids of the liposomal formulation, without incorporating the active pharmaceutical ingredient for Myocet® (Lip-Myo) [133], Doxil® (Lip-Dox) [4, 134], and Ambisome® (Lip-Amb) [18]. In the presented study heparin concentrations of 0 - 4 U/ml, which are physiologically compatible and clinically relevant, were applied.

3.3.1 The effect of heparin on the uptake of splenic phagocytes *in vitro*

Previously, the uptake of polystyrene nanocarriers by HeLa and RAW 264.7 cells was significantly influenced by the presence of heparin in the biomolecular corona [12]. To build on this findings, “Lip-Dox liposomes were incubated with HeLa and RAW 264.7 cells in a solution containing human serum and heparin (Supplement 1 A). Similar results to polystyrene nanocarriers were obtained, with a sharp decrease of the uptake in HeLa in the presence of heparin (Supplement 1 B). For RAW 264.7, the results are less straightforward. Initially, a decrease of the uptake is observed at low heparin concentration (0.25 U/mL), yet again the increase of uptake observed previously was detected but the uptake level at 4.0 U/mL is equal to the no-heparin condition (Supplement 1 C, D). Therefore, it would appear that low heparin concentrations affect the uptake of Lip-Dox into RAW 264.7 macrophages rather than high as shown previously [12]. This trend confirms the importance of further studies of the uptake of liposomal formulation in phagocytes in a more clinically relevant setup as described thereafter.”[10] Indeed, the aim was to investigate the effect of heparin on uptake of splenic phagocytes as the unspecific uptake into the RES potentially influences liposomal therapy. The whole spleen cell suspension was cultured in 5% mouse serum to provide the similarity to the *in vivo* nanocarrier’s protein corona. Heparin was added at a final concentration of 0, 0.25, 1 and 4 U/ml to the cell culture media followed immediately by the addition of the liposomes (Figure 15 A).

[10] This section was contributed by Dr. [redacted] group of Prof. Volker Mailänder, Max Planck Institute for Polymerresearch.

Based on the assumption that specific characteristics of the cell can be responsible for the cell-type specific response to heparin, we used a flow cytometry staining approach in order to determine the subsets of spleen macrophages (Supplement 2 A, Table 23). Following populations were defined by flow cytometry: Monocytes (Mono), Red pulp macrophages (RPM), White pulp macrophages (WPM), marginal zone macrophages (MZM), dendritic cells (DC), eosinophils (Eos) (Figure 15 B). The signal of the liposomes' dye, DiD, was measured in order to evaluate the cellular uptake (Supplement 2 B).

The proportion of cells that are positive for DiD within the entire population, '% of uptake', for three of the formulations were highest for the MZMs (43% Lip-Amb (DiD), 56% Lip-Myo (DiD), 36% Lip-Dox (DiD), 20% Lip-Myo-PEG (DiD)) (Figure 15 C), which was underlined by the data of the median fluorescence intensity (MFI) of DiD (Supplement 3 A). This observation is in accordance with the finding of Demoy et al. [57] describing the strong capacity of MZMs to internalize particles *in situ*. For all tested formulations, the uptake into the Mono population was strikingly lower for both parameters. In line with the theory, PEGylation reduced uptake by macrophages comparing the formulations Lip-Myo (DiD) and Lip-Myo-PEG (DiD). The measured values for Lip-Myo-PEG (DiD) were overall convincingly lower than for Lip-Myo (DiD) (Figure 15 C, Supplement 3 A).

We examined the effect of the presence of heparin in the culture medium on cellular uptake. Figure 15 C showed an increase of '% of uptake' for Lip-Amb (DiD) ($\zeta\sim$ -45 mV) at the highest concentration of 4 U/ml heparin (Figure 15 C, D, Supplement 3 A, B). The increase of '% of uptake' was significant for DCs (+ 34%) (Figure 15 C, D). In contrast, the other formulations, Lip-Dox (DiD) ($\zeta\sim$ -14 mV), Lip-Myo (DiD) ($\zeta\sim$ -11 mV), Lip-Myo-PEG (DiD) ($\zeta\sim$ -17mV), that were lower charged tended to show a decrease of uptake (Figure 15 C, D, Supplement 3 A, B), which was significant in RPMs for Lip-Dox (DiD) (-26% '% of uptake', Figure 15, C). The heparin induced alteration of uptake showed similar effects for the MFI values as the '% of uptake' values (Figure 15 C, D, Supplement 3 A, B). On the contrary to the previous data on HeLa cells (Supplement 1 B) and the study of Champanhac et al [129] the primary splenic cells in this study showed an effect only at high concentrations of heparin (4 U/ml) and not already at low concentrations, as is the case with HeLa cells (Supplement 1 B, [129]). In addition, the effect appeared less pronounced in the primary splenic populations (Figure 15 C, D, Supplement 3 A, B). The difference between the high negatively charged Lip-Amb (DiD) (~-45mV) and the lower charged formulations Lip-Dox (DiD), Lip-Myo (DiD) and Lip-Myo-PEG (DiD) (~-11mV/ -14mV/ -17mV) indicates a surface charge-depending effect (Figure 15 D, Supplement 3 B), as already described in the study by Champanhac et al. [129]. Of the negatively low charged liposomes tested, the formulation Lip-Dox (DiD) overall showed the most striking decrease of cellular uptake in almost all populations of interest (Figure 15 D, Supplement 3 B).

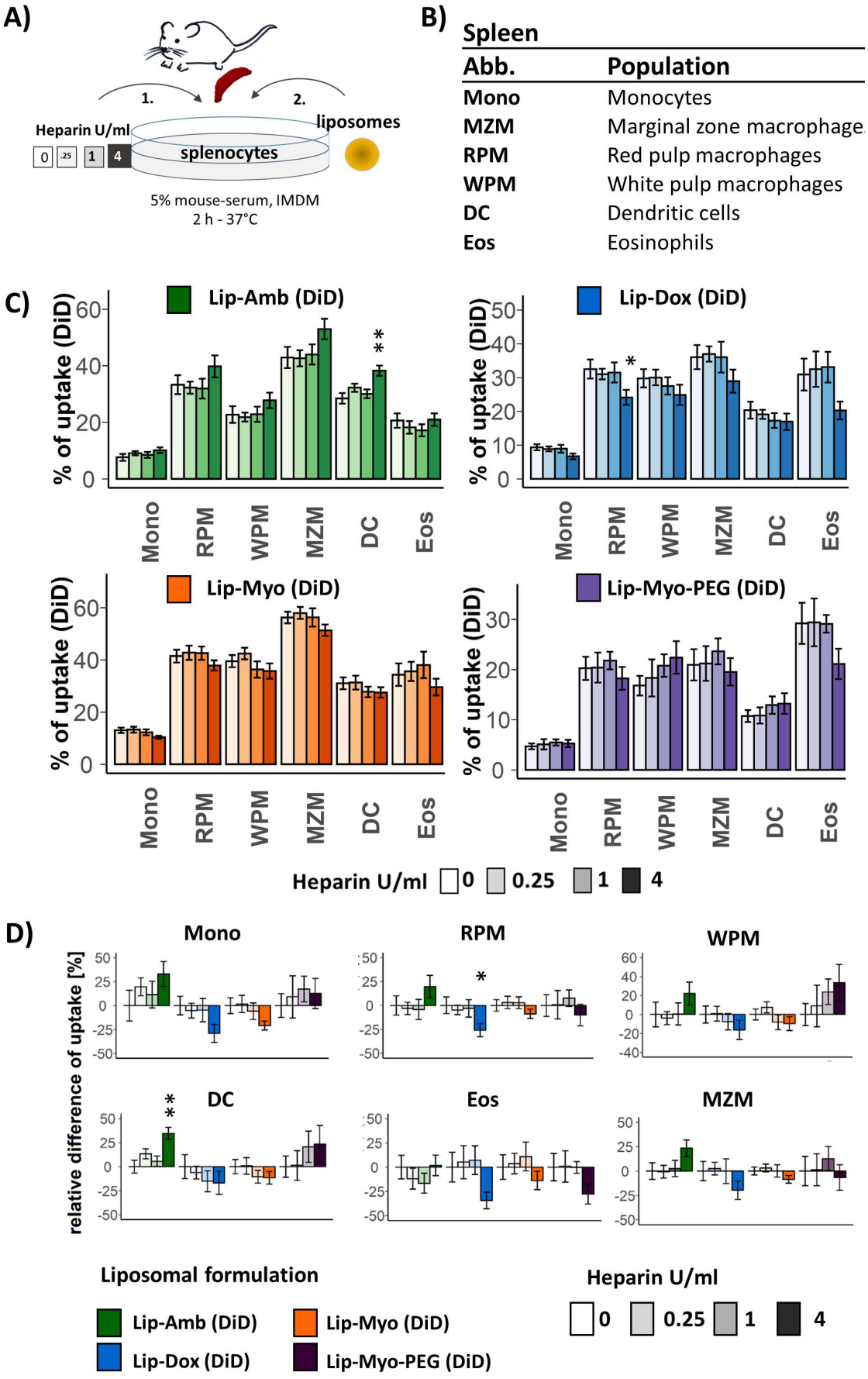

Figure 15: The uptake of DiD-labelled liposomes into slpenocytes in presence of heparin *in vitro.*

A: Experimental scheme of the *in vitro* experimental setup. Murine splenocytes were cultured in 5% mouse serum and increasing concentrations of heparin (0, 0.25, 1, 4 U/ml) and incubated for 2 h with 75 µg/ml of liposomes (Lip-Myo (DiD), Lip-Myo-PEG (DiD), Lip-Dox (DiD), Lip-Amb (DiD)) before flow cytometric evaluation. **B:** Spleen cell populations of interest. The table lists the spleen cell populations and abbreviations which were investigated in C and Supplement 3 A. The gating strategy is presented in Supplement 2. The expression markers of fluorophores are described in Table 23. **C:** Percentage of cells, which are positive for DiD within the defined spleen cell population (abbreviations see B). The whole cell suspension was treated with increasing concentrations of heparin (0, 0.25, 1 and 4 U/ml) and 75 µg/ ml of DiD labelled liposomal formulations (see A) *in vitro*. The graph represents the (mean and SEM) of the percentage of liposome (DiD) positive cells. Each group (0.25, 1 and 4 U/ml) was compared to the group of 0 U/ml heparin by a Wilcoxen test. $p < 0.05$ = *. n = 8, four batches of each liposomal formulation were used. **D:** Relative effect of heparin on uptake of liposomes (DiD). Represented is the mean +/- SEM (%) of the difference of each measured '% of uptake' value (C) towards the mean of the non-heparin treated samples. Values with a SEM > mean are not represented in the graph. Each group (0.25, 1 and 4 U/ml) was compared to the group of 0 U/ml heparin by a Wilcoxen test. $p < 0.05$ = *.

3.3.2 The effect of heparin on biodistribution *in vivo*

Since the *in vitro* tests showed a relevant effect at a concentration of 4 U/ml (Figure 15, Supplement 3), we wanted to investigate if a high-dose i.v. heparin treatment alters biodistribution of Lip-Dox *in vivo*. Doxil®, which shares the lipid composition of Lip-Dox, is a clinically well-known and relevant chemotherapeutic agent. In order to analyze the influence of a heparinization *in vivo*, comparable to a dose during heart surgery, mice were given an initial bolus of 272 U/kg bodyweight (in heart surgery 300 U/kg [123]), aiming at a final blood concentration of 4 U/ml (Figure 16, A). As described in Figure 16 A 15 minutes after heparin administration, the injection of Lip-Dox (DiD/DiR) was delivered into the, tail vein. Three time points were examined: 30, 120 and 360 minutes (Figure 16 A). A time point longer than 360 minutes was not investigated with respect to the estimated half-life of heparin which was calculated in two independent studies for humans conferring around 120 minutes for similar doses (107 minutes [122] and 153 minutes [123]). Using the *In Vivo* Imaging Spectrum (IVIS) system, time kinetics were established for the accumulation of liposomes in the spleen and liver during this time. Therefore, images of the signal for DiR were taken in regular intervals of the animal (Figure 16 B) and fluorescence was evaluated for the regions of interest (Figure 16 C, D). The curves describe the total radiant efficiency of the spleen and liver *in vivo* and show a higher accumulation of Lip-Dox (DiD/DiR) for the heparinized animal in the beginning. In the spleen, these curves converge at 120 minutes (Figure 16 C), which means that the measured difference, caused by heparinization, equalized between the different test groups. In the liver, the difference was still significant at 240 minutes and evened out at 360 minutes (Figure 16 D). Higher fluorescence intensity values for the heparin treated animals, were also detected for the 30 minutes and 120 minutes groups (Supplement 4 A, B).

In order to evaluate accumulation of Lip-Dox (DiD/DiR) in the organs more precisely, the fluorescence of heart, lung, spleen, liver and kidney was measured *post mortem*. The total radiant efficiency for each organ was determined using the *IVIS* system (Figure 16 E). The tissue density of liposomes, were determined by normalizing of the total radiant efficiency

values (Supplement 4 C) with the organ's weight. The spleen, followed by the lungs and liver, harbored the highest density of liposomes (Figure 16 F). The data on biodistribution (Figure 16) substantiates the "emerging role of the spleen" for the pharmacokinetics of liposomes [61]. However, the highest uptake, was found in the largest organ, the liver, followed by the spleen, lung and kidney (Supplement 4 C). While the total radiant efficiency remained rather equal or increased only slightly between the time points, the liver showed a marked increase between 30 minutes and 120 minutes (approximately 2×10^{11} to 3×10^{11}) (Supplement 4 C). The significant differences go along with the *in vivo* data (Figure 16 C, D): Heparin treated animals exhibited a slightly and significantly increased liposome density in the spleen at 30 minutes and 120 minutes. Even without the normalization of weight, these significant differences in the heparinized animals are evident for the absolute values of fluorescence (Supplement 4 C). Going along with the *in vivo* kinetics (Figure 16 C, D), the *ex vivo* measurements also showed that after 6 h, the differences in liposome accumulation in the organs were equalized for both groups.

The density values of liposomes in the blood were somewhat higher than in the heart, rather equal to the kidney and only slightly lower than in the liver (Figure 16 F). This finding underlines the long circulation time of Lip-Dox (DiD/DiR) (Figure 16, F), respectively Doxil® [5]. The images of the blood cells taken by the Amnis® ImageStream®XMark II (Supplement 11 E) show that a large proportion of the liposomes are still floating freely in the blood after 6 h.

Within the IVIS analysis of the living animal and the isolated organs, we've shown that heparin does cause an increased liposome accumulation in liver and spleen. In contrast, we have shown before a decrease of cellular uptake *in vitro* for phagocyte RES-cells in presence of heparin. This contradictory finding leads us to conclude, that heparin *in vivo* causes effects of other mechanisms ranging beyond the effect of cellular uptake.

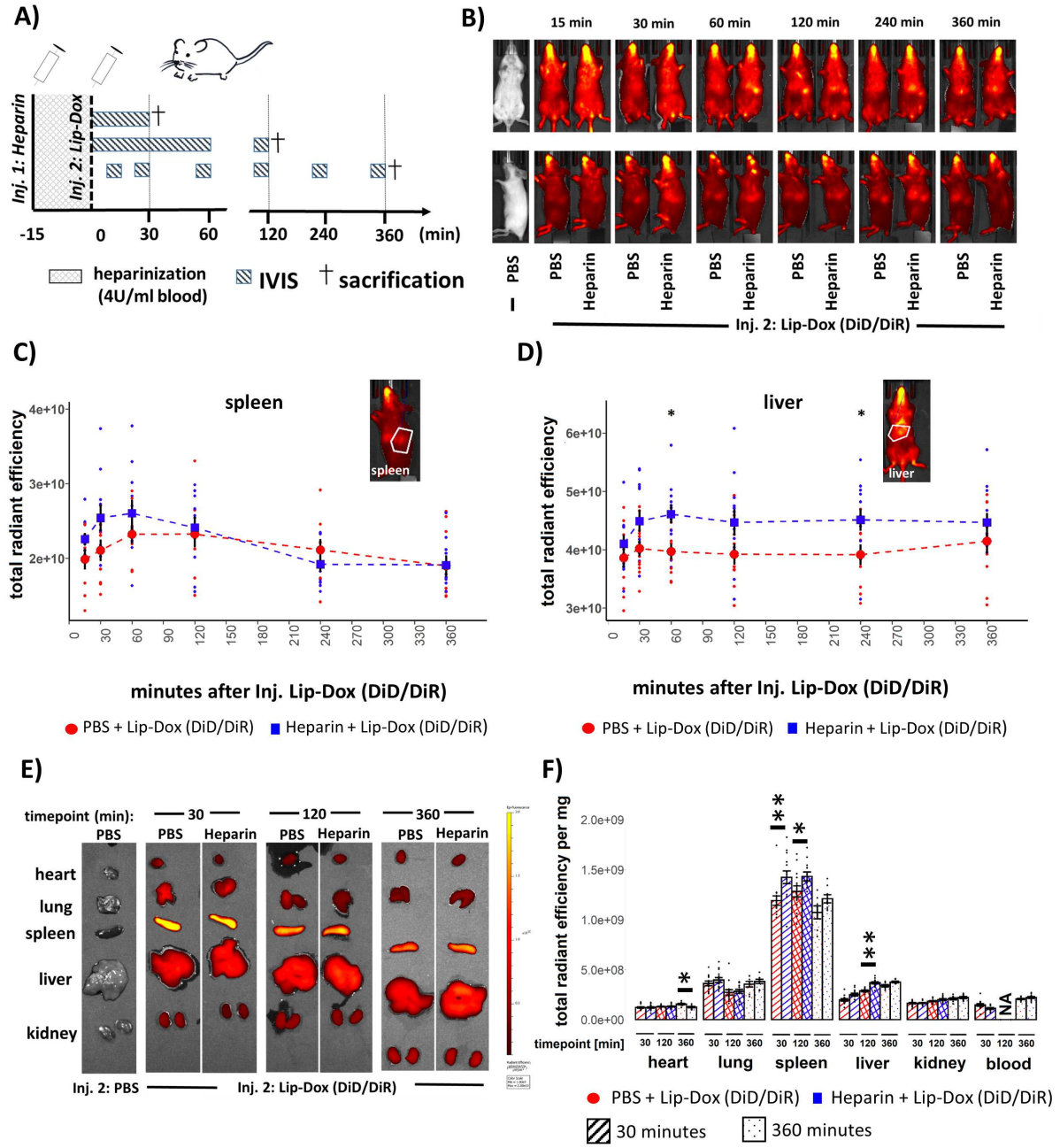

Figure 16: The effect of an i.v. heparinization on biodistribution of Lip-Dox (DiD/DiR).

A: Experimental scheme of the *in vivo* experimental setup: Animal were heparinized i.v. with a single bolus to a blood concentration of 4 U/ml, 15 minutes prior to injection of Lip-Dox (DiD/DiR, initial blood concentration of 600 µg/ml). **B:** Biodistribution of Lip-Dox (DiD/DiR) *in vivo*. Lateral and visceral IVIS acquisition of a representative animal for each group (‚PBS + PBS', 'PBS + Lip-Dox (DiD/DiR)', 'Hep + Lip-Dox (DiD/DiR)'). The heat map indicates the radiant efficiency of DiR. **C:** Spleen accumulation of Lip-Dox (DiD/DiR) *in vivo*. Total radiant efficiency of DiR (mean +/- SEM) of the spleen for 360 minutes. The equally shaped region was placed as indicated. For each time point the values for the two groups were compared by a Wilcoxon-test. $p < 0.05$ = *. n = 8-10 **D:** Liver accumulation of Lip-Dox (DiD/DiR). For each time point the values for the two groups were compared by a Wilcoxon test. $p < 0.05$ = *. n = 8-10 **E:** Organ distribution of Lip-Dox (DiD/DiR). IVIS acquisition of organs (heart, lung, spleen, liver and kidneys) of representative animal for each group ('PBS + PBS', 'PBS + Lip-Dox (DiD/DiR)', 'Hep + Lip-Dox (DiD/DiR)'). The heat map indicates the radiant efficiency. **F:** Relative density of Lip-Dox (DiD/DiR) in organs. Represented is the mean +/- SEM of the total radiant efficiency. Of each time point the two test groups of all organs were compared by a Wilcoxon test. $p < 0.05$ = *. n = 8-14.

3.3.3 The effect of heparin on cellular uptake *in vivo*

Since we observed a reduction in cellular uptake of Lip-Dox for most splenic macrophages when simulating a heparinization *in vitro* (see 3.3.1, Figure 15), we then investigated the cellular uptake of liposomes while i.v. heparin treatment *in vivo*. For this purpose, flow cytometry staining panels were applied, in order to differentiate RES cells in liver and spleen (Supplement 5 - Supplement 7). Approaching the *in vivo* question, the cell populations of interest, which were examined *in vitro* before (3.3.1), were extended with marginal metallophilic macrophages (MMM), subtypes of dendritic cells (see Figure 17 A), B- and T-cells (Figure 17 A). In addition to the spleen cell panels, two liver flow cytometry panels (Supplement 7 A, B) were established to examine non-parenchymal liver cells, such as Kupffer cells (Kupf) and liver sinusoidal endothelial cells (LSECs) (Figure 17 A). The signal of the liposomal dye, DiD, was measured in order to evaluate the uptake of liposomes (Supplement 5 B, Supplement 6 B, Supplement 7 C). The distribution of the DiD intensity in the *in vitro* setup (see 3.3.1) resulted in a shift of the total peak, when treated with Lip-Dox (DiD) (Supplement 2 B). In contrast, *in vivo* two peaks were visible for some populations (e.g. WPM, MZM, MMM). This may be due to anatomical and structural reasons; and therefore, distinct parts of the population have not been in contact with the liposomes, yet.

Similar to *in vitro* (see 3.3.1), also *in vivo*, the MZM population showed a comparatively high uptake, of 91% at 30 minutes and 84% at 360 minutes (Figure 17 D). While the RPMs at 30 minutes displayed a relatively low uptake, at 360 minutes the fluorescence increased (Figure 17 D). This is consistent with the literature that MZM have a high capacity to internalize the liposomes [57]. RPMs, which are located in the red pulp, take up the foreign bodies [65] with a time delay, after they have been filtered inside the sinusoids [61]. Immunofluorescence measurements exhibited a strong accumulation of Lip-dox (DiD/DiR) in the red pulp (Supplement 8 A, Supplement 9) and the marginal zone already after 30 minutes (Supplement 8 B). The uptake in the white pulp was lower, as can be seen by immunofluorescence (Supplement 8 A, Supplement 9 A) and confirmed by the flow cytometer data of WPM (51% at 30 minutes and 57% at 360 minutes) (Figure 17 D, F). It is very intriguing that Monos had a very high uptake of Lip-Dox (DiD/DiR) *in vivo,* of 89% at 30 minutes and 90% at 360 minutes, which is reflected in both ‘% of uptake’ and MFI (Figure 17 D, F). In contrast, the *in vitro* uptake study for this population showed very low levels of Lip-Dox (DiD) (Figure 15 C, Supplement 3 A). These finding underlines, how differently cells behave when kept in culture, away from their physiological environment in the organism.

A)

Spleen		Liver	
Abb.	**Population**	**Abb.**	**Population**
DC	*Dendritic cells*	**Mono**	Monocytes
CD11b +	*CD11b + cells*	**KC**	Kupffer cells
MO	*Macrophages*	**CD68⁺ MO**	Macrophages
Mono	Monocytes	**CD11b⁺ MO**	Macrophages
RPM	Red pulp macrophages	**DC**	Dendritic cells
WPM	White pulp macrophages	**LSEC**	Liver sinusoidal endothelial cells
MZM	Marginal zone macrophages		
MMM	Metallophilic marginal zone macrophages		
cDC1	Conventional dendritic cells type 1		
cDC2	Conventional dendritic cells type 2		
mDC	Macrophage derived dendritic cells		
Eos	Eosinophils		
pDC	Plasmacytoid dendritic cells		
B-Cells	B-cells		
T-Cells	T-cells		

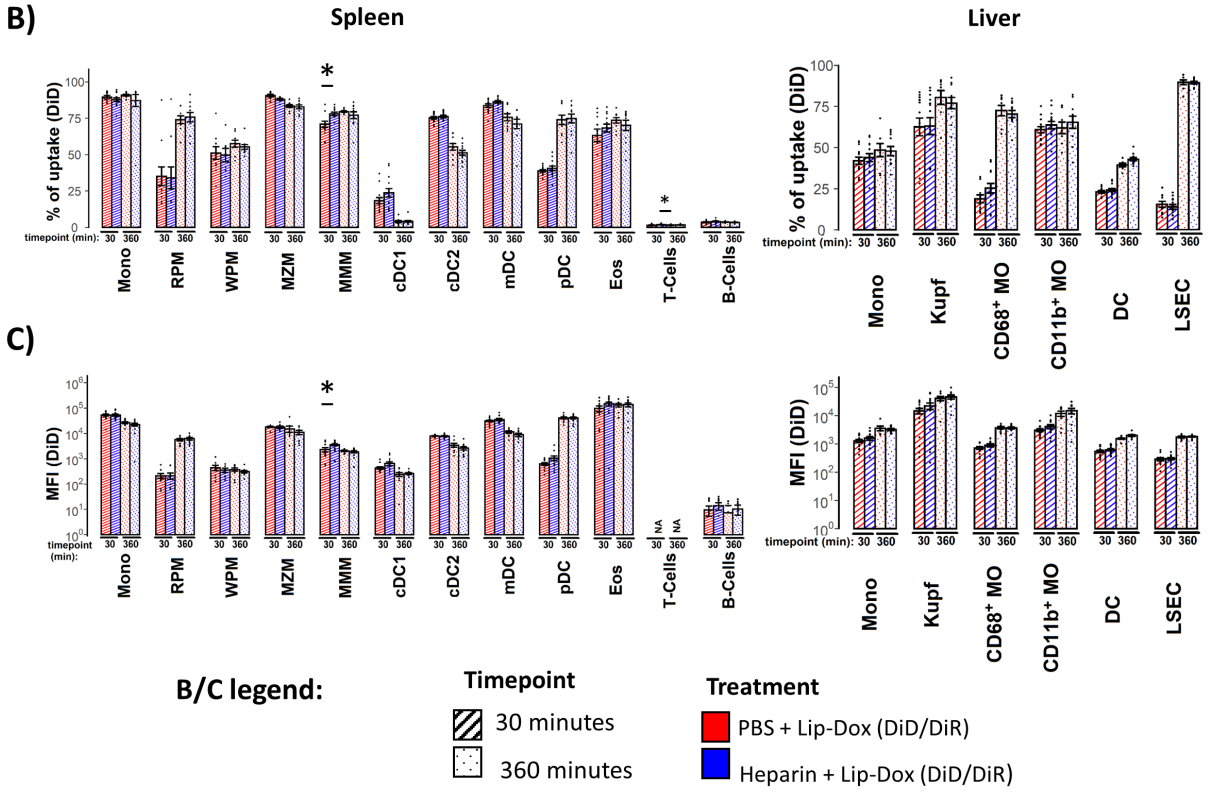

Figure 17: The effect of an i.v. heparinization on cellular uptake of Lip-Dox (DiD/DiR) into RES-cells.

A: RES-cell populations of interest. The table lists the spleen and liver cell populations and abbreviations, investigated in B-E. The gating strategy and fluorescence intensity histograms for DiD are represented in Supplement 5, Supplement 6 and Supplement 7. The expression markers of fluorophores are listed in Table 24. **B:** '% of uptake' (mean +/- SEM) of Lip-Dox (DiD/DiR) in defined spleen and liver cell populations (abbreviations see A). Of each time point, the two test groups of all organs were compared with each other by a Wilcoxon test. $p < 0.05$ = *. n = 10-14. **C:** MFI(DiD) (mean +/- SEM) of Lip-Dox (DiD/DiR) in defined spleen and liver cell populations (abbreviations see A). The two groups were compared by a Wilcoxon test for each time point. $p < 0.05$ = *. n = 10-14.

Similar to the *in vitro* data (Figure 15 C, Supplement 3 A), *in vivo* Eos showed the highest MFI values - of 95,000 and 130,000 rel. units (Figure 17 C). B-cells and T-cells exhibited, as expected, a low uptake, below 5% (Figure 17 B). Nevertheless, the numerical representation of leukocytes in the spleen (Supplement 6 C) may mean, that even this low percentage of Lip-Dox (DiD/DiR) positive cells contributed significantly to the 'DiD-positive' cells and to the absolute uptake of nanocarrier and maybe therefore also be a reservoir of cells to be considered further.

Looking at the dendritic cell subpopulations, the uptake was relatively high, especially for mDCs - of 84% and 76%. pDCs, like RPMs, showed a delayed increase of liposome accumulation - 39% for 30 minutes increasing to 74% for 360 minutes (Figure 17 B). Of the conventional DCs, cDC2s exhibited a higher uptake of 75% at 30 minutes, which decreased to 51% after 360 minutes (Figure 17 B). On the other hand, less cDC1 were positive for Lip-Dox (DiD) - at 30 minutes (18%), after 360 minutes is only 4% (Figure 17 B). Overall, the MFI values mainly reflected the '% of uptake' values for the spleen (Figure 17 C) *in vivo.*

A significant but weakly pronounced change due to heparin could be recognized when looking at the population MMM at 30 minutes (Figure 17 B, C). The '% of uptake' at 30 minutes showed an 8% increased for the heparin treated group (Figure 17 B) (from 71% to 78%) and similar did reflect the MFI value (1.9×10^3 and 2.0×10^3 rel. units) for the heparin treated group (Figure 17 C). This heparin-induced increase of uptake into MMMs might not necessarily lead back to a cellular change in uptake capacity, but rather may be caused by other heparin induced circumstances: The Lip-Dox (DiD/DiR) amount in the spleen was elevated for the heparin treated group (Figure 16, Supplement 4 C).

Moreover, we examined the cellular uptake by the liver cells. As the literature has predicted [39], Kupf had the largest absorbing capacity as shown by the value of the MFI – 14,690 rel. units at 30 minutes and 40,355 rel. units at 360 minutes (Figure 17 C). Although the MFI values showed that LSECs had a lower absorption capacity compared to Kupf (287 rel. units at 30 minutes and 1,742 rel. units at 360 minutes) (Figure 17 C), the '% of uptake' value of all LSECs that have taken up Lip-Dox (DiD/DiR) increased from 15% to 30 minutes at 360 minutes to 90% (Figure 17 B). Overall, a time dependent increase in Lip-Dox (DiD/DiR) uptake could be seen for all liver cell populations from 30 minutes to 360 minutes (Figure 17 B, C). This could also be recorded in the previously shown data of the organ distribution (Figure 16 F, Supplement 4 C).

An effect by heparin on cellular level for the Lip-Dox (DiD/DiR) uptake, was not recognizable neither at 30 minutes nor at 360 minutes for the investigated non-parenchymal liver cells (Figure 17 B, C). No structurally specific fields of liposome localization were visible in the confocal microscopy acquisitions of DiD in the liver (Supplement 10). The homogeneous

distribution of DiD on the immunofluorescence images of liver sections, may derive from the hepato-bilaric elimination pathway of which in turn are liposomes metabolized in the parenchymal cells of the liver [39]. Also DiD and DiR are lipophilic dyes and therefore very likely cleared and digested by the hepatobiliary system – leading to the homogenous staining od the tissue sections (Supplement 10).

Within the flow cytometry study, we have shown that heparin has no influence on the uptake of Lip-Dox for most of the investigated cell-populations (Figure 17 B, C) at the time of 30 minutes and 360 minutes. A slight but significant change of uptake was observed for MMMs. In addition, we have gained a deep insight into the cellular distribution of Lip-Dox (DiD/DiR) among cells of the RES that can be transferred to Doxil®.

3.4 Discussion

Focus of this study was to investigate if a heparinization does influence the biodistribution into RES-organs of i.v. liposomal therapies and thereby has potential to effect therapy outcome. Because of the growing clinical usage of liposomal therapies and the broad use of heparin, a simultaneous application of both medications is very likely. These experiments open new views on the pharmacovigilance of liposomal nanotherapies. This study has shown that a high dosed heparinization does alter the biodistribution and cellular uptake of liposomes into the RES-organs statistically significantly, yet to a small extend and thereby influences pharmacokinetics slightly. We cannot draw an exact conclusion how heparin behaves on pharmacodynamics of liposomal cancer therapies, as we did not use a pathological model here nor used liposomes loaded with the active ingredient. Though we create an assumption, basing on the only marginally altered pharmacokinetics of liposomes, that a high dosed heparinization doesn't alter pharmacodynamics in a relevant manner. The assumption bases on the here provided data on biodistribution in healthy wild type high dosed heparinized animal and is limited to the liposomic formulations mentioned.

In the previous study of Champanhac et al. [129] we showed, that pre-coating nanoparticles with heparin and serum proteins caused a significant reduction of uptake in distinct cancer cells e.g. HeLa cells and primary monocytes from human blood. In this study, also for Lip-Dox a similar behavior was observed for HeLa cells in prescence of heparin. The uptake of liposomal formulations into phagocytes of the spleen was investigated in the presence of heparin *in vitro,* for the formulations of the commercially available liposomal drugs: Myocet®, Ambisome® and Doxil® [7]. *In vitro,* heparin concentration-dependent alterations of uptake were shown (Figure 15, Supplement 1), which are specific for each liposomal formulation and the defined cellular population. The strongest change of uptake was observed for the formulation Lip-Dox with a significant reduction of uptake (~-25 %) at 4 U/ml of heparin for the RPMs. We suspect that differences in surface charge play a role here, as presence of heparin

causes an increase of uptake for the negatively charged (~-45 mV) Lip-Amb. In contrast, slight negatively charged formulations (Lip-Dox, Lip-Myo, Lip-Myo-PEG were taken up less by increasing concentrations of heparin (Figure 15). Clearly our study is lacking positively charged liposomal nanocarriers, but as they have not been in clinical use we did not include these in the studies here.

Biodistribution and cellular uptake was investigated in mice having received an initial i.v. heparin bolus to a final blood concentration of 4 U/ml, 15 minutes prior to liposome injection of DiD/DiR labelled Lip-Dox. *In vivo* fluorescence analysis using IVIS has shown a marginally but significantly increased accumulation of Lip-Dox in the spleen and liver within the first two hours (Figure 16). *In vivo* analyses go along with the results of the more precise *ex vivo* measurements of the organs (Figure 17). At 360 minutes the differences of biodistribution were equilibrated between the heparinized mice and the PBS treated ones. Cellular uptake of Lip-Dox into phagocytes of the spleen and liver was not reduced for the heparin treated group as the primary *in vitro* data let assume. A slight but significant increase of uptake occurred in the MMMs of the spleen upon heparinization. There has not been carried out research yet on the effect of concomitant heparinization while liposomal therapy before.

In this study the differences in organ accumulation in the liver and spleen were equal at 360 minutes. It should be noted that the number of animals for that time point were lower (n ~ 8) than for the other timepoints (n ~ 12). Nevertheless, knowledge about the half-life of heparin suggests, that the described effect on biodistribution is dependent on the current blood concentration of the negatively charged polysaminoglycan. The data from a cohort of subjects undergoing heart surgery and receiving a comparable initial bolus of 300 U/kg, the heparin half-life was estimated on around 120 minutes taking the average of two independent studies (107 minutes [122] and 153 minutes [123]). Therefore, we assume that after 360 minutes the heparin level has dropped dramatically and the increased liposomal accumulation in liver and spleen are equilibrated for both groups. This points out, that the significant changes of biodistribution are dependent on the current blood concentration of heparin. The long circulation time of these particles, as fluorescent imaging of the blood shows (Figure 16, Supplement 11), may compensate the ‘heparin-effect’, which occurs within the first 120 minutes. This hypothesis could be tested by repeated administration of subsequent boluses of heparin to the animal.

The primary *in vitro* data on splenocytes (Figure 15, Supplement 3) would have let us expect a reduction in uptake into the spleen of Lip-Dox with heparinization *in vivo*, caused by a reduction of cellular uptake into RES-macrophages in presence of heparin. Interestingly, both *in vivo* and *ex vivo* IVIS data showed increased accumulation of Lip-Dox in heparin-treated animals (Figure 16). The cellular uptake into the cells of interest for both organs did not alter

in a relevant manner between the groups. An increase of uptake in MMMs was observed for the heparin treated group (Figure 17). This finding however does not explain the significant increase of accumulation into the spleen, as the population of MMM is only a minor cell population when looking at the flow cytometer gating for the CD169+ cells in Supplement 6 C. Still, other cell populations, not investigated in the flow cytometer analysis (Figure 17) might have increased Lip-Dox uptake while heparinization. In the liver, parenchymal cells were not investigated and constitute a considerable number of cells [86]. The homogenous immunofluorescent images of DiD (Supplement 10) point out that these cells were positive for Lip-Dox.

In vitro, the uptake was reduced in the presence of heparin for Lip-Dox for most splenic macrophage subtypes and significantly for RPM. The finding *in vivo* points out, that heparin has more than one effect on the behavior on nanocarriers. *In vivo*, heparin theoretically could influence the accumulation of liposomes in RES-organs also by other mechanisms than cellular uptake, like endothelial interactions influencing the filtering capacities of liver [89] and spleen [65]. An increased extravasation of liposomes into the organs, can lead to a higher liposomal accumulation in the respective organ in the extracellular matrix [135]. An endothelial barrier strengthening effect of heparin in context with metastasis and inflammation has been reported in literature more often [136, 137]. This finding however does not explain the increased accumulation in liver and spleen (Figure 16). Nevertheless, we must keep in mind that both liver and spleen differ from other tissues, in terms of endothelial lining and filtering capacity from other organs. Both liver [89] and spleen [61, 65] have special microanatomical vascular structures that are relevant for the filtering of larger objects beyond the size of molecules, such as liposomes from the blood [39, 63]. Possibly, heparin can interact with these structures and cause the effect of elevated organ uptake in the spleen and liver.

The former findings, reporting a decrease of uptake by Lip-Dox on cultured primary spleen cells cannot be explained by these experiments. Champanhac et al. [129] and Schöttler et al. [45] hypothesized, that presence of heparin influences the corona's composition and therefore the characteristics of the nanocarriers. When nanocarriers get in contact with fluid, as for example blood, a corona is formed, which is specific for the components of the medium and defines the pharmacokinetics of the nanocarriers [138]. Specific proteins, like complement factors, are associated with a stronger uptake of nanocarriers into macrophages. In contrast, 'stealth proteins' are associated with a reduced uptake by primary immune-cells [138]. Applying this setup of heparin co-treatment (Figure 15 A), we assume that heparin is incorporated into the protein corona as well and influences its composition, but also can interact with the cells directly. A pilot *in vitro* experiment on heparin pre-treated splenocytes supported the idea that heparin can influence uptake of liposomes as the molecule itself as well, though this effect might have less impact on the results described in Figure 15; A

significant change of uptake was observed after 24 hours of pre-treatment, but not after 2 hours (Supplement 13). This result opposes that in this study heparin does have an effect on cells directly.

In this study unfractionated heparin (UFH) was investigated. Nowadays LMWHs are more widely used in the clinic due to several advantages [110, 139]. Another *in vitro* experiment investigating the uptake of liposomes in presence of the LMWHs enoxaparin, tinzaparin and fondaparinux, showed a less pronounced alteration on cellular uptake than UFH (Supplement 14). Also, this finding alleviates the concern, that a clinical heparinization may influence pharmacodynamics of liposomal therapies. Nevertheless, it should be emphasized that LMWHs are characterized by a longer circulation time [128] as they are mainly excreted renally and are less absorbed by the RES [114]. Since we attribute the temporary slightly increased organ accumulation in the liver and spleen to the concentration of heparin in the blood, this effect, may last longer when heparinized with LMWHs due to the longer circulation time.

While this study focused primarily on unwanted uptake into the spleen and liver, no conclusions can be drawn about the accumulation of Lip-Dox in tumor tissue, the site of action of Doxil® [9]. Nevertheless, the RES plays an important role in the pharmacokinetics and therapeutic outcome of liposomal drugs [61].

All in all, this data reveal that a heparinization significantly influences biodistribution of liposomes *in vivo* – albeit to a relatively small extend. The here described increased accumulation in liver and spleen normalizes after more than 2 hours, with the expected drop of the heparin blood concentration [122, 123]. The cellular uptake of liposomes in spleen and liver among various analyzed RES-cells, only in MMMs a slight but significant increase of Lip-Dox uptake was observed *in vivo*. These data do not suggest that a heparinization significantly influences the outcome of a liposomal therapy. For the clinic, this means that an accompanying heparinization in liposomal therapy is probably not critical for the course of therapy and therefore co-administration of heparin and a clinicially approved liposomal drug is safe. As pointed out before, this may change with the advent of new formulations of liposomes and should be again looked in another study.

4 Chapter 2: Heparin and Ovalbumine Nanocapsules

This chapter represents the second part of the main project of the thesis (co-medication of heparin) and is written in form of a scientific paper. The manuscript is planned to be published in 2021. The work was a collaboration with the group of [redacted], Max Planck Institute for Polymer Research. [redacted] and [redacted] in close collaboration kindly provided the protein-based nanocapsules for in vivo studies. [redacted] and [redacted] produced nanocapsules for the in vitro experiments. [redacted] from the group of [redacted], Max Planck Institute for Polymer Research, supported the characterization of the nanocapsules with new techniques. Further group members assisted when carrying out the animal experiments.

The Potential of Heparin for evoking a passive Targeting for Protein-based Nanovaccines towards Dendritic cells by Regulating the Uptake into Macrophages

[redacted]

[a] Department of Dermatology, University Medical Center of the Johannes Gutenberg-University Mainz, Langenbeckstrasse 1, 55131 Mainz, Germany

[b] Max Planck Institute for Polymer Research, Ackermannweg 10, 55128 Mainz, Germany

[c] Institute of Pharmaceutical and Biomedical Sciences, Johannes Gutenberg University, Staudingerweg 5, 55126 Mainz, Germany

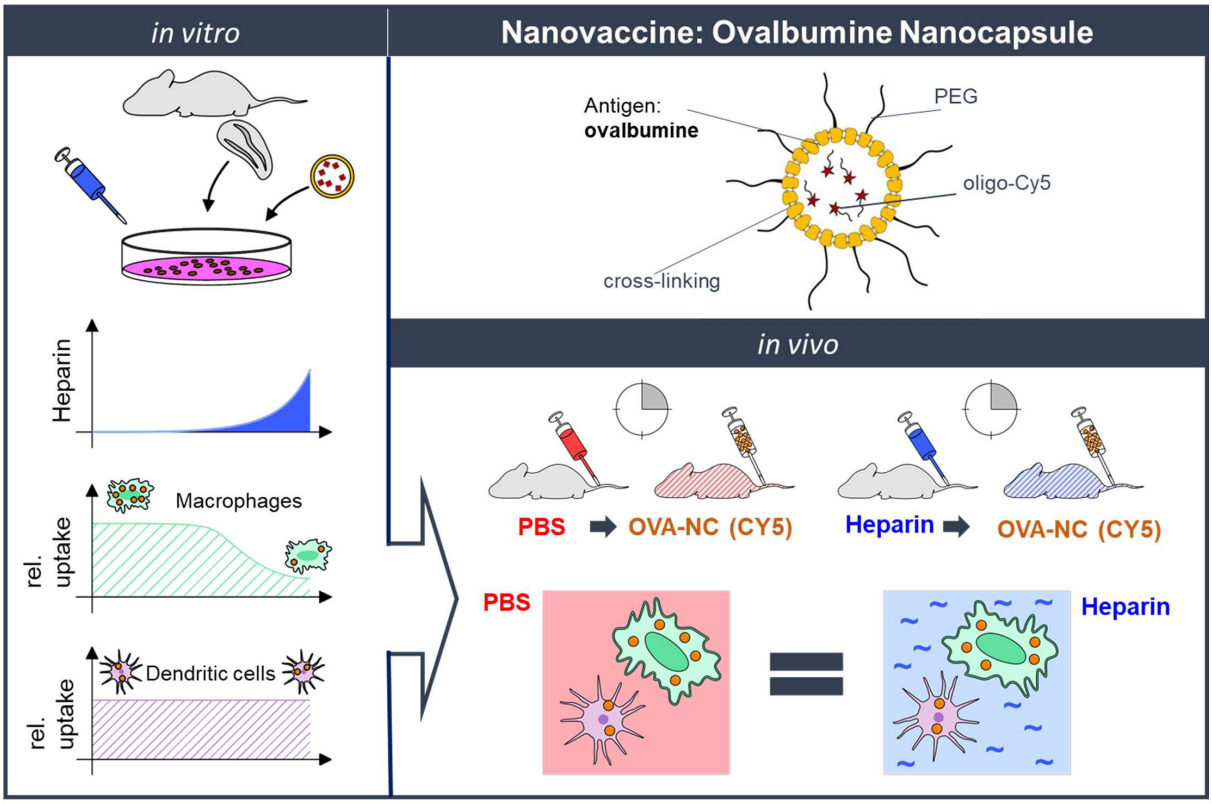

Figure 18: Graphical abstract chapter 2 - Heparin and Ovalbumine nanocapsules.

4.1 Abstract

In order to enhance efficacy of protein-based nanovaccines, there is an urge to find targeting strategies, which increase the uptake into dendritic cells (DCs). Herein we show the potential of heparin to modulate the uptake of nanocarriers into macrophages and DCs.

Fluorescently labelled polystyrene particles (PS-particles) and protein capsules were incubated with a spleen cell mixture in presence of heparin. The *in vitro* experiments revealed that heparin has an uptake-modulatory effect on PS-particles, which extend depends on surface modification of the particle. For the ovalbumin-capsule (OVA-NC), a protein-based nanovaccine, heparin selectively reduced uptake into macrophage subtypes, but not DCs at 4 U/ml. This finding points out a passive targeting mechanism of heparin.

Moreover, we investigated, if a high dose heparinization (4 U/ml blood) can lead to the favorable indirect targeting effect also *in vivo.* However, flow cytometry analysis revealed no differences for the heparin treated group in terms of cellular uptake of OVA-NC. On the level of organ distribution, the high dose heparinization caused a slightly increased accumulation of OVA-NC in the liver within the first 30 minutes. To our knowledge, the *in vivo* cellular distribution of the OVA-NC has been described in detailed for the first time in this study.

4.2 Introduction

Nanovaccines have played an emerging role in vaccination development within the last decade, not least in turn of the COVID-19 pandemic [6, 140]. Initial clinical data on immunization against patient-specific neoantigens in malignant melanoma showed promising results [21]. In contrast to established subunit vaccines, the advantage of nanovaccines is, the preferential uptake of the nano-sized particles into dendritic cells (DCs) [132]. The encapsulation of both the antigen and the adjuvant together, increases the effectiveness of the vaccine as the antigen and adjuvant end up in the same cell [30].

In recent years we developed a novel approach of nanovaccines: Intracellular degradable protein-based capsules with a cross-linked protein-based shell consisting of the antigens. The aqueous core can be loaded with adjuvants, enhancing the adaptive immune response [29, 30]. This type of nanovaccine has the potential to be developed as personalized anti-tumor vaccination; E.g using individual neoantigens, which are extracted from the tumor. For research purposes the shell was composed out of ovalbumin (OVA) [30], a protein originating from the chicken eggs [141]. OVA is an established model antigen; Experimental tools (OT-I / OT-II mouse strains) have been developed to evaluate the anti-OVA immune response and to distinguish the cytotoxic T-cell response ($CD8^+$) from the T helper cell response ($CD4^+$) [31]. This is the main reason that the OVA-antigen in the development of novel nanovaccines is frequently used [32, 33].

There are three different routes to apply nanovaccines in the organism: *intravenously (i.v.)* reaching spleen and liver, *intranodal* or *subcutaneously*. Many studies have shown that especially the i.v. administration form induces a strong anti-tumor immune response [21, 32, 71, 72]. Dölen et al. [32] observed a stronger cytotoxic T-cell response, higher systemic IFN-ɣ level and anti-OVA-IgG2 serum levels in naïve mice upon i.v. injection of a PLGA based capsules with incorporated OVA-antigen, than for intranodal and subcutaneous administration.

The spleen as a versatile organ with the function to clean the blood from pathogens and to sort out dysfunctional blood cells [67] also harbors a myriad of immune cells [64]. The white pulp consists of the T-cell and B-cell compartments and thus plays a crucial role in initiating the adaptive immune response by interacting with DCs [64].

The high number of macrophages in the spleen, as well as their high phagocytotic capacity, causes these cells to compete with the DCs for the foreign body-like particles [132]. An immune response would be all the more effective, the more DCs take up the antigen/adjuvant complex and the higher their carriage. Active targeting of DCs promises an enhanced pharmacological effect of the nanovaccine. Current approaches consist mainly of targeting the mannose receptor, CD11c integrin and DC-SIGNR molecule on the surface of DCs. For this purpose, nanocarriers are modified with mannan and other sugars [132, 142]. The most obvious

approach, to modify capsules with antibodies, still presents unsolved difficulties. Interactions of the immune system with the Fc structure of the antibody is one of the main obstacles of immuno-targeting [138, 143].

Based on the findings from Champanhac et al. [129] we asked, whether heparin can alter the uptake of nanovaccines into DCs and the macrophages in the spleen. For improved efficacy and tolerability of nanovaccines, it is essential to increase uptake into target cells, which mediate the immune response, DCs, and to reduce uptake into the other phagocytes. A high accumulation in the spleen is desirable for anti-tumor vaccination with nanocarriers [21, 32]. Heparin is a negatively charged polysaminoglycane [100], interacting with numerous proteins [144]. The molecule is a widely established anticoagulant in clinic applied in low doses for thrombosis prophylaxis and is high dosed during cardio vascular events [110, 123].

4.3 Results

4.3.1 The role of the nanoparticles surface charge on the regulation of uptake into DC in presence of heparin

Heparin is a strongly negatively charged biomolecule [100]. It is known, that the surface charge of particles can influence the uptake of nanoparticles [129]. Two polystyrene particle systems with similar hydrodynamic diameter and opposite charge were produced by alteration of surface groups (PS-COOH: 138 nm, - 53 mV; PS-NH_2: 128 nm, + 53 mV). The particles were fluorescently labeled using bodypy 630/ 650 (BP) (Supplement 15 A). A splenic cell suspension was cultured in 5 % mouse serum and 0 – 4 U/ml heparin containing medium. Cells were incubated with the fluorescence labeled nanoparticles for 2 h (Figure 19 A) and the uptake into specific splenic immune cells were analyzed via flow cytometry (Figure 19 , Supplement 17).

A significant and strong reduction of uptake was observed for DCs (CD11c+) in presence of heparin but not for the other defined phagocyte splenic populations (RPM, MZM, WPM) (abbreviations described in Figure 19 B) for PS-NH_2 (BP) (Figure 19 C). The MFI of BP for the 4 U/ml heparin treated group was 91 % lower than for the control group and at at 1 U/ml amounting 82 % less (Figure 19 E). Looking at the parameter of percent of uptake (‘% of uptake’), a significant difference was observed at 1 and 4 U/ml as well (Supplement 17 A, C). In accordance with the results of Champanhac et al. [129], negatively charged particles did not show the striking uptake reducing effects as positively charged particles for the investigated populations (Figure 19 D, Supplement 17 B). Due to the different fluorescent properties of the PS-particles (Supplement 15), the intensity values of the two particle systems must not be compared to each other. Comparing the uptake to the other spleen cell populations, the MFI (Figure 19 C, D) and percentage (Supplement 17) of DCs was relatively low for PS-COOH (BP) (113 rel. U. (DCs) and 1039 rel. U (RPMs)) and comparably high for PS-NH_2 (BP) (370 rel. U. (DCs) and 35 rel. U. (RPMs)). From this finding we can delineate, that negatively charged systems are preferably taken up by DCs compared to positively charged systems. The MFI of the BP positive gated cells behaved constantly for both PS-COOH (BP) and PS-NH_2 (BP) (Supplement 17 F, E).

Taken together these findings showed a selective effect of heparin on DCs. The effect is also influenced by the nanocarrier system. Presumably surface modification and surface charge of the particle system herewith are critical. The selective heparin effect reported in Figure 19 was confirmed in a second independent experiment (data not shown).

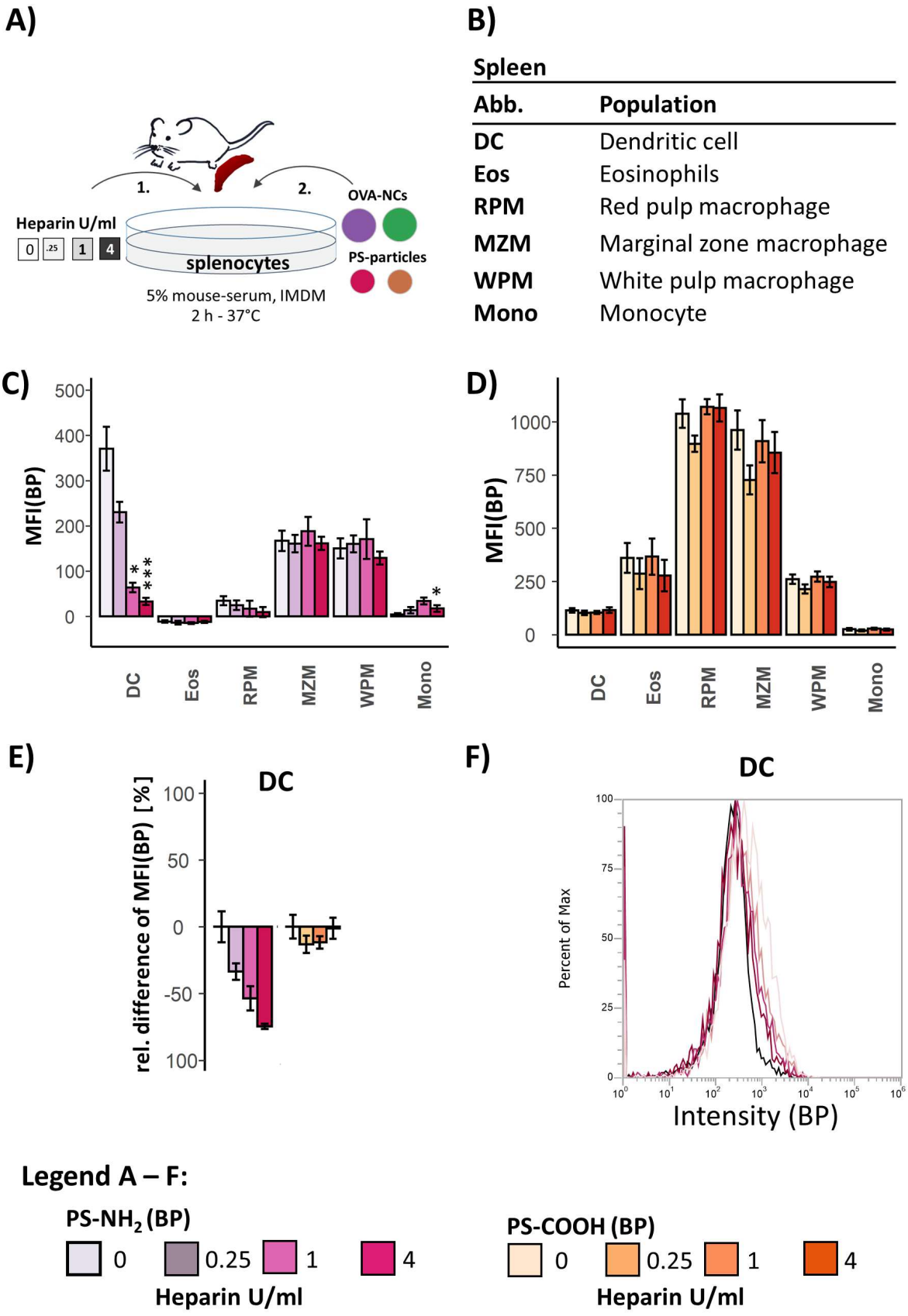

Figure 19: Heparin selectively reduces the uptake of PS-NH_2 (BP) into DCs.

A: The sketch describes the setup of the following *in vitro* experiments. **B:** Populations of interest with abbreviations. The marker expression of each population is listed in Table 23. The gating strategy is described in Supplement 18. **C/D:** The uptake of C) PS-NH_2 (BP) and B) PS-COOH (BP) into

splenocytes when cultured in presence of heparin (0 – 4 U/ml). Represented is the mean +/- SEM of the median fluorescence intensity (MFI) of BP. The control group was compared with the groups of treatment by Wilcoxen tests. $p < 0.05$ = *, n = 5-7, batches = 1. **E:** The graph represents the mean +/- SEM of the normalized difference of the MFI towards the control group (0 U/ml) of the DC population for PS-NH_2 (BP) (pink) and PS-COO (BP) (orange). The relative difference was calculated from the values in C/D. **F:** The histogram shows the relative intensity of BP within the population DC for representative samples. The black line represents the PS-NH_2 (BP) untreated control (background).

4.3.2 The potential of heparin to regulate the uptake of protein-capsules

Having shown a selective effect for DCs, whereas not for macrophages on uptake of PS-NH_2 (BP), we want to analyze in which way heparin influences the uptake of a protein based nanovaccine with an antigen-shell [29]. A modulatory effect on uptake by heparin, which is selective for DCs, might influence the efficacy of the nanovaccine. The previously described OVA-NC were loaded with Oligo-Cy5 in order to analyze uptake by flow cytometry as represented in Supplement 20 A, B.

The goal was to investigate the effect of heparin co-treatment on the uptake of OVA-NC (Cy5) and PEG-OVA-NC (Cy5) into DCs and other phagocyte cells of the spleen (experimental setup described in Figure 19 A). The average size of the three OVA-NC (Cy5) batches was 336 +/- 176 nm and of the n = 3 PEG-OVA-NC (Cy5) batches, 312 +/- 139 nm (mean +/- SD Table 29). The average zeta-potential was -29 mV for OVA-NC (Cy5) and -28 mV for PEG-OVA-NC (Cy5) (Table 29). The surface charge of PEG-OVA-NC (Cy5) does not differ significantly from that of non-PEGylated capsules in the *in vitro* experiments.

In this experiment, the uptake of PEGylated capsules was stronger for most of the populations of interest (Figure 20 A, B and Supplement 19 A, B). This may be due to manufacturing deviations, which are relatively largely due to the elaborate protocol for the capsules (see 8.1.4). For most of the investigated cell-types, Eos, RPM, MZM, WPM and MMM, a significantly lower uptake of OVA-NC (Cy5) was observed in presence of 4 U/ml heparin (Figure 20 A, Supplement 19 A). The normalized difference of the MFIs between the 4 U/ml heparin treated group and the control group was – 57 % (Eos), - 49 % (RPM), - 56 % (MZM), - 66 % (WPM), - 28 % (MMM) (Figure 20 C). Surprisingly, the difference caused by presence of heparin was not significant for DCs (-2.5 %) (Figure 20 A, C).

In contrast to OVA-NC (Cy5), for the PEGylated system, PEG-OVA-NC (Cy5), the difference of the MFI between the group 0 and 4 U/ml overall were even more pronounced (Figure 20 B). Also for this system, the difference between the control group and the highest heparin concentration was not significant for DCs. In contrast to not-modified OVA-NC (Cy5), PEG-nanocapsules showed an increased uptake at 0.25 and 1 U/ml heparin, which was significant for Eos (Figure 20 A, C, Supplement 19 A, C). The evaluations on the percent of uptake of each population showed a significant decrease of Cy5 positive cells at 4 U/ml for Eos, RPM,

MZM and WPM (Supplement 19 B, C). All findings were confirmed in a second independent experiment. PEGylation is a commonly applied modification for nanodimensional drugs to prolong circulation time. PEGylation of nanocarriers therefore improves the pharmacological effectiveness. However, at the lower concentrations (0.25, 1 U/ml), the uptake into phagocytes increases for the PEG-OVA-NC (Cy5) and this significant for the Eos. Thus, heparin can be used to further enhance the PEG-effect [50]. However, the DC-promoting effect can change into the opposite, at low concentrations of heparin.

While heparin reduces uptake for PS-NH_2 (BP) selectively in DCs (4.3.1), heparin does not for OVA-NC (Cy5). In contrast for OVA-NC (Cy5), heparin reduces the uptake into the RES cells which mainly are macrophages. We conclude a selective passive regulating effect of heparin. The heparin regulating effect is also influenced by the type of the nanocarrier. To what extent this effect can be attributed to surface charge is questionable, because the much more negatively charged PS-COOH (BP) particles (-53 mV) did not show any significant effect of heparin on macrophages compared to OVA-NC (Cy5) (-29 mV) (Figure 19 and Figure 20). It should be added, that by adsorption on serum proteins, all systems settle to a surface potential between -20 and -30 mV (PS-particles: Table 28, OVA NC: Table 30).

Studying the uptake of OVA-NC (Cy5) and PEG-OVA-NC (Cy5) on BMDCs, no significant changes were revealed for the heparin treated groups but a slight increase of the MFI (Cy5) and percent of uptake (Supplement 20 D, E). When investigating HSA-NC (Cy5) another types of protein capsules composed of human serum albumin (HSA), and comparing the effect of heparin with the one of OVA-NC (Cy5) it turned out, that the uptake reduction caused in the presence of heparin cannot be transferred to the other protein-based type of nanocapsules (Supplement 22 A, B). This result indicates that not every protein capsule can be modulated in terms of uptake by heparin.

The heparin effect on OVA-NC (Cy5) and PEG-OVA-NC (Cy5) could bear promising potential as a passive targeting molecule driving the uptake into DCs by reducing selectively the unspecific uptake into the macrophages of the RES. The selective downregulation of capsule-uptake into macrophages can improve pharmacokinetics of nanovaccines. This effect was observed in two independent experiments.

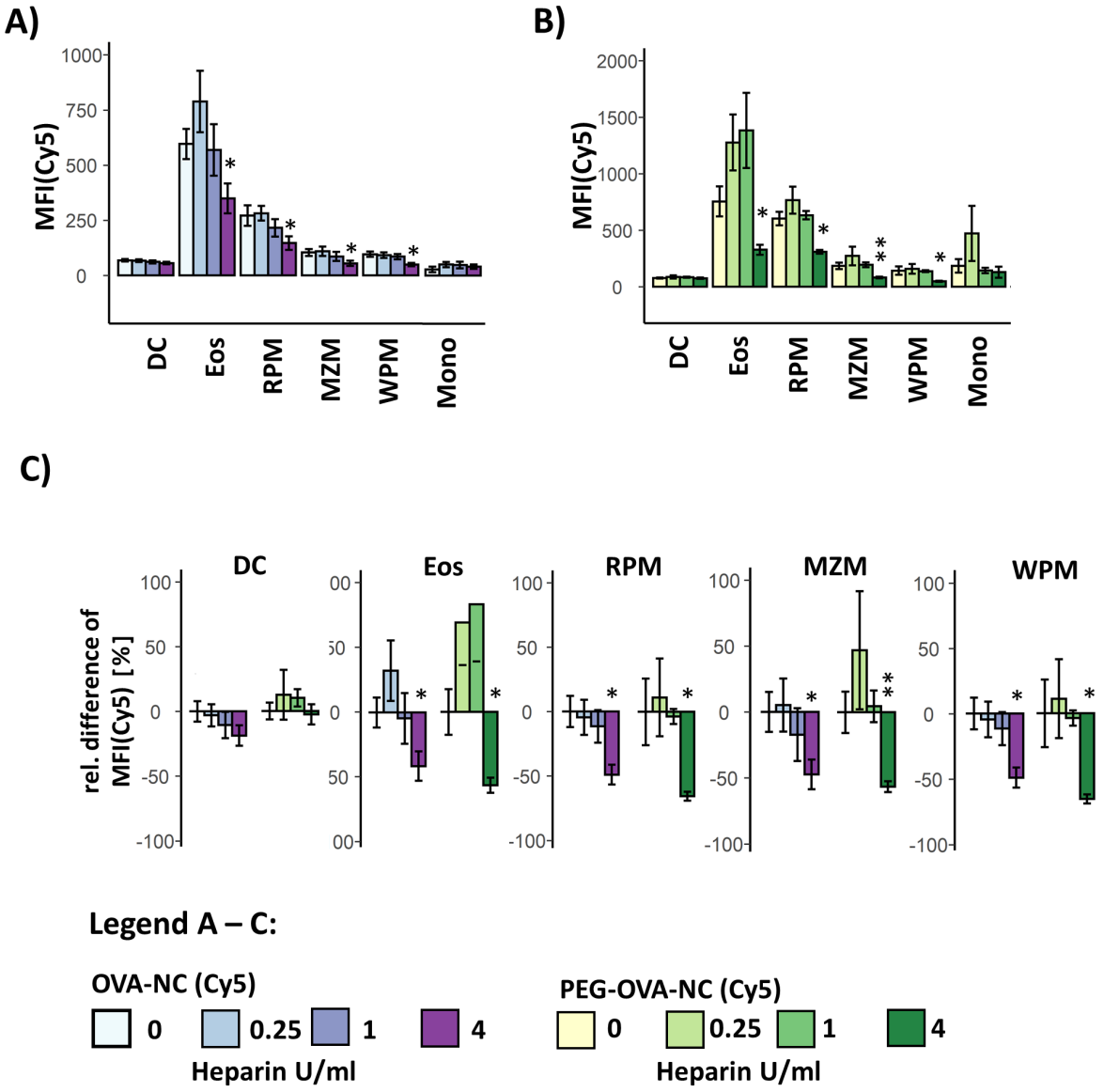

Figure 20: Presence of heparin favors cellular distribution of OVA-NC (Cy5) and PEG-OVA-NC (Cy5) towards DCs.

For this experiments the setup described in Figure 19 was used. Populations of interest were defined according to Table 23. The gating strategy is described in Supplement 20. **A/B:** The uptake of A) OVA-NC (Cy5) and B) PEG-OVA-NC (Cy5) into splenocytes when cultured in presence of heparin (0 – 4 U/ml). Represented is the mean +/- SEM of the median fluorescence intensity (MFI) of Cy5 for specifically defined spleen cell populations. The control group was compared by Wilcoxen tests with the groups of treatment. $p < 0.05$ = *, n = 9, batches = 3. **C:** The graph represents the mean +/- SEM of the normalized difference of the MFI (Cy5) towards the control group (0 U/ml) for OVA-NC (Cy5) particles (blue) and PEG-OVA-NC (Cy5) (green). The relative difference was calculated from the MFI-values in A/B.

4.3.1 The potential of heparin to regulate the organ accumulation protein-capsules *in vivo*

In the experiments described above (4.3.2), we have demonstrated the potential of heparin to modify the uptake of a protein-based nanovaccine into cells of the RES and thereby favor selectively the uptake into DCs.

Here, we will first investigate the effect of heparin on the biodistribution of OVA-NC (Cy5) *in vivo*. Animal were heparinized 15 minutes prior to injection of OVA-NC (Cy5) i.v. aiming a blood concentration of 4 U/ml. The fluorescence was detected in the living animal, with the *In Vivo* imaging spectrum (IVIS). After 30 and 360 minutes, the animals were sacrificed (Figure 21 A) and organs were examined more closely by fluorescence imaging and flow cytometry. For each time point a different batch of OVA-NC (Cy5) was produced (Table 29), leading to different fluorescent properties as well (Supplement 16). This allows only a limited comparison of the two time points with each other. By fluorescence cross correlation spectroscopy (FCCS), the capsules were proven to be stable in mouse plasm for a period of 24 h.

The total radiant efficiency of Cy5 in the liver decreased over the time of 360 minutes for both groups, ‘PBS + OVA-NC (Cy5)’ and ‘Heparin + OVA-NC (Cy5)’ (Figure 21 B). Between the two groups, no significant difference was observed *in vivo* (Figure 21 B). *Ex vivo* measurements revealed, that the overall uptake of OVA-NC (Cy5) was highest in the liver (Figure 21 D, E, Supplement 23), whereas the density of OVA-NC (Cy5) was strongest in lung (Supplement 23 C, D). At 30 minutes, the liver accumulation was significantly stronger for the heparin treated group (Supplement 23 B). The uptake into the spleen, where the adaptive immune response for i.v. nanovaccines is mainly mediated, was comparably low. At 360 minutes the fluorescence signal in the lung was significantly less for the heparin treated group (Figure 21 E). When injected in the blood, aggregates can form (see 1.2.3) [145] which immediately are sticking in the small arterial blood vessels of the lung. Heparin seems to reduce the aggregation in this study. We assume that the capsules are enzymatically degradaded in lysosomes, as Piradashvilli et al. [29] has shown. The metabolic products likely are excreted via the hepatobiliary route; explaining the high abdominal fluorescent signal interfering the *in vivo* liver signal.

These results indicate a slightly and significantly altered biodistribution in the liver within the first 30 minutes while heparinization. A desirable increase in ovalbumin capsules in the spleen by heparin was not observed.

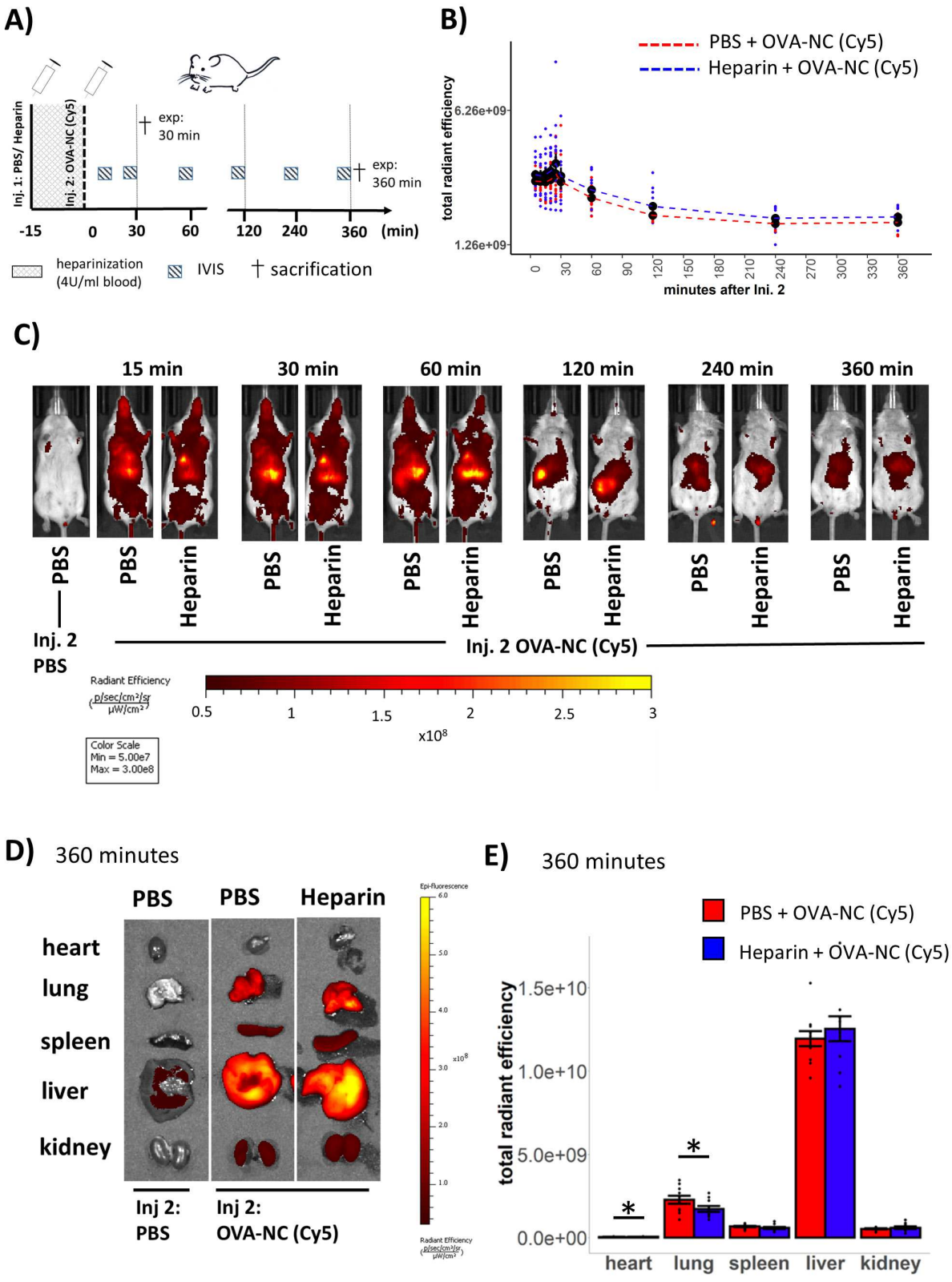

Figure 21: Biodistribution of OVA-NC (Cy5) in heparinized mice.

A: The scheme represents the experimental procedure: The time points of 30 minutes and of 360 minutes are independent and time-shifted experiments with use of different batches of OVA-NC (Cy5) not allowing a quantitative comparison. **B:** Time kinetic of total radiant efficiency (Cy5) of the liver *in vivo*. The migrating signal (C), presumably in the small intestine, presumably is responsible for the initial peak at around 30 minutes. **C:** The images show IVIS acquisitions of representative animals. The

heatmap represents the total radiant efficiency (Cy5). **D:** Organ distribution of OVA-NC (Cy5) at 360 minutes. The images show IVIS-acquisitions of representative animal at 360 minutes. The heatmap represents the values of the total radiant efficiency (Cy5). **E:** Represented is the mean+/- SEM of the total radiant efficiency (Cy5) at 360 minutes. The two groups were compared with each other by a Wilcoxen test for each organ, $p < 0.05$ = *. n = 11/10.

4.3.2 The potential of heparin to regulate the cellular uptake of protein-capsules *in vivo*

After having assessed the bio-distribution (see 4.3.1) in organs, we measured the uptake of OVA-NC (Cy5) into the specific immune cell populations of spleen and liver. To investigate whether heparin causes differences in cellular uptake in the RES, as suggested by the *in vitro* results (see 4.3.2), flow cytometry analysis were carried out. Four panels were applied (Supplement 26 and Supplement 27) for defining cell populations by following combinations of maker expression (Table 24) in order to identify the phagocyte RES cells and evaluate the uptake of OVA-NC (Cy5). Thereby also the cells mainly relevant to the nonspecific uptake of OVA-NC were identified. In addition, the uptake into the four subtypes of DCs was examined. Keeping in mind that especially cDC1 cells play an important role in mediating the anti-tumor immune responses.

No significant differences of cellular uptake ('% of uptake' and MFI) were observed for heparinized animal towards PBS pretreated animal for the investigated cell types (Figure 22, Supplement 24 and Supplement 25).

The liver, the organ with the highest uptake of OVA-NC (Cy5), exhibited the highest MFI (Cy5) values. The MFI of Cy5 was highest at 360 minutes for CD68+ MO (88,125/93,030 rel. U.) (Figure 22 B) and was highest for LSECs (21,528/21,214 rel. U.) at 30 minutes (Supplement 24 A). The data on the percent of uptake go along with the MFI values. At both time points more than 80% of LSEC were Cy5 positive (Supplement 24 B, C). Of all Cy5 positive cells in the liver (Supplement 29 E), with around 40% LSECs were the strongest represented at both time points followed by $CD68^+$ MO with ~25 % at 30 minutes and ~10 % at 360 (Supplement 29 C, D). This flow cytometry analysis on the non-parenchymal cells underlined the relevance of $CD68^+$ MOs and LSECs for the clearance of OVA-NC (Cy5).

While according to the literature around one third [87] to one fourth [86] of all non-parenchymal cells are Kupfs, the population Kupf seems clearly under-represented in this flow cytometry study (Supplement 27 A, Supplement 30 C, D). CD163 is a sensitive surface marker for this population [146]. Further, a methodological influence probably distorts the surface marker expression: through enzymatic processing of liver cells (see 8.3.4.1), surface proteins can be denatured or destroyed [147]. Nevertheless, CD68 is expressed as a pan-marker on infiltrated and resident macrophages and therefore presumably mainly includes Kupfs as well [146]. The

intention behind the choice of more and sensitive markers was to determine populations as accurately as possible in order to detect a possible effect of heparin.

The spleen showed a weak but recognizable Cy5 signal (Figure 21 D, E, Supplement 23). The MFI values of Cy5 into the investigated spleen cell populations were overall lower compared to the signal measured in the liver cells (< 500 rel. U.) (Figure 22 C, D, Supplement 25 A, D). Overall, the uptake of OVA--NC (Cy5) was highest in the macrophage cell populations (Mono, RPM, WPM, MZM) (Figure 22 D, Supplement 25 B, D, F). The population of mDCs of the four subtypes of DCs investigated (mDCs, cDC1, cDC2 and pDCs) was the one with the strongest OVA-NC (Cy5) uptake. At 360 minutes, the MFI was ~280 rel. U with 33% of uptake for mDCs (Figure 22 D, Supplement 25 B, D, F). The percent of uptake with 12 % for cDC1 and 8 % for cDC2 at 30 minutes (Supplement 25 D) and lower at 360 minutes (Supplement 25 F), meaning less uptake into DCs compared to other phagocyte populations, Eos, RPM, MZM and Mono. pDCs overall showed the lowest uptake of OVA-NC (Cy5) among the four subtypes of DCs (Figure 22 D, Supplement 25 B, D, F). To all Cy5 positive cells in the spleen, the wide defined populations DC and MO contributed at 30 minutes with ~4 % (DC)and ~13% (MO) (Supplement 30 A), whereas at 360 minutes with ~14 % (DC) and 5 %(MO) (Supplement 30 B) respectively. Taken together this flow cytometer data reveal that *in vivo* heparin does not alter cellular uptake of RES cells. The cellular distribution of the OVA-NC has never been described in such detail before.

A)

Liver

Abb.	Population
Mono	Monocyte
Kupf	Kupffer cells
CD68⁺ MO	CD68+ macrophage
CD11b⁺ MO	CD11b+ marcophage
DC	Dendritic cells
LSEC	Liver sinusoidal endothelial cells

Spleen

Abb.	Population
DC	*Dendritic cell*
MO	*Macrophage*
Mono	Monocyte
MZM	Marginal zone macrophage
RPM	Red pulp macrophage
WPM	White pulp macrophage
pDC	Plasmacytoid dendritic cell
mDC	Monocyte derived dendritic cell
cDC1	Conventional dendritic cell type 1
cDC2	Conventional dendritic cell type 2
Eos	Eosinophil

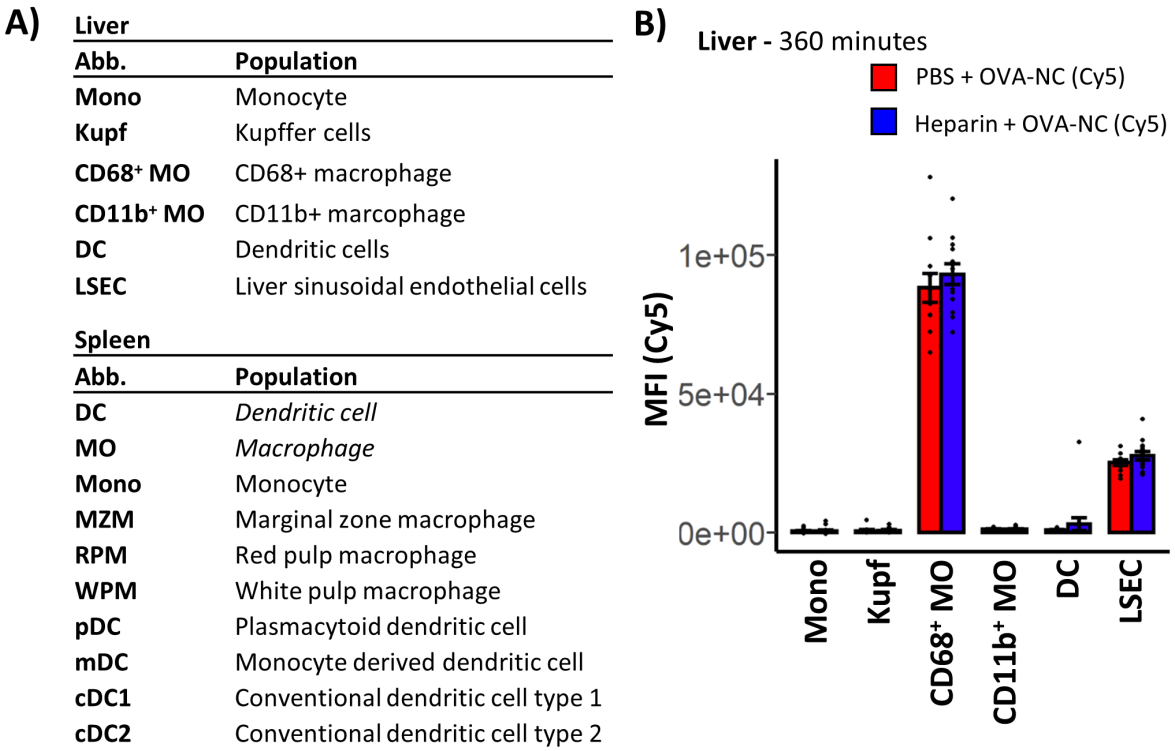

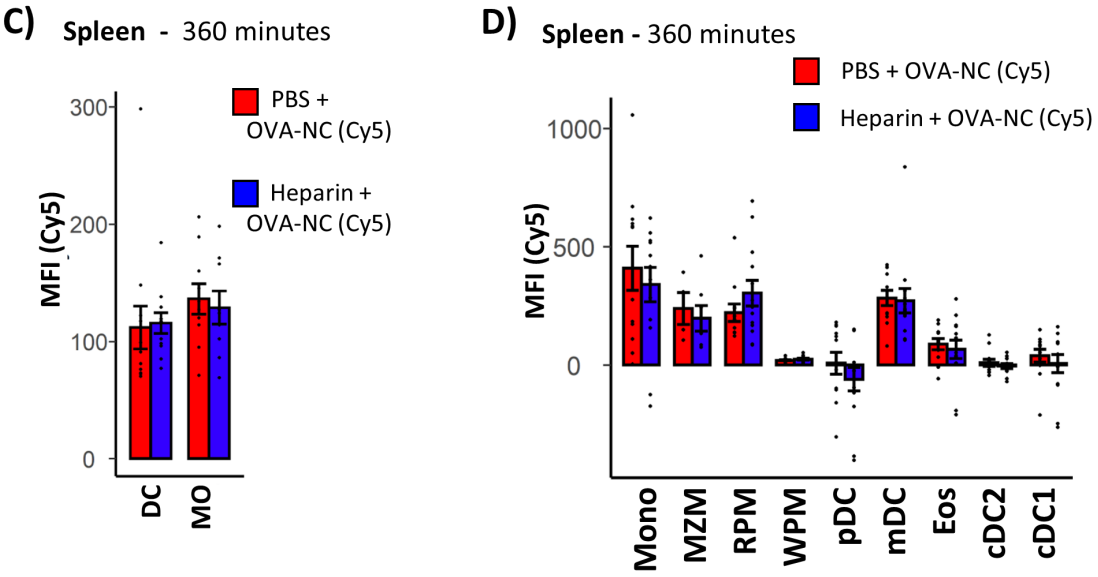

Figure 22: Cellular uptake in liver and spleen of OVA-NC (Cy5) in heparinized mice at 360 minutes.

A: The table lists the abbreviations and names of populations of the spleen and the liver, which were investigated and defined by flow cytometry analysis. **B:** The graph represents mean +/- SEM of the MFI (Cy5) for liver cell populations at 360 minutes. n = 9-14. **C:** The graph represents mean +/- SEM of the MFI (Cy5) for DCs and MOs in the spleen at 360 min. n = 12. **D:** The graph represents the mean +/- SEM of the MFI of Cy5 for specifically defined populations of the spleen at 360 min. n = 11-13, n (MZM) = 4/7. B-D: The two groups were compared by a Wilcoxon test for each organ, $p < 0.05$ = *.

4.4 Discussion

I.v. applied nanovaccines are a promising approach for cancer therapy. However, unspecific uptake by spleen and liver macrophages hampers the evocation of an effective immune response. There is an urge to find more active and passive targeting mechanisms to increase the uptake of the nanocarriers into DCs.

In this study, we investigated heparin as an uptake modulator of protein-based nanovaccines into DCs. First, we have shown the ability of heparin to modify uptake into DCs for polystyrene particles with positive surface charge (PS-NH_2 (BP)) (Figure 19 C, E, Supplement 17 A, C). This effect was not found for polystyrene particles with negative surface charge (PS-COOH (BP)) (Figure 19 D, E, Supplement 17 B, C). This finding indicated the role of the surface modifications. An exact opposite behavior to the PS-NH_2 particles was observed for the OVA-antigen shell nanovaccine (OVA –NC): *In vitro* heparin favored the cellular distribution of OVA-NC (Cy5) and PEG-OVA-NC (Cy5) in spleen cells towards DCs at high doses of 4 U/ml (Figure 20 A, B, C, Supplement 19 A, B, C). This demonstrates the importance of the nanocapsule material.

In vivo heparin did not change the uptake of OVA-NC (Cy5) into cellular subpopulations of spleen and liver (Figure 22). In terms of organ distribution, slight effects were detected (Figure 21 E and Supplement 23 B, C, D). At 30 minutes, the heparinization leaded to a significant increase of the Cy5 signal in the liver and kidney (Supplement 23 B, C). At 360 minutes heparin caused a reduced accumulation of OVA-NC (Cy5) in the lung (Figure 21 E, Supplement 23 D). An increased accumulation of nanocarriers in the liver goes along with our study on liposomes (chapter 1), in which heparin caused an increased accumulation in liver and spleen within the first 2 h.

Piradashvili et al.[29] have examined the biodistribution of these capsules and have shown the high liver accumulation of OVA-NC as well (Figure 21). While the liver sequestrated the highest amount of OVA-NC (Cy5) (Figure 21 E, Supplement 23 B) and shares the highest density of capsules (Supplement 23 C, D), the spleen shows a comparatively low uptake. Although the total uptake is highest in the liver (Figure 21 E and Supplement 23 B), to which ultimately also the size of the organ contributes, leading to a multiple higher accumulation. The tissue density of the capsules in turn, is ‘only’ around twice as much in the liver compared to the spleen at both time points (Supplement 23 C, D).

We can show that nanocarriers enter the spleen. For an i.v. administered anti-tumor nanovaccine a high accumulation in the spleen is desirable to evoke a strong adaptive immune response [21, 32, 71, 72]. Accumulation in the liver could have an unfavorable effect, since immune tolerance is mediated in the liver [85]. Whereas in the liver particles with a large diameter range can be sequestered, particle size plays a decisive role for spleen accumulation

[61]. Particles of 100-200 nm are internalized by resident macrophages [57] in the marginal zone and trapped by the slits of the sinusoids [65]. Based on the literature, it is assumed that the smaller capsules are trapped in the spleen, while the larger ones are trapped in the liver (and lungs) [39, 61]. However, we assume that smaller capsules emit less fluorescence because the encapsulation volume is smaller, too. For small capsules, the 'shell : volume' must therefore be higher as well. This means for capsules distributed in the body in a size-specific manner, that the Cy5 signal is not equivalent to the amount of the antigen ovalbumin. As the liver and the lung are prone to take up larger particles compared to the spleen, we expect a higher antigen concentration than derived from the Cy5 signal (Figure 21 E, Supplement 23 B), in the spleen.

Taking a look at the cellular distribution in spleen, where the immune response of parenterally applied nanovaccines is mediated mainly by DCs [21]: Thus, we see the DCs with the highest uptake capacity are mDCs (Figure 22 D, Supplement 25 B, D, F). For the mediation of the immune response cDC1s are the most essential key players [80]. The cytotoxic CD8+ T-cells, recognize the antigen and finally cause the tumor cell elimination. At 30 minutes, cDC1 showed a higher uptake than cDC2 and especially pDCs. This higher uptake of cDC1 is desirable to induce a successful anti-tumor immune response [80]. Nevertheless, the low MFI values for cDC1, cDC2 and pDC underline that there is still a need for research in the field of DC targeting, especially targeting cDC1s. In addition, macrophages of the marginal zone, which bear a higher potential for uptake of nanoparticles [61] have shown being able to initiate a successful $CD8^+$ T-cell immune-response as well [148]. With regard to the experimental setup of this study, we cannot make any statement about final efficacy of the vaccination. This requires adjuvant-loaded capsules as used in the *in vitro* study of Passlick et al. [30] and other systems determining the extent of the T-cell response.

While *in vitro,* for most of the macrophage populations a convincing decrease of OVA-NC (Cy5) uptake was observed, this effect could not be transferred to heparinized animals, being subjected do an equally high dose of 4 U/ml. The *in vitro* data point out that the modulatory effect of heparin on OVA-NC (Cy5) is dependent on the heparin concentration as no significant changes occurred at the concentrations 1, and 0.25 U/ml but 4 U/ml (Figure 20 A, C, Supplement 19 A, C). That the favorable effect of heparin towards DCs did not occur on a cellular level *in vivo*, might be caused by a lowered concentration due to degradation and clearance mechanism of heparin [111, 114, 117]. We can assume that at the time of injection of the OVA-NC, which is 15 minutes after the heparin injection, the level of heparin has already fallen to a lower level. The half-life for doses in the range of 272 mg/kg (dose was applied for mice in this study), according to the literature in human the elimination half-life is around 120 minutes (107 and 153 minutes) looking at patients having received an initial bolus of 300 U/kg in two pharmacokinetic studies [122, 123]. Considering the initial steep decline described [114,

123], we expect a reduction of the heparin concentration by significantly more than the resulting concentration of 3.5 U/ml with linear clearance. Blood heparin level might be retained to a higher level over time by administering repeated boluses, like carried out in cardio vascular surgery [122, 123]. For creating a locally increased heparin concentration by other means, an approach could be the pre-coating of the capsules with heparin according to Champanhac et al. [129]. It is theoretically possible that the heparin effect can be used for subcutaneously applied nanovaccines *in vivo*. Subcutaneous injected heparin can allow higher locally concentrations, as the polysaminoglycane is released slowly into the blood causing its anticoagulant effect [114].

Despite the fact that the *in vitro* effect could not be transferred *in vivo* with this setup of co-medication, we want to discuss heparin as a passive targeting compound for nanovaccines to favor uptake into DCs. In contrast to other targeting approaches (see introduction) including surface modifications, this systemically applied approach bears some advantages: Heparin, discovered in 1916 [102] since then, became an established and frequently used medication [110]. Thus, it is probably less effort and risks using heparin as a molecule of passive targeting instead novel molecules. Co-applied targeting fully retains the structure of the particle system. Especially for protein-based antigen-shell nanovaccines, in which the antigen should be delivered in its natural formation, in order to evoke a specific immune response. Regarding additional side effects of heparin, the polysaminoglycan could further support and hamper the therapeutic effect of the protein based anti-tumor nanovaccine. Besides its anticoagulant effect, heparin exhibits anti-inflammatory effects as well [149], which could weaken the evocation of an immune response by a co-applied nanovaccine [150]. Heparin hinders the translocation of NF-κB [150] into the nucleus and thereby downregulates the expression of inflammatory molecules. Going along with an immunization mediated by DCs, NF-κB mediated downstream processes are relevant for induction of the adaptive immune response [151, 152]. A recent study by Moser et al. [153] outlines the beneficial role of selective NF-κB inhibitors for vaccines, reducing the adjuvants caused inflammation and keeping or rather strengthening the protective response. To determine the effects of heparin on immune response, a different experimental setup using adjuvant-loaded OVA-NC is required. Taking a closer look at the surface charge of particles having formed a protein corona (Table 28, Table 30) we see only marginal differences of which we expect having minor influence on cellular uptake. Presence of heparin doesn't influence surface charge significantly neither. For OVA-NC (Cy5), it was shown that the negative charge is slightly reduced by heparin (Table 30, Supplement 19 F). Grabbe et al. [21] showed that there is a surface charge dependence on the accumulation in the spleen of i.v. injected RNA-lipoplexes in mice. A slight positive surface potential resulted in the highest amount of RNA-lipoplexes in the spleen, whereas highly charged lipoplexes were not favorable for spleen accumulation. *In vitro*, positively charged particles are taken up

stronger compared to anionic and neutral particles by DCs and support their maturation [154]. In this study, PS-NH_2 (BP) (+53mV) particles were also found to have a higher uptake into DCs compared to PS-COOH (BP) (-53mV) at 0 U/ml heparin (Figure 19). The low uptake by DCs of the negatively charged particles in contrast to the high uptake of positively charged particles, PS-NH_2 (BP), underlines the findings of Thiele et al. [154]. In presence of heparin, in turn, uptake of the positively charged PS-NH_2 particles was reduced to a comparable low level.

All together in this study, we have underlined the potential of heparin to significantly regulate uptake into phagocyte spleen cells *in vitro*. In particular, we demonstrated passive targeting properties of heparin for a protein-based antigen-shell nanovaccine carrier favoring the uptake by DCs. This passive targeting property could not be transferred *in vivo* with a high-dosed heparinization. Nevertheless, heparin emerges as a interesting DC targeting molecule for further research. This biodistribution is adding to the growing knowledge of cellular distribution of nanoparticles and goes beyond the organ distribution demonstrated before. Furthermore, this study reveals the cellular distribution of the protein-based nano-vaccine OVA-NC in the RES.

5 Chapter 3: Characterization of the Polydexamethason Silica Nanocapsule

Encapsulation of Polyprodrug in Nanocontainers for Controlled Delivery and Release of Water-Soluble Drugs[11]

The data of this chapter are about to be submitted. This work was a collaboration with [redacted] *and* [redacted] *group of* [redacted] *of the Max Planck Institute for Polymer Research. Myself contributed the following represented data on biodistribution and cellular uptake. Further, I worked with the existing data of* [redacted] *and* [redacted]*, group of* [redacted]*, Pediatric Clinic of the Medical University Center Mainz.*

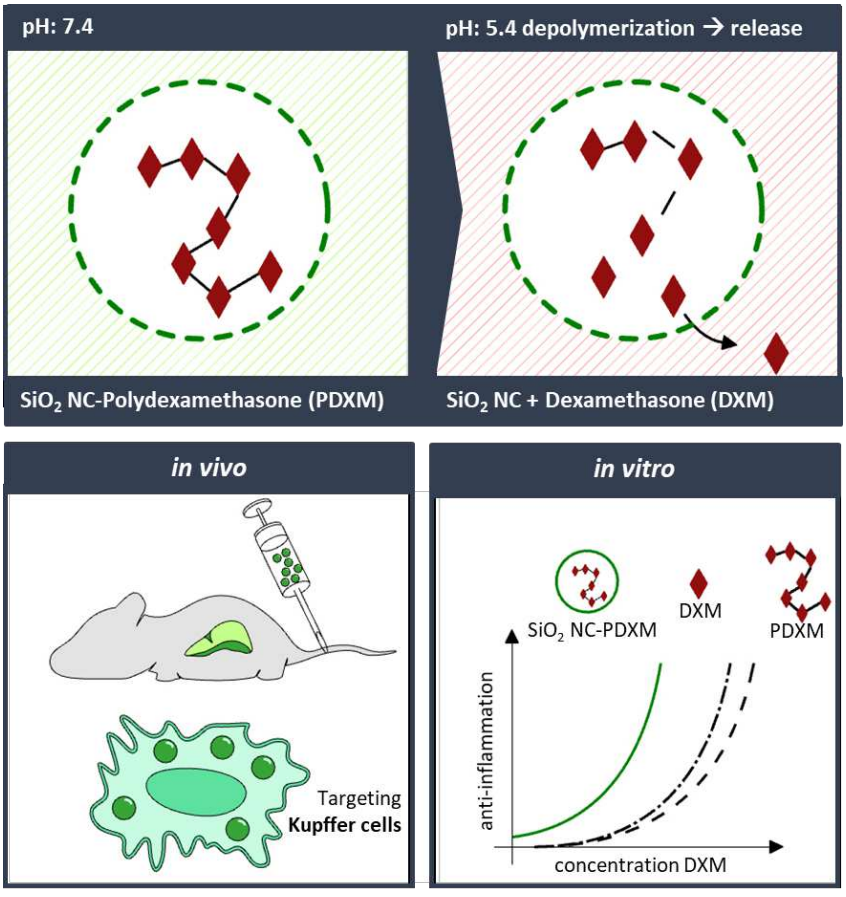

Figure 23: Graphical abstract chapter 3 - Characterization of Polydexamethasone Silica Nanocapsule

[11] The original title of the manuscript was adapted 155. Li Mengyi, et al., *Encapsulation of Polyprodrugs enables an Efficient and Controlled Release of Dexamethasone*. 2021: About to submit.

5.1 Abstract

Herein, a polydexamethasone loaded mesoporous silica nanocontainer was investigated. The strategy of this system is to improve pharmacodynamics by enabling a controlled drug release and a targeted delivery. The concept was evaluated by means of Kupffer cells (Kupf), which are key players in pathology of hepatitis, where corticosteroids can intervene the inflammatory process.

This *in vivo* study showed the preferential uptake of the polydexamethasone loaded nanocontainers into Kupf. Murine non-parenchymal murine liver cells, significantly reduced the release of the inflammatory cytokine interleukin-6 (IL-6) response upon lipopolysaccharide stimulation, indicating the effective suppression of the inflammatory response *in vitro*. We could show that the encapsulated polydexamethasone nanocontainer has a higher suppressive effect compared to the drug monomer, dexamethasone.

Taken together this example of a polyprodrug-loaded nanocontainer, underlines the therapeutic potential of targeted delivery and controlled release, what can be reached both by pH-responsive polyprodrug loaded nanocontainers.

5.2 Introduction

Targeted delivery and site-specific release of therapeutics are detrimental for reducing side effects and improving pharmacodynamics of drug-loaded nanocarriers *in vivo*. Controlling the release of water-soluble drugs enables a higher local concentration, while reduced systemic levels. Herein, polydexamethasone (PDXM) was synthesized as a model for a water-soluble polyprodrug that can degrade into effective dexamethasone phosphate (DXM) monomers upon mildly acidic conditions (Figure 25 A). The water-soluble polyprodrug was encapsulated in mesoporous silica nanocontainers ($SiNO_2$ NC), so that it was protected from early depolymerization and leakage at physiological pH value (Figure 25 B).[12] The length of PDXM slightly influences the release at acidic pH (Figure 25 B). Mildly acid conditions occur in the cellular lysosome of macrophages like Kupffer cells. This principle of drug delivery allows not only controlled release but also targeted delivery. Packaging in nanocontainers ensures that predominantly phagocytotic cells, mostly macrophages, take up the active substances.

The transcription factor nuclear factor kappa-light-chain-enhancer (NF-κB) is a key player in inflammation pathways, leading to secretion of IL-6 [156] and other inflammatory mediators [157]. Downstream effectors of NF-κB are involved in the process of liver fibrosis accompanying the inflammation. Kupffer cells and infiltrated monocyte-derived macrophages contribute to the pathogenesis of hepatitis and fibrosis by secretion of stimulatory molecules e.g., tissue necrosis factor-alpha (TNF-alpha) and IL6 [158]. These molecules induce cell

[12] paraphrased from 155. Ibid.

death of hepatocytes and activation of hepatic stellate cells leading to fibrosis [94]. The active monomer DXM, activates glucocorticoid receptors and thereby impedes the pro-inflammatory downstream effects of NF-κB [159] (Figure 24 B). We hypothesized that encapsulation of the polyprodrug PDXM leads to a higher effectiveness than the monomer drug (DXM).

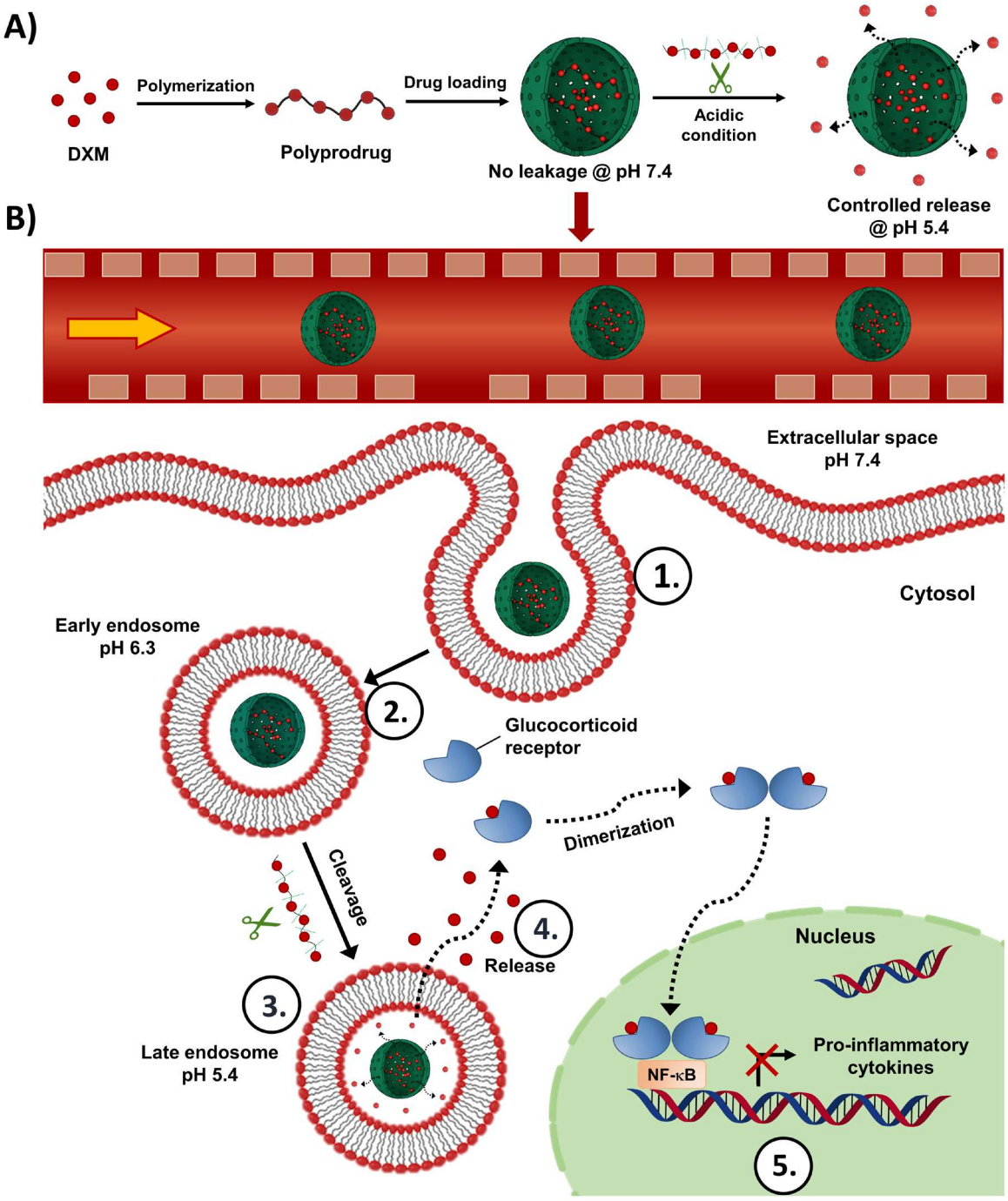

Figure 24: Schematic principle of the polyprodrug loaded mesoporous silica capsules.[13]

A: The anti-inflammatory drug DXM was polymerized and loaded into the mesoporous silicacapsule. At low pH (pH 5.4) the polyprodrug, which is sequestrated in the capsule depolymerizes and the pharmaceutical active agent can evade. **B:** By drug delivery within nanocontainers, primarily phagocyting cells take up the drug (1.). The nanocapsule is transported intracellularly (2.). The mildly

[13] The figure and description are adapted from 155. Ibid.

acidic condition of the late lyposomes causes degradation of the polyprodrug (3.). DXM monomers are released into the cytosol and can activate glucocorticoid receptors (GR) (4.) leading to inhibition of NF-κB activity (5.), what causes the anti-inflammatory response by downregulating transcription of pro-inflammatory factors.

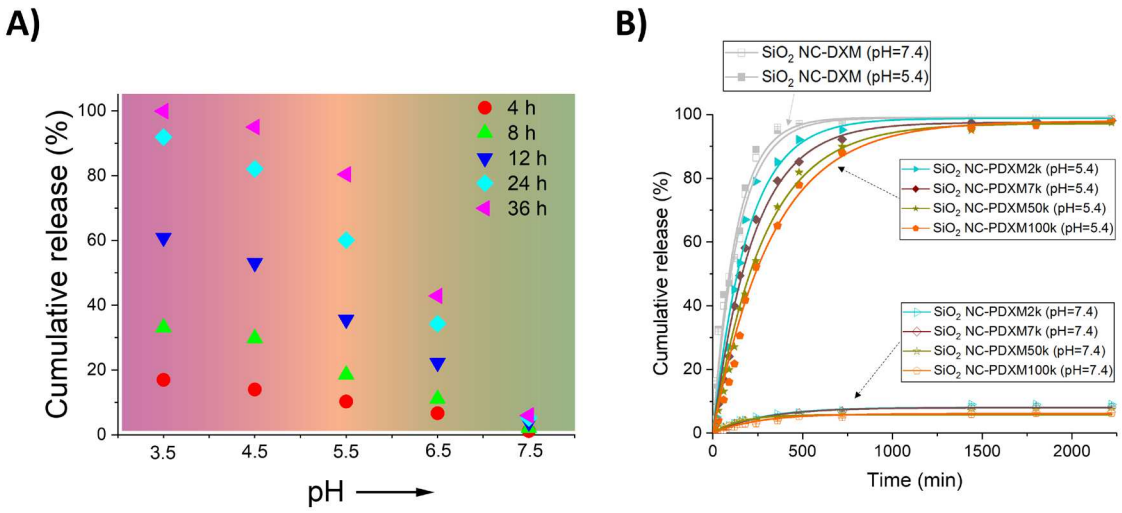

Figure 25: pH dependent release of DXM from SiO_2 NC-PDXM [14]

A: Time- and pH-dependent degradation profiles of PDXM7k. The red background covers the range of pH values in different acidic extra- and intracellular environments reported in the literature [160, 161]. The green background represents physiological pH values (around pH 7.4).[15] **B:** Release profiles of PDXM2k-PDXM100k from SiO_2 NC at pH 7.4 and 5.4 (at 37 °C, mean ± SD, n = 3).

5.3 Results

5.3.1 Biodistribution and cellular uptake of Cy5-SiO_2 NCs

First, the organs and cells were identified into which the SiO_2 NC enter and potentially deliver PDXM. The empty SiO_2 NCs were covalently labeled with Cy5 for studying their accumulation in the murine organism by using the *In Vivo* imaging Spectrum (IVIS). A strong epifluorescence signal of the Cy5-SiO_2 NCs loomed in the liver 5 minutes after i.v. injection, which slightly diminished within the next 2 h (Figure 26 A). The epifluorescence for Cy5-SiO_2 NCs was strongest in the liver on organ analysis after 2 h of circulation (Figure 26 B, C).

Immunofluorescence of CD68, a pan marker for both resident macrophages as monocyte derived macrophages [146], confirms the uptake of Cy5-SiO_2 NCs into non-parenchymal cells of the liver. An uptake into hepatocytes was not seen (Figure 26 D and Supplement 31). Flow cytometry analysis using specific marker expression patterns confirmed the strong cellular uptake into distinct macrophage populations in liver and spleen (Figure 26 E, Supplement 32 and Supplement 33). The graph in Figure 26 F shows that of the populations of Kupf, Mono and the MO, a considerable proportion takes up Cy5-SiO_2 NC *in vivo*: respectively 87%, 87% and 44%**.** The high median fluorescence intensity (MFI) of Kupf and Mono (Figure 26 G)

[14] Adapted from 155. Ibid.
[14] Paraphrased from 155. Ibid.

illustrates the high loading of Cy5-SiO_2 NC into these cells compared to the other presented populations of liver and spleen.

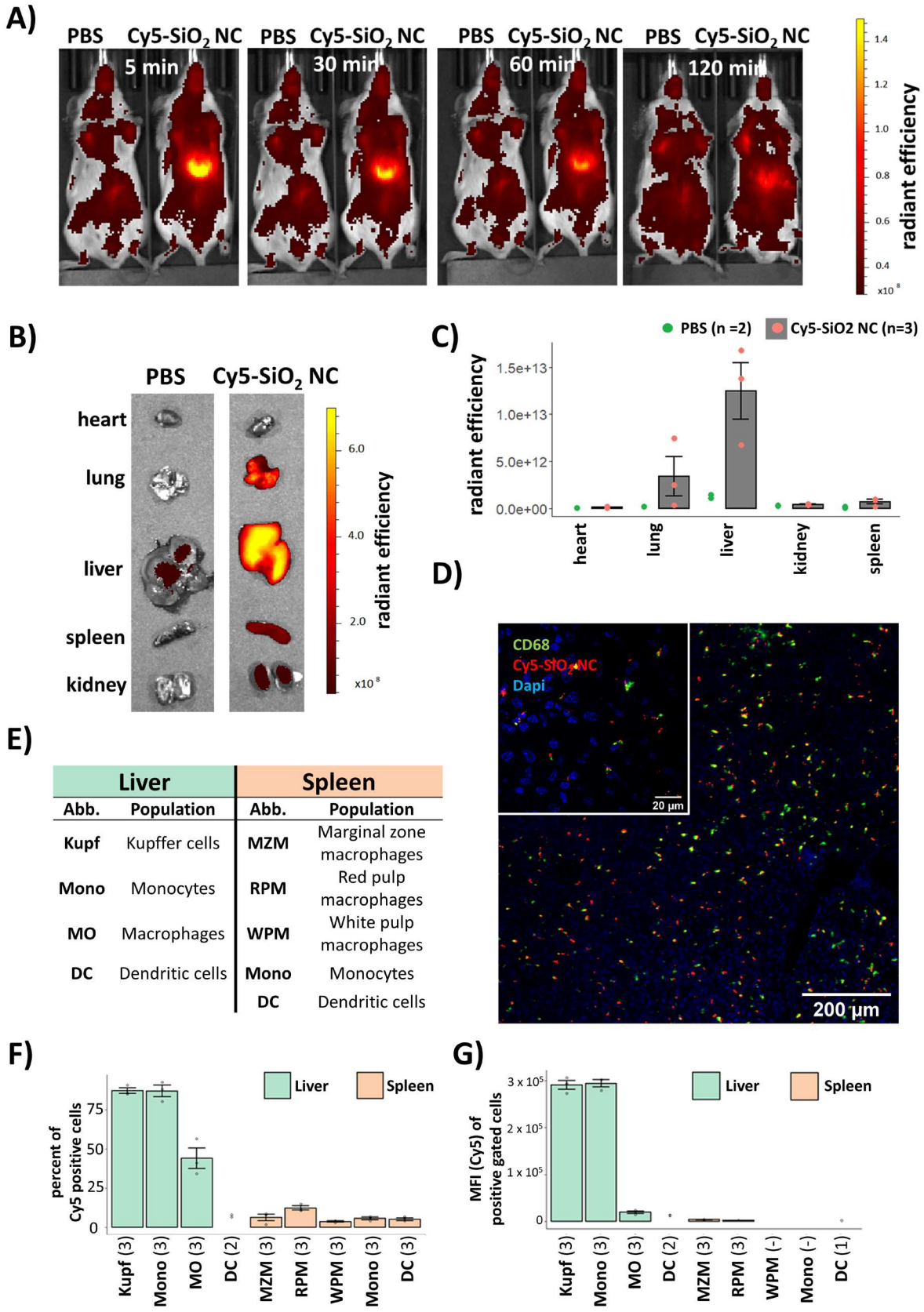

Figure 26: *In vivo*, Cy5-SiO_2 NC accumulate in the liver and are taken up by NPCs, especially Kupfs.

A: *IVIS* of Cy5-SiO2 NCs treated mice at different time points. Cy5-SiO2 NCs dispersions were injected intravenously to a final concentration of 300 µg ml^{-1} in the blood. **B:** *Ex vivo* fluorescence images of organs after intravenous injection of Cy5-SiO2 NCs at a blood concentration of 300 µg ml^{-1} for 2 h. **C:** Radiant efficiency of organs from the mice sacrificed at 2 h post injection The graph shows the mean ± SD of Radiance efficiency for three animals obtained (grey balks and blue points). The red points represent the background intensity counts of two control animals injected with PBS. **D:** Confocal microscopy of Cy5-SiO_2 NC and CD68 on liver sections. The image shows the overlay (yellow) of Cy5-SiO_2 NC (red) and CD68 (green). Nuclei were stained for Dapi (blue). The big image was acquired using the 10x objective, the small image (upper left) was taken using the 63x oil immersion objective at a different spot. **E:** Cell populations and abbreviations of interest. The gating strategies are outlined in Supplement 32 and Supplement 33 **F:** Percentage of Cy5-SiO_2 NC positive cells. The graph shows the mean (+/-SEM) of Cy5-positive gated cells of each population, described in E. If the population included less than 50 cells, the value was excluded from analysis because of susceptibility to errors. In the brackets the number of animals analyzed is given. **G:** Median fluorescence intensity of Cy5-SiO_2 NC positive cells. The graph shows mean (+/-SEM) of the median fluorescence intensity of Cy5 of the Cy5 positive gated cells in F. If the positive gated population included less than 50 events, the value was excluded from analysis because of susceptibility to errors. F/G: In the brackets the number of animals analyzed is given.

These data confirm the preferential uptake of SiO_2 NCs into Kupf, Mono and MO (Figure 26 F, G) in the liver. As the uptake into splenic macrophage subpopulations and DCs was apparently lower (Figure 26 F, G and Supplement 34) compared to the phagocytes of the liver, we underline that this capsules are preferentially delivered to the Kupfs. This finding substantiates the benefits of an encapsulation, which enables a targeted drug delivery and thereby potentially reduces side effects and increases drug efficacy.

As an equivalent amount of Cy5-NHS ester alone, only showed a weak enrichment in the liver and within the respective cell populations (Supplement 35), we can exclude any false positive results by free dye or targeting effects by the Cy5-NHS ester modification.

5.3.2 Biological and functional analysis of PDXM and SiO_2 NC-PDXM.

We evaluated the potential of PDXM and PDXM-containing SiO_2 NCs to decrease the LPS-induced secretion of the pro-inflammatory IL-6. Cell culture supernatants of LPS stimulated NPCs were analyzed using an IL-6 ELISA (Figure 27 A, B). Free PDXM was able to significantly suppress the secretion of IL-6 by NPCs in a dose-dependent manner regardless of the PDXM chain-length and molecular weight with a similar activity compared to DXM as a positive control (Figure 27 A). When PDXM was formulated into SiO_2 NC the same level of IL-6 reduction was reached at a final concentration of the whole drug (NC + PDXM) at already 0.1 µg/ml. In Figure 27 C the conditions, presented in Figure 27 A and B (10 µg/ml, 1 µg/ml, 0.1 µg/ml PDXM respectively SiO_2 NC PDXM) were plotted against the concentration of PDXM. The graph illustrates the higher efficacy of SiO_2 NC-PDXM. To reach a 20% expression of IL-6, instead of 10 µg/ml active substance only 10 ng/ml of active substance were required when PDXM was formulated in SiO_2 NC. This is a 1000 times reduction of active substance. It should be noted that empty SiO_2 NCs did cause an increase (~30%) on IL-6 expression on LPS treated cells (Figure 27 B). “These efficient downregulating effect on IL-6 by SiO_2 NC-PDXM

(Figure 27 B), indicates an efficient release of DXM out of SiO_2 NCs which is triggered by the degradation of PDXM to DXM due to lower pH in endosomes and lysosomes and the subsequent diffusion through the endosomal and lysosomal membranes into the cytoplasm in order to bind to glucocorticoid receptors leading to the transcriptional blockade of pro-inflammatory cytokines including IL-6 in the nucleus. [162-164]“ [16]

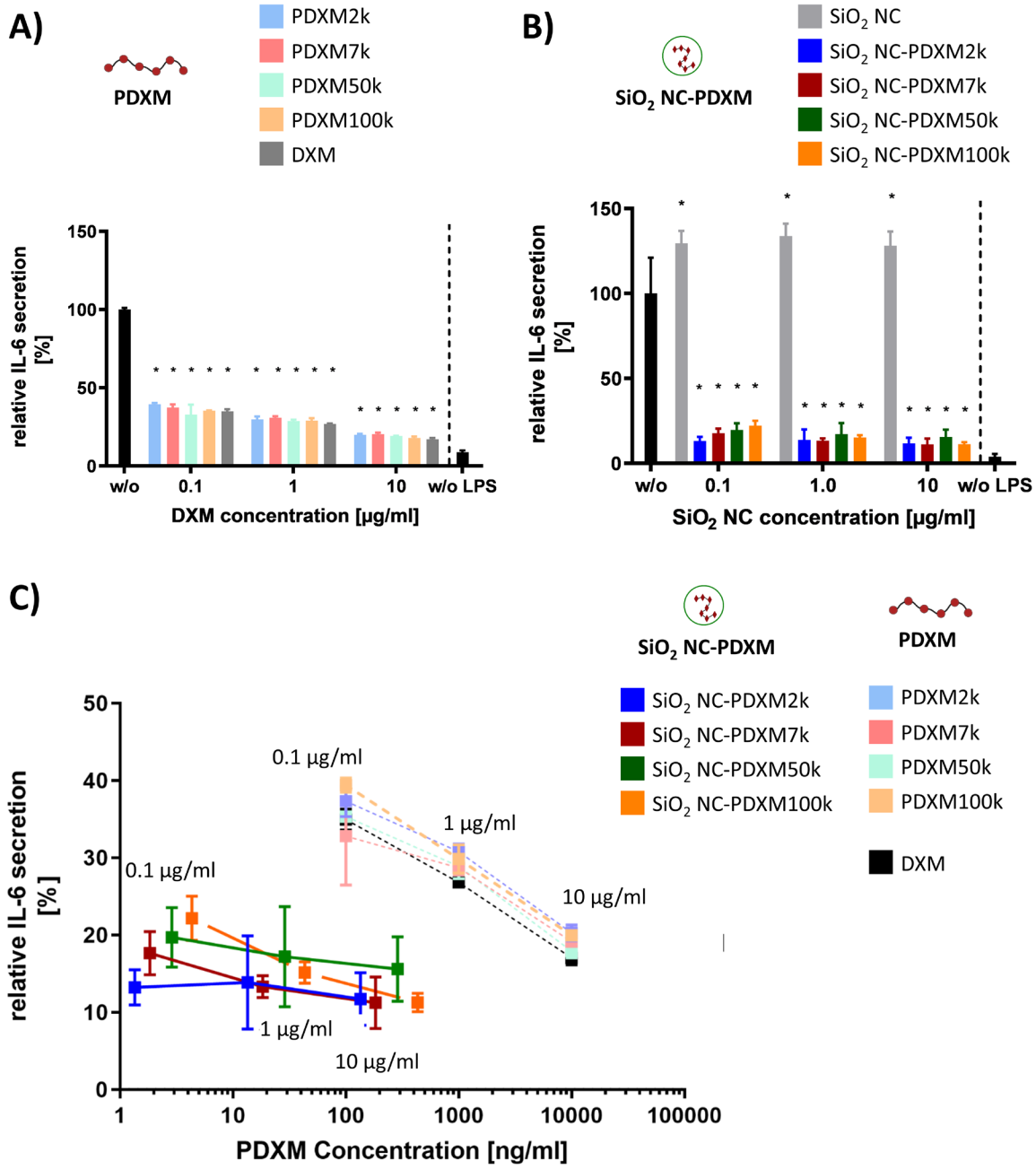

Figure 27: IL-6 secretion from NPCs after SiO_2 NC-PDXM stimulation.[17]

A: Relative IL-6 secretion of NPCs after stimulation with different PDXM formulations at different concentrations and with or without 2.5 μg mL^{-1} LPS. Given is the mean ± SD of 3 replicates. The IL-6

[16] Written by the other authors 155. Li Mengyi, et al., *Encapsulation of Polyprodrugs enables an Efficient and Controlled Release of Dexamethasone*. 2021: About to submit.

[17] The experiments were carried out by [redacted] and [redacted], group of [redacted], Pediatric Clinic of the Medical University Center Mainz. Myself did the evaluations.

expression was normalized on the untreated, LPS stimulated condition (black). **B:** The effect of SiO_2 NC-PDXM on IL-6 secretion. Relative IL-6 secretion of NPCs after stimulation and treatment with SiO_2 NC-PDXM formulations at 10 μg mL^{-1}, 1 μg mL^{-1} and 0.1 μg mL^{-1}. The IL-6 expression was normalized on the LPS-stimulated control, without treatment (black). Data are represented as the mean ± SD of three independent experiments (n = 3). All conditions were compared to the control group (LPS stimulated, without drug treatment) and significance is given with $P < 0.001$ (*) (One-way ANOVA). **C:** The relative IL-6 expression from Figure 6a and 6b was plotted against the applied final concentration of PDXM in the cell culture medium.

5.4 Discussion

We showed the preferred accumulation of SiO_2 NC in Kupfs by flow cytometry using the sensitive marker CD163, which is specific for the resident macrophage population of the liver [146]. This lets us expect a selectively high suppression of NF-κB by DXM in these cells for application of SiO_2 NC-PDXM. Further, we could show that this concept of drug delivery, encapsulation of a polyprodrug, needs less active substance for evoking the same anti-inflammatory effect when using the monomer drug, DXM. "*In vitro* cell culture experiments showed, that the formulated polyprodrugs, SiO_2 NC PDXM, were very effective in reducing the production of the pro-inflammatory cytokine IL-6 and require 1000 times less active substance to evoke a similar anti-inflammatory effect." [155] We hypothesize that the targeted cellular uptake, as well as the controlled release, may contribute to this increased drug efficacy.

The authors believed, "that this example has potential for therapies where inflammatory responses need to be suppressed in a targeted manner, such as in autoimmune hepatitis or inflammatory bowel disease. …The concept of encapsulation of polyprodrug could be generalized to other drugs with two reactive groups." [155]

From an immunological point of view, SiO_2, which is regarded a chemically inert component [165] is able to stimulate immune responses [166]. An increased IL-6 expression was observed in this study for the unloaded SiO_2 NC (Figure 27 B). Therefore, the shell material has to be questioned for use as an anti-inflammatory drug. To develop this drug further, it is also required that the shell shows biodegradability. Possibly, a protein capsule as shown previously in chapter 2 might be suitable as well for loading an anti-inflammatory polyprodrug, as these also show strong accumulation in the liver macrophages. In this case, however, the capsule should not consist of an antigen but rather of an endogenous protein. Though, a mesoporous structure and a slow capsule-degradation might be critical for the slow-release effect and the favorable effects on pharmacokinetics – this in turn limits the selection of materials. The mesoporous silica capsule selected here is thus a great model to proof the concept. Toxicity studies showed an increase of toxicity at a concentration of 100 µg/ ml what was interpreted as a "low toxicity profile" [155].

The systemic side effects of corticosteroids are more relevant on a long term as they are then causing diabetes, hormonal disorders, change in bone metabolism and other effects [167]. A high need for this targeted and slow release concept exists, if the compound has severe and

acute systemic adverse effects - most exemplified for chemotherapeutics. Injection of a nanocarrier also implies that a larger foreign body enters the organism. This could cause immunological reactions and, in the example of the here represented approach of liver disease treatment, increase the inflammation and fibrosis [168].

This principle could also be extended to other diseases, e.g. rheumatism - the capsules could be administered locally into the rheumatic tissue. There, macrophages, which primarily take up the nanosized materials, play a critical role in the inflammatory process, too. Macrophage activated syndrome can be a “fatal consequence” in rheumatic disorders [169]. The principle presented here, could potentially be used for the clinical and acutely life-threatening picture of hemophagocytosis, a disorder characterized by increased activation of macrophages [170]. The form of administration of corticosteroids presented here could lead to high accumulations of corticosteroids in the disease-driving macrophages. In this context, one can think about polymerizing other active ingredients. Methrotrexate, which has a much higher toxicity than corticosteroids and is also used in rheumatic disorders, could be an example here [167, 171]. The two amino and two carboxy groups of methrotexate can be used for polymerization [172].

With the experiment shown here, it was demonstrated that the principle of encapsulation of a pH-responsive polyprodrug is feasible and results in favourable effects. A basis is created to extend and improve this concept on further indications.

6 Chapter 4: Amnis® Imagestream®XMark II - Intracellular Release of DXR from Liposomes

Chapter 4 represents a methodological concept to study the intracellular release of DXR from liposomes.

This chapter is a collaboration with the SFB 1066 members, [redacted] (group of [redacted] Dermatology of the University Medical Center Mainz), and [redacted] and [redacted] (group of [redacted], Pharmacy and Biochemistry of the Johannes Gutenberg University Mainz). In collaboration with [redacted], my work was establishing the settings of the Amnis® ImageStream®XMark II, the gating and evaluation strategy with the IDEAS® software as well the evaluation parameters for answering the question of uptake and release.

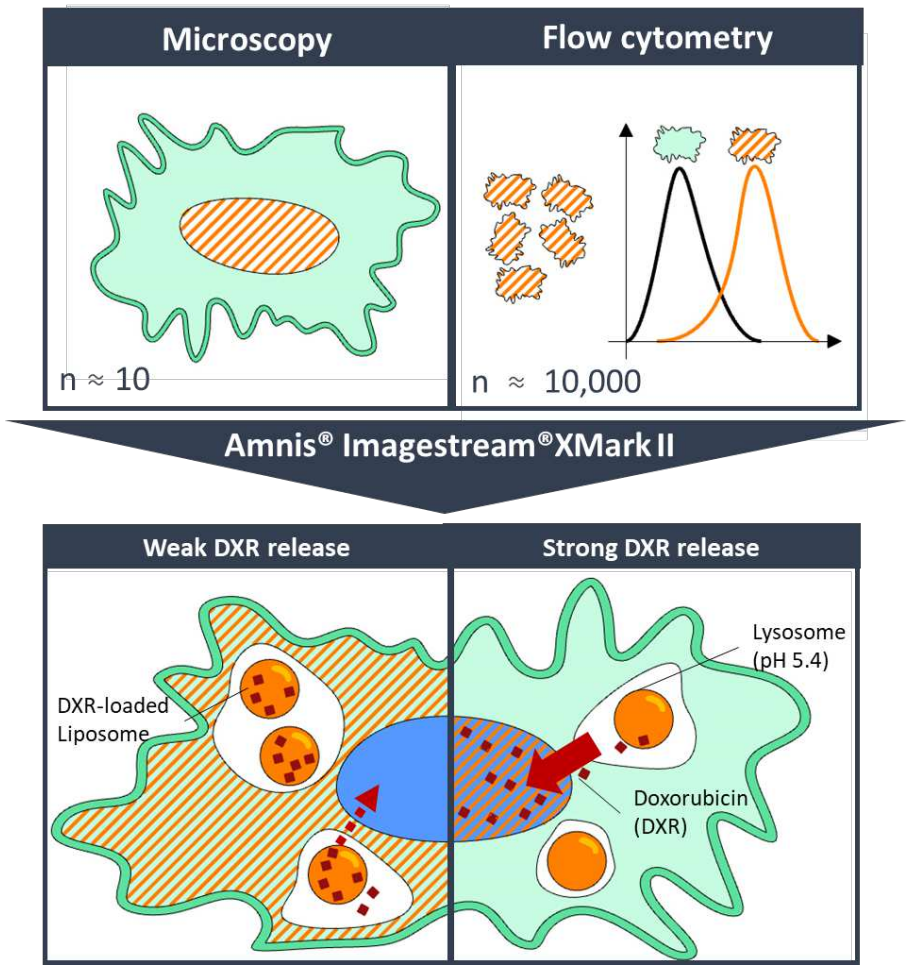

Figure 28: Graphical abstract chapter 4 - Amnis® Imagestream®XMark II - Intracellular Release of DXR from Liposomes.

6.1 Abstract

Using the Amnis® Imagestream®XMark II, we investigated the intracellular release of Doxorubicin (DXR) from liposomes, combining flow cytometry and microscopy. *De novo* lipid compositions, with an optimal ratio of extracellular stability and intracellular release capacity, created by the Helm's group, were characterized on their behavior inside cells.

UKRV-Mel-15a cells and primary differentiated human macrophages were treated with DXR-loaded liposomes for 30 minutes and 4 hours in order to evaluate the release of DXR. The fluorescent properties of DXR as well the high binding affinity to DNA enabled us to distinguish the free DXR in the compartment of the nucleus from the liposomal DXR in the cytoplasm separately. Comparing DXR fluorescence of the nucleus with the DXR fluorescence of the cytoplasm, provided insights into the intracellular stability.

Having established the evaluation parameters 'ratio of release' and the 'release speed' we identified the formulation with the strongest intracellular release properties, DOPG : DOTAP : CHEMS (mol-%: 66.5 : 28.5 : 5). Furthermore, we demonstrated that surface modifications with linear polyethlyenglycol (linPEG) and hyperbranced polyglycol (hbPG) have no influence on intracellular release.

6.2 Introduction

The Amnis® ImageStream®XMark II combines fluorescence microscopy and flow cytometry with a modern image-analysis approach [173]. Using the Amnis® ImageStream®XMark II a higher statistical validity is achieved than with conventional fluorescence microscopy. In contrast to conventional flow cytometry, qualitative information on localization of the fluorescent element and the cellular structure can be gained.

As outlined in the introduction (1.2), the uptake into the target cell but also the intracellular release of the pharmaceutical agent is decisive for the efficacy of nanodimensional drugs. For development of liposomal drug vehicles, it is a challenge to find the optimal balance of extracellular stability and intracellular lability. The extracellular stability of liposomes is an important factor for transporting the drug molecule to the target cell - the principle of nanocarriers. The intracellular release capacity of the nanocarrier finally ensures the bioavailability of the loaded drug. Voigt et al. identified *de novo* lipid compositions which were as stable as necessary but also afforded sensitive responsiveness to release cargo at acidic pH [174]. Within the screening approach for liposomal compositions [redacted], three formulations emerged (Table 8). Retention and release properties of liposomes were assessed *in vitro* by [redacted] using the small fluorescent model cargo sulforhodamine B (565 nm).

Table 8: Overview on investigated liposomal formulations.

Formulation:	L0	L2c	L11c	L15c
Lipid composition	EPC : CHOL	DMPC : DODAP : CHEMS	DOPC : DODAP : CHEMS	DOPG : DOTAP : CHEMS
Molar ratio mol-%	(55 : 45)	(66.5 : 28.5 : 5)	(63 : 27 : 10)	(66.5 : 28.5 : 5)

by [redacted] discovered liposomal formulations with high release capacity [174]

For measuring the intracellular retention and release properties of liposomes, DXR was used as a model cargo. Because of its fluorescent property and the uptake into the nucleus of the free molecule, when not sequestered in liposomes, DXR is also suitable as a model cargo [175]. The fluorescent nuclear signal at the same time indicates the bioavailability of the chemotherapeutic agent [176]. DXR, also called ‘adriamycin’ belongs to the antharacyclines which intercalate with DNA (Figure 29 A) and cause a deformation of the base-pairs (Figure 29 B). Thereby DNA-synthesis because of inhibition of topoisomerase II and oxidative stress is blocked. Further, torsion induced destabilization of the nucleosome, causes cell death [177, 178]. Doxorubicin has fluorescent properties with an emission peak at 590 nm [179]. By intercalation with DNA, it shifts slightly to the left of the wavelength spectrum (shorter wavelengths) and the intensity becomes slightly more intense [180] (Figure 29 C). When cells are treated with DXR, most of the molecule associate with DNA [180], what causes a fluorescent signal of DXR in the nucleus, as depicted in fluorescent images of literature [181,

182]. Herein we show an approach, combining both flow cytometry and fluorescence microscopy, to evaluate uptake and release of the three *de novo* lipid formulations (L2c, L11c and L15c) (Table 8). Further, we investigated the influence of surface-modification with hyperbranched Polyglycol (hbPG) and linear Polyethyleneglycole (linPEG) on uptake and release.

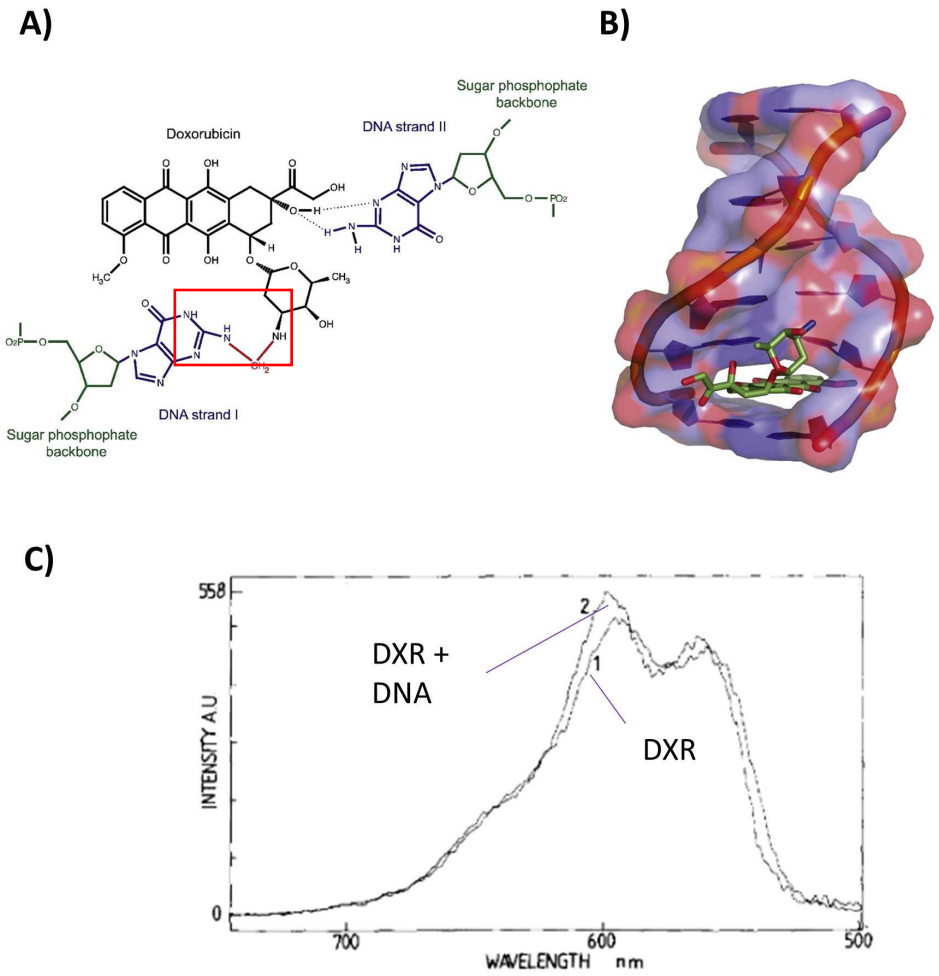

Figure 29: DXR intercalating with DNA base pairs.

A: DXR covalently binds guanine (red square) [18] **B:** Structure of DXR-DNA complex.[19] **C:** Fluorescence emission spectrum of DXR and DXR-DNA. Excitation: 457.9 nm. Free DXR (1.), DXR-DNA (2.). Normalized on integrated surfaces. [20]

[18] Reproduced with permission of the publisher from 183. Yang, F., et al., *Doxorubicin, DNA torsion, and chromatin dynamics.* Biochimica et Biophysica Acta (BBA) - Reviews on Cancer, 2014. **1845**(1): p. 84-89. (Creative Commons Attribution-NonCommercial_ShareAlike License)

[19] Reproduced with the permission of the publisher from 183. Ibid. (Creative Commons Attribution-NonCommercial_ShareAlike License)

[20] Adapted with permission of the publisher from 180. Gigli, M., et al., *Quantitative study of doxorubicin in living cell nuclei by microspectrofluorometry.* Biochimica et Biophysica Acta (BBA) - Gene Structure and Expression, 1988. **950**(1): p. 13-20. Copyright (1988) Elsevier

6.3 Results

Combining flow cytometry and fluorescent microscopy with the new means of data analysis, we started an approach evaluating the intracellular release and bioavailability of DXR with the Amnis® ImageStream®XMark II. Melanocytes (UKRV-Mel-15a) and primary differentiated (dif) human macrophages were treated with 1 µmol/L DXR in form of liposomes with altered lipid constitutions for 30 min ($t_{0.5}$) and 4h (t_4). Instead of measuring the overall intensity for different filter/ laser configurations, during the flow, partial images are generated for the specific laser/ filter configuration and computed into an overall image. While flow cytometry provides information about the size, granularity and the fluorescence intensity, the individual images from the Amnis® ImageStream®XMark II provide additional information; such as the shape and distribution density of the fluorescence intensity on the image.

6.3.1 Features and parameters for analyzing the intracellular release of DXR

The information on distribution of (fluorescence) intensity can be used for automated and standardized definition of adapted ROIs, which we call ‘masks’. For definition of the mask of the nucleus, the fluorescence intensity distribution of Höchst was enclosed with the adaptive erode. The mask of the nucleus was named ‘nM’. The region of the cytomplasms, ‘pM‘, was generated by subtracting ‘nM’ from the mask of the whole cell ‘wcM’ which is the adaptive erode of the brightfield (Figure 30 B, C). The masks were used for establishment of features (Figure 30 C). Features quantitatively measure the parameter of interest, within the specific mask. The feature for DXR-intensity in the nucleus, ‘nDXR’ and the cytoplasm ‘pDXR’ was generated with the masks ‘nM’ and ‘pM’ (Table 9). By means of the features, parameters were calculated which can be weighted differently to make a statement. Both uptake of liposomes as well as intracellular release determine the values of the features ‘nDXR’ and ‘pDXR’. The parameter MFI (nDXR) however is not only determined by intracellular release but also influenced by the total cellular uptake of DXR loaded liposomes. In order gain values, which are less influenced by the total cellular uptake, other parameters were calculated. Furthermore, the varying fluorescence behavior of DXR in the different compartments of the cell should be taken into consideration [180]. Calculating the ‘ratio of release’ by the ratio of the delta ΔMFI(nDXR – pDXR) and the MFI(pDXR) the influence of the uptake and the compartment specific fluorescence behavior was diminished (Table 9). Therefore, this parameter, as well the ‘relative release speed’ is more suitable to characterize the intracellular release properties of the liposomes. It happened that the values for MFI(nDXR) and MFI(pDXR) turned out negative. These negative values, can occur depending on adjustments of the device and compensations, but distort the results when the values are used as a factor/divisor within the calculations of parameters. Therefore, a number of 10,000 was added to the divisor of the ratio for each condition (Table 9). This mathematical operation has to be taken into account for

comparison and classification of the parameter of ‘release ratio’ and ‘relative release speed’. This operation scales down the relative differences but enables us to recognize the formulation with the strongest release capacity.

The value of the ‘total uptake’ gives an idea of the uptake of DXR loaded liposomes into the cell and is calculated by the sum of MFI(nDXR) and MFI(pDXR). For measuring bioavailability of DXR, the parameter MFI(nDox) would be the most suitable.

A)

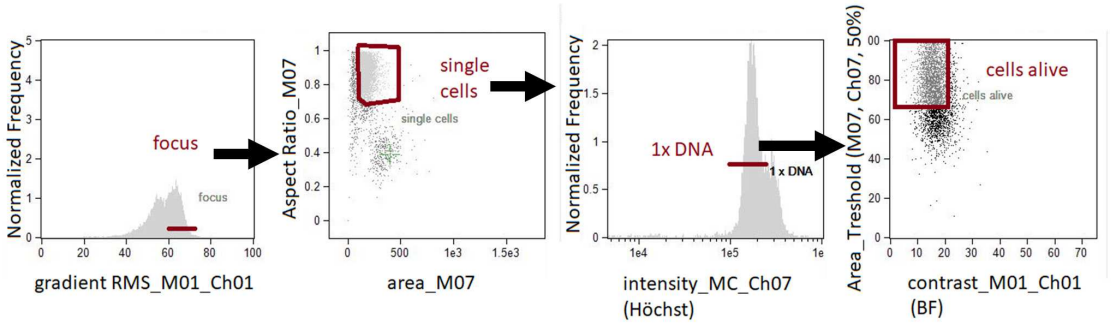

B)

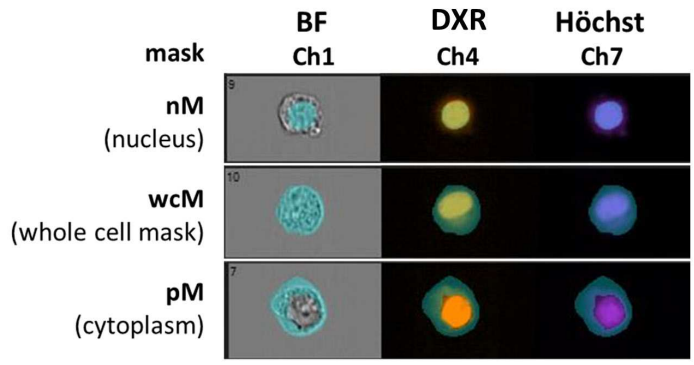

C)

Mask	Description	Function	Treshhold	Feature	Description	Function
nM	nucleus	adaptive erode (Höchst, Ch7)	98%	**nDXR**	nuclear DXR	intensity_nM_Ch 4
wcM	whole cell	adaptive erode (BF, Ch1)	98%	(pDXR)		
pM	cytoplasm	**wcM - nM**	(combined)	**pDXR**	cytoplasmatic DXR	intensity_pM_Ch 4

Figure 30: Amnis® ImageStream®XMark II features for nuclear and cytoplasmatic DXR.

A: Gating strategy on UKRV-Mel-15a. Predefined wizards were applied for defining cells of focus, single cells, mononuclear cells and alive cells. **B:** Images of UKRV-cells treated with DXR loaded liposomes (L2c) for 4h. Representation of channels (Ch1 = BF, Ch4 = DXR, Ch7 = Höchst, Ch11 = DiD) and masks (C) **C:** Definition of masks and features. The table describes the masks and features with their programmed functions.

Table 9: Description of Amnis® ImageStream®XMark II evaluation parameters for uptake and intracellular release of DXR.

Parameter	Math operation	Uptake	Release	Comment
nuclear DXR ~ released DXR	MFI(nDXR)	**↗	***↗	
cytoplasmatic DXR ~ liposomal contained DXR	MFI(pDXR)	***↗	**↘	
total uptake ~ total DXR	MFI(pDXR) + MFI(nDXR)	***↗	***↗	in complex with DNA DXR (nDXR) changes fluorescence behavior [180]
ratio of release	ΔMFI(nDXR-pDXR) / (MFI(pDXR)+10 000)	*←→	***↗	operation (‚divisor + 10.000') causes distortion)
relative release speed	Δt4[ΔMFI(nDXR-pDXR) / (MFI(pDXR)+10.000)] – t0.5[ΔMFI(nDXR-pDXR) / (MFI(pDXR)+10.000)]	*←→	***↗	influenced by initial value ($t_{0.5}$)

The table shows the calculation of parameters using the features, nDXR and pDXR, described in Figure 30. The yellow columns are an estimation on the impact of the factors uptake and release to classify the data (* = low, *** = high, ↗ = increases value, ↘ = decreases value).

6.3.2 The intracellular release of the formulation L11c, L2c and L15c

In a first approach, the formulations of L2c, L11c and L15c were compared to the one of L0 for the intracellular release of cargo (as described 6.3.1). The destabilized formulations, L2c, L11c and L15c, show a stronger accumulation in the nucleus at already 0.5h in UKRV-Mel-15a cells (Figure 31 A, Supplement 36 A, B). The overall uptake of DXR for L15c seems less than for L11c and L2c in this experiment (Supplement 36 C). The high 'release ratio' (Supplement 36 D) and 'release speed' (Figure 31 B) of the destabilized liposomes (L2c, L11c and L15c) compared to L0 goes along with the preliminary *in vitro* experiments by Matthias Voigt et al. [174].

The liposomal formulations were tested additionally on human primary different (dif.) macrophages (Supplement 37). The overall uptake was higher for dif. macrophages compared to UKRV-Mel-15a cells (Supplement 38 A and Supplement 39 C). Also for dif. macrophages the formulation of L15c was the one with the strongest release (Supplement 38 B and Supplement 39 D). In the experiment 6.3.3, the significantly higher 'release ratio' and 'release speed' of DXR for L15c was confirmed (Supplement 40 D and Figure 32 B).

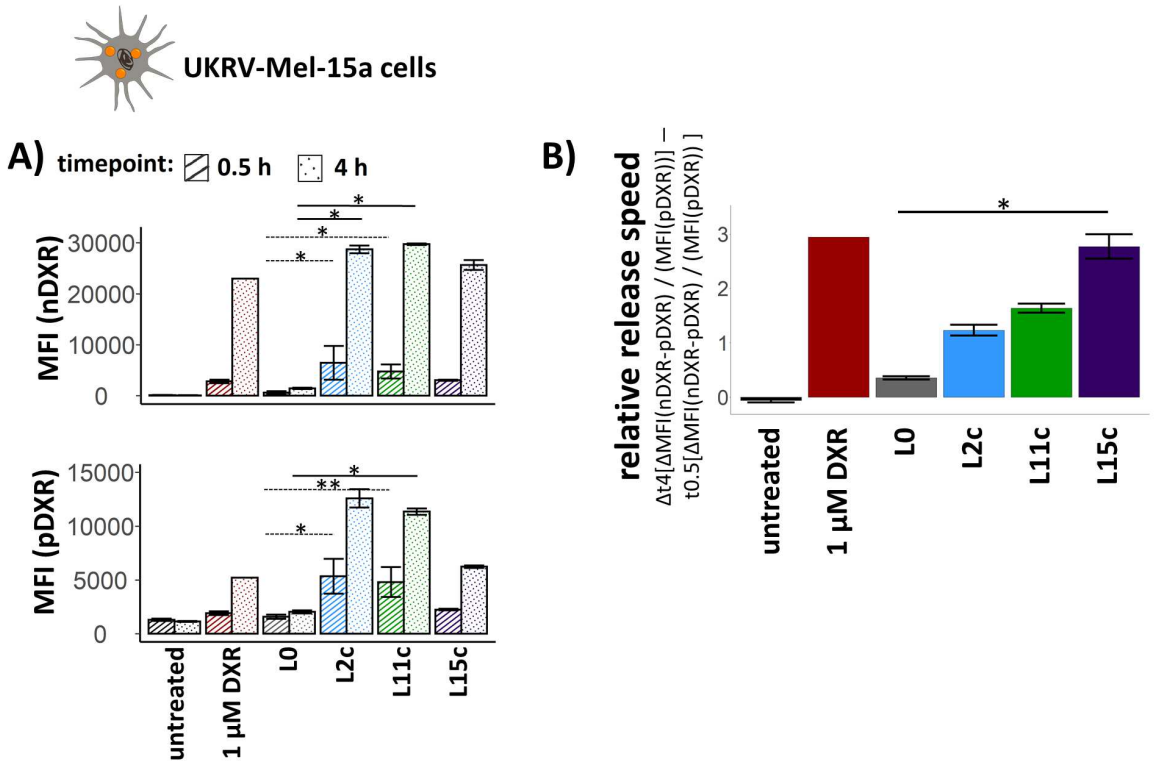

Figure 31: Intracellular release of DXR from L0, L2c, L11c and L15c into UKRV-Mel-15a cells and primary dif. macrophages.

A: DXR accumulation in nucleus and cytoplasm of UKRV-Mel-15a cells. *Top:* The MFI of DXR in nuclei (MFI(nDXR)) (mean +/- SEM). *Bottom:* The MFI of DXR in cytoplasm (MFI(pDXR)) (mean +/- SEM). n = 3, except for '1 µM DXR' t_4 n = 1, 'L0' t_4 n=2, for 'L11c' t_4, n =2. Values were compared with each other by a Dunn Test following a Kruskal-Wallis test. $p < 0.05$ = * **B:** The 'relative release speed' (mean +/- SEM) of DXR in UKRV-Mel-15a cells. The parameter was calculated according to Table 9. Values were compared with each other by a Dunn Test following a Kruskal-Wallis test. $p < 0.05$ = *, $p < 0.005$ = **. n = 3, except for '1 µM DXR' t_4 n = 1, 'L0' t_4 n = 2, for 'L11c' t_4, n = 2.

6.3.3 The effect of hbPG and linPEG on intracellular release of L0 and L15c

Having shown the high intracellular release capacity for the *de novo* formulation L15c on cellular systems (UKRV-Mel-15a and dif. macrophages), we then investigated the effect of PGylation and PEGylation on the L15c and the L0 formulation.

The data shown confirm the high intracellular release for the L15c formulation compared to the L0 formulation (Figure 32 B and Supplement 40 D). The destabilized L15 formulations (L15c, L15c + hbPG, L15C + linPEG) showed a strong nuclear signal at 4 h, whereas the L0 formulations at 4 h still hold a high cytoplasmatic signal and the nucleus appears shadowed (Figure 32 A Supplement 40 A, B). The stealth effect caused by the hbPG and linPEG modification became apparent by the reduced 'total uptake' compared to the control for the L15 formulations, whereas not for L0 (Supplement 40 C). The values describing the release properties do not differ for the hbPG and linPEG modified liposomes towards the controls.

Taken together the presented data have shown that hbPG and linPEG do not affect the intracellular stability of liposomes in UKRV-Mel-15a cells.

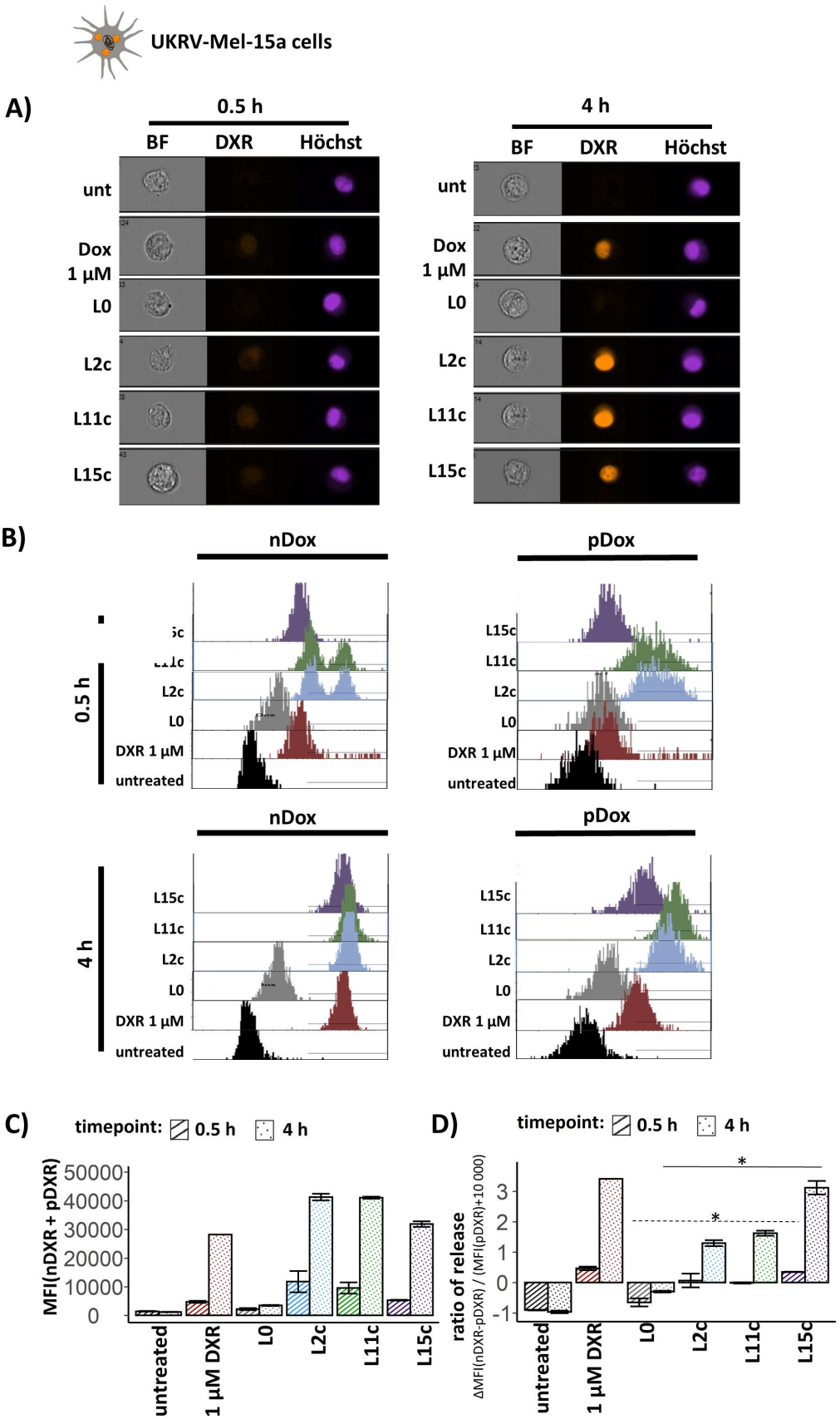

Figure 32: The effect of liposomal modification with hbPG and linPEG on intracellular release of DXR.

A: DXR accumulation in nucleus and cytoplasm of UKRV-Mel-15a cells. *Top:* The MFI of DXR (mean +/- SEM) in nuclei (MFI(nDXR)). *Bottom:* The MFI of DXR (mean +/- SEM) in cytoplasm (MFI(pDXR)). Values of the groups 'L0' and 'L15c' were compared with each other for each time point other by a Dunn test (package R, method = "none") following a Kruskal-Wallis test. $p < 0.05$ = *. n = 3. **B:** The 'relative release speed' (mean +/- SEM) of DXR in UKRV-Mel-15a. The parameter was calculated according to Table 9. Values of the groups 'L0' and 'L15c' were compared with each other by a Dunn Tests (package R, method = "none") following a Kruskal-Wallis test. $p < 0.05$ = *, $p < 0.005$ = **. n = 3.

6.4 Discussion

The Amnis® ImageStream®XMark II approach enabled to assess the amount of nuclear and cytoplasmatic DXR within the cellular compartments. This information was used for further computations (Table 9) in order to characterize the intracellular release of DXR from liposomes. We could show a stronger release for the formulation L2c, L11c, L15c in dif. macrophages and UKRV-Mel-15a towards L0, with the parameters 'release ratio' and 'release speed'. Within these experiments, L15c emerged as the liposomal formulation with the lowest intracellular stability. Furthermore, neither surface modulation with hbPG nor linPEG, effects the intracellular stability in UKRV-Mel-15a.

Matthias Voigt [174] observed a comparable retention rate of 90% for all formulations (L0, L2c, L11c and L15c) at pH 7.4. The pH dependent release at pH 5.4 was ~10% for L0, ~40% for L2c, ~50% for L11c and ~60% for L15c. Also, the Amnis® ImageStream®XMark II data shown here confirms L15c as the formulation with the highest pH-dependent release capacity (Figure 31 B, D).

In order to evaluate uptake and release, [redacted] [174] carried out flow cytometry and confocal microscopy, on cells treated exactly the same way as described in 8.2.2. The flow cytometry data, comparing free DXR, L2c, L11c, L15c showed the lowest fluorescence for L0. [redacted] assumed that the DXR fluorescence was quenched by the high local concentration of DXR inside of the intact liposomes. Basing on this hypothesis of quenching behavior, a released DXR-molecule emits a higher fluorescence intensity than a liposomally sequestered. Assuming similar uptake of liposomes and equal loading of DXR amount – a higher fluorescence intensity means a higher release. Using this interpretation, however the factor of cellular uptake was neglected. The concentration of liposomes used for cell-treatment was normalized on on the level of DXR. Therefore, fluorescence spectroscopy was applied to estimate the amount of the drug and indirectly the amount of liposomes. The multi-step procedure of production and DXR-loading (see 8.1.2.1) can cause systemic deviations of the amount of drugload. Altered degree of drugload reduces comparability of the total fluorescence intensity when using this size for drawing a conclusion on the intracellular release. Another systemic error can occur when normalizing the liposome concentration on the level of DXR. One single batch of liposomes was used for each triplicate group. The normalization of liposomes on fluorescence intensity of DXR might bear mistakes caused by the quenching effect. Nevertheless, the flow cytometric data of [redacted] also show a higher intensity

with the formulation L15c. Statistical tests were not available. Nevertheless, we believe that by offsetting the intensity in the different compartments, using the described approach, the influence of errors and deviations could be reduced. By confocal microscopy, [redacted] [174] also determined the DXR intensity in region of the nucleus. The nuclear intensity values were highest for the formulation L15c, followed by L2c, L22c and L0. In both assays (flow cytometry and confocal microscopy), the relative intensity values were higher for the dif. macrophages. Statistical tests were not available. In the context of the preliminary flow cytometric and microscopic analysis, the toxicity of DXR-loaded liposomes using a resazurin assay was examined [174]. Viability of UKRV-Mel-15a cells and dif. macrophages for the formulation L2c, L11c and L15c was below 40%. For the L0 liposomes, viability accounted for the same value as of non-DXR-loaded L0 liposomes. The prevention of mitosis by DXR might have falsified the results in this assay. Therefore, the Amnis® ImageStream®XMark II approach offered a chance to minimize the influence of ‘toxicity and mitosis’. The gating strategy based on the images of cells and nucleus were used to exclude also mitotic and apoptotic cells (Figure 30 A, Supplement 37 A).

Not only the high number of cells, but also the automated selection of cells and standardized definition of cellular compartments contribute to the high statistical value of the Amnis® ImageStream®XMark II approach. However, these images do not represent such precise information about the localization of a molecule in the cell as confocal microscopy does. The image is not a direct single acquisition of the cell but a computer integration (time delay integration) of more acquisitions [184]. These further background calculations could in turn introduce errors and inaccuracies into the image. For the investigations in this study, which focus on the cell nucleus, a region that can be relatively large and clearly defined by Höchst staining, the factor of the dime delay integration should play less of a role. With smaller and thinner regions however, as for example the investigation of the cell membrane the method might bear more difficulties. Nevertheless, this error can be compensated by the high number of images evaluated.

DXR is both a fluorescent and chemotherapeutic agent. The nuclear localization of DXR, which is used as a reporter for ‘release’ in this assay, also can be a marker of bioavailability. Ultimately, the bioavailability and not necessarily the intracellular release of the molecule determines the effectiveness of a drug. However, the bioavailability of drugs could be further influenced by nuclear transport and cellular trafficking, steps which follow the lysosomal ‘release’.

Taken together we have demonstrated a novel approach to measure the intracellular release of the drug DXR from liposomes. However, this new approach can only be applied to compounds with localisation into the nucleus. For another relevant cargo that does not

accumulate in the nucleus, such as mRNA, a new concept would be needed for evaluation of the intracellular release capacity.

7 Summary, Conclusion and Outlook

The highlights of this thesis are summarized in order to draw an overall conclusion.

7.1 Summary

In this work, we have shown in which way a co-administered heparinization, can influence the pharmacokinetics of nanocarriers and how the constitution of nanocarrier systems can influence the bioavailability of the loaded drug.

For answering the question how heparin can alter pharmacokinetics, we focused on the effect on the unspecific uptake by the reticulo endothelial system. A screening *in vitro* setup and an *in vivo* setup were established to simulate the clinical situation of a heparinization while treatment with nanocarriers. *In vitro*, four liposomal formulations without drug loading and two protein capsules were analyzed on cellular uptake in presence of heparin on specific splenocytes. Flow cytometry panels defining subtypes of phagocytotic populations of the spleen, were designed in order to assess the uptake of the fluorescently labelled nanocarrier systems. *In vivo*, the formulation of Doxil® and the non-PEGylated ovalbumine nanocapsules were investigated in mice. Previously to nanocarrier injection, the animals received an intravenous heparin bolus, that lies 15 minutes in the past, theoretically achieving a high dose of 4 U/ml blood. The biodistribution of fluorescently labelled nanocarriers was evaluated using the *In Vivo* imaging spectrum (IVIS) for the time points of 30 minutes, 120 minutes and 360 minutes. The main focus of the read-out were the RES organs, liver and spleen, which were additionally analyzed by flow cytometry. Again, elaborated flow cytometry panels were applied to investigate specific phagocytotic subpopulations, which potentially contribute to the nonspecific uptake of the particles.

On the level of biodistribution, we found a significantly increased accumulation with co-administration of high-dosed heparin in the liver and spleen of liposomes. The time-limited increase correlates with the estimated heparin concentration in the blood. However, we suspect that in the case of liposomal therapies a concomitant heparinization does not have a significant effect on the outcome of the therapy itself, as the effect of heparinization was not pronounced *in vivo*. *In vitro*, we have shown that a high dose of heparin differentially modulates uptake of the tested formulations into phagocytosing splenocytes. A reduction of the uptake into macrophages was observed, which was significant for red pulp macrophages for low-negatively charged formulations like the Doxil® one – whereas an increase of uptake was recognized for the formulation of Ambisome®.

For the protein capsule consisting of ovalbumin, it became clear that heparinization reduces the uptake into macrophages but not into dendritic cells. This may be a favorable effect for the

innovative nanovaccine, which carries the antigen in its shell with respect to a DC-mediated adaptive immune response. *In vivo*, we could not detect this 'passive DC-targeting effect' during a high dosed heparinization. In addition, the distribution of this capsule system into different phagocytosing cells was deciphered for the first time. However, uptake into cells potentially relevant for mediating the immune response was low.

For the divergent effects of heparin on cellular uptake *in vitro* and *in vivo*, several factors may play a role; *In vivo*, microanatomical structures affect the accessibility of nanocarriers to cells. The physiological clearance of heparin and the existence of multiple compartments and fluidics contributes to the complexiit.

A second focus of this work was to study new drug delivery systems and the bioavailability of their loaded substance.

We have shown how bioavailability of the loaded drug can be improved by combination of the favorable factors ‘targeted delivery’ with ‘controlled release’, using a novel concept of nanocarrier systems: The polyprodrug loaded mesoporpous silica nanocapsule. The packaging in a nanocapsule enabled targeted uptake into macrophages of the liver, the cells which were to be addressed by the anti-inflammatory drug (DXM). The pH-responsive polyprodrug (PDXM), only decays inside the target cell – leading to a higher effectiveness by lower drug concentration. In this thesis, the preferred accumulation of the silica nanocapsule into the macrophages of the liver was confirmed by flow cytometry. In addition, the anti-inflammatory effect of DXM when delivered as PDXM in the mesoporous silica nanocapsule was more effective than of DXM alone. A preferential uptake into liver inflammation triggering macrophages and the controlled release of DXM inside the target cell likely cause this beneficial effects. This new drug delivery system can serve as concept and be adapted in further designs and applications with higher biocompatibility.

De novo liposomal formulations, with acid pH-sensitive destabilization, thus increasing the intracellular release of the substance, were investigated. By combining flow cytometry and microscopy, a new approach was established in order to measure the intracellular release of the drug DXR with the Amnis® Imagestream®XMark II. The fluorescent properties of DXR and the strong nuclear drive were used to draw conclusions about the ratio of free DXR towards encapsulated DXR inside the cell. In this assay UKRV-Mel 15 a cells and human differentiated macrophages were treated with DXR-loaded liposomes for 30 minutes and 4 hours. The numerous images were evaluated on the intensity of DXR with an algorithm determining the area of the nucleus and the cytoplasm using the brightfield and the channel of the nuclear dye. We confirmed the high intracellular release of DXR from *de novo* liposomal formulations, as were pointed out by other analytical tests before (flow cytometry, confocal microscopy).

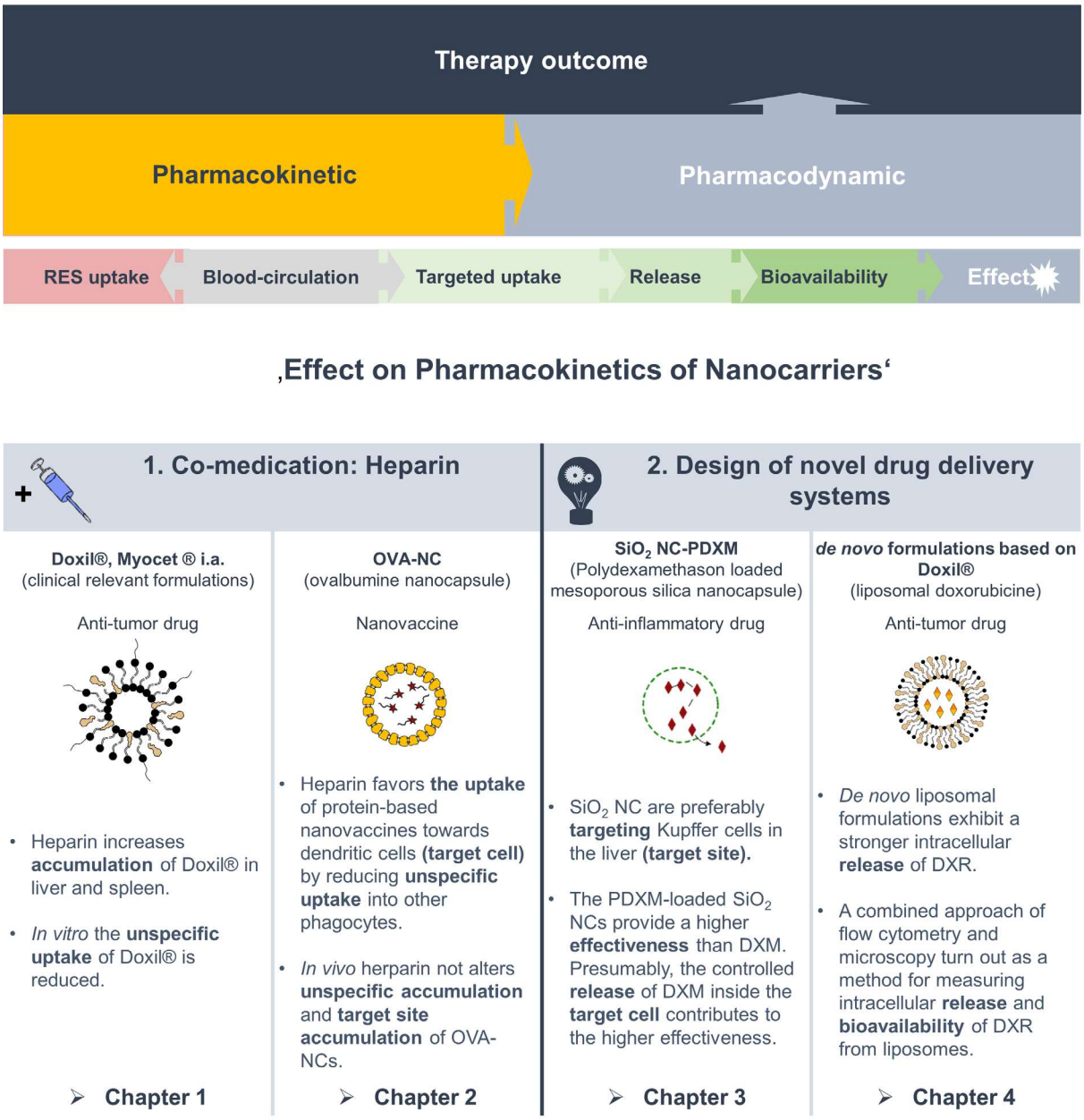

Figure 33: Key findings of the work ‘Modulation of Pharmacokinetics of Nanodimensional Drug Carriers’.

7.2 Conclusion and Outlook

The packaging of active ingredients in nanocarriers decisively determines the pharmacological behavior of the active substances. Not only the metabolism of the active drug molecule, but mainly the nanocapsule in the end, influences the pharmacokinetics. Both the unspecific uptake, up to the targeted uptake and intracellular release, are variables which define pharmacokinetics of nanocarriers and therefore potentially the therapeutic effect. Although we did not ultimately investigate the therapeutic effect for the study on liposomes and ovalbumin capsules, we realized nevertheless that the non-specific uptake by the RES is very significant for nanotherapies. Thus, this represents an important parameter for the development of

therapies. As can be seen from the still industry-leading method of PEGylation (see 1.1.1), there is a high need to create nanocarriers in a way that reduces nonspecific uptake by the innate immune system. Not only ways and means that complement PEGylation, but also methods that can replace PEGylation are necessary for the further development of nanodimensional therapies. Especially approaches with endogenous substances can be prmising compounds; Heparin, which is physiologically produced by the body is less likely to cause humoral immune reactions, as it can be the case with PEG. Thus, the co-application of other substances, could also be used in conjunction to surface modifications to improve the pharmacology of nanodimensional therapeutics.

As the extend of the heparin-effect was dependent on the nature of the nanodimensional system (see chapter 1 and chapter 2) we can conclude that the composition and design of nanocarriers determine pharmacovigilance and nanocarrier-drug interactions. In addition, it should be noted that only negatively charged liposomal formulations were investigated in this study. Thus, heparin could behave completely differently together with positively charged liposomes. In the future, we expect an increase in the frequency of use and variety of nanotherapeutics in the clinic. Drug interactions and pharmacovigiliance can only be transferred from one system to the other to a limited extent. Broad observation and research are necessary for the safe and effective use of nanotherapies.

The novel complexity of nanodimensional drugs on the one hand complicates the prediction of pharmacological effects on the other hand offers many approaches to control them. To gain more control over (novel) nanotherapies in the future, a lot of research and data generation is needed. Especially research in living organisms is indispensable for this knowledge. The current state of *in vitro* setups cannot simulate these complex interconnections, which are given *in vivo*. We conclude that it is crucial to investigate nanocarrier systems in mice as early as possible. Especially the important factor ‘non-specific uptake’ by the innate immune system and other clearance mechanisms can only be determined in this way. Through *in vivo* experiments, it can be determined, how the system must be modulated in order to develop the pharmacological efficacy and not be impeded by factors which were not predictable in *in vitro* experiments.

In Chapter 3, we presented a concept that combines two principles, ‘targeted delivery’ and ‘controlled release’, and thereby promises potential for further drug development. There may be much more suitable applications for this than inflammatory liver disease, for which this concept was generated. However, finding suitable applications requires interdisciplinary teams that systematically search for suitable indications and approach them from a clinical and biological perspective. It can be a meaningful proceeding, to first engineer concepts from the chemical side - and then to develop these further driven by a biological point of view. This

requires good understanding and intensive collaboration from both disciplines. In this way, it is possible to manage the complexity of novel nanodimensional therapeutics and efficiently exploit the advantages of these for the development of new therapeutics.

8 Material and Methods

In this section, are described the methods used in this work. The background of each method will not be discussed further to avoid expansion of volume. The establishment of many assays required a deep understanding of the method. Procedures that were performed by others are marked.

8.1 Nanocarriers

8.1.1 Table of compounds for nanocarrier production

In Table 10 compounds needed for production of nanocarriers are listed.

Table 10: Compounds for production of nanocarriers

Abb.	Name	Company
	Liposomes[21]	
α-Toc	alpha-Tocopherol	Sigma Aldrich, St Louis, Germany
Amph	Amphotericin B	Sigma Aldrich, St Louis, Germany
CHEMS	Cholesteryl-hemisuccinate	Merck, Darmstadt, Germany
CHOL	Cholesterol	VWR, Radnor, USA
	Chloroform	Carl Roth, Karlsruhe, Germany
EPC	Egg phosphatidyl choline 3	Lipoid, Ludwigshafen, Germany
DSPG	1,2-Distearoyl-sn-glycero-3-phospho-rac-(1-glycerol)	Sigma Aldrich, St. Louis, USA
DSPE-PEG(2000)	1,2-Distearoyl-sn-glycero-3-phosphoethanolamine-N-[amino(polyethylene glycol)-2000]	Sigma Aldrich, St. Louis, USA
DiD	1,1'-Dioctadecyl-3,3,3',3'-tetramethylindodicarbocyanine, 4-chlorobenzenesulfonate salt	Thermo Fisher, Waltham, USA
DiR	1,1'-Dioctadecyl-3,3,3',3'-tetramethylindotricarbocyanine iodide	Thermo Fisher, Waltham, USA
DMPC	1,2-dimyristoyl-sn-glycero-3-phosphocholine	Merck, Darmstadt, Germany
DODAP	1,2-dioleoyl-3-dimethylammonium-propane	Merck, Darmstadt, Germany
DOPC	1,2-dioleoyl-sn-glycero-3-phospho-ethanolamine	Merck, Darmstadt, Germany
DOPG	1,2-dioleoyl-sn-glycero-3-phospho-rac-(1-glycerol) sodium salt	Merck, Darmstadt, Germany
DOTAP	N-[1-(2,3-dioleoyloxy)propyl]-N,N,N-trimethylammonium chloride	Merck, Darmstadt, Germany
DPPC	1,2-dipalmitoyl-sn-glycero-3-phsopho-rac-(1-glycerol) sodium salt	Merck, Darmstadt, Germany

[21] Liposomes were produced and characterized by [redacted] and [redacted] group of [redacted], Department of Biochemisty and Pharmacy, Johannes Gutenberg-University Mainz.

DXR	Doxorubicine hydrochloride	Merck, Darmstadt, Germany
HSPC	hydro soy phosphatidylcholine	Sigma Aldrich, St. Louis, USA
-	MilliQ-water	Merk, Darmstadt, Germany
PBS	Dulbecco's phosphate buffered saline	Thermo Fisher, Waltham, USA
	PS-particles[22]	
-	Acrylic acid	Sigma Aldrich, St. Louis, USA
AEMH	2-aminoethyl methacrylate hydrochloride	Santa Cruz Biotechnology, Santa Cruz, USA
BP	Bodipy (630 nm/650 nm)	Produced by Sabrinna Brand, Max Planck Institute for Polymer Research
CTMA-Cl	Cetyltrimethylammonium hydrochlorid	Sigma Aldrich, St. Louis, USA
HD	Hexadecane	Acros, Geel, Belgium
SDS	Sodium dodecyl sulfate	Sigma Aldrich, St. Louis, USA
-	Styrene	Provided by Jürgen Thiel, Max Planck Institute for Polymer Research
-	V59	Wako, Urmitz, Germany
	Proteinbased NC[23]	
Cy5-oligo	Cyanine 5-5'-CCA CTC CTT TCC AGA AAA CT (0.1 nmol μL^{-1} in PBS buffer)	IBA Lifesciences, Göttingen, Germany
-	Cyclohexane	Carl Roth, Karlsruhe, Germany
HSA	Human serum albumine	Sigma Aldrich, St Louis, USA
-	HPLC grade water	VWR, Radnor, USA
NaCl	Sodium chloride (≥99.0%)	Sigma Aldrich, St Louis, USA
OVA	Ovalbumine (lyophilized powder, ≥98%)	Sigma Aldrich, St Louis, USA
P((E/B)-*b*-EO)	Poly((ethylene-*co*-butylene)-*block*-(ethylene oxide)	The surfactant P((E/B)-*b*-EO), consisting of a poly(ethylene-*co*-butylene) block (NMR: M_n = 3,900 g mol^{-1}) and a poly(ethylene oxide) block (NMR: M_n = 2,700 g mol^{-1}) was synthesized according to a reported procedure [185].
PEG-5k$_{0.2}$	Isocyanate-mPEG molecular weight = 5 kDa	Nanocs, New York, USA
SDS	Sodium dodecyl sulfate (99%)	Thermo Fisher, Waltham, USA
TDI	2,4-Toluene diisocyanate (99%)	Sigma Aldrich, St Louis, USA
	SiO_2 NC-PDXM[24]	
	The compounds are listed in [155]	

[22] PS-particles were produced by [redacted], group of [redacted], Max Planck Institute for Polymer Research.
[23] Nanocapsules for the *in vitro* experiments were produced [redacted] and [redacted], group of [redacted], Max Planck Institute for Polymerresearch.
[24] PDXM SiO2-NCs were produced by [redacted] and [redacted], group of [redacted], Max Planck Institute for Polymerresearch.

8.1.2 Liposomes

8.1.2.1 Production of liposomes[25]

Dissolved lipids (Table 10) were transferred into tubes (Kisker Biotech, Steinfurt, Germany) according to the desired molar ratio of the formulation (Table 11). The solvent chloroform, was removed by centrifugation in the SpeedVac® vacuum centrifuge (Eppendorf, Hamburg, USA) at 30° C for 48 hours. For complete removal of solvents, lipids were freeze-dried at -80°C (Martin Christ Gefriertrocknungsanlagen, Osterode, Germany) overnight and stored in a freezer until use at -20°C. Dried lipids were incubated together with 325 mg SiLibeads® (Typ ZY-S 0.3 – 0.4 mm (Sigmund Lindner, Warmensteinach, Germany) and 9.3 µl PBS for 10 min at room temperature. For DXR-loading (chapter 4) instead of PBS, 50 mM DXR in PBS was used. Samples were run for 20 min by dual centrifugation (Andreas Hettich, Tüttlingen, Germany) to form a phospholipid gel. Centrifugation temperature for PBS-loaded formulations (chapter 1) was 4°C, for DXR-loaded liposomes (chapter 4) 25°C. To finally form liposomes, the gel was homogenized with 77.2 µl PBS and centrifuged again twice for 2 min as described before.

Table 11: Compositions of liposomal formulations

	Description	Compound	Molar ratio (mol-%)	Chapter
Lip-Amb	Approximated formular of Ambisome® [18]	HSPC : CHOL : DSPG : Amph : α-Toc	9.5 : 47.8 : 23.7 : 18.6 : 0.3	1
Lip-Dox	Approximated formular of Doxil® [134]	HSPC : CHOL : MPEG-DSPE-(2000) : DiD	55.9 : 39 : 5 : 0.1	1 *(in vitro)*
		HSPC : CHOL : MPEG-DSPE-(2000) :	55.8 : 39 : 5 : 0.1 : 0.1	1 *(in vivo)*
Lip-Myo/ L0	Approaximated formular of Myocet® [133]	EPC : CHOL : DiD	55 : 44.9 : 0.1	1/ 4
Lip-Myo-PEG	Adapted formular of Myocet® with PEG	EPC : CHOL : DSPE-PEG(2000) : DiD	50: 44.9: 5: 0.1	1
L2c	[redacted] [174] discovered liposomal formulations with high release capacity	DMPC : DODAP : CHEMS : DiD	66.5 : 28.4 : 5 : 0.1	4
L11c		DOPC : DODAP : CHEMS : DiD	63 : 26.9 : 10 : 0.1	4
L15c		DOPG : DOTAP : CHEMS : DiD	66.5 : 28.4 : 5 : 0.1	4

8.1.2.2 Optimization of DiD/DiR amount for *in vivo* imaging

For finding the optimal molar amount and ratio of lipophilic dye for the *in vivo* experiments, batches of Lip-Dox were produced varying the amount and ratio of DiD/DiR. The intensity was measured with the *IVIS* (Perkin Elmer, Waltham, USA) (excitation/ emission of 745/ 800). The optimal molar ratio of DiD/DiR turned out 0.1:0.1 mol-% within the formulation of Lip-Dox

[25] Liposomes were produced and characterized by [redacted]gt and [redacted], group of [redacted], Department of Biochemisty and Pharmacy, Johannes Gutenberg-University Mainz.

(Supplement 12). For *in vivo* imaging experiments, fluorophores emitting long wavelength are more favorable because of higher tissue-penetrating properties [186].

8.1.3 Polystyrene particles[26]

8.1.3.1 Production of PS-NH_2 (BP)

Amino-functionalized polystyrene particles (PS-NH_2) were produced by first preparing a macroemulsion. This was generated by slowly adding the continuous phase to the disperse phase. The disperse phase consisted of 5.83 g styrene, 114.7 mg hexadecane, 5.4 mg BP and 103.8 mg initiator V59. The continuous phase contained 509.4 mg CTMA-Cl, 0.18 AEMH and 23.5 g H_2O. The macroemulsion was ultrasonicated with ice cooling for 2 min at 450 W, 90% amplitude (1/2" tip, 6.5 mm diameter). The resulting mini emulsion was polymerized for 24 h at 72°C in oil bath. It was paid attention to sterile production.

8.1.3.2 Production of PS-COOH (BP)

Carboxyl-functionalized polystyrene particles (PS-COOH) were produced by first preparing a macroemulsion. This was generated by slowly adding the continuous phase to the disperse phase. The disperse phase consisted of 17.46 g styrene, 452.1 mg HD, 545.2 acrylic acid, 22.7 mg BP and 300.7 mg V59. The continuous phase contained 300.3 mg SDS, 72 g H_2O.The macroemulsion was treated with the microfluidizer: Y-shape, 15,000 PSI. The resulting mini emulsion was polymerized for 24 h at 72°C in the oil bath. Intensive attention was paid to sterile production.

8.1.4 Protein capsules[27]

8.1.4.1 Production of OVA-NC (Cy5), PEG-OVA-NC (Cy5) and HSA-NC (Cy5) (*in vitro* experiments)[28, 29]

"50 mg OVA (or HSA – for HSA-NC (see 4.3.2)) was dissolved in 0.4 g pharmaceutical grade water. 7.2 mg NaCl and 100 µL Cy5-labeled oligonucleotides were added to the protein solution. Separately, a lipophilic phase was created by dissolving 35.7 mg of surfactant P((E/B)-*b*-EO) in 7.5 g of cyclohexane. The mixture was poured to the stirred aqueous protein solution. The two-phase mixture was homogenized by ultrasonication (1/2" tip, 70% amplitude, 3 min, 20 sec on, 10 sec off) (Branson 450 W, BRANSON Ultrasonics Corporation, Danbury,

[26] PS-particles were produced by [redacted], group of [redacted], Max Planck Institute for Polymer Research.
[27] Portein capsules were provided by the group of [redacted], Max Planck Institute for Polymer Research.
[28] Nanocapsules for the *in vitro* experiments were produced by [redacted], group of [redacted], Max Planck Institute for Polymerresearch.
[29] HSA-NC (Cy5) were produced by [redacted] group of [redacted], Max Planck Institute for Polymer Research.

USA). A solution of 10.7 mg P((E/B)-*b*-EO) and 11 mg TDI in 5 g of cyclohexane was then added drop wise to the stirred mini emulsion (500 rpm) over a period of two minutes. For polymerization the mixture was stirred for 24 h at 25°C in oil bath. After TDI-induced polymerization the solution was redispersed in 2.5 ml anhydrous cyclohexane after centrifugation (1664 g, 30 min) in order to remove excessive surfactant. For conjugation of OVA-NCs with $PEG5k_{0.2,}$ the resulting dispersion was sonicated for 30 s at 10% amplitude in a pulse regime (5 s sonication, 5 s pause) using inverse sonication to reduce aggregation. 2.5 mL anhydrous cyclohexane were added into the dispersion at 500 rpm at 25°C. 40 mg of $PEG5k_{0.2}$ was dissolved in 0.63 g (800 µl) anhydrous acetone and added dropwise into the OVA-NC dispersion and the reaction was allowed to take place for 4 h. The non-PEGylated OVA-NCs were treated with the respective volume of acetone only. After the reaction, the dispersion was transferred into a tube and centrifuged at 750 g for 30 min in order to remove non-coupled PEG. Subsequently, the pellet was redispersed in 600 µl of anhydrous cyclohexane. OVA-NC were then transferred into aqueous medium by adding 600 µl of the cyclohecxane OVA-NC dispersion into 5 ml 0.1 wt% SDS aqueous solution while mechanical stirring. The samples were sonicated for 3 min at 25°C (25 kHz) in the ultrasound bath. The samples were stirred open overnight under the sterile working fume for 24 h at 25°C in order to evaporate cyclohexane. Afterwards the samples were centrifuged (3 x 1664 g, 30 min) with centrifugal filters (Molecular weight cutoff =100k) to remove excessive SDS. Solid content was determined gravimetrically after freeze drying."[30]

8.1.4.2 Production of OVA-NC (Cy5) (*in vivo* experiments)[31]

"For the *in vivo* experiment the protocol was slightly changed in order to increase fluorescence and stability. Instead of 100 µl, 250 µl Cy5-labeled oligonucleotides were added to the protein solution. The SDS concentration was increased on 0.2 wt-% and samples were sonicated for 5 minutes. After evaporation of the cyclohexane the samples were centrifuged (3 times for 30 min, 500 g) with centrifugal filters (molecular weight cutoff = 100k) to remove excessive SDS. Then the sample was dialyzed against 0.01 wt-% SDS overnight (MWCO = 16kDa) to remove excess Cy5 Oligo. Solid content was determined gravimetrically after freeze drying."[32]

[30] Contributed by [redacted], group of [redacted] Max Planck Institute for Polymer Research.
[31] OVA-NC (Cy5) for the *in vivo* experiments were produced by [redacted] and [redacted], group of [redacted], Max Planck Institute for Polymer Research.
[32] Written by other authors 155. Li Mengyi, et al., *Encapsulation of Polyprodrugs enables an Efficient and Controlled Release of Dexamethasone*. 2021: About to submit.

8.1.5 Production of PDXM SiO_2-NCs[33]

The production of PDXM SiO_2-NCs was described by Li and Jiang et al. [155].

8.1.6 Characterization and Quality assurance of nanocarriers

8.1.6.1 Hydrodynamic diameter and surface potential[34]

For physicochemical charachterization of liposomes, 20 µL purified liposome suspension (1 wt-%) was diluted in 1 mL MiliQ-water. Size was measured in a disposable folded capillary cell (Malvern, Worcestershire, United Kingdom) at 25°C by using a Malvern Zetasizer Nano series (Malvern, Worcestershire, United Kingdom). The refractive index was set to 1.59 with a water viscosity of 0.8872 and the scattering angle was configured to 173. (Data see Table 26)

PS-particles were measured by dynamic light scattering with the Malvern Zetasizer Nano Series at a temerpature of 23 °C in MiilliQ-water. 1-2 µl of capsule/particle suspension (0.5 – 1 wt-%) were diluted in 100 µl MiiliQ-water in a glass capillary (0.5 cm diameter) (Malvern, Worcestershire, United Kingdom) and analyzed as described above by dynamic light scattering. (Data see Table 27 and Table 29).

OVA-NC (Cy5), PEG-OVA-NC (Cy5) and SiO2-NC were measured by dynamic light scattering on the Nicomp 380 submicron particle sizer (Nicomp Particle Sizing Systems, USA) in PBS at a fixed scattering angle of 90° at 25°C.

Surface potential (ζ-potential) of Liposomes and coated PS-particles and OVA-NC was measured with folded capillary cell (Malvern, Worcestershire, United Kingdom) at 25°C by using a Malvern Zetasizer Nano series.

For measuring the ζ-potential of particles in experimental conditions, particles and capsules were coated with the same culture medium as in the *in vitro* uptake experiments in 4.3.1 and 4.3.2. PS-particle were coated with IMDM, 5% MS and heparin (see Table 12). After 24 h, culture medium was removed by centrifugation (PS-particles: 10,000 g, 30 minutes, 4°C; OVA-NC: 300 g, 30 minutes, 30 minutes, 4°C). (Data see Table 28 and Table 30)

8.1.6.2 Fluorescence cross-correlation spectroscopy (FCCS)[35]

“FCCS experiments were performed using a commercial setup LSM 880 (Carl Zeiss, Oberkochen, Germany). For excitation of the Cy5-Oligo a He/Ne-laser (633 nm) were used.

[33] PDXM SiO_2-NCs were produced by [redacted] and [redacted] group of [redacted], Max Planck Institute for Polymer Research.

[34] Liposomes were characterized by [redacted] group of [redacted], Department of Pharmacy and Biochemistry of the Johanes Gutenberg-Universtiy Mainz. Protein-capsules were characterized by [redacted] group of [redacted], Max Planck Institute for Polymer Research.

[35] FCCS was performed by [redacted] group of [redacted], Max Planck Institute for Polymer Research.

The excitation light was focused into the sample by a high numerical aperture water immersion objective (C-Apochromat 40x/1.2 W, Carl Zeiss, Oberkochen, Germany). The fluorescence was collected with the same objective and after passing through a confocal pinhole, directed to a spectral detection unit (Quasar, Carl Zeiss, Oberkochen, Germany). In this unit emission is spectrally separated by a grating element on a 32-channel array of GaAsP detectors operating in a single photon counting mode. The emission of Cy5-Oligo was detected in the spectral range 642-696 nm. The observations volume was calibrated using Atto Fluor 643® as reference dye with known diffusion coefficients.

After the respective incubation time in mouse plasma, the OVA capsules were poured into eight-well polystyrene-chambered coverglass (Laboratory-Tek, Nalge Nunc Internation, Penfield, NY, USA) and measured. For each solution, a series of twenty measurements with a total duration of 3 min were performed. The obtained experimental autocorrelation curves were fitted with the theoretical model function for an ensemble of freely diffusing fluorescence species [187]. The fits yielded the diffusion times of the fluorescent species from which the respective diffusion coefficients were evaluated. Finally, the hydrodynamic radii (Rh) were calculated (assuming spherical particles) by using the Stokes-Einstein relation:

$$R_H = \frac{kBT}{6\pi\eta D}$$

In this equation, kB is the Boltzmann constant, T is the temperature, D the diffusion coefficient and η is the viscosity of the solvent."[36]

8.1.6.3 Endotoxins[37]

The FDA-limit of 0.05 EU/ml [188] was set as a benchmark for the nanocarriers for *in vivo* application. The analysis was performed using the Pierce™ LAL Chromogenic Endotoxin Quantitation Kit (Thermo Fisher, Waltham, USA) or the Endosafe Cartridge Technology (Charles River Laboratories, Wilmington, USA) according to the manufactures' instructions. The nanocapsules were diluted on 600 µg/ml for the analysis. To avoid interferences the liposome concentration was downscaled 10 times for measurements and the value multiplied by 10.

8.2 Cell experiments

8.2.1 Heparins, culture media and other compounds

In Table 12 compounds needed for cellular uptake experiments are listed.

[36] Contributed by [redacted] group of [redacted] Max Planck Institute for Polymer Research.
[37] LAL-assays were performed by the SFB 1066 core facility.

Table 12: Compounds for cell culture and *in vitro* experiments,

Generic name	Brand name	Company
Heparins		
Enoxaparin	Clexane®	Sanofi, Paris, France
Fondaparinux	Arixtra®	Aspen, München, Germany
Heparin (UFH)	-	Panpharma, Luitré, France
Tinzaparin	Innohep ®	LEO Pharma GmbH, Ballerup, Denmark
Abb.	**Name**	**Company/ Supplyer**
Cell culture media and supplements		
DMEM	Dulbecco's Modified Eagle's Medium	Thermo Fisher, Walham, USA
EMEM	Eagle's Minimum Essential Medium	Thermo Fisher, Walham, USA
FCS	fetal bovine serum	Thermo Fisher, Walham, USA
Gln	Glutamin	PAN Biotech, Aidenbach, Germany
GlutaMAX		Thermo Fisher, Walham, USA
GM-CSF	Granulocyte-macrophage colony-stimulating factor	Merck, Darmstadt, Germany
HS	Horse serum	Sigma Aldrich, St. Louis, Germany
hPC	Human plasma	see 8.2.1.1
IMDM	Iscove's Modified Dulbecco's Medium	Thermo Fisher, Walham, USA
LPS	Lipopolysaccharides	Thermo Fisher, Walham, USA
M-700 CSF	M-700 colony-stimulating factor	Immuno Tools, Friesoythe, Germany
M-CSF	Macrophage colony-stimulating factor	R&D Systems, Minneapolis, USA
MEM	Minimal essential medium	PAN Biotech, Aidenbach, Germany
MS	Balb/c mouse serum	Innovative Research, Peary Court, USA
Pen-Strep	Penicillin-streptomycin	PAN Biotech, Aidenbach, Germany
	Primocin	Invivogen, San Diego, USA
	RPMI-1640	Sigma Aldrich, St. Louis, USA
ß-Me	ß-Mercaptoethanol	Carl Roth, Karlsruhe, Germany
Saline buffers, solutions and compounds		
Saline buffers		
HBSS	Hank's balanced salt solution	Sigma Aldrich, St. Louis, Germany
PBS	Dulbecco's phosphate buffered saline	Thermo Fisher Scientific, Walham, USA and PAN Biotech, Aidenbach, Germany

Solutions		
Histodenz	5-(N-2,3-Dihydroxypropylacetamid)-2,4,6-triiod-N,N′-bis(2,3-dihydroxypropyl)isophthalamid, N,N′-Bis-(2,3-dihydroxypropyl)-5-[N-(2,3-dihydroxypropyl)-acetamino]-2,4,6-triiod-isophthalamid	Sigma Aldrich, St. Louis, USA
-	**Biocoll**	Sigma Aldrich, St. Louis, USA
Compounds		
EDTA	Ethylenediaminetetraacetic acid	Carl Roth, Karlsruhe, Germany
-	**Glucose**	Carl Roth, Karlsruhe, Germany
KCL	Kaliumchloride	Carl Roth, Karlsruhe, Germany
$KHCO_3$	Kaliumhydrogencarbonat	Sigma Aldrich, St. Louis, Germany
KH_2PO_4	Potassium dihydrogen phosphate	Carl Roth, Karlsruhe, Germany
NaCl	Natriumchloride	Carl Roth, Karlsruhe, Germany
NH_4Cl	Ammonium chloride	Sigma Aldrich, St. Louis, Germany
NaH_2PO	Monosodium phosphate	Carl Roth, Karlsruhe, Germany
PFA	Paraformaldehyde	Carl Roth, Karlsruhe, Germany

8.2.1.1 Human plasma (hPC)

“Buffy coats from donors were centrifuged for 15 min at 400 g and room temperature without a density gradient. The supernatant was subjected to a second and third centrifugation step for 15 minutes at 800 g and 1000 g respectively at room temperature to further reduce the cellular content. Plasma from at least 5 different donors was pooled and incubated at 56°C for 20 minutes to deactivate the complement system. Insoluble denatured protein was removed by centrifugation at 3000 g for 15 minutes at room temperature. Human plasma was stored at -20°C until use.”[38]

8.2.2 Cell lines: HeLa, RAW 264.7[39] and UKRV-Mel-15a[40]

All cells were cultured at 37°C in a 5 % CO_2 atmosphere. To prevent mutation of the cells, passaging was kept under 30.

HeLa (human cervix adenocarcinoma (CCL-2)) cells were purchased from American Type Culture Collection (ATCC, Manassas, USA) and maintained in EMEM. RAW 264.7 (murine macrophage (TIB-71)) were purchased from ATCC and maintained in DMEM. Both media were supplemented with FCS (10 %) and Pen-Strep (100 U/mL). UKRV-Mel-15a human melanoma cell lines (provided by Prof. Dr. Dirk Schadendorf, University hospital Essen) were

[38] Contributed by [redacted], group of [redacted], Dermatology of the University Medical Center Mainz.
[39] Experiments with HeLa and RAW 264.7 were performed by [redacted], group of Prof. Dr. Volker Mailänder, Max Planck Institute for Polymer Research.
[40] Experiments on UKRV-Mel-15a cells were performed by [redacted], group of [redacted], Dermatology of the University Medical Center Mainz.

cultured with RPMI-1640 medium supplemented with 10 % FBS, 1 % GlutaMAX and 0.1 % primocin.

Liposome uptake study HeLa and RAW 267.4

For the uptake study in chapter 1 (see 3.3.1), cells were seeded into 24 well plates to a number of 10^5 cells/ well. Heparin was mixed with 10% hPC and liposomes and then added to cells aiming at a final concentration of heparin of 0 to 4 U/ml according to the scheme in Supplement 1 A. After 3h incubation at 37°C cells were recovered with 1x trypsin, washed with PBS, and analyzed for cellular uptake by flow cytometry using the 633nm laser of the Attune Nxt Flow Cytometer (Thermo Fisher, Waltham, USA).

DXR-release study on UKRV-Mel-15a cells

“For the release study in chapter 4 (see 6) UKRV-Mel-15a cells were cultured in 24 well plates at a density of 2.5 x 105 cells per well in 1 ml cell culture medium (see above) for 2 days. Cells were treated with different DXR containing liposome species or with the free substance as control for 30 minutes and 4 hours. Both time points ended simultaneously. After the treatment, cells were harvested with accutase (Thermo Fisher, Waltham, USA) for 15 minutes at 4°C, sedimented by centrifugation at 400 g, 5 minutes, 4°C and stained with 10 µM Höchst 33342 (PromoCell, Heidelberg, Germany) for 30 minutes at 4°C. Cells were fixated in 4% PFA (Carl Roth, Karlsruhe, Germany) containing PBS for 15 minutes at 4°C. Shortly before measurement, cells were centrifuged in 5 ml polystyrene round bottom tubes with cell strainer caps (Corning, New York, USA) to remove aggregates.”[41]

8.2.3 **Spleen cells**

The spleens of 9 - 16 weeks old BALB/c mice (Charles River Laboratories, Wilmington, USA) were dissociated by squeezing through a 40 µm nylon sieve with a syringe plunger in IMDM. After centrifugation (300 g, 7 min), the pellet was lysed for 1 min in Gey’s lysis buffer (155 mM NH_4Cl/ 10 mM $KHCO_3$/ 0.1 mM EDTA; pH 7,3) and subsequently diluted in IMDM after a second step of centrifugation. As described in the scheme Figure 19 cells were cultivated in IMDM 5% MS: 5 x 10^6 cells were seeded into 6 well suspension plates (Greiner Bio-One, Frickenhausen, Germany) in 900 µl IMDM. 500 µl of the MS/ IMDM solution, 30 µl of the heparin/ PBS solution and 30 µl of liposomes were added to a total volume of 1.5 ml. The final mixture consisted of 5% MS, 75 µg/ml liposomes (or PS-particles (75 µg/ml) and OVA-NCs (32.5 µg/ml) respectively) and 0 - 4 U/ml heparin. The cells were incubated for 2 h at 37°C and 10% CO_2.

[41] Contributed by [redacted] group of [redacted], Dermatology of the University Medical Center Mainz

8.2.4 BMM

Bone marrow cells were taken from tibia of 11 week old Balb/c mice and centrifuged (300g, 4°C, 10 min). Blood cells were lysed adding 1 ml of Gey's lysis buffer (see 8.2.3) for 1 min and washed with washing medium (MEM/ 2% FCS/ 1% Pen-Strep). 3 x 10^6 cells were cultured in 10 ml complete medium (IMDM/ 5% HS/ 5% FCS/ 2mM Gln/ 1% Pen-Strep/ 50 µM ß-Me) including 25 ng/ml M-CSF in suspension petri dish. At day four, 4 ml of complete medium was added to the culture and at day six, 4 ml of culture medium were replaced with fresh culture medium. At day eight, adherent cells were harvested in Versen (1mM EDTA/ 1.1 mM Glucose/ 2.6 mM KCl/ 1.4 mM KH_2PO_4/ 136.8 mM NaCl/ 8.1 mM NaH_2PO_4; pH 7.2) after 20 min of incubation. The day before the uptake experiments, cells were seeded at a density of 5 x 10^4 cells per well in a 24 well plate (Greiner Bio-One, Frickenhausen, Germany) and cultured in complete medium without M-CSF. For the experiment the adherent cells were washed with PBS and cultured in 5% MS/ IMDM. Heparin and PS-particles/ OVA-NC (Cy5) were added to the aimed concentrations reaching a final concentration of 0, 0.25 and 4 U/ml heparin and 75 µg/ml PS-particles or 32.5 µg/ml OVA-NCs (Cy5). The cells were further defined by flow cytometry as described in Supplement 21.

8.2.5 BMDC

BMDCs were generated by culturing 2 x 10^6 of isolated bone marrow cells (as described in 8.2.4) in 10 ml (IMDM/ 5% FCS/ 2 mM Gln/ 1% Pen-Strep/ 50 µM ß-Me) including 10 ng/ml GM-CSF. At day 3 and day 6, 5 ml of GM-CSF containing medium were added. At day 9, the non-adherent cells were isolated and centrifuged at 300g for 10 min at 4°C and seeded into 24 well plates (1,5 x 10^4 cells/ well) in 5% MS/ IMDM for the uptake experiment (see 8.2.4). The cells were further defined by flow cytometry as described in Supplement 21.

8.2.6 Non-parenchymal liver cells (NPCs)[42]

„For the functional *in vitro* experiments (Figure 27), the murine NPCs were isolated from livers as described previously [189, 190]. Briefly, mice were anesthetized with Ketamin/Rompun and livers were perfused with 20 mL Ca^{2+}- and Mg^{2+}-free HBSS containing 100 $U \cdot L^{-1}$ collagenase A (Roche Diagnostics GmbH, Mannheim, Germany), 5% heat-inactivated FCS, and 10 $\mu g \cdot mL^{-1}$ DNase I (AppliChem, Darmstadt, Germany). Following dissection, the livers were incubated for 15 min at 37°C and grinded through a 70 µm cell strainer to generate single cell suspensions. Hepatocytes were pelleted and discarded after centrifugation for 15 min at 4°C and 30 g. Non-parenchymal cell fraction remaining in the supernatant was further purified by centrifugation at 300 g, resuspended in Histodenz solution in HBSS to reach a final concentration of 20 % and overlaid with HBSS, followed by centrifugation at 1500 g for 20 min.

[42] Experiments on NPCs were performed by Sebastian Wirsching and [redacted] of the group of [redacted], Pediatric Clinic of the Medical University Center.

NPCs were collected at the Histodenz/HBSS interface and washed with RPMI 1640 medium containing 5 % FCS and 1% Pen-Strep. Then cell suspensions were cultured in HEPES-buffered RPMI 1640 medium containing 10% FCS, 1% Pen-Strep, 1 mM Gln, 1% essential and non-essential amino acids, 1 mM sodium pyruvate, 50 nM ß-Me, and with or without 2.5 $\mu g \cdot mL^{-1}$ LPS at a concentration of 10^6 $NPCs \cdot mL^{-1}$. Different formulations of SiO_2 NCs containing DXM or PDXM, or free DXM or PDXM were added at different concentrations and incubated for 24 h.“[43]

8.2.7 Human derived macrophages[44]

“Buffy coats were obtained from healthy volunteers, with approval by the local ethical committee (Landesärztekammer Rhineland Palatine No. 837.019.10 (7028), approved on 4 March 2010). PBMC were isolated using density gradient centrifugation with Biocoll Separating Solution at 800 g. 30 min and room temperature. After removal of the layer of PBMC at the interface, the PBMC were washed two to three times with cold PBS containing 1 m EDTA (AppliChem, Darmstadt, Germany) by centrifugation at 350 g, 7 min and 4°C. Cell were then suspended and stored in PBS containing 1 mM EDTA at 4°C.”[45] Monocytes were extracted by plastic adherence. After culture for six days in RPMI-1640 supplemented with human plasma, GlutaMAX, Primocin and 0.1 ng/m human M-700 CSF cells were harvested using accutase (Thermo Fisher Scientific). Cells were treated as described in 8.2.2.

8.3 Biodistribution of nanocapsules in mice

8.3.1 Compounds of injection

In Table 13 compounds for injection are listed.

Table 13: Compounds for injection

Abb. / Brand name	Name	Company
Cy5-SiO_2 NC	Silica Nanocapsule	see 8.1.5
Lip-Dox (DiD/DiR)	Liposomal formulation of Doxil ®	see 8.1.2
Narketan®	Ketamin	VetoAquinol, Ismaning, Germany
OVA-NC (Cy5)	Ovalbumine Nanocapsules	see 8.1.4.2
PBS	Dulbecco’s phosphate buffered saline	PAN Biotech, Aidenbach, Germany
Rompun®	Xylazine	Bayer HealthCare, Leverkusen, Germany
UFH	Heparin	Panpharma, Luitré, France

[43] This section was written by other authors and adapted 155. Li Mengyi, et al., *Encapsulation of Polyprodrugs enables an Efficient and Controlled Release of Dexamethasone*. 2021: About to submit.
[44] Carried out by [redacted]p, gourp of [redacted], Dermatology Clinic of the University Medical Center Mainz.
[45] Written by [redacted], gourp of [redacted], dermatology of the University Medical Center Mainz.

8.3.2 Preparation for injections

For the *in vivo* studies, 9 - 16 weeks old BALB/c mice were obtained from Charles River (Charles River Laboratories, Wilmington, USA). Mice were kept in the animal facility of the Translational Animal Research Center of the University Medical Center Mainz, Germany. Animal were hold under following conditions: 12 h/ 12 h dark/ light cycle with food and water supply ad libitum. All experiments were approved by the local animal care and use Committee (Landesuntersuchungsamt Rheinland-Pfalz); Reference: G 17-1-068.

The animals were anesthetized with a constant flow of 2.5 % isoflurane and oxygen with a five-mask narcosis system (Rothacher, Heitenried, Switzerland). A PBS-loaded catheter was inserted into the tail vein. The catheter consisted of a 10 cm piece of tubing fine pore (Thermo Fisher, Waltham, USA) and a broken 26 G microlance (Becton Dickinson, Franklin Lakes, USA). This system allowed a precise timing of the following injections. Maximal five animal were injected simultaneously.

8.3.3 Injections

Volume and concentration of Injection 1 (timepoint: -15 minutes) and Injection 2 (timepoint: 0) are listed in Table 14 for all *in vivo* experiments. The control groups received the corresponding volume of PBS.

Table 14: Injections of heparin and nanocarriers

	Injection	Compound	Concentration	Volume [µl]/ bodyweight [g]
Chapter 1: Heparin and Liposomes	Inj. 1	Heparin	68 U/ml	4 µl/g
	Inj. 2	Lip-Dox (DiD/DiR)	10 µg/µl	4 µl/g
Chapter 2: Heparin and Ovalbumine nanocapsules	Inj. 1	Heparin	136 U/ml	2 µl/g
	Inj. 2	OVA-NC (Cy5)	5 µg/µl	8 µl/g
Chapter 3: Characterization of the Polydexamethason Silica Nanocapsule	Inj. 2	Cy5-SiO_2 NC	5 µg/µl	4.1 µl/g
	Inj. 2	Cy5-ester	Diluted with PBS on the fluorescence intensity of the Cy5-SiO_2 NC solution, using the SPARK Multimode Microplate Reader (TECAN, Männedorf, Switzerland).	

Time point of injection 1, was 15 minutes prior ('-15 minutes') to injection 2 ('0 minutes').

8.3.1 Sacrification

Animal were sacrificed by cardiac punction under a lethal intraperitoneal dose of 120 mg/kg ketamin (Narketan®) (Vetoquinol, Ismaning, Germany) and 16 mg/kg xylazine (Rompun®) (Bayer HealthCare, Leverkusen, Germany). The organs, heart, lung, liver, kidney, were removed and kept at 4°C until further processes.

8.3.2 IVIS *in vivo*

Immediately after injection 2 animal were transferred into the chamber of the IVIS (Perkin Elmer, Waltham, USA) and anesthetized for 1 h with 2.5 % isoflurane oxygen. IVIS settings are described in Table 15. For the evaluations, equally sized regions of interest (ROI) for each organ, were placed around the images of the organs. Values of the total radiant efficiency ([p/sec/cm^2/sr]/[µW/cm^2]) were exported into Microsoft Excel (Microsoft, Redmond, USA) and evaluated in R Studio (R). The background total radiant efficiency, calculated from untreated animal, was subtracted from each value.

Table 15: IVIS settings for *in vivo* and *ex vivo* analysis

	Dye	Imaging object	Field of view	exposure time	excitation/ emission
Chapter 1: Heparin and Liposomes	DiR	mice (*in vivo*)	D	1	745 nm/ 800 nm
		organs (*ex vivo*)	C	0.1	745 nm/ 800 nm
Chapter 2: Heparin and Ovalbumine nanocapsules	Cy5	mice (*in vivo*)	D	7	640 nm/ 700nm
		organs (*ex vivo*)	C	7	640 nm/ 700nm
Chapter 3: Characterization of the Polydexamethason Silica Nanocapsule	Cy5	mice (*in vivo*)	D	7	640 nm/ 700nm
		organs (*ex vivo*)	C	2	640 nm/ 700nm

The procedure of organ analysis is described in 8.3.3.

8.3.3 IVIS and organ preparations

The whole organs were placed on a black plate and measured with the IVIS (Perkin Elmer, Waltham, USA) applying settings described in Table 15. For analysis of blood, 25 µl whole blood and 25 µl of plasma (see 8.3.4.3) were pipetted into a black 69 well plate (Greiner) and diluted with 175 µl PBS for imaging with the equal settings as for organs (Table 15).

Using the living image software (Perkin Elmer, Waltham, USA), rectangular ROI were placed around each organ, for obtaining the radiant efficiency ([p/sec/cm^2/sr]/[µW/cm^2]) of each ROI. The mean total radiant efficiency of untreated animals (PBS + PBS) for each organ was defined as background and subtracted from each value.

8.3.4 Processment of organs

8.3.4.1 Liver

The large lobe of the liver (one third) was dissociated with the Liver Dissociation Kit (Miltenyi Biotec, Bergisch Gladbach, Germany) for flow cytometer analysis. After depletion of the red

blood cells (Gey's lysis, see 8.2.3), 7 x 10^6 and 5 x 10^6 cells were transferred into tubes and processed for flow cytometer staining as described in 8.4. This represents a different reprocessing method than described in 8.2.6.

8.3.4.2 Spleen

One third of the spleen was prepared for flow cytometry using a cell sieve as described above (see 8.2.3). 4 x 10^6 cells and 7 x 10^6 cells were transferred into the staining tube and processed for flow cytometer staining as described in 8.4.

8.3.4.3 Blood

A volume of 10 % of the blood volume harvested by cardiac punction was added immediately of anticoagulant citrate-dextrose solution (Terumo, Zaventem, Belgium). Plasm was gained by centrifugation (2,000 g, 4°C, 10 min) and a subsequent centrifugation of the supernatant (2,000g, 4°C, 15 minutes). The supernatant was transferred into storing tubes.

8.4 Flow cytometry

8.4.1 Compounds for flow cytometry staining

In Table 16 the compounds for flow cytometry staining are indicated

Table 16: Compounds for flow cytometry staining

Antigen	Clone	Fluorophore	Company
Antibodies			
Fc	2.4G2	none (FC-block)	Beckton Dickinson, New York, USA
Ly6G	Rea526	FITC	Miltenyi Biotec, Bergisch Gladbach, Germany
CD11b	M1/70	Super Bright 600	Thermo Fisher, Waltham, USA
CD11b	M1/70	FITC	Thermo Fisher, Waltham, USA
CD11c	N418	PE-eFluor 610	Thermo Fisher, Waltham, USA
CD11c	N418	APC eFluor 780	Thermo Fisher, Waltham, USA
CD146	ME-9F1	PE	Thermo Fisher, Waltham, USA
CD163	TNKUPJ	Super Bright 702	Thermo Fisher, Waltham, USA
CD19	1D3	FITC	Thermo Fisher, Waltham, USA
CD19	1D3	PE	Thermo Fisher, Waltham, USA
CD209b	REA125	PE	Miltenyi Biotec, Bergisch Gladbach, Germany
CD3	17A2	FITC	Thermo Fisher, Waltham, USA
CD3	REA641	PE	Miltenyi Biotec, Bergisch Gladbach, Germany
CD31	PECAM-1	FITC	Thermo Fisher, Waltham, USA
CD45	30-F11	PE-Cyanine 7	Thermo Fisher, Waltham, USA
CD45R	RA3-6B2	FITC	Thermo Fisher, Waltham, USA
CD49b	HMa2	FITC	Thermo Fisher, Waltham, USA
CD49b	DX5	PE	Miltenyi Biotec, Bergisch Gladbach, Germany
CD68	FA-11	PE-Cyanine7	Thermo Fisher, Waltham, USA
CD68	FA-11	eFluor 660	Thermo Fisher, Waltham, USA
CD8a	53-6.7	PE-Cyanine7	Thermo Fisher, Waltham, USA
F4/80	BM8	eFluor 450	Thermo Fisher, Waltham, USA
Ly6C	HK1.4	PerCP-Cyanine5.5	Thermo Fisher, Waltham, USA
Ly6G	Rea526	FITC	Miltenyi Biotec, Bergisch Gladbach, Germany
Ly6G	1A8	PE	Miltenyi Biotec, Bergisch Gladbach, Germany
MHCII	M5/114.15.1	eFluor 450	Thermo Fisher, Waltham, USA
MMM	7-239	CD169	Thermo Fisher, Waltham, USA
Siglec-F	1RNM44N	PerCP-eFluor 710	Thermo Fisher, Waltham, USA
Siglec-H	eBio440c	PE	Thermo Fisher, Waltham, USA
Abb.	**Name**		**Company**
Other Compounds			
EDTA	Ethylenediaminetetraacetic acid		Carl Roth, Karlsruhe, Germany
FBS	Fetales Bovines Serum		Pan Biotech, Aidenbach, Germany
FVD eFluor 506	Fixable viability dye eFluor 506		Thermo Fisher, Waltham, USA
PBS	Dulbecco's phosphate buffered saline		PAN Biotech, Aidenbach, Germany
PFA	Paraformaldehyde		Carl Roth, Karlsruhe, Germany

8.4.2 Flow cytometry staining

8.4.2.1 Flow cytometry of spleen cells and liver cells

All steps were performed on ice or at 4°C. Cells were transferred into round bottom tubes for the staining procedure. The number of cells can be taken from the tables below (Table 17- Table 21). After centrifugation (300 g, 7 min) and washing with PBS, the pellet was dissociated and cells were stained with FVD for 20 min (see Table 17 - Table 21). The reaction was stopped with 2 ml flow cytometry buffer (PBS/ 1% FBS/ 2mM EDTA) following a centrifugation step. The dissociated cell pellet was incubated with Fc-block (2.4G2) 1 µg/ 100 µl for 10 min in flow cytometry buffer. Cells were incubated with the respective antibody mixture (see Table 17- Table 21) solved in flow cytometry buffer for 45 minutes on the shaker. After washing (2 ml flow cytometry buffer), cells were fixated with 'FACS-Fix' (PBS/ 0.7 % PFA/ 2 mM EDTA).

8.4.2.2 Flow cytometry staining of blood

All steps were performed on ice or at 4°C. 50 µl of whole blood (from 8.3.4.3) were used for flow cytometry analysis and lysed 3 times with 300 µl Gey's lysis buffer (see 8.2.3). Lysis was stopped with flow cytometry buffer (8.4.2) and subsequent centrifugation at 300 g for 7 min. Bevor applying FVD (see Table 22) for 20 min, cells were washed with pure PBS.

8.4.1 Flow cytometer analysis

The Attune Nxt Flow Cytometer (Thermo Fisher, Waltham, USA) equipped with four lasers, 405 nm (channel VL1-VL4), 488 nm (channel BL1- BL3), 568 nm (channel YL1-4), 633 nm (channel RL1-3), was used for all flow cytometry experiments. The compensations were calculated by the software using compensation beads (Thermo Fisher, Waltham, USA), which were stained with the respective antibody according to the manufacturer's protocol. Technical adjustments of FCS/SSC and speed are indicated in Table 17 - Table 22. The respective flow cytometry plots with a representative gating strategy and 'uptake histograms' can be found in the supplements. Values have been exported as .csv-file and evaluated with Excel (Microsoft, Redmond, USA) and R-studio (R).

8.4.2 Flow cytometry compounds and settings of panel 1-8

Six panels were designed for analysis of cell populations in spleen, liver and blood. In Table 17 - Table 22 for each panel the settings of the Attune Nxt Flow cytometer (Thermo Fisher, Waltham, USA) are listed (grey shaded). The staining protocol is given in 8.4.2

Table 17: Panel 1, dendritic cells, macrophages and monocytes of the spleen

Panel 1	**DCs, macrophages and Mono of the spleen**				
Number of cells:	7 x10^6	**Volume of blocking buffer:**	50 µl	**Volume of antibody mixture:**	200 µl
FSC/ SSC:	300/360	**Speed:**	500 µl/min	**Volume of sample:**	1.6 ml

Antigen	**Fluorophore**	**Concentration [µg/ml]**	**Channel**
MHCII	eFluor 450	0.5	VL1
FVD	eFluor 506	0.4	VL2
CD11b	Super Bright 600	0.7	VL3
CD3	FITC	1.25	BL1
CD49b	FITC	1.25	BL1
Ly6G	FITC	0.225	BL1
Ly6C	PerCP-Cyanine5.5	0.5	BL3
Siglec-H	PE	0.5	YL1
CD11c	PE-eFluor 610	0.5	YL2
CD8a	PE-Cyanine7	0.5	YL4

The table describes the antibodies/ dye used for the staining procedure and the settings of the Attune Nxt Flow Cytometer. DiD/DiR labelled or Cy5-labelled nanocapsules (*in vivo*) were analyzed in the 'RL1' channel. For each experiment a representative gating strategy is shown in Supplement 5 and Supplement 26.

Table 18: Panel 2, macrophages of the spleen.

Panel 2	**Macrophages of the spleen**				
Number of cells:	4 x10^6	**Volume of blocking buffer:**	50 µl	**Volume of antibody mixture:**	200 µl
FSC/ SSC:	300/360	**Speed:**	200 µl/min	**Volume of sample:**	0.8 ml

Antigen	**Fluorophore**	**Concentration [µg/ml]**	**Channel**
FVD	eFluor 506	0.4	VL2
F4/80	eFluor 450	0.5	VL1
CD11b	Super Bright 600	0.7	VL3
CD3	FITC	1.25	BL1
CD19	FITC	0.5	BL1
CD49b	FITC	1.225	BL1
***Ly6G**	FITC	0.225	BL1
Ly6C	PerCP-Cyanine5.5	0.5	BL3
CD11c	PE-eFluor 610 (APC eFluor 780)†	0.5	YL2 (RL3)†
CD209b	PE	0.375	YL1 (BL2)†
CD68	PE-Cyanine7 (eFluor 660)†	0.5	YL4 (RL1)†

The table describes the antibodies/ dye used for the staining procedure and the settings of the Attune Nxt Flow Cytometer. DiD/DiR-labelled or Cy5-labelled nanocapsules (*in vivo*) were analyzed in the 'RL1' channel. *this compound was not included into the panel for *in vitro* studies. †For flow cytometry of spleen cells treated BP-labelled PS-particles, settings were adapted: PS-NH_2 (BP) and PS-COOH (BP) were analyzed in the 'YL2' channel. For each experiment a representative gating strategy is shown in Supplement 2, Supplement 6, Supplement 18, Supplement 20, Supplement 26 and Supplement 33.

Table 19: Panel 3, B- and T-cells of the spleen,

Panel 3	B- and T-cells of the spleen				
Number of cells:	1.5 x10^6	**Volume of blocking buffer:**	25 µl	**Volume of antibody mixture:**	100 µl
FSC/ SSC:	300/360	**Speed:**	200 µl/min	**Volume of sample:**	0.5 ml

Antigen	Fluorophore	Con-centration [µg/ml]	Chan-nel
FVD	eFluor 506	0.4	VL2
CD3	FITC	1.25	BL1
CD19	PE	0.5	YL1
MMM	CD169	0.75	YL4

The table describes the antibodies/ dye used for the staining procedure which is described above and the settings of the Attune Nxt Flow Cytometer. DiD/DiR-labelled or Cy5-labelled nanocapsules (*in vivo*) were analyzed in the 'RL1' channel. For each experiment a representative gating strategy is shown in Supplement 6 and Supplement 26.

Table 20: Panel 4, macrophages of the liver

Panel 4	**Macrophages of the liver**				
Number of cells:	7 x10^6	**Volume of blocking buffer:**	50 µl	**Volume of antibody mixture:**	200 µl
FSC/ SSC:	240/300	**Speed:**	500 µl/min	**Volume of sample:**	1.6 ml

Antigen	Fluorophore	Con-centration [µg/ml]	Chan-nel
FVD	eFluor 506	0.4	VL2
CD163	Super Bright 702	0.5	VL4
CD11b	FITC	0.125	BL1
Ly6C	PerCP-Cyanine5.5	0.5	BL3
CD3	PE	0.225	YL1
CD49b	PE	0.225	YL1
Ly6G	PE	0.225	YL1
CD11c	PE-eFluor 610	0.5	YL2
CD68a	PE-Cyanine7	0.5	YL4

The table describes the antibodies/ dye used for the staining procedure which is described above and the settings of the Attune Nxt Flow Cytometer. DiD/DiR-labelled or Cy5-labelled nanocapsules (*in vivo*) were analyzed in the 'RL1' channel. For each experiment a representative gating strategy is shown in Supplement 7, Supplement 27and Supplement 32.

Table 21: Panel 5, LSECs

Panel 5	**LSECs of the liver**				
Volume of FVD	2 x10^6	**Volume of blocking buffer:**	25 µl	**Volume of antibody mixture:**	100 µl
FSC/ SSC:	240/300	**Speed:**	500 µl/min	**Volume of sample:**	0.5 ml

Antigen	Fluorophore	Concentration [µg/ml]	Channel
FVD	eFluor 506	0.4	VL2
CD31	FITC	0.625	BL1
CD146	PE	0.25	YL1
CD45	PE-Cyanine 7	0.25	YL4

The table describes the antibodies/ dye used for the staining procedure which is described above and the settings of the Attune Nxt Flow Cytometer. DiD/DiR-labelled or Cy5-labelled nanocapsules (*in vivo*)

were analyzed in the 'RL1' channel. For each experiment a representative gating strategy is shown in Supplement 7 and Supplement 27.

Table 22: Panel 6, granulocytes of the blood.

Panel 6	**Granulocytes of the blood**				
Volume of blood:	50 µl	**Volume of blocking buffer:**	25 µl	**Volume of antibody mixture:**	100 µl
FSC/ SSC:	240/300	**Speed:**	500 µl/min	**Volume:**	0.5 ml

Antigen	**Fluorophore**	**Concentration [µg/ml]**	**Channel**
FVD	eFluor 506	0.4	VL2
CD11b	Super Bright 600	0.125	VL3
CD45R	FITC	0.062	BL1
CD3	FITC	0.062	BL1
CD49b	FITC	0.062	BL1
Siglec-F	PerCP-eFluor 710	0.062	BL3
Ly6G	PE	0.125	YL1

The table describes the antibodies/ dye used for the staining procedure which is described above and the settings of the Attune Nxt Flow Cytometer. DiD/DiR-labelled or Cy5-labelled nanocapsules (*in vivo*) were analyzed in the 'RL1' channel. A representative gating strategy is shown in Supplement 11.

8.4.3 Definition of fluorescent markers for determination of cellular population

Table 23 and Table 24 show the marker expressions for flow cytometric definition and abbreviations of cellular populations. For definition of the populations MO, DC, Eos and Mono (e.g. Supplement 2, Supplement 5) the gating strategy of Rose et al. [191] was adapted and expanded with the markers for F4/80, CD68 and CD209b in order to define RPM, MZM and WPM [67, 69] (e.g. Supplement 2, Supplement 6). For determination of the fourth type of spleen macrophages, MMM, the $CD169^+$ population was defined [192] after exclusion of the $CD19^+$ and $CD3^+$ population (Supplement 6). The subpopulations of dendritic cells cDC1, cDC2, pDC and mDC were defined orienting at Dong et al. [74]. The macrophage populations of the liver were defined by pan-markers for macrophages CD68, CD11b as well as Ly6C (Monocytes) [146, 193] and CD11c for the liver DC [194]. For definition of Kupf the selective marker CD163 [146] was stained. LSECs were defined as described by Seckert et al. [195].

Table 23: Flow cytometry definition of cellular populations *in vitro.*

Definition of cell populations *in vitro* (spleen)		
Abb.	**Population**	**Marker expression**
-	lineage	$CD3^+$, $CD49b^+$
Mono	Monocytes	$lineage^-$, $CD11c^-$, $CD11b^+$, $Ly6C^+$
MZM	Marginal zone macrophages	$lineage^-$, $CD11c^-$, $CD11b^+$, SSC^{low}, $Ly6C^-$, $F4/80^-$, $CD209b^+$
RPM	Red pulp macrophages	$lineage^-$, $CD11c^-$, $CD11b^+$, SSC^{low}, $Ly6C^-$, $CD68^+$, $F4/80^+$
WPM	White pulp macrophages	$lineage^-$, $CD11c^-$, $CD11b^-$, SSC^{low}, $Ly6C^-$, $CD68^+$, $F4/80^-$
DC	Dendritic cells	$lineage^-$, $CD11c^+$
Eos	Eosinophils	$lineage^-$, $CD11c^-$, $CD11b^+$, SSC^{high}

The panel (Table 18) which is represented in Supplement 2, Supplement 18 and Supplement 20 (*inter alia*) was applied for determination of the splenic populations.

Table 24: Flow cytometry definition of cellular populations *in vivo.*

Definition of cell populations *in vivo*			
Abb.	**Population**	**Marker expression**	**Panel**
		spleen	
	lineage1	$CD3^+$, $CD19^+$, $CD49b^+$, $Ly6G^+$	1
	lineage2	$CD3^+$, $CD19^+$, $CD49b^+$	2
DC	Dendritic cells	$lineage1^-$, $CD11c^+$	1
CD11b+	$CD11b^+$ cells	$lineage1^-$, $CD11c^+$, $CD11b^+$	1
MO	Macrophages	$lineage1^-$, $CD11c^-$, $CD11b^+$, SSC^{low}, $Ly6C^-$	1
Mono	Monocytes	$lineage1^-$, $CD11c^-$, $CD11b^+$, $Ly6C^+$	1
RPM	Red pulp macrophages	$lineage2^-$, $CD11c^-$, $CD11b^+$, SSC^{low}, $Ly6C^-$, $CD68^+$, $F4/80^+$	2
WPM	White pulp macrophages	$lineage2^-$, $CD11c^-$, $CD11b^-$, SSC^{low}, $Ly6C^-$, $CD68^+$, $F4/80^-$	2
MZM	Marginal zone macrophages	$lineage2^-$, $CD11c^-$, $CD11b^+$, SSC^{low}, $Ly6C^-$, $F4/80^-$, $CD209b^+$	2
MMM	Metallophilic marginal zone macrophages	$CD19^-$, $CD3^-$, $CD169^+$	3
cDC1	Conventional dendritic cells type 1	$lineage1^-$, $Siglec\text{-}H^-$, $CD11c^+$, (CD11blow), $MHCII^+$, $CD8^+$	1
cDC2	Conventional dendritic cells type 2	$lineage1^-$, $Siglec\text{-}H^-$, $CD11c^+$, $(CD11b^{low})$, $MHCII^+$, $CD8^-$	1
mDC	Macrophage derived dendritic cells	$lineage1^-$, $Siglec\text{-}H^+$, $(CD11c^{low})$, $CD11b^+$, $MHCII^+$, $Ly6C^-$	1
Eos	Eosinophils	lineage1-, $CD11c^-$, $CD11b^+$, SSC^{high}	1
pDC	Plasmacytoid dendritic cells	$lineage1^-$, $Siglec\text{-}H^+$, $CD11c^+$	1
B-Cells	B-cells	$CD19^+$	3
T-Cells	T-cells	$CD19^-$, $CD3^+$	3
		liver	
	lineage	$CD3^+$, $Ly6G^+$, $CD49b^+$	4
Mono	Monocytes	$lineage^-$, $CD11c^-$, $CD163^-$, $Ly6C^+$	4
KC	Kupffer cells	$lineage^-$, $CD11c^-$, $CD163^+$	4
$CD68^+$ MO	$CD68^+$ Macrophages	$lineage^-$, $CD11c^-$, $CD163^-$, $Ly6C^-$, $CD68^+$	4
$CD11b^+$ MO	$CD11b^+$ Macrophages	$lineage^-$, $CD11c^-$, $CD163^-$, $Ly6C^-$, $CD68^+$	4
DC	Dendritic cells	$lineage^-$, $CD11c^+$	4
LSEC	Liver sinusoidal cells	$CD45^-$, $CD31^+$, $CD146^+$	5

Multiple panels (Table 17-Table 21) were applied to determine these populations.

8.4.4 Evaluation parameters

The median fluorescence intensity (**MFI**) (DID/ Cy5) of each value was calculated by subtracting the mean MFI of DiD (or Cy5) of the untreated controls from each value. Values were excluded if the gate of the population was <100 counts.

The percent of uptake, (**'% of uptake'**) (DiD/ Cy5), was calculated by placing a gate at a representative untreated control sample. The mean value of the untreated background samples (<5 %) was subtracted from each value. Values were excluded if the gate of the population was <100 counts.

The **MFI of Cy5-positive/ BP-positive cells** were calculated by measuring the MFI of the '% of uptake' (Cy5 / BP) gate. Values were excluded if the '% of uptake' (Cy5 / BP) gate accounted for <100 counts.

8.5 Microscopy

In Table 25 compounds for microscopy sample preparation are listed.

Table 25: Compounds for staining of samples for microscopy

Antibodies		
Antibody	**Clone**	**Company**
Rat anti-CD68	FA-11	Thermo Fisher, Waltham, USA
CD209b PE	REA125	Miltenyi Biotec, Bergisch Gladbach, Germany
Goat anti-rat Alexa Fluor 488	Polyclonal	Thermo Fisher, Waltham, USA
Other compounds		
Abb.	**Name**	**Company**
	Goat serum	Merck, Darmstadt, Germany
BSA	Bovine serum albumine	Carl Roth, Karlsruhe, Germany
	Glycin	Carl Roth, Karlsruhe, Germany
PBS	Phosphate Buffered Saline	PAN Biotech, Aidenbach, Germany
	Fluorescence Mounting Medium	Dako, Glostrup, Denmark
	Gold anti Fade Dapi	Thermo Fisher, Waltham, USA
Höchst	Höchst 33342	PromoCell, Heidelberg, Germany

8.5.1.1 Immunofluorescence

Organs were fixated at -80°C and cut into 10 µm thick slices using the microtome (Leica, Wetzlar, Germany). The tissue sections were dryed for 20 minutes onto the glass slides at room temperature and fixated in PBS/ 4% paraformaldehyde for 20 minutes at RT. The sections were washed twice with PBS and a third time with addition of 30 mM glycine before starting the blocking: blocking buffer (PBS/ 2.5 % goat serum/ 5% BSA) was incubated for 2h at RT. The antibodies were applied to the section in staining buffer (PBS/ 0.05 %/ 2.5% BSA and 1.24 % goat serum and Rat anti-CD68: 1 µg/ml; CD209b PE, 5µg/ml) and incubated overnight at 4°C in a humid chamber.

The primary antibody staining was washed of thoroughly in 3 times PBS and depending on the first staining, the secondary antibody mix was applied (Goat anti-rat Alexa Fluor 488: 5 µg/ml) for 2 h at RT.

Sections were washed thoroughly with PBS and stained for 5 min with Höchst (1 : 15,000) and covered in Fluorescence Mounting Medium with cover slides (Marienfeld, Lauda-Königshofen, Germany).

The stained tissue sections of liver and spleen were scanned with the confocal laser scanning microscope LSM510 (Zeiss, Oberkochen, Germany). The images in chapter 1 (Supplement 8 and Supplement 9) were processed in Fiji (ImageJ). Brightness and contrast were adapted automatically.

8.5.2 **Amnis® ImageStream® X Mark II**

8.5.2.1 Blood

For the Amnis® ImageStream X Mark II analysis, 20 µl blood from 8.3.4.3 was mixed with 10 µl of 'FACS-Fix' (protocol see 8.4.2). The filtered blood (nylon sieve) was analyzed with the Amnis®ImageStream®X Mark II (Luminex, Austin, USA) and the software ISX (Luminex, Austin, USA) until 10,000 cells (predominantly erythrocytes) were imaged under a 'slow' flow speed with the 40x objective. The measurement files were evaluated and processed in IDEAS (Luminex, Austin, USA).

8.5.2.2 Cells

1 x10^6 cells (experiment see 8.2.2 and 8.2.7) were concentrated to a volume of 50 µl and analyzed using Amnis® ImageStream® (Luminex, Austin, USA). It was used the 40x objective and flow speed was adjusted 'low'. The following channels have been used for analysis Ch1 (brightfield (BF)), Ch4 (DXR), Ch7 (Höchst), Ch11 (DiD), Ch12 (SSC). A compensation matrix (.cif – file) was generated using a single stained sample for each (DiD, DXR and Höchst) in order to recalculate the fluorescence intensities of all measurements (.rif-files). Following gating strategy was applied to gate for 'focused', 'single' and 'alive cells' (Figure 30 A).

For the evaluation of the required parameters, new features were manually established. Using the adaptive erode function, masks were established for the 'whole cell' (wcM) and the 'nucleus' (nM) (Figure 30 B) which in turn served to set up the required features (Figure 30 C). The Mask for cytoplasm was created by calculating: cM = wcM – nM. For comparison of the 'uptake' and 'release' of DXR from the investigated liposomal formulations, parameters (described in Table 9) were analyzed.

9 Supplements

9.1 Supplements Chapter 1

Table 26: Physicochemical characteristics of liposomal formulations in chapter 1.

	Experiment	Batch	Size [nm]	SEM Size [nm]	ζ [mV]	SEM ζ [mV]
Lip-Amb	*in vitro*	1	236	2.52	-42.10	0.66
		2	188	0.92	-46.30	2.64
		3	138	1.69	-42.00	1.87
		4	150	1.06	-48.20	4.65
		⌀	178	1.54	-44.65	2.45
Lip-Dox	*in vitro*	1	132	1.28	-12.77	0.76
		2	125	1.35	-16.93	0.74
		3	248	2.24	-13.07	0.52
		4	134	2.89	-11.87	0.37
		⌀	160	1.94	-13.66	0.60
	30 min *(in vivo)*	1	145	4.30	-12.70	0.88
	120 min *(in vivo)*	2	158	1.32	-11.37	0.37
	360 min *(in vivo)*	3	124	10.32	-12.31	0.81
Lip-Myo	*in vitro*	1	206	6.44	-12.30	0.59
		2	218	1.91	-12.40	0.45
		3	170	4.12	-11.20	0.16
		4	183	4.02	-11.13	0.74
		⌀	194	4.12	-11.76	0.49
Lip-Myo-PEG	*in vitro*	1	108	2.23	-17.47	1.04
		2	201	3.47	-16.13	0.60
		3	125	0.97	-17.90	1.70
		4	138	0.99	-17.57	0.68
		⌀	143	1.91	-17.27	1.01

Indicated is the hydrodynamic mean + SEM diameter (size) and mean + SEM surface potential (ζ-potential) measured as described in 8.1.6.1. For the *in vitro* experiments, each batch was used n = 2. The averages of all batches are given in the darker shaded rows.

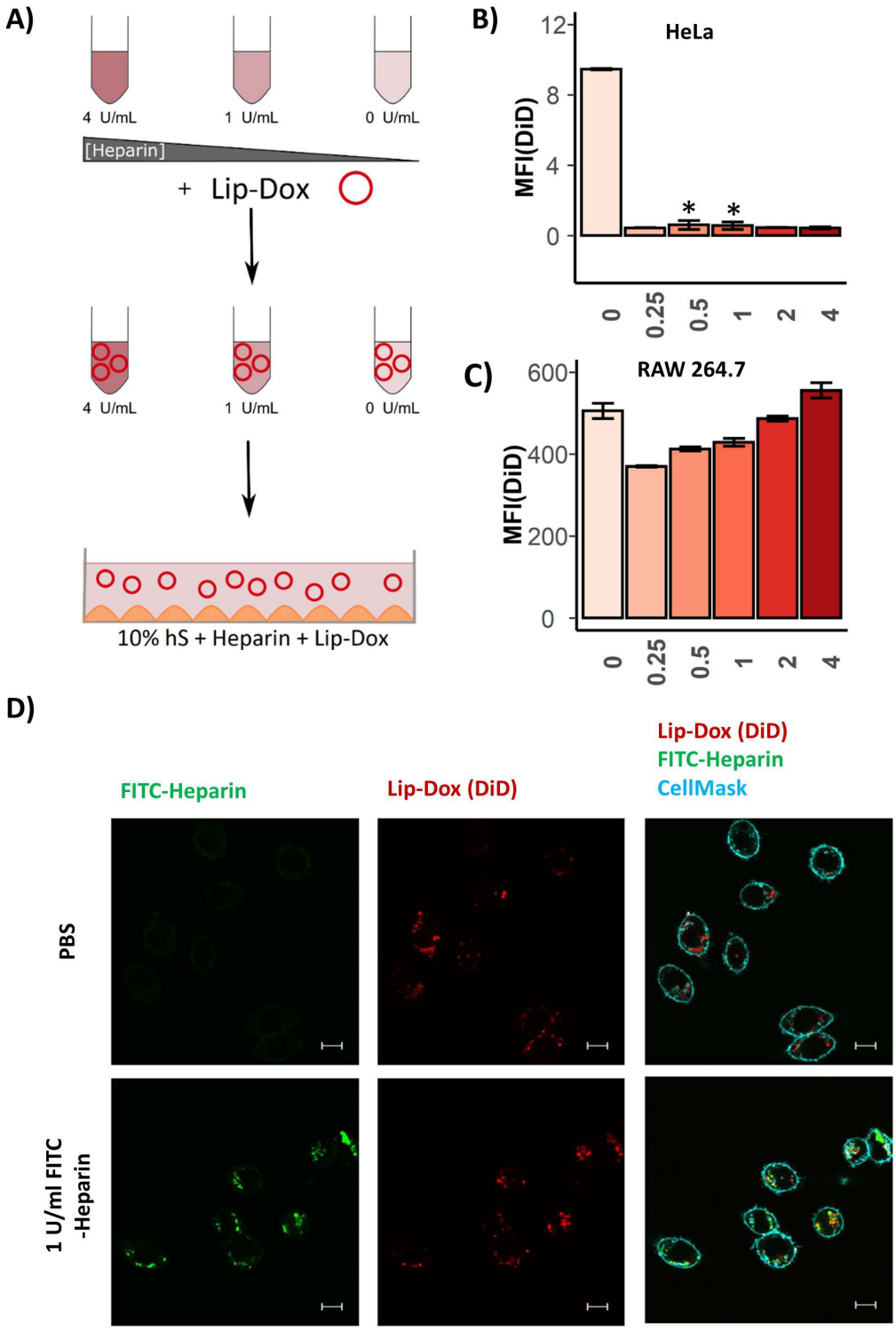

Supplement 1: Uptake of Lip-Dox (DiD) into HeLa cells and RAW 264.7 cells in presence of heparin.

A: Experiment scheme for testing the uptake of liposomes in cell lines in presence of heparin. **B:** Uptake of Lip-Dox (DiD) into cell lines after 3h incubation at 37°C. The graph represents the MFI (DiD) (mean +/- SEM), treated according to the scheme in A. A Wilcoxen test was used to compare the group 0 U/ml with the other conditions. n = 2-3 **B:** HeLa cells **C:** RAW 264.7 cells. **D:** The immunofluorescence shows the uptake of Lip-Dox (DID) and heparin into RAW 264.7 cells. Cells were treated with 1U/ml of FITC-heparin and 32.5 µg/ml Lip-Dox (DiD-labelled) for 3h at 37°C.

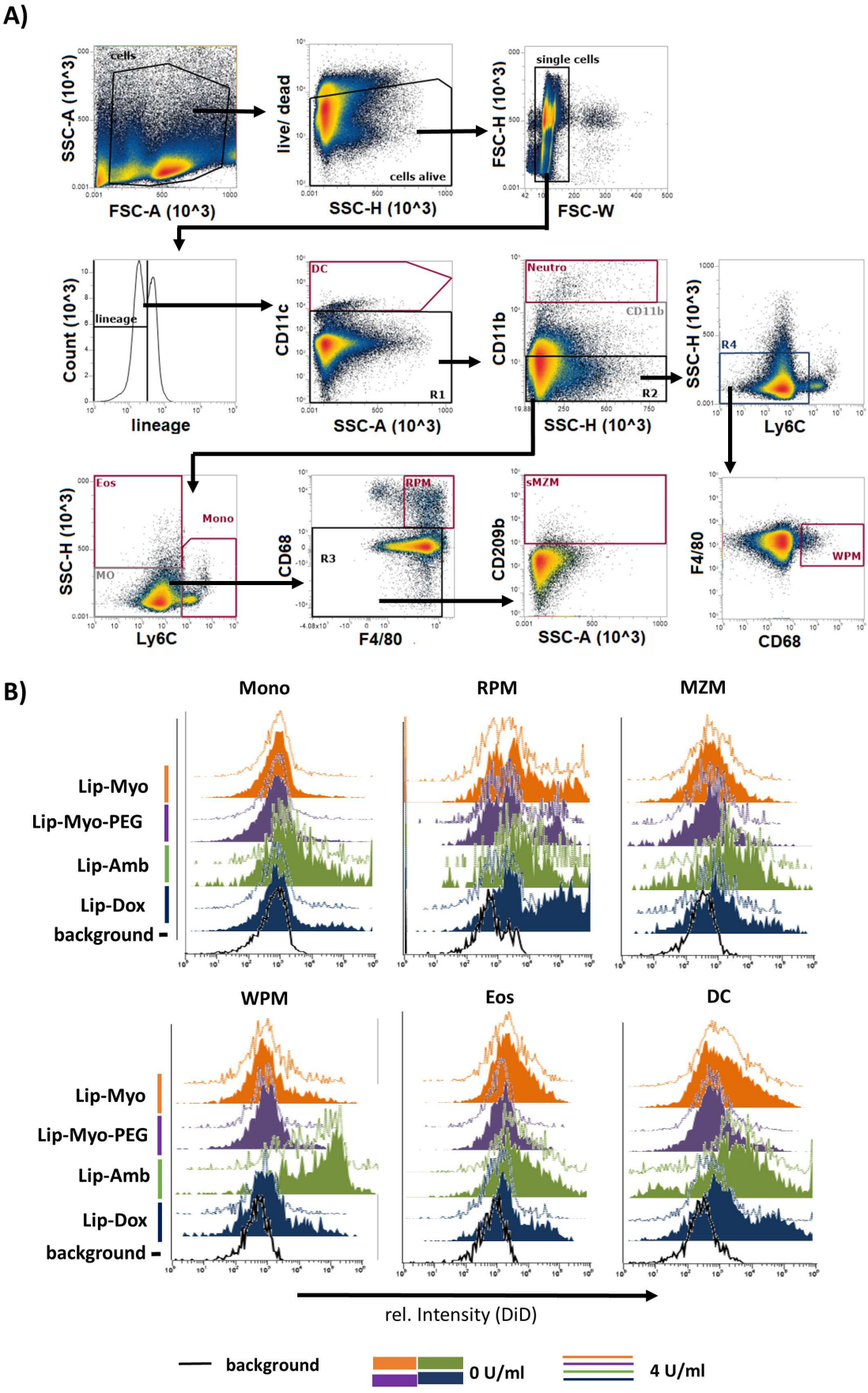

Supplement 2: Panel 2, flow cytometry gating strategy for RES-cells of the spleen (*in vitro*- experiments)

A: *Panel 2:* The gating strategy describes the flow cytometric definition of the spleen cell populations investigated in section 3.3.1. Dead cells (FVD^+) and doublets were excluded from analysis as described in Supplement 5 A. Lineage negative cells ($CD49b^-$, $CD3^-$) were subclassed into $CD11c^+$ and $CD11c^-$. First were defined as dendritic cells (DCs). Second were defined as $CD11b^+$ and $CD11b^-$. The $CD11b^+$, $Ly6C^+$, $SSC\text{-}H^{low}$ were defined as monocytes (Mono). $CD11b^+$, $Ly6C^-$, $SSC\text{-}H^{low}$, were defined as macrophages (MO). The $Ly6C^{low}$, $SSC\text{-}H^{high}$ cells were defined as eosinophils (Eos). Red pulp macrophages (RPM) then were specifically defined from the MO population as $F4/80^+$, $CD68^+$. Marginal zone macrophages (MZM) were defined from the MO population as $CD68^-$, $F4/80^{low/-}$, $CD209b^+$. The white pulp macrophages (WPM) were defined as $CD11b^-$, $Ly6C^-$, $SSC\text{-}H^{low}$, $F4/80^-$, $CD68^+$. **B:** Histograms of distribution of the relative DiD intensity for defined spleen cell populations (A). The stacked overlay represents the normalized intensity distribution curve detected in the channel ‘RL1-H’ of DiD for Lip-Myo (DiD), Lip-Myo-PEG (DiD), Lip-Amb (DiD), Lip-Dox (DiD) in the particular spleen cell population. The filled curve represents a sample treated with 0 U/ml, the line represents a sample treated with 4 U/ml heparin. The untreated control is shown as a black line.

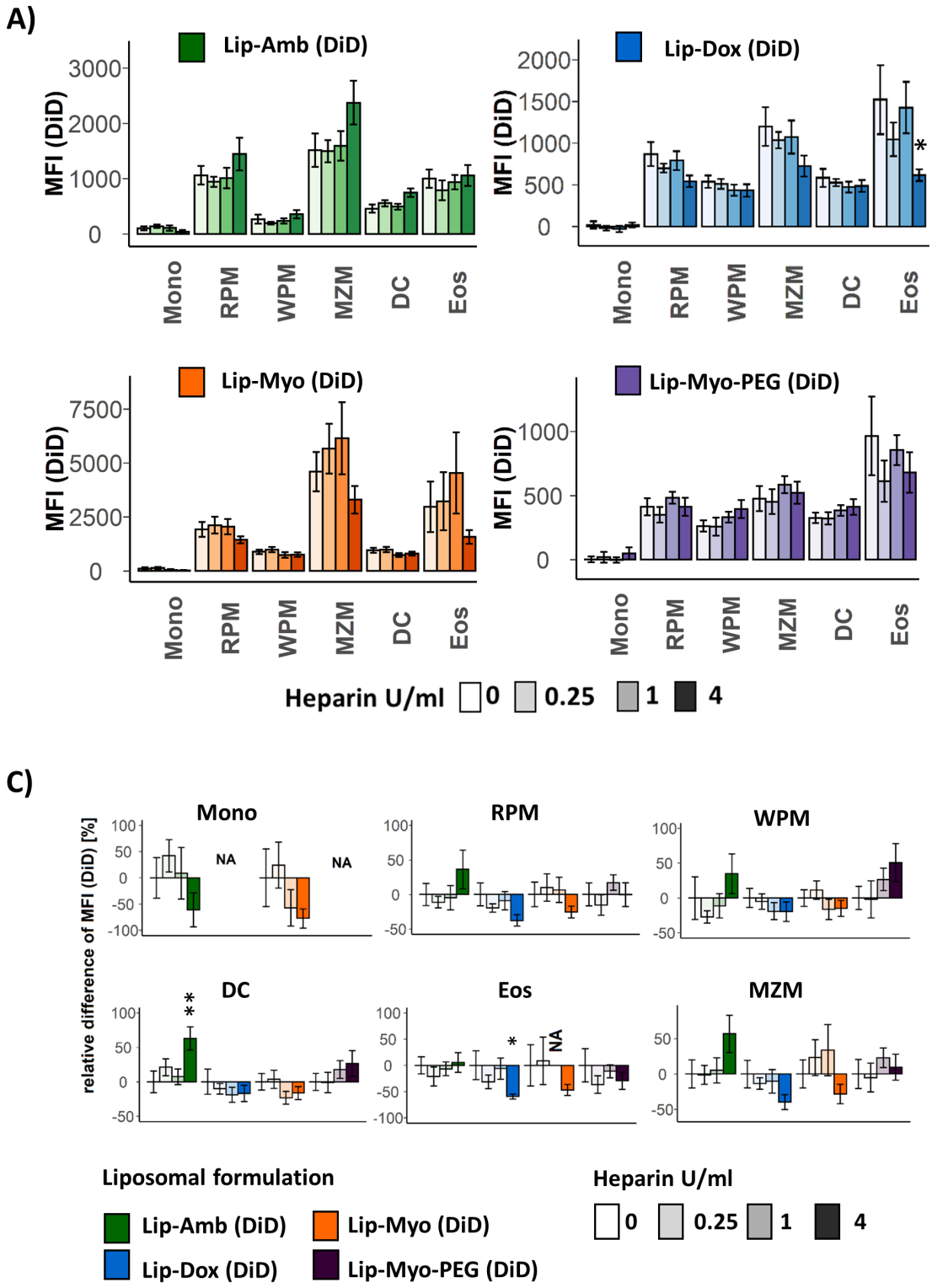

Supplement 3: The uptake of DiD-labelled liposomes into slpenocytes in presence of heparin *in vitro*.

A: MFI (DID) of defined spleen cell populations Marker definition and abbreviations see Table 23. The graph represents the (mean +/- SEM). Each group (0.25, 1 and 4 U/ml) was compared to the group of 0 U/ml heparin with a Wilcoxen test. $p < 0.05$ = *. n = 8, four batches of each liposomal formulation were used. **B:** Relative effect of heparin on uptake of liposomes (DiD). Represented is the mean +/- SEM (%) of the difference of each measured value MFI (DID) A) towards the mean of the non-heparin treated samples. Values with a SEM > mean is not shown. Each group (0.25, 1 and 4 U/ml) was compared to the group of 0 U/ml heparin by a Wilcoxen test. $p < 0.05$ = *. n = see C.

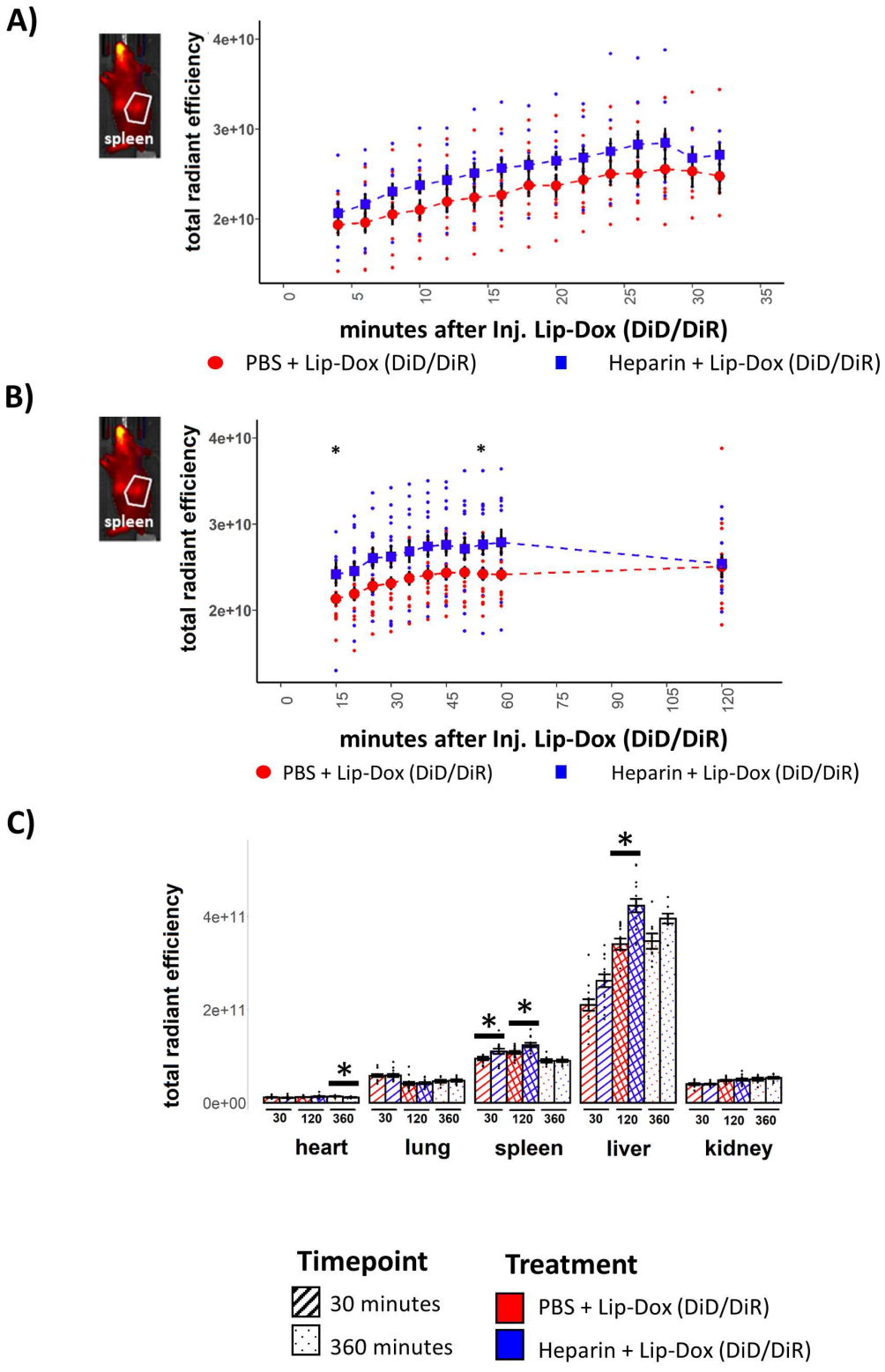

Supplement 4: The effect of an i.v. heparinization on biodistribution of Lip-Dox (DiD/ DiR) *in vivo*.

A/B: Spleen accumulation of Lip-Dox at 30 and 120 minutes *in vivo*. The total radiant efficiency (mean +/- SEM) of DiR in the indicated region of interest. **A:** 30 min **B:** 120 min. The two test groups were compared with a Wilcoxen test. $p < 0.05$ =*. (A) n = 4 - 10. (B) n = 10 **C:** Total accumulation of Lip-Dox (DiD/DiR) in organs of interest. The graph shows the total radiant efficiency (mean +/- SEM) of DiR for the organs of interest at 30, 120 and 360 minutes. For each time point and organ the test groups were compared with a Wilcoxen test. $p < 0.05$ = *. n = 8 – 14.

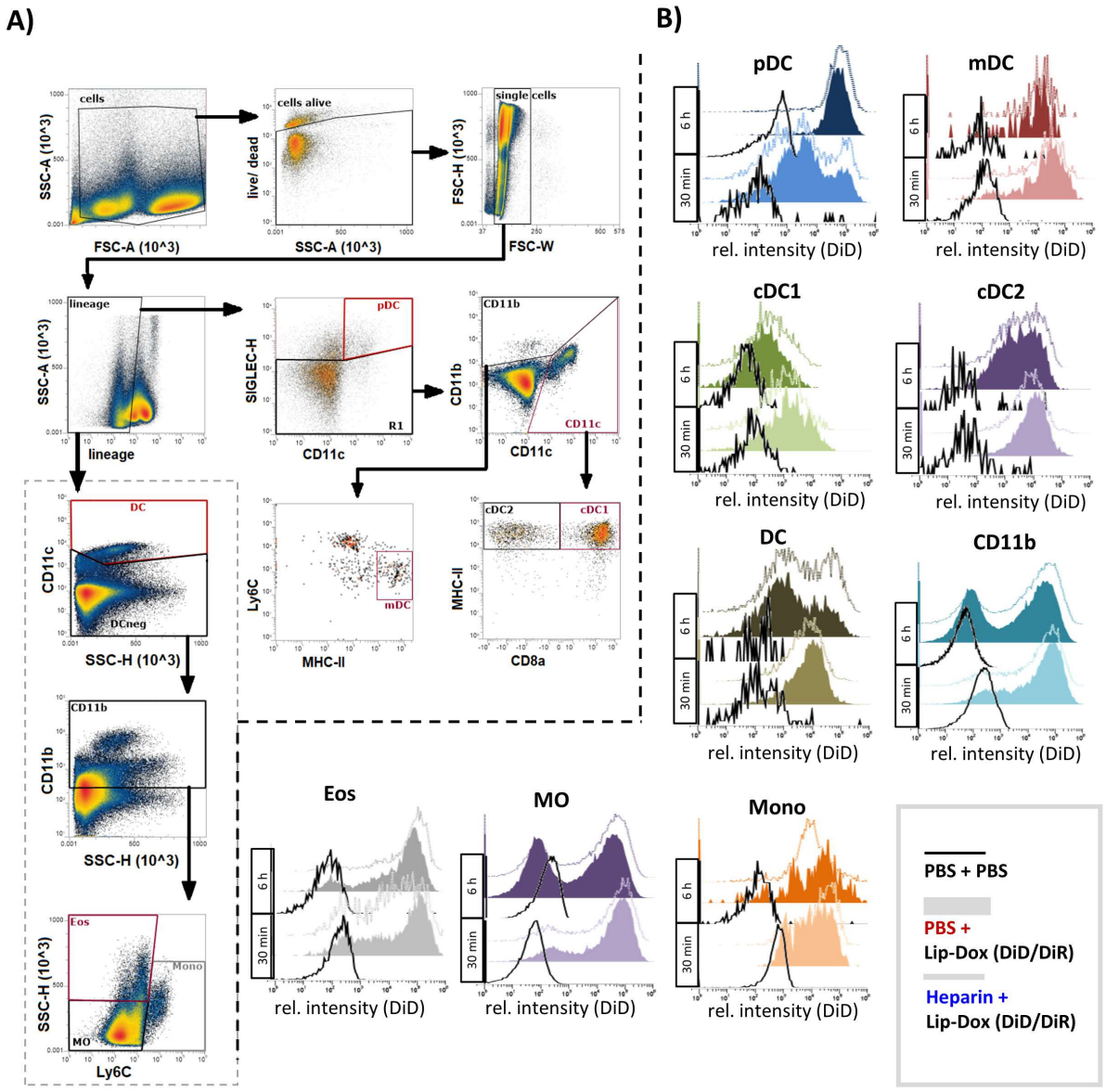

Supplement 5: Panel 1, gating strategy for splenocytes *in vivo*.

A: *Panel 1:* The gating strategy describes the flow cytometry definition of the spleen cell populations investigated in section 3.3.3. Dead cells (FVD$^+$) and doublets were excluded from analysis. Lineage negative cells (CD49b$^-$/ Ly6G$^-$/ CD19$^-$/ CD3$^-$) were applied against SIGLEC-H and CD11c. The pDCs were defined as SIGLEC-H$^+$, CD11c$^+$. The SIGLEC-H$^-$ cells were applied against CD11c and CD11b. The CD11c positive, CD11b$^{low/-}$ cells were specified into conventional dendritic cells type 1 and 2 (cDC1, cDC2) by CD8 and MHCII. The CD11b$^+$, CD11c$^{low/-}$ population was then specified into monocyte derived dendritic cells by Ly6C and MHCII. The analysis of the general spleen cell populations, MO, DC, CD11b$^+$, Mono and Eos: first dead cells (FVD$^+$), doublets and cells expressing lineage markers (CD49b/ CD3/ CD19 and Ly6G) were excluded from further analysis. CD11c+ cells were defined as DCs. CD11c$^-$ cells were defined into CD11b$^+$ cells. Subsequently MO were characterized as CD11c$^+$, CD11b$^+$, Ly6C$^-$, SSC-H$^{-/low}$ cells. Mono as CD11c$^+$, CD11b$^+$, Ly6C$^+$, SSC-H^{low}. Eos as CD11c$^+$, CD11b$^+$, Ly6C$^-$, SSC-H^{high} cells. **B:** Normalized distribution of relative fluorescence intensity (DiD) for defined spleen cell populations (A) representing the uptake behavior of the investigated cell types for Lip-Dox (DiD/DiR). For both 30 minutes (bright) as 360 minutes (dark) an example is shown for each test group 'PBS + Lip-Dox (DiD/DiR)' (filled), 'Heparin + Lip-Dox (DiD/DiR)' (line), as of the 'PBS + PBS' treated control (black line).

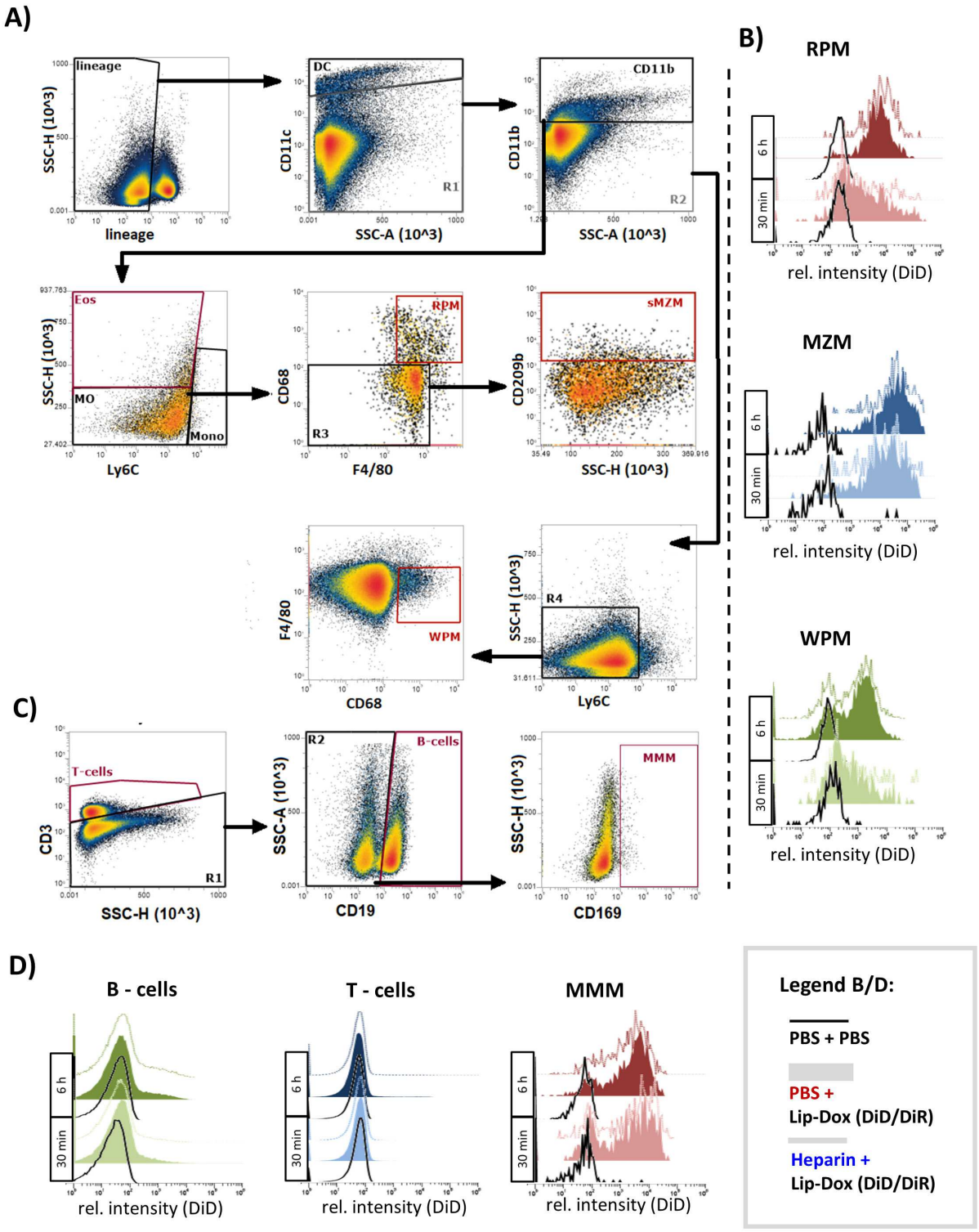

Supplement 6: Panel 2/3, gating strategy for splenocytes *in vivo.*

A: *Panel 2:* The gating strategy describes the flow cytometric definition of the spleen cell populations investigated in section 3.3.3. D/F and described in Table 24. Dead cells (FVD^+) and doublets were excluded from analysis as described in Supplement 5. Lineage negative cells ($CD49b^-$, $CD3^-$, $Ly6G^-$) were subclassed into $CD11c^+$ and $CD11c^-$. First were defined as dendritic cells (DCs). Latter were subclassed into $CD11b^+$ and $CD11b^-$. RPMs were specifically defined from the MO population as $F4/80^+$, $CD68^+$. MZMs were defined from the MO population as $CD68^-$, $F4/80^{low/-}$, $CD209b^+$. The WPMs were defined as $CD11b^-$, $Ly6C^-$, $SSC\text{-}H^{low}$, $F4/80^-$, $CD68^+$. **B:** Normalized distribution of relative fluorescence intensity (DiD) for defined spleen cell populations (A) representing the uptake behavior of the

investigated cell types for Lip-Dox (DiD/DiR). For both 30 minutes (bright) as 360 minutes (dark) an example is shown for each test group ‘PBS + Lip-Dox (DiD/DiR)‘ (filled), ‘Heparin + Lip-Dox (DiD/DiR)‘ (line), as of the ‘PBS + PBS’ treated control (black line).**C:** *Panel 3***:** The gating strategy for the analysis of B-cells, T-cells and MMMs investigated in D/F and described in section 3.3.3. Dead cells (FVD^+) and doublets were excluded as described in Supplement 5. T-cells were defined by $CD3^+$ and B-cells were defined by $CD3^-$, $CD19^+$. The metallophillic marginal zone macrophages (MMM) are cells expressing $CD169^+$. **D:** see B.

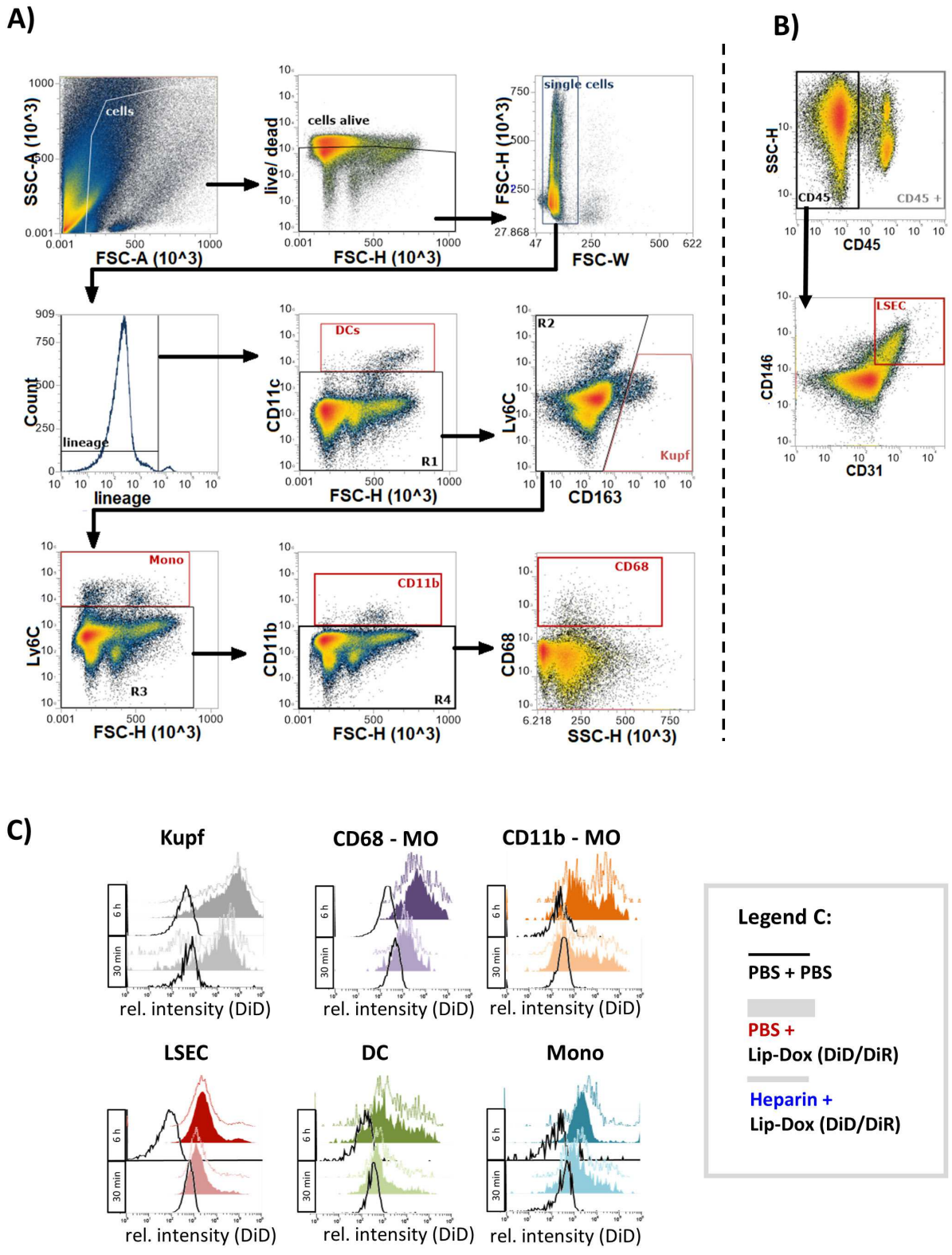

Supplement 7:Panel 4/5, gating strategy for liver cells *in vivo.*

A: *Panel 4:* The gating strategy describes the flow cytometry definition of the liver macrophages investigated in section 3.3.3. E/G and described in Table 24. Dead cells (FVD^+), and doublets were excluded from analysis. Lineage negative cells ($CD49b^-$, $CD3^-$, $Ly6G^-$, $CD19^-$) were sub classed into $CD11c^+$ and $CD11c^-$. First were defined as dendritic cells (DCs). Latter were sub classed into $CD163^+$, which is a sensitive marker for the Kupffer cell population [146]. The $Ly6C^+$, $CD11c^-$, $CD163^-$ cells were defined as monocytes (Mono). Then the remaining population was defined into $CD11b^+$ MO ($CD11b^+$ macrophages) and $CD68^+$ MO ($CD68^+$ macrophages). **B:** *Panel 5:* The gating strategy describes the

flow cytometry definition of the liver sinusoidal endothelia cells (LSECs) investigated in section 3.3.3. E/G and also described in Table 24. Preliminary to the $CD45^+$ subclassification, dead cells (FVD^+) and doubletts were excluded as described in A for panel 4. The LSEC population was defined as $CD45^-$, $CD31^+$, $CD146^+$. **C:** Normalized distribution of relative fluorescence intensity (DiD) for defined spleen cell populations (A) representing the uptake behavior of the investigated cell types for Lip-Dox (DiD/DiR). For both 30 minutes (bright) as 360 minutes (dark) an example is shown for each test group ‘PBS + Lip-Dox (DiD/DiR)‘ (filled), ‘Heparin + Lip-Dox (DiD/DiR)‘ (line), as of the ‘PBS + PBS’ treated control (black line).

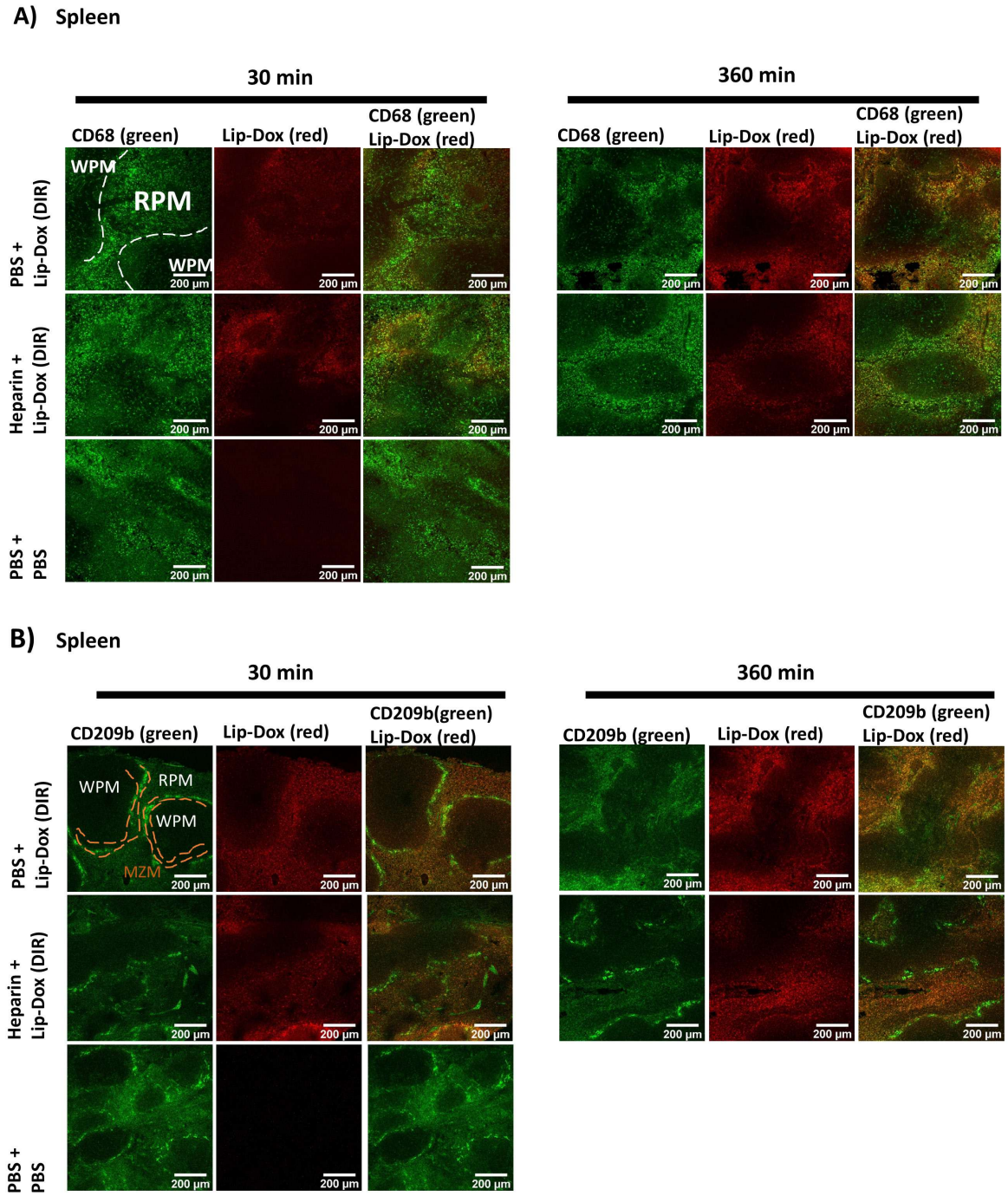

Supplement 8: Structural distribution of Lip-Dox (DiD/DiR) in the spleen.

A: Structural distribution of Lip-Dox (DiD/DiR) in the red pulp (RP) and white pulp (WP) of the spleen. The images are taken with the confocal laser scanning microscope of cryosections and show representative samples of the experimental groups 'PBS + Lip-Dox (DiD/DiR)' and 'Heparin + Lip-Dox (DiD/DiR)' for 30 and 360 minutes. It is shown CD68 (green) and Lip-Dox (DiD/DiR) (red) as well the overlay on the right side. The structures of the spleen can be distinguished: The RP contains a higher density of $CD68^{+}$ macrophages and the WP a lower density. These two zones are sketched in the first quadrant. The 10x objective was used for these images. **B:** Structural distribution of Lip-Dox (DiD/DiR) in the the marginal zone (MZ) of the spleen. The images are taken with the confocal laser canning microscope of cryosections and show representative samples of the experimental groups 'PBS + Lip-Dox (DiD/DiR)' and 'Heparin + Lip-Dox (DiD/DiR)' for 30 and 360 minutes. It is shown CD209b (green) and Lip-Dox (DiD/DiR) (red) as well the overlay on the right side. The CD209b specifically target MZMs in the MZ. The zones are shown as examples in the first quadrant. The 10x objective was used for these images.

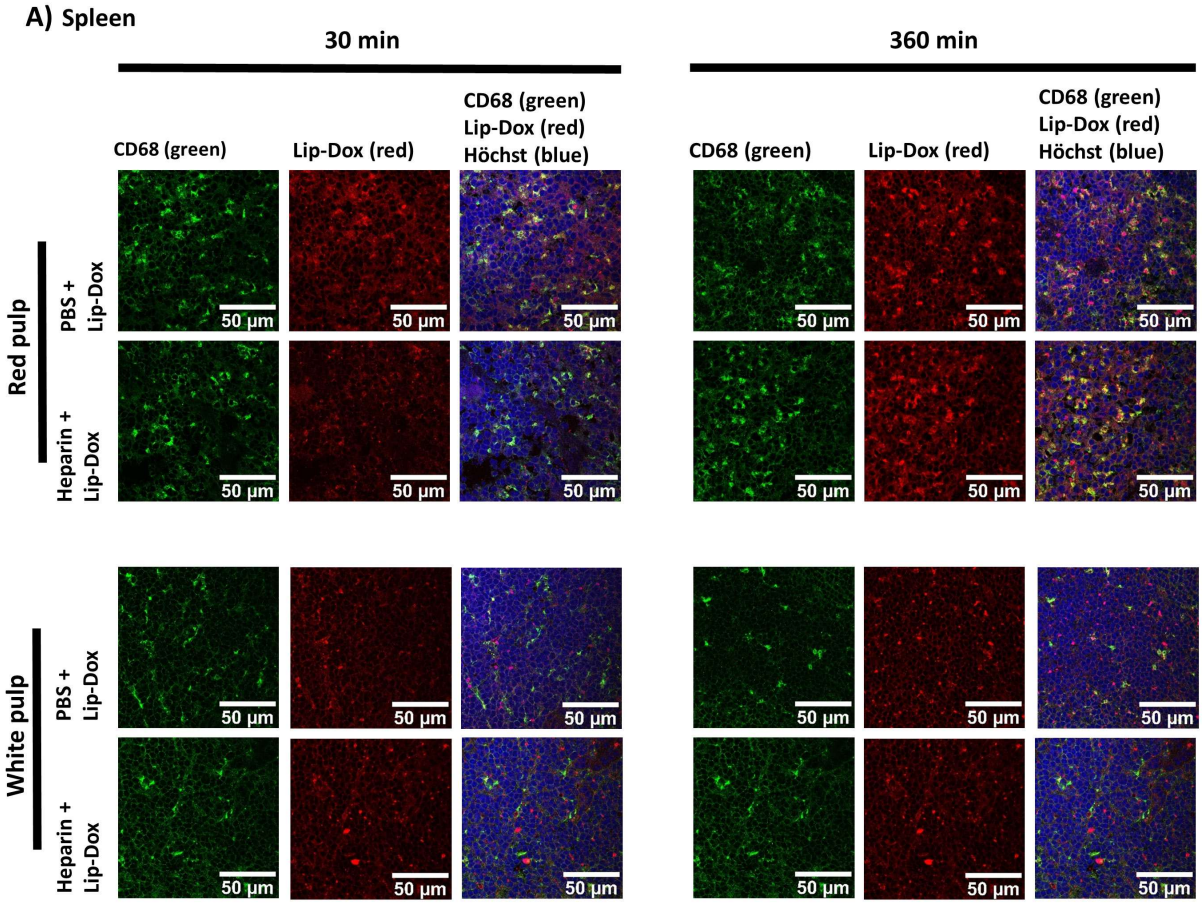

Supplement 9: Co-localization of Lip-Dox (DiD/DiR) with CD68⁺ macrophages in the red pulp and white pulp of the spleen.

A: The images show the localization of Lip-Dox (DiD/DiR) and the CD68⁺ macrophages in RP or in the WP of the spleen. The images are taken with the confocal laser canning microscope of cryosections and show representative samples of the experimental groups 'PBS + Lip-Dox (DiD/DiR)' and 'Heparin + Lip-Dox (DiD/DiR)' for 30 and 360 minutes. It is shown CD68 (green) and Lip-Dox (DiD/DiR) (red) as well the overlay on the right side with Höchst (blue). The 63x oil objective was used for these images.

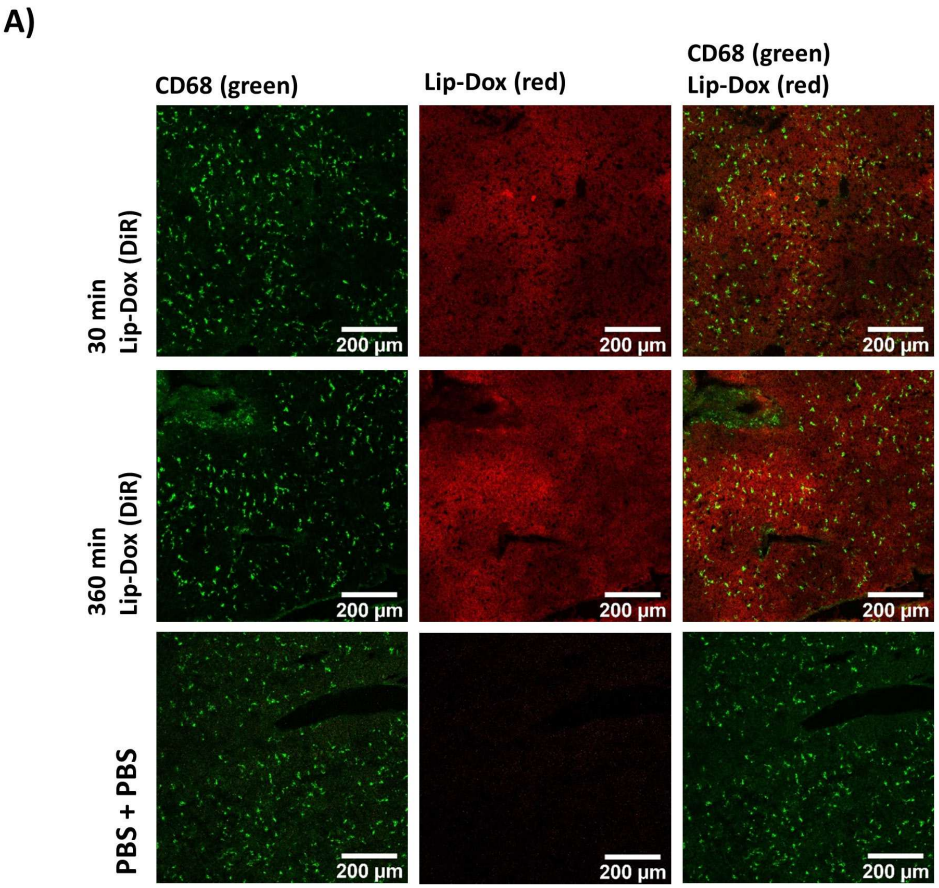

Supplement 10: Distribution of Lip-Dox (DiD/DiR) in the liver.

A: These representative images of CD68⁺ macrophages in the liver, show the distribution of the Lip-Dox (DiD/DiR) in this organ. The images are taken with the confocal laser canning microscope of cryosections and show representative samples of the group 'PBS + Lip-Dox (DiD/DiR)' for 30 and 360 minutes. A sample of ‘PBS + Lip-Dox’ treated animal is shown. The 10x lens was used for these images.

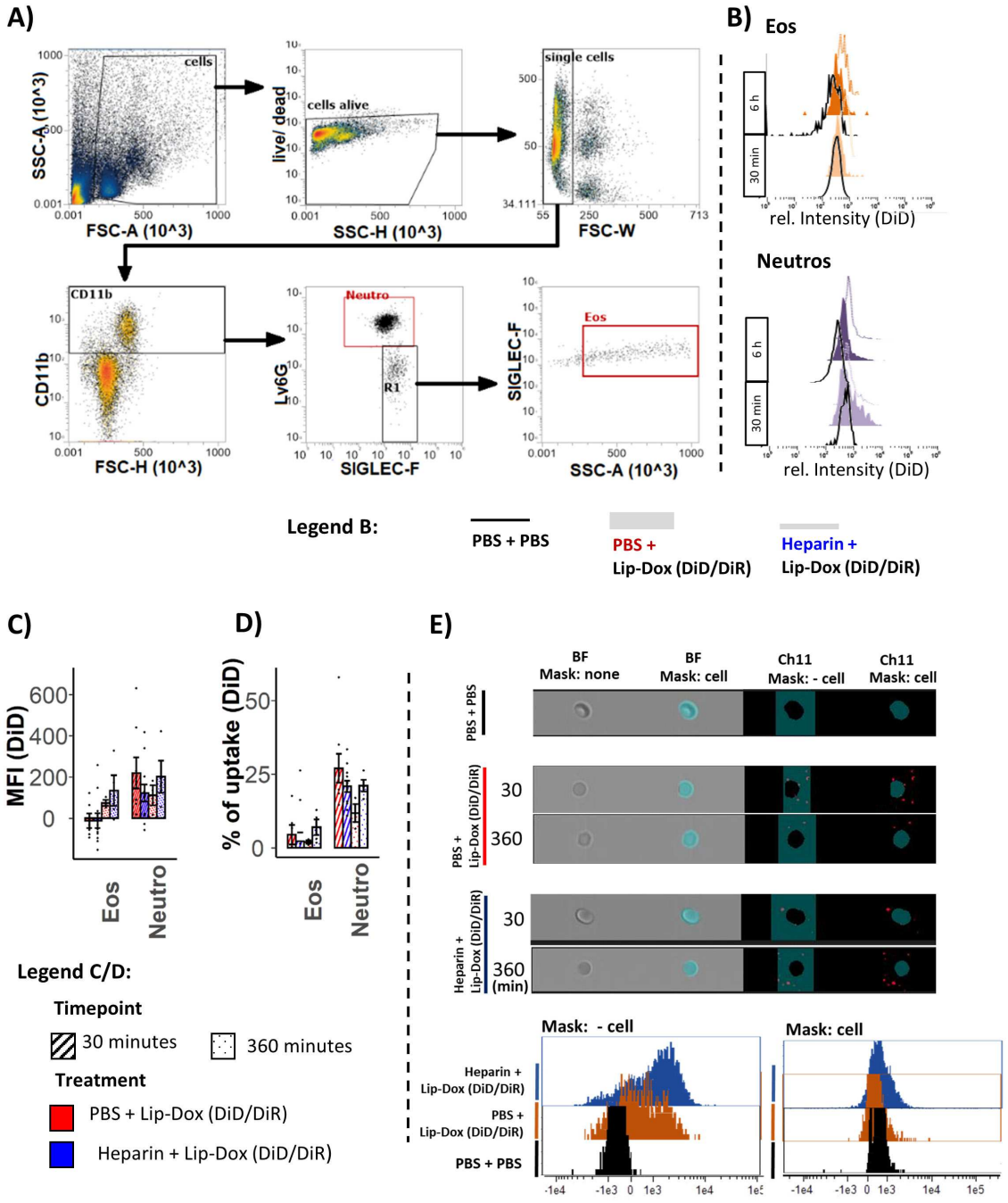

Supplement 11: The effect of i.v. heparinization on Lip-Dox (DiD/DiR) in the blood.

A: Panel 6: The gating strategy for granulocytes of the blood. Dead cells (FVD^+) and doublets were excluded from analysis. A lineage gate has been applied ($CD45R^-$, $CD3^-$, $CD49b^-$). $CD11b^+$ cells were sub classified into $Ly6G^+$ (neutrophils (Neutro)) and $Siglec\text{-}F^+$, SSC-Hhigh (eosinophils (Eos)). **B:** Normalized distribution of relative fluorescence intensity (DiD) for defined blood cells (A) representing the uptake behavior of the investigated cell types for Lip-Dox (DiD/DiR). For both 30 minutes (bright) as 360 minutes (dark) an example is shown for each test group 'PBS + Lip-Dox (DiD/DiR)' (filled), 'Heparin + Lip-Dox (DiD/DiR)' (line), as of the 'PBS + PBS' treated control (black line). **C:** Uptake capacity for Lip-Dox (DiD/DiR) in defined blood cells (see A). Represented is the mean +/- SEM of the MFI (DiD). n = 4-12. **D:** Percentage of cells which are positive for Lip-Dox (DiD/DiR) in blood cells (see A). Represented is the mean +/- SEM of '% of uptake'. n = 4-12. **E:** Amnis image stream acquisition of the blood cells for representative samples. Represented are acquisitions of the brightfield and Ch11 (DiD). Images of a low aspect ratio < 0.5 and area >30 rel. U were defined as blood cells. Masks were created, defining the 'cell' and the area outside the cell '-cell'. The histograms show the measured MFI of DiD for the defined masks.

A)

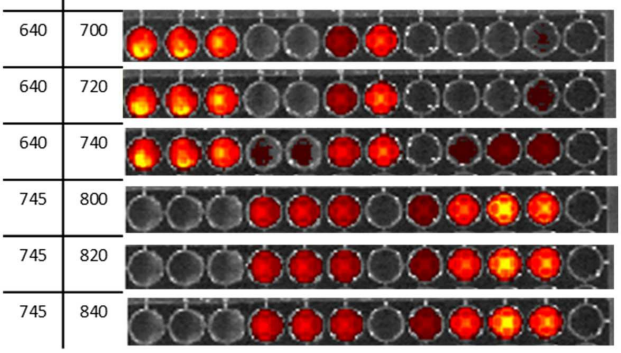

approach	1a	1b	1c	2a	2b	3	4	5	6	7*	8	bg
DiD (mol %)	0.1	0.1	0.1			0.05	0.1	0.1	0.05	0.1	0.05	-
DiR (mol %)				0.1	0.1	0.05		0.3	0.15	0.1	0.05	-

Supplement 12: Finding the optimal concentration of DiD and DiR for the *in vivo* application of Lip-Dox.

A: Different concentrations of DiD and DiR have been incorporated into the formulation of Lip-Dox. The fluorescence intensity was evaluated using the IVIS with the listed filter set compositions. The optimal amount of DiD and DiR in combination was a molar ratio of 0.1: 0.1 (mol-%). The high emission at longer wavelength is favorable for *in vivo* experiments as long wavelength more easily penetrate tissue.

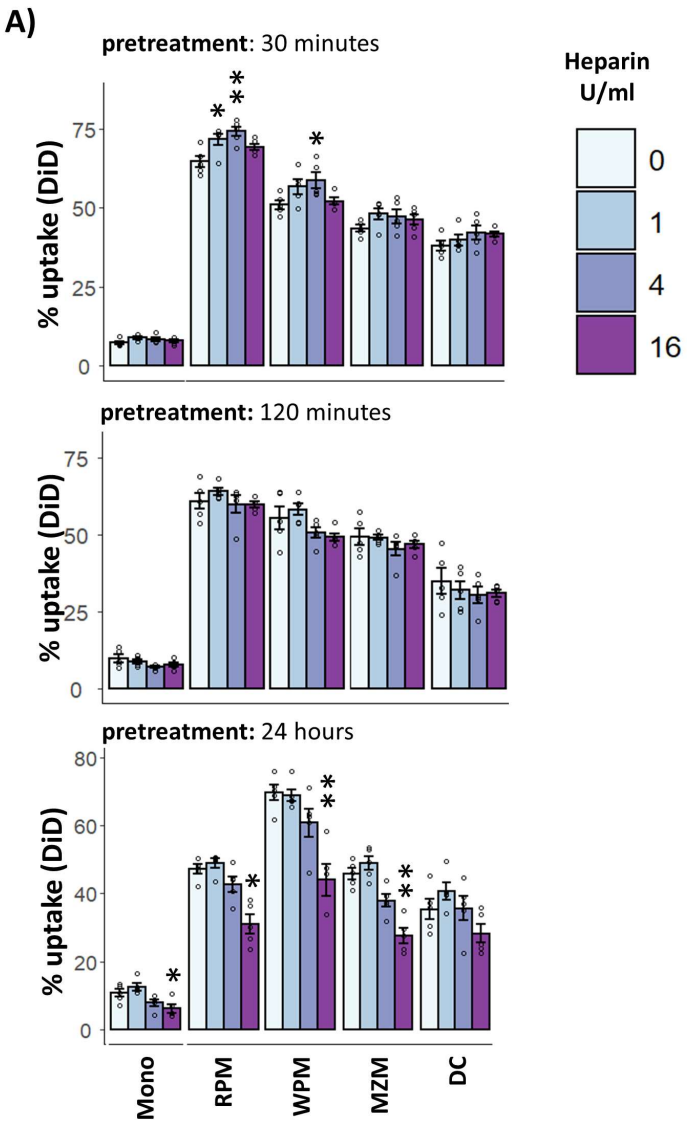

Supplement 13: The effect of heparin pretreatment on uptake of liposomes into RES-cells of the spleen *in vitro.*

A: The uptake of liposomes (DiD) into splenic populations after heparin-pretreatment. Splenoncytes were treated with heparin for 30, 120 minutes and 24 h at concentrations of 0, 1, 4 and 16 U/ml before washing and 2h incubation with liposomes (Lip-Myo (DiD)) (75 µg/ml). The values represent mean +/- SEM of the percent of DiD-positive gated cells. The populations are defined by flow cytometry as described in Supplement 6 and described in Table 23. The control group of 0 U/ml was compared to the other groups of treatment with a Wilcoxen test, p< 0.05 =*, p >0.005 = **. n = 5.

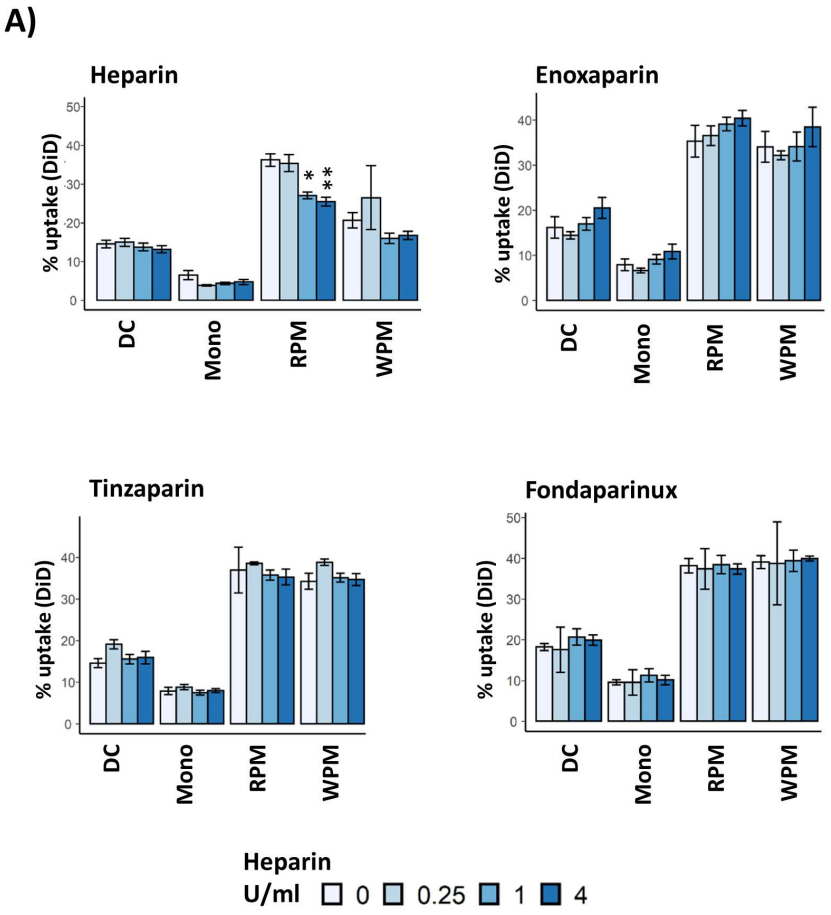

Supplement 14: The effect of LMWHs on uptake of Lip-Dox (DiD) into into RES-cells of the spleen *in vitro.*

A: Splenoncytes were treated with heparin, enoxaparin, tinzaparin and fondaparinux to final concentrations of 0, 0.25, 1 and 4 U/ml while incubation with liposomes (75µg/ml) for 2h. The values represent mean +/- SEM of the percent of DiD-positive cells within each population. Of each value the background value of the untreated background control was subtracted. The populations were defined by flow cytometry as described in Supplement 6 and described in Table 24. The control group of 0 U/ml was compared to the other groups of treatment with wilkoxen test, $p < 0.05$ = *, $p > 0.005$ = **. n = 5. The data on Lip-Myo (DiD) (not shown) confirmed as well, the strongest decrease of uptake in presence of the UFH.

9.2 Supplements Chapter 2

Table 27: Overview on physicochemical properties of PS-particles.

	Batch	Diameter nm	SD nm	ζ-potential mV
PS-NH_2 (BP)	1	138	5.46	-53.17
PS-COOH (BP)	1	128	8.78	53.23

Values were obtained as described in 8.1.6.1. Particles were solved in H_2O.

Table 28: Surface charge of heparin-coated PS-particles.

		ζ-potential [mV]				
	Heparin [U/ml]	0	0.25	1	4	untreated§
PS-COOH (BP)	ø	-22.92	-22.70	-24.28	-24.72	-53.17
	batch 1	-23.40	-23.13	-23.77	-24.63	
	batch 2	-22.43	-22.27	-25.50	-24.83	
	batch 3	NA	NA	-23.57	-24.70	
PS-NH_2 (BP)	ø	21.10	-22.98	-24.02	-23.20	53.23
	batch 1	-19.13	-21.07	-23.37	-24.00	
	batch 2	-21.00	-23.63	-25.00	-24.53	
	batch 3	-23.17	-24.23	-23.70	-21.07	

ζ -potential of PS-particles coated with the same culture medium as in the *in vitro* uptake experiments in chapter 2 (see 4.3.1) as described in 8.1.6.1. §Values are copied from Table 27.

Table 29: Overview on physicochemical properties of OVA-NC.

	Experiment	Batch	size [nm]	SD [nm]	ζ-potential [mV]
OVA-NC (Cy5)	*in vitro*	1	317	141.00	-28.77
		2	309	132.00	-28.33
		3	311	143.00	-28.73
		ø	312	138.67	-28.61
PEG-OVA-NC (Cy5)	*in vitro*	1	313	167.00	-29.13
		2	312	151.00	-29.93
		3	382	209.00	-22.83
		ø	336	175.67	-27.30
OVA-NC (Cy5)	30 minutes (*in vivo*)	1	315	78.67	NA
	360 minutes (*in vivo*)	1	170	23.55	NA

Values were obtained as described in 8.1.6.1. Particles were solved in PBS.

Table 30: Surface charge of heparin-coated OVA-NC (Cy5).

	ζ-potential [mV]				
Heparin [U/ml]	**0**	**0.25**	**1**	**4**	untreated§
ø	**-27.59**	**-30.83**	**-27.86**	**-25.3**	-28.61
batch 1	-24.07	NA	-25.23	-28.13	-28.77
batch 2	-30.00	-30.90	-27.33	-21.67	-28.33
batch 3	-28.70	-30.77	-31.00	-26.10	-28.73

ζ -potential of OVA-NC coated with the same culture medium as in the *in vitro* uptake experiments in chapter 2 (see 4.3.2) as described in 8.1.6.1. § Values are copied from Table 29

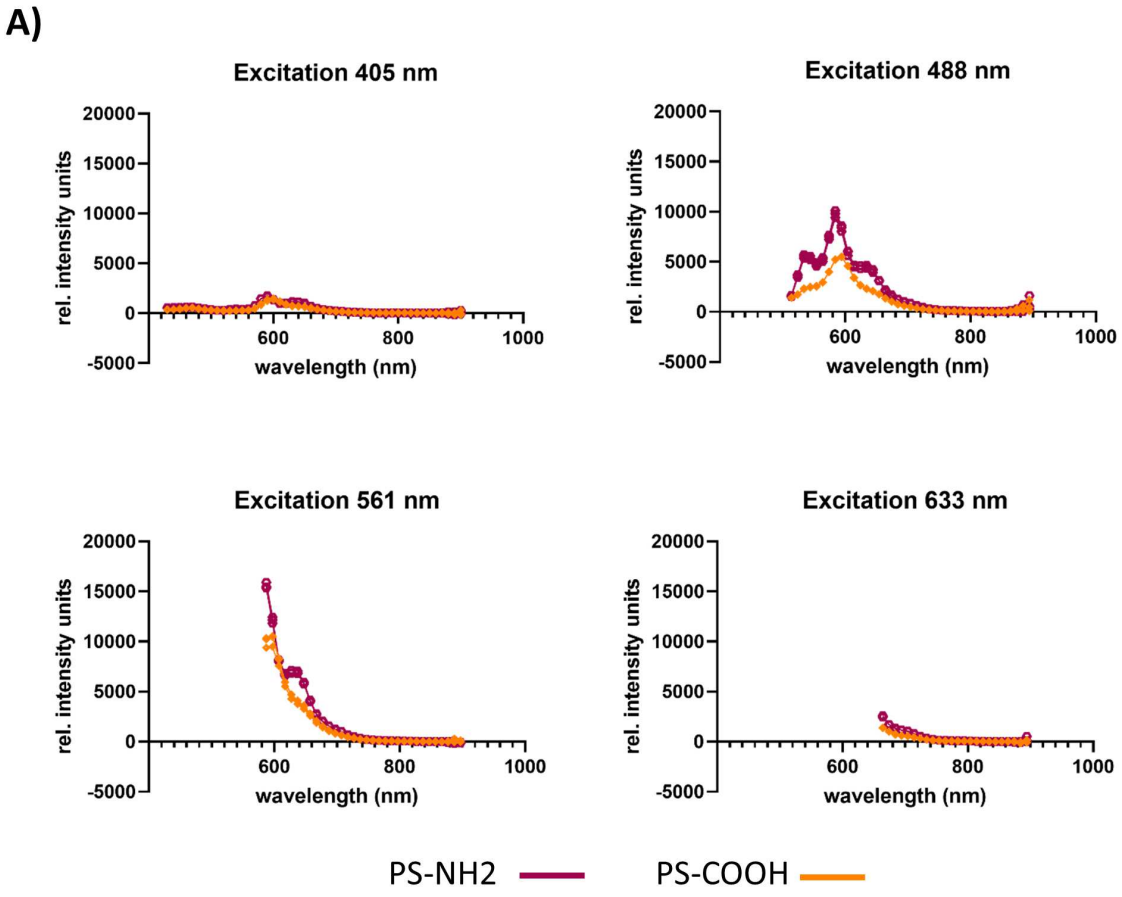

Supplement 15: Fluorescence emission spectra of PS-NH_2 (BP) and PS-COOH (BP).

A: The equally diluted particles PS-NH_2 (BP) (pink) and PS-COOH (BP) (orange) were excited at four different wavelengths (405 nm, 488 nm, 661 nm and 633 nm), which are relevant for the flow cytometer studies.

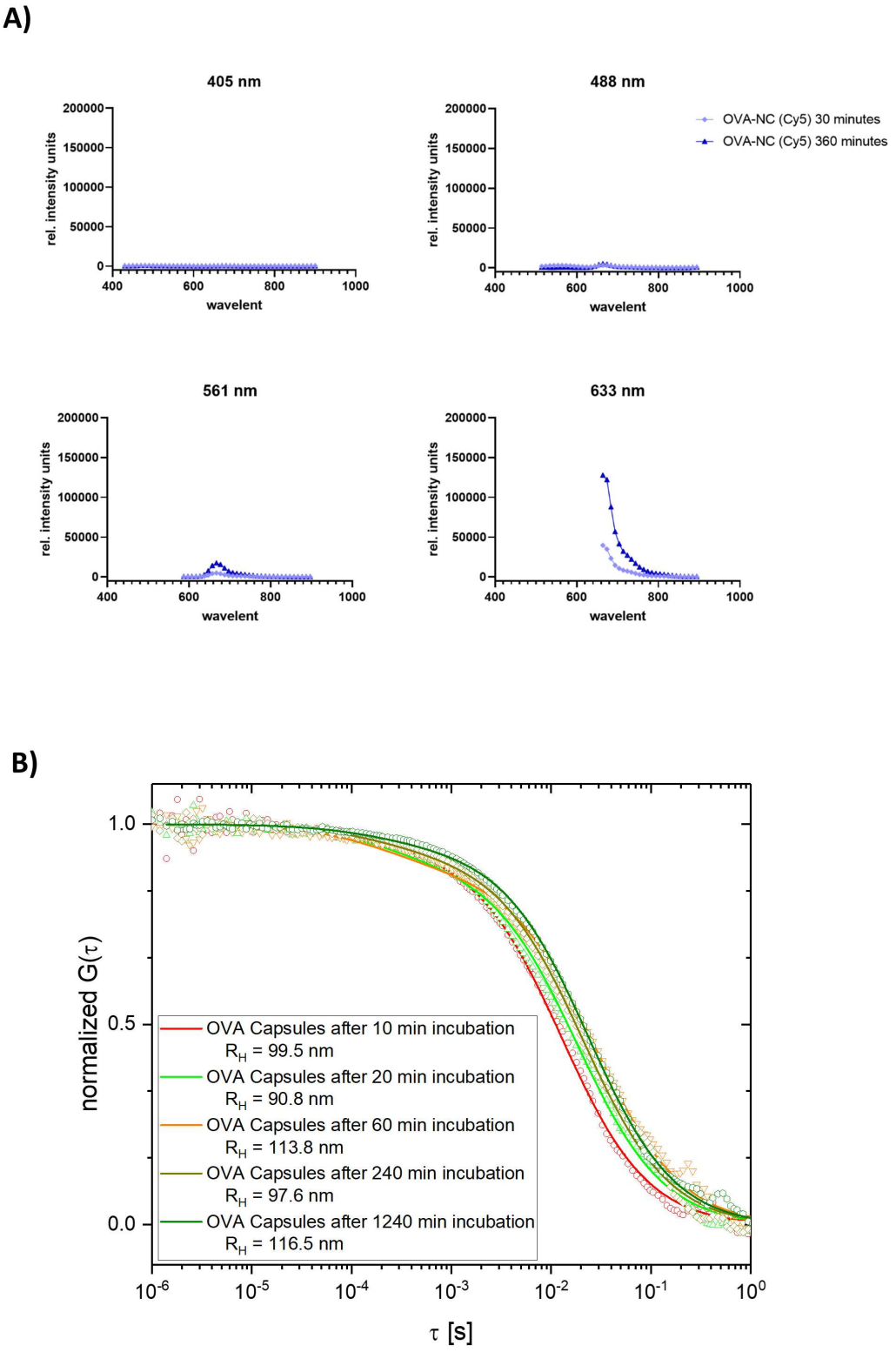

Supplement 16: Characterization of OVA-NC (Cy5) *in vivo* experiment.

A: The equally diluted OVA-NC (Cy5) were excited at four different wavelengths (405 nm, 488 nm, 661 nm and 633 nm), which are relevant for the flow cytometer studies. Encapsulation efficiency turned out higher for the batch at 360 minutes. **B:** FCCS of OVA-NC (Cy5) (360 minutes *in vivo* experiment). Represented is the normalized G(τ) for OVA-NC with encapsulated Oligo-Cy5. Capsules were incubated in 100% mouse plasm for different time points (10 – 1240 minutes).[46]

[46] Provided by [redacted] group of Dr. [redacted] Max Planck Institute for Polymer Research.

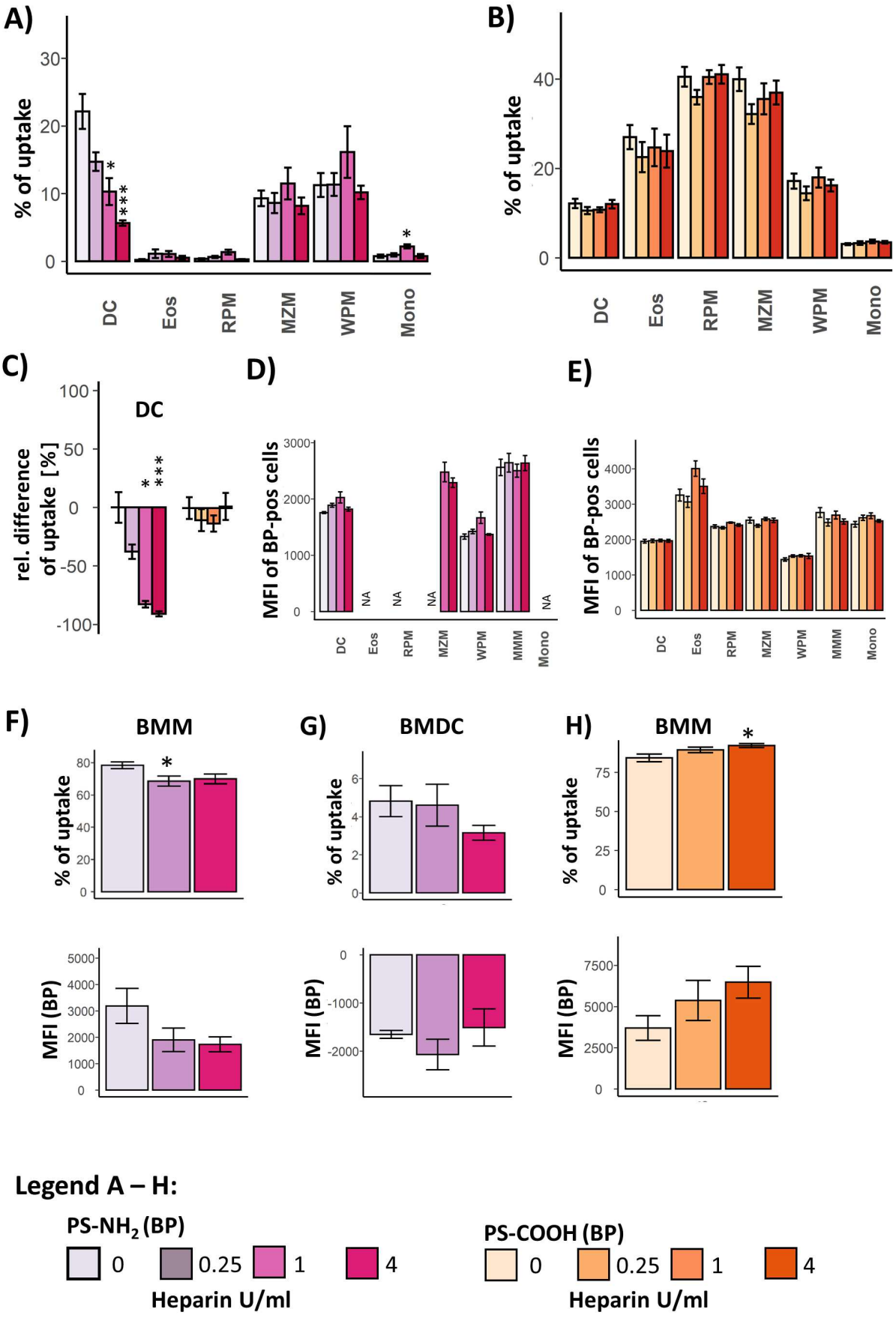

Supplement 17: Heparin selectively reduces the uptake into DCs of PS-NH_2.

The setup described in Figure 19 was used and populations of interest were defined according to Table 23. **A/B:** The uptake of particles A) PS-NH_2+ B) PS-COOH into splenocytes when cultured in presence of heparin (0 – 4 U/ml). Represented is the mean +/- SEM of "% of uptake". The test groups were compared to the control group by Wilcoxen tests $p < 0.05$ = *, n = 5-7, batches = 1. **C:** The graph represents the normalized difference of "% of uptake" of BP towards the control group (0 U/ml) of the DC population. Represented is the mean +/- SEM. The relative difference was calculated from the values in A/B. **D/E:** The MFI (BP) of D) PS-NH_2- E) PS-COOH positive cells in presence of heparin (0 – 4 U/ml). Represented is the mean +/- SEM of the cells positive for BP within the specifically defined spleen cell populations. The test groups were compared to the control group by Wilcoxen tests $p < 0.05$ = *.**F/G:** The uptake of PS-NH_2 into F) BMMs G) BMDCs when cultured in presence of heparin (0 – 4 U/ml). Top: Represented is the mean +/- SEM of the "% of uptake". Bottom: Represented is the mean +/- SEM of the MFI of BP. The test groups were compared to the control group by Wilcoxen tests $p < 0.05$ = *, n = 4, batches = 1. **H:** The uptake of PS-COOH into BMMs when cultured in presence of heparin (0 – 4 U/ml). Top: Represented is the mean +/- SEM of the "% of uptake". Bottom: Represented is the mean +/- SEM of the MFI of BP. The test groups were compared to the control group by Wilcoxen tests $p < 0.05$ = *, n = 4, batches = 1.

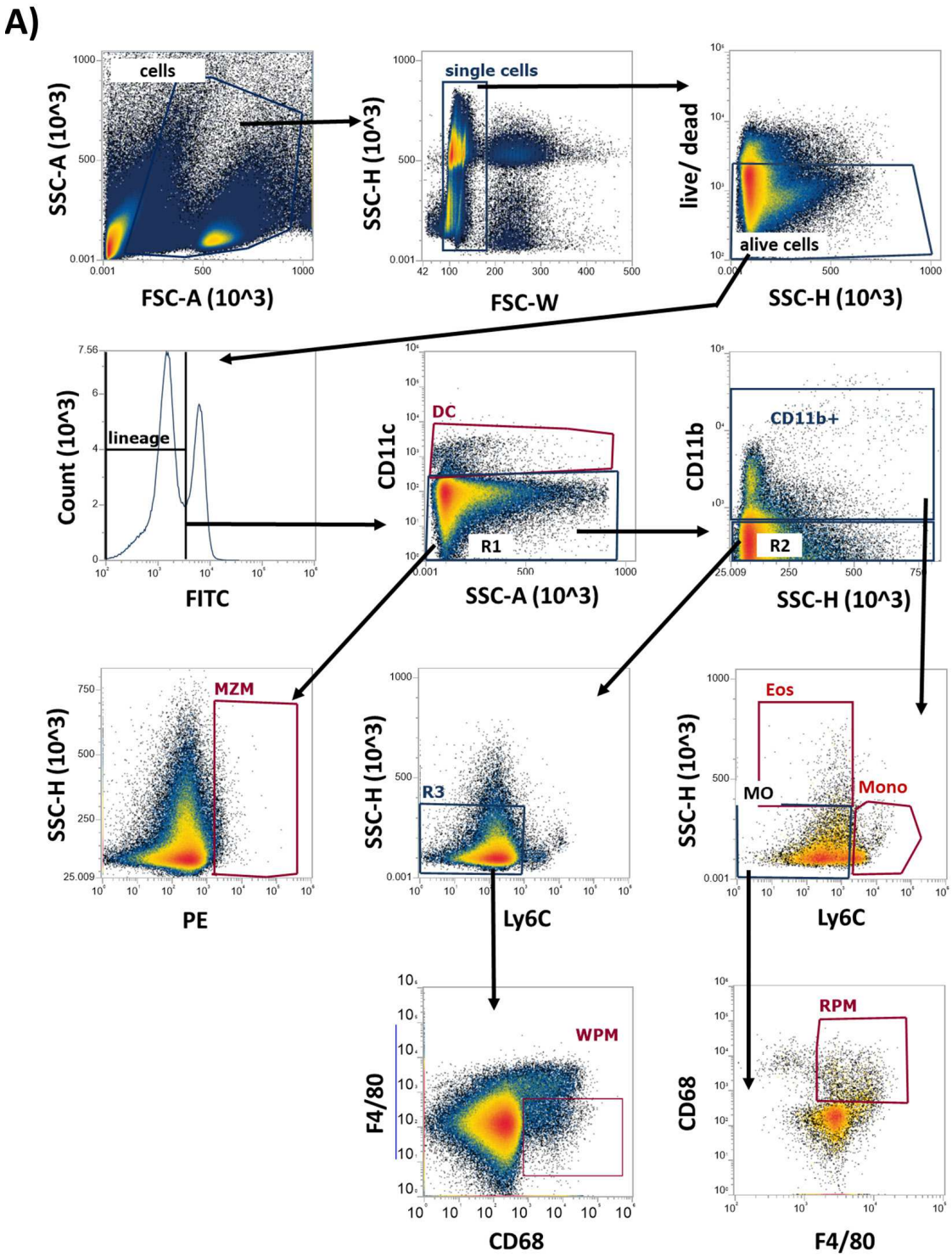

Supplement 18: *Panel 2*, flow cytometry gating strategy for RES-cells of the spleen (*in vitro* experiments) on BP labelled PS-particles.

A: *Panel 2:* The gating strategy describes the flow cytometry definition of the spleen cell populations investigated in Figure 19 and Supplement 17. Lineage negative cells ($CD49b^-$, $CD3^-$) were classified into $CD11c^+$ and $CD11c^-$. First were defined as DCs. $CD11b^+$ and CD11b. The $CD11b^+$, $Ly6C^+$, SSC-H^{low} were defined as monocytes (Mono). $CD11b^+$, $Ly6C^-$, SSC-H^{low}, were defined as macrophages (MO). The $Ly6C^{low}$, SSC-H^{high} cells were defined as eosinophils (Eos). Then Red pulp macrophages (RPM) were specifically defined from the MO population as $F4/80^+$, $CD68^+$. Marginal zone macrophages (MZM) were defined from the MO population as $CD68^-$, $F4/80^{low/-}$, $CD209b^+$. The white pulp macrophages (WPM) were defined as $CD11b^-$, $Ly6C^-$, SSC-H^{low}, $F4/80^-$, $CD68^+$.

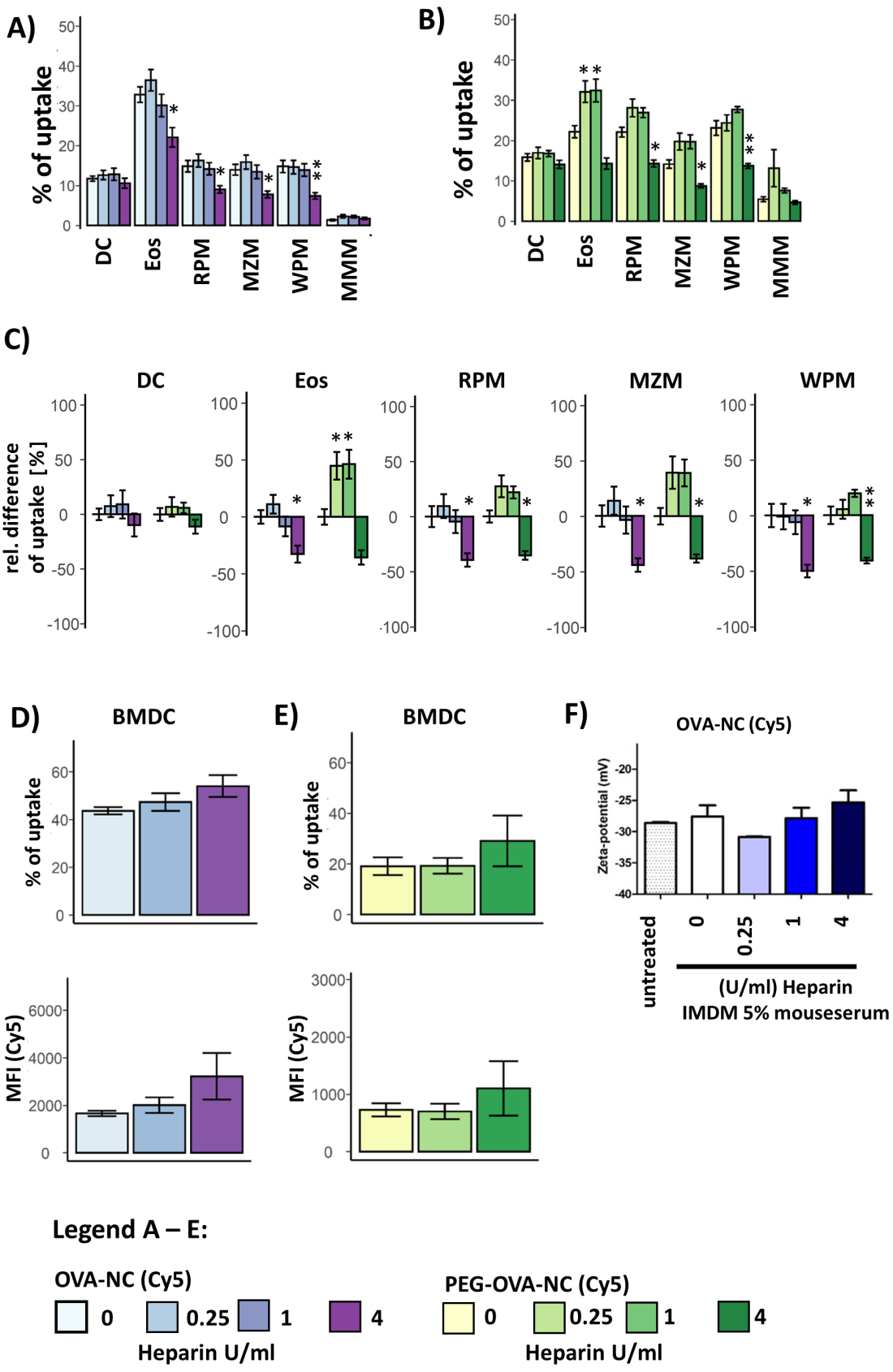

Supplement 19: Presence of heparin favors cellular distribution of OVA-NC (Cy5) and PEG-OVA-NC (Cy5) towards DCs.

A/B: The uptake of particles A) OVA-NC (Cy5) B) PEG-OVA-NC (Cy5) into splenocytes when cultured in presence of heparin (0 – 4 U/ml). Represented is the mean +/- SEM of “% of uptake”. The test groups were compared to the control group by Wilcoxen tests $p < 0.05 = *$, $n = 9$, batches = 3. **C:** The graph represents the normalized difference of “% of uptake” of OVA-NC (Cy5) and PEG-OVA-NC (Cy5) towards the control group (0 U/ml) Represented is the mean +/- SEM. The relative difference was calculated from the values in A/B. **D/E:** The uptake of D) OVA-NC (Cy5) and E) PEG-OVA-NC (Cy5) into BMDCs. Top: Represented is the mean +/- SEM of the “% of uptake” for Cy5. Bottom: Represented is the mean +/- SEM of the MFI of Cy5. The test groups were compared to the control group by Wilcoxen tests $p < 0.05 = *$, $n = 5$, batches = 1. **F:** Zetapotential of OVA-NC (Cy5) coated in 5% mouse serum IMDM and heparin. The control group (0 U/ml) was compared with the heparin treated groups by Wilkoxen tests. $p < 0.05 = *$, $n = 3$, batches = 1.

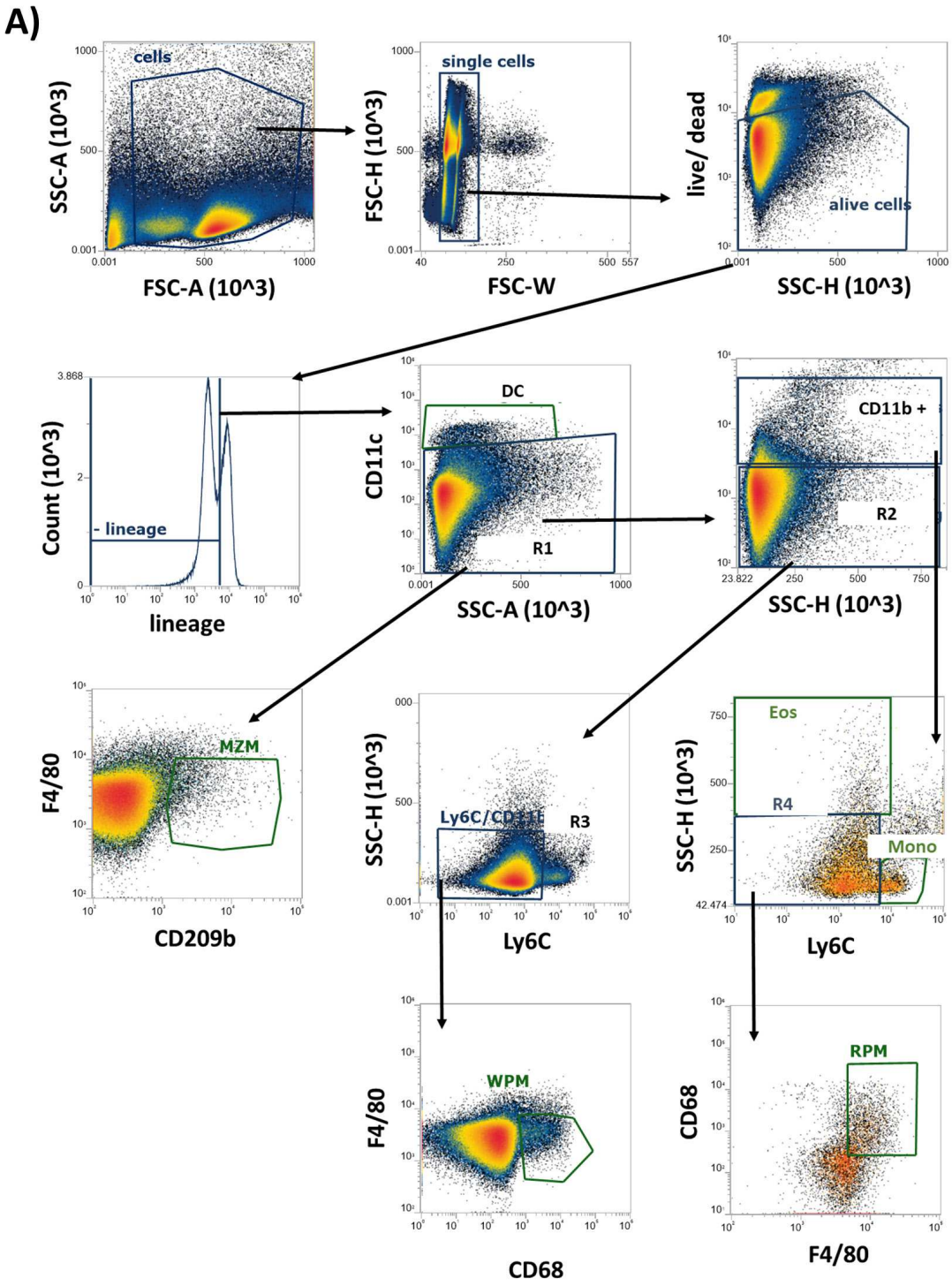

- The figure proceeds on the next page -

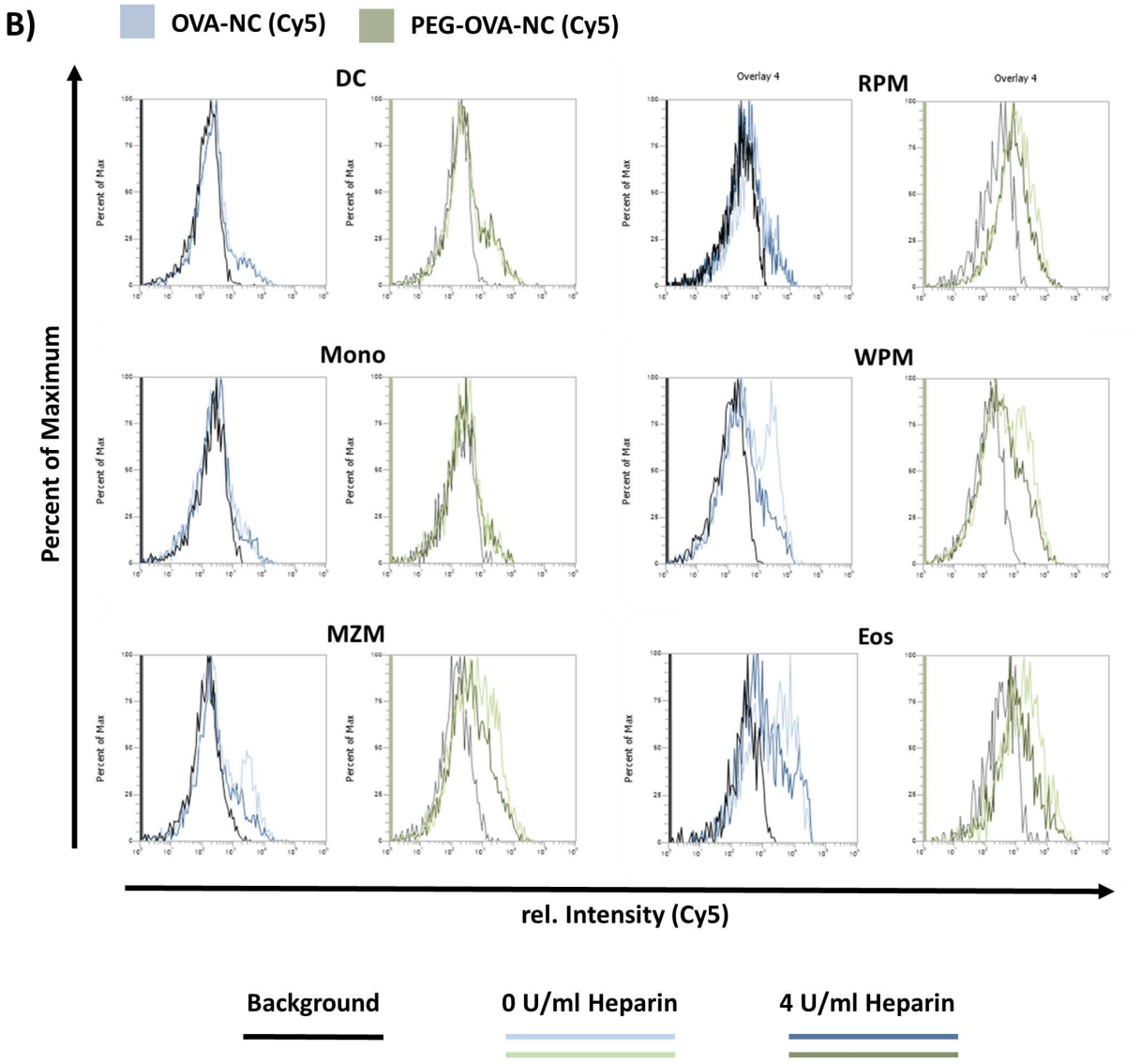

Supplement 20: *Panel 2*, flow cytometry gating strategy for RES-cells of the spleen (*in vitro* experiments) on OVA-NC (Cy5) and PEG-OVA-NC (Cy5).

A: *Panel 2:* The gating strategy describes the flow-cytometry definition of the spleen cell populations investigated in Figure 20 and Supplement 19. Lineage negative cells ($CD49b^-$, $CD3^-$) were classified into $CD11c^+$ and $CD11c^-$. First were defined as DCs. $CD11b^+$ and CD11b. The $CD11b^+$, $Ly6C^+$, SSC-H^{low} were defined as monocytes (Mono). $CD11b^+$, $Ly6C^-$, SSC-H^{low}, were defined as macrophages (MO). The $Ly6C^{low}$, SSC-H^{high} cells were defined as eosinophils (Eos). Red pulp macrophages (RPM) were specifically defined from the MO population as $F4/80^+$, $CD68^+$. Marginal zone macrophages (MZM) were defined from the MO population as $CD68^-$, $F4/80^{low/-}$, $CD209b^+$. The white pulp macrophages (WPM) were defined as $CD11b^-$, $Ly6C^-$, SSC-H^{low}, $F4/80^-$, $CD68^+$. **B:** Relative Cy5 intensity distribution for defined spleen cell populations (A). The overlay represents the normalized intensity distribution curve measured with the channel 'RL1-H' for OVA-NC (Cy5) (blue), PEG-OVA-NC (Cy5) (green) and an untreated control (black). For the conditions of 0 U/ml and 4 U/ml, a representative sample was selected.

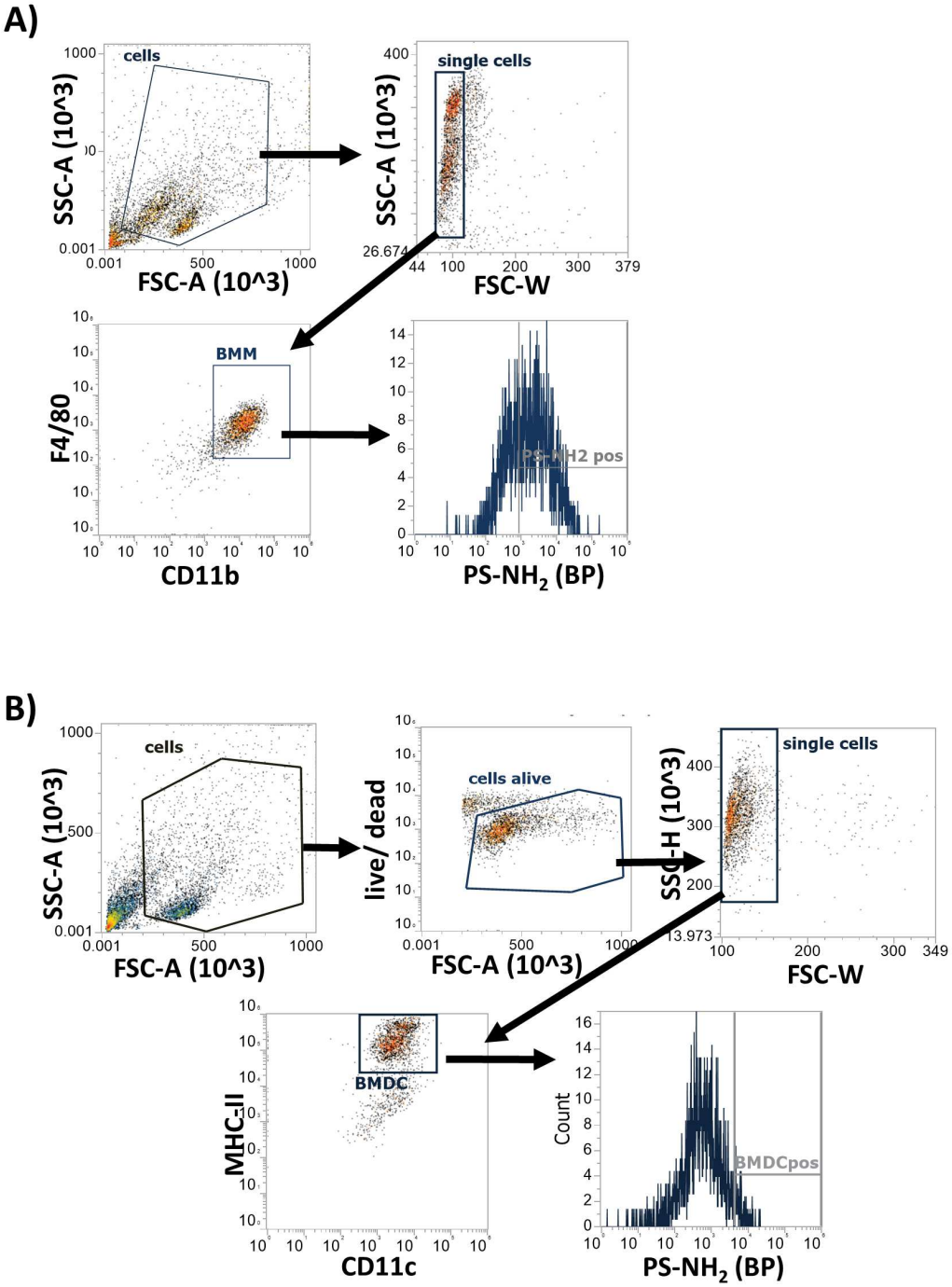

Supplement 21: Flowcytometry definition of BMMs and BMDCs.

A: Definition of BMMs. The gating strategy describes the flow cytometry definition of the BMMs investigated in Supplement 17. Dead cells (FVD^+) and doublets were excluded from analysis. Further BMMs were defined by expression of F4/80 (eFluor 450, VL1-H) and CD11b (FITC, BL1-H). The Intensity of BP was measured in the 'YL-2' channel. **B:** Definition of BMDCs. The gating strategy describes the flow-cytometry definition of the BMDCs investigated in Supplement 17(and Supplement 19). Dead cells (FVD^+) and doublets were excluded from analysis. BMDCs were defined by expression of MHCII (eFluor 450, VL1-H) and CD11c (FITC, BL1-H). The Intensity of BP (and Cy5 – not represented) was measured in the 'YL2-H' channel. The intensity of Cy5 (Supplement 19) in the 'RL1-H' channel.

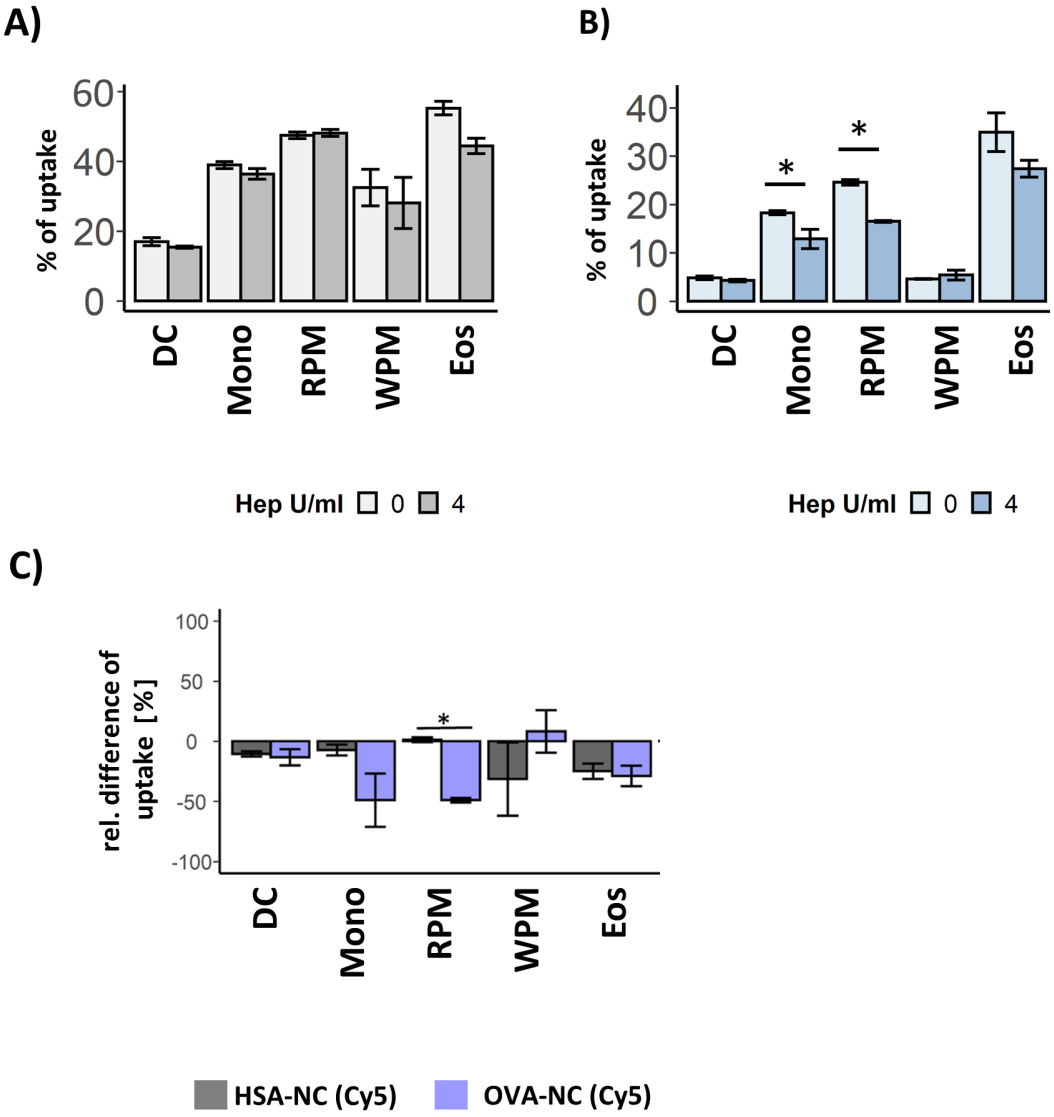

Supplement 22: Cellular uptake of HSA-NC (Cy5) and OVA-NC (Cy5) in presence of heparin.

For this experiments the setup described in Figure 19 was used and populations of interest were defined according to Table 23. The panel is equivalent to Supplement 20 A, without CD209b.**A/B:** The uptake of A) HSA-NC (Cy5) and B) OVA-NC (Cy5) into splenocytes when cultured in presence of heparin (4 U/ml). Represented is the mean +/- SEM of "% of uptake". The groups were compared by Wilcoxen tests. $p < 0.05$ = *, n =3, batches =1. **C:** The graph represents the mean +/- SEM of the normalized difference of the '% of uptake (Cy5)' of heparin treated groups towards the control group (0 U/ml) of HSA-NC (Cy5) (grey) and OVA-NC (Cy5) (blue). The relative difference was calculated from '% of uptake (Cy5)' values in A/B. The groups were compared by Wilcoxen tests. $p < 0.05$ = *, n =3, batch =1.

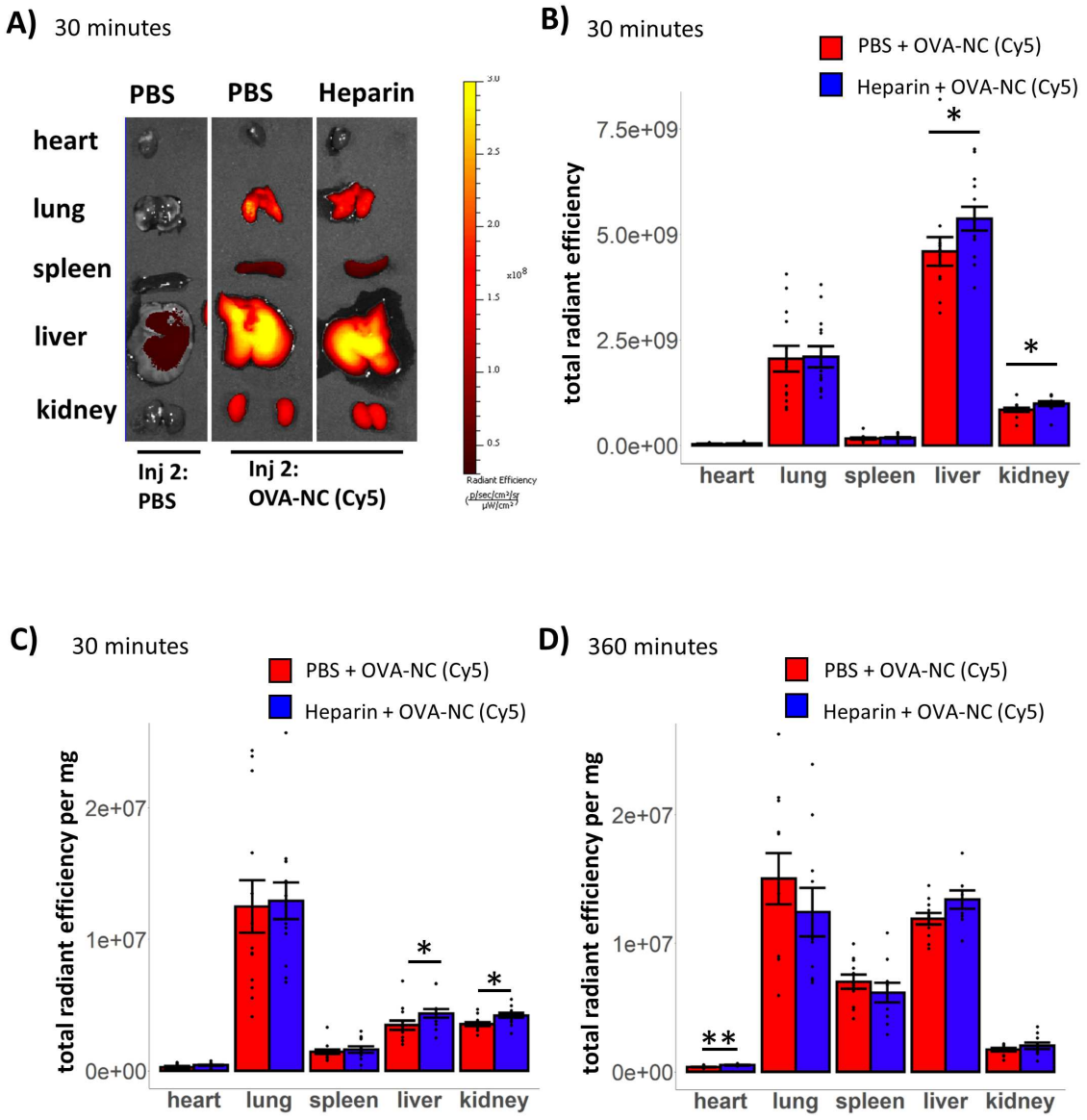

Supplement 23: Organ distribution of OVA-NC (Cy5) in heparinized mice.

A: IVIS-acquisitions of the organs of a representative animal at 30 minutes. The heatmap indicates the values of the total radiant efficiency of Cy5. **B:** Mean +/- SEM of the total radiant efficiency of Cy5 of heart, lung, spleen, liver and kidney at 30 minutes. n = 13/13. **C:** Mean +/- SEM of the OVA-NC (Cy5) organ density at 30 minutes. n = 11/10. **D:** Mean +/- SEM of the OVA-NC (Cy5) organ density at 360 minutes. n = 13/13. B-D: The two groups were compared by a Wilcoxon test for each organ, $p < 0.05$ = *.

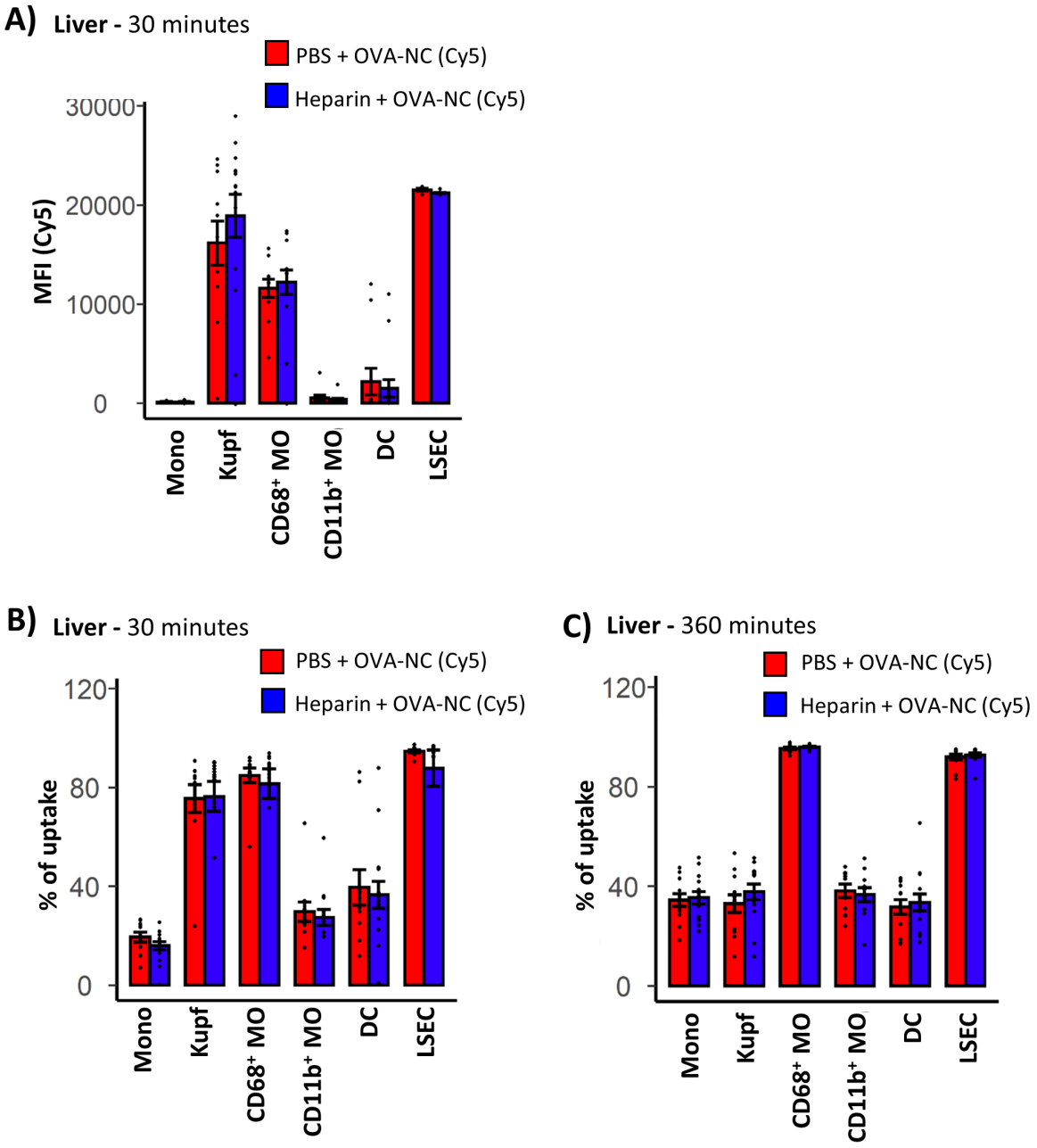

Supplement 24: Cellular uptake of OVA-NC (Cy5) in liver cells of heparinized mice.

A: The graph represents the mean +/- SEM of the MFI of Cy5 for defined populations of the liver at 360 min. From all values, the mean of an untreated control was subtracted. n = 11-15. **B/C:** The graph represents mean +/- SEM of the percent of cells, which are positive for Cy5 for defined populations of the liver at B) 30 min (n = 11-15) and C) 360 min (n = 11-13). A-C: The two groups were compared by a Wilcoxon test for each organ, $p < 0.05$ = *.

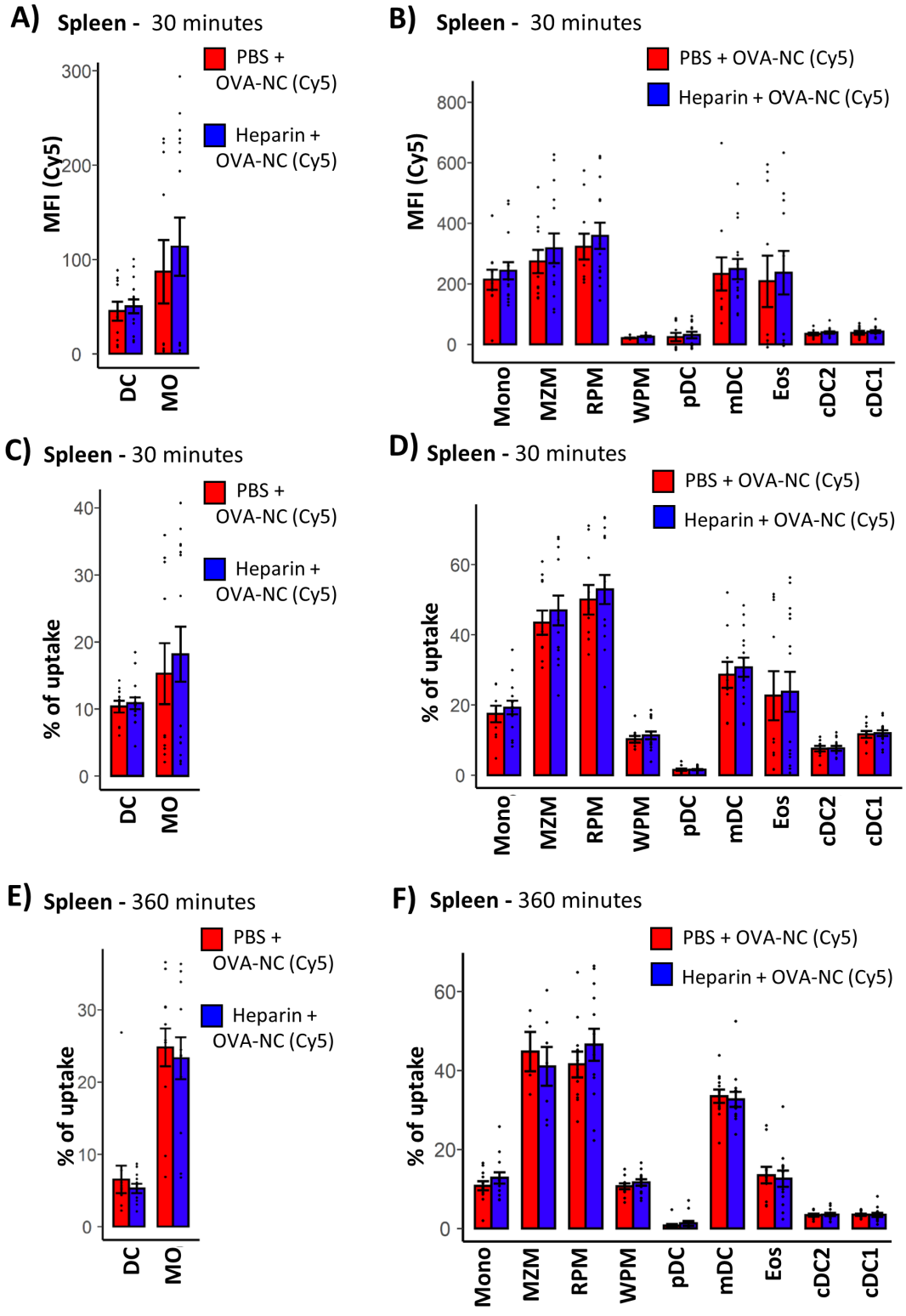

Supplement 25: Cellular uptake of OVA-NC (Cy5) into splenocytes in heparinized mice.

A: The graph represents mean +/- SEM of the MFI of Cy5 of DCs and MOs of the spleen at 30 min. n = 10-15. **B:** The graph represents mean +/- SEM of the MFI (Cy5) for defined populations of the spleen at 30 min. n = 11-14. **C:** The graph represents mean +/- SEM of "% of uptake" of the group of DCs and MOs in the spleen at 30 min. n = 10-15. **D:** The graph represents mean +/- SEM of "% of uptake" for defined populations of the spleen at 30 min. n = 10-15. **E:** The graph represents mean +/- SEM of "% of uptake" of the group of DCs and MOs in the spleen at 360 min. n = 12. **F:** The graph represents mean +/- SEM of "% of uptake" for defined populations of the spleen at 30 min. at 360 min. n = 11-13. A-F: The two groups were compared by a Wilcoxon test for each organ, $p < 0.05$ = *.

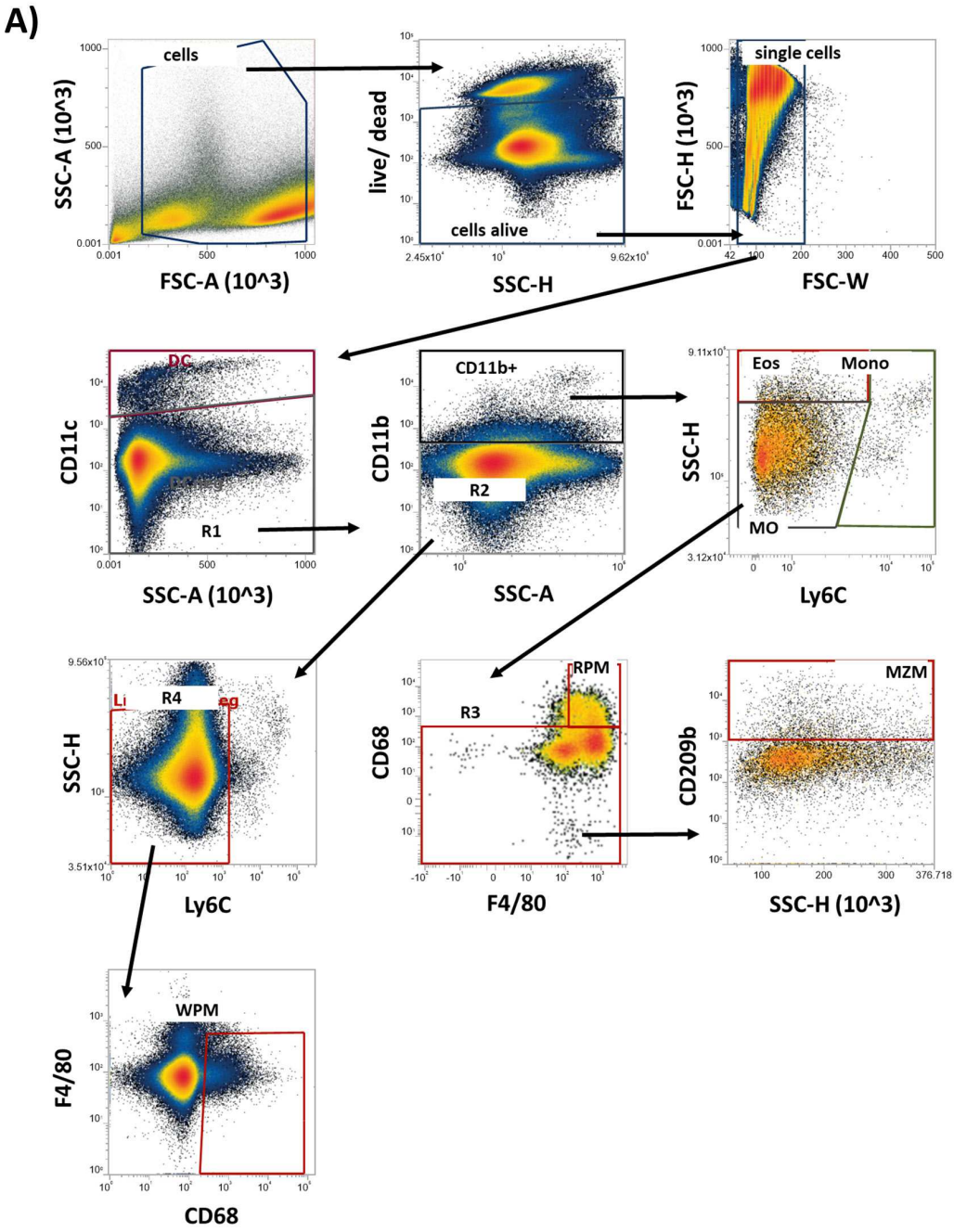

- The figure proceeds on the next page -

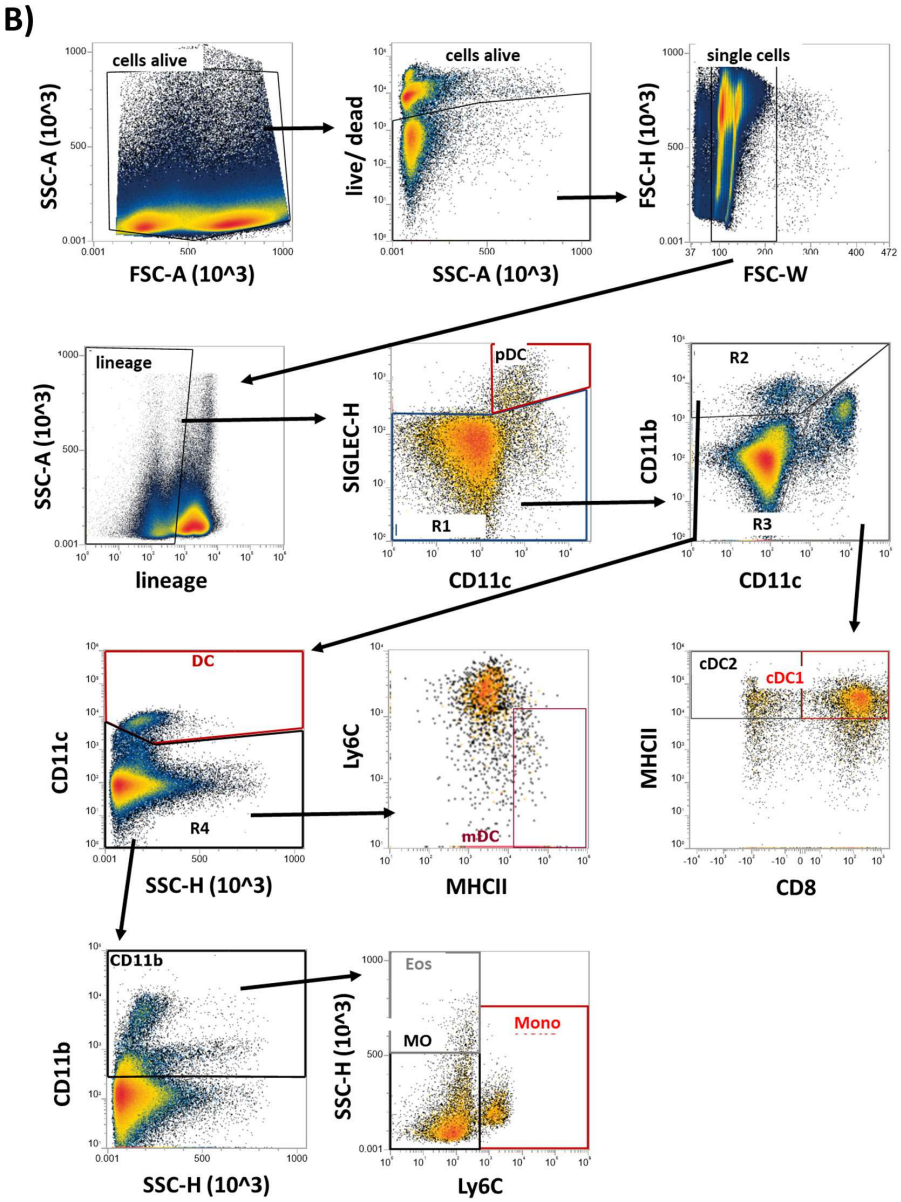

Supplement 26: Flow cytometry gating strategy for RES-cells of the spleen (*in vivo* experiments).

A: *Panel 1,* The gating strategy describes the flow cytometric definition of the spleen cell populations investigated in Figure 22C/D, Supplement 25. Dead cells (FVD$^+$) and doublets were excluded from analysis as described in Supplement 5. Lineage negative cells (CD49b$^-$, CD3$^-$, Ly6G$^-$) were subclassed into CD11c$^+$ and CD11c$^-$. First were defined as DCs. Latter were subclassed into CD11b$^+$ and CD11b$^-$. Red pulp macrophages (RPM) were specifically defined from the MO population as F4/80$^+$, CD68$^+$. Marginal zone macrophages (MZM) were defined from the MO population as CD68$^-$, F4/80$^{low/-}$, CD209b$^+$. The white pulp macrophages (WPM) were defined as CD11b$^-$, Ly6C$^-$, SSC-H^{low}, F4/80$^-$, CD68$^+$. **B:** *Panel 2,* Gating strategy for definition of DC populations. The gating strategy describes the flow cytometry definition of the spleen cell populations investigated in Figure 22C/D, Supplement 25. Dead cells (FVD$^+$) and doublets were excluded from analysis. Lineage negative cells (CD49b$^-$/ Ly6G$^-$/ CD19$^-$/ CD3$^-$) were applied against SIGLEC-H and CD11c. The pDCs were defined as SIGLEC-H$^+$, CD11c$^+$. The SIGLEC-H$^-$ cells were applied against CD11c and CD11b. The CD11c positive, CD11b$^{low/-}$ cells were specified into conventional DCs type 1 and 2 (cDC1, cDC2) by CD8 and MHCII. The CD11b$^+$, CD11c$^{low/-}$ population was then specified into monocyte derived DCs by Ly6C and MHCII. The analysis of the general spleen cell populations, MO, DC, CD11b$^+$, Mono and Eos: first dead cells (FVD$^+$), doublets and cells expressing lineage markers (CD49b/ CD3/ CD19 and Ly6G) were excluded from further analysis. CD11c+ cells were defined as DCs. CD11c- cells were defined into CD11b$^+$ cells. Subsequently MO were characterized as CD11c$^+$, CD11b$^+$, Ly6C$^-$, SSC-H$^{-/low}$ cells. Mono as CD11c$^+$, CD11b$^+$, Ly6C$^+$, SSC-H^{low}. Eos as CD11c$^+$, CD11b$^+$, Ly6C$^-$, SSC-H^{high} cells.

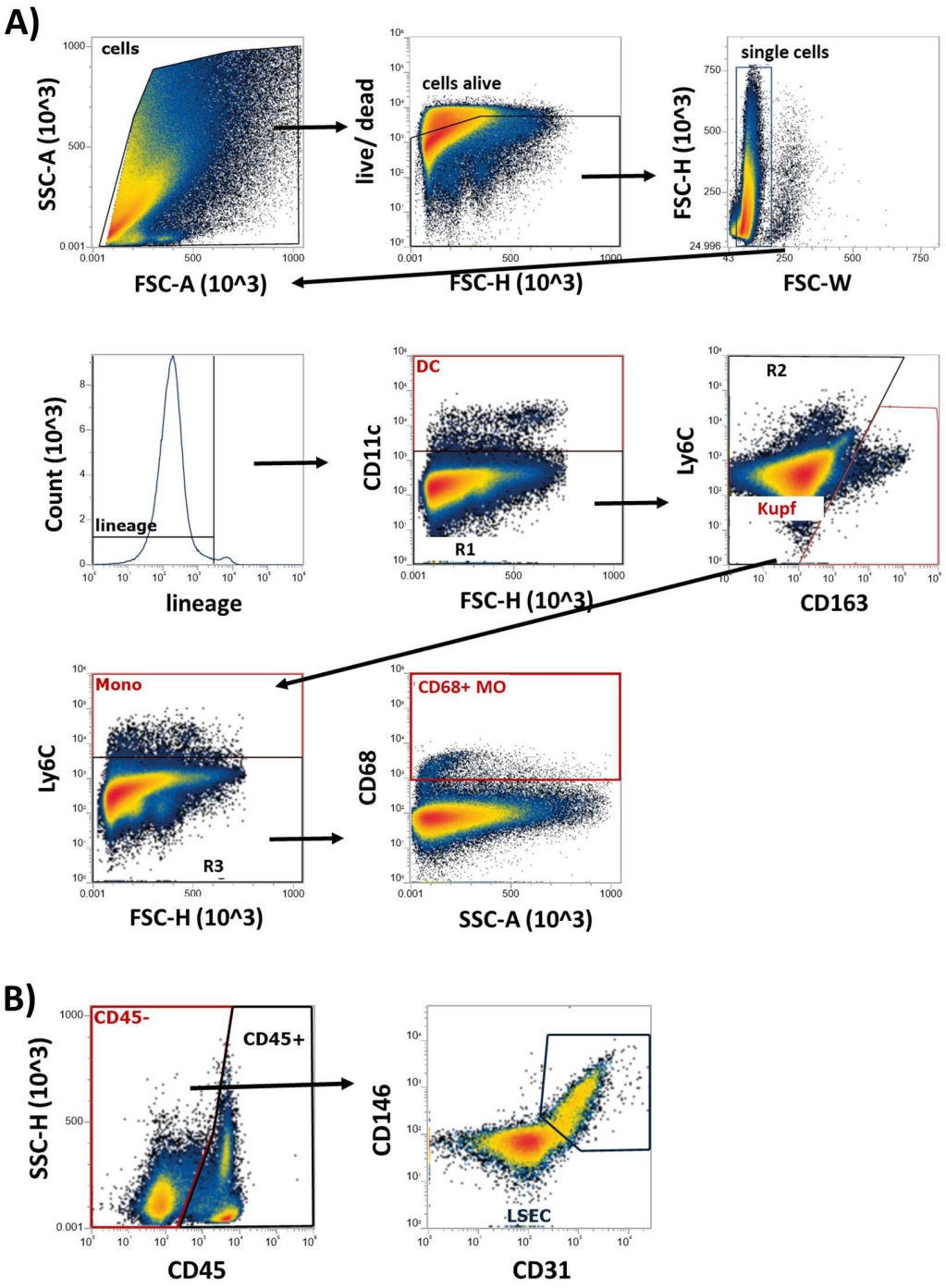

Supplement 27: Gating strategy for definition of liver cell populations for investigation of the cellular uptake of OVA-NC (Cy5) *in vivo*.

A: *Panel 3,* The gating strategy describes the flow cytometry definition of the liver macrophages investigated in Figure 22 B and Supplement 24. Dead cells (FVD$^+$) and doublets were excluded from analysis. Lineage negative cells (CD49b$^-$, CD3$^-$, Ly6G$^-$, CD19$^-$) were classified into CD11c$^+$ and CD11c$^-$. First were defined as DCs. Latter were classed into CD163$^+$, which is a sensitive marker for the Kupffer cell population [146]. The Ly6C$^+$, CD11c$^-$, CD163$^-$ cells were defined as monocytes (Mono). The remaining population was defined into CD11b$^+$ MO (CD11b$^+$ macrophages) and CD68$^+$ MO (CD68$^+$ macrophages).C: Gating strategy for definition of LSECs of the liver for investigation of the cellular uptake of OVA-NC (Cy5) *in vivo*. **B:** *Panel 4,* The gating strategy describes the flow cytometry definition of the liver sinusoidal endothelia cells (LSECs) investigated in Figure 22 B and Supplement 24. Preliminary to the CD45$^+$ classification, dead cells (FVD$^+$) and doubletts were excluded as described in A for panel 3. The LSEC population then was defined as CD45$^-$, CD31$^+$, CD146$^+$.

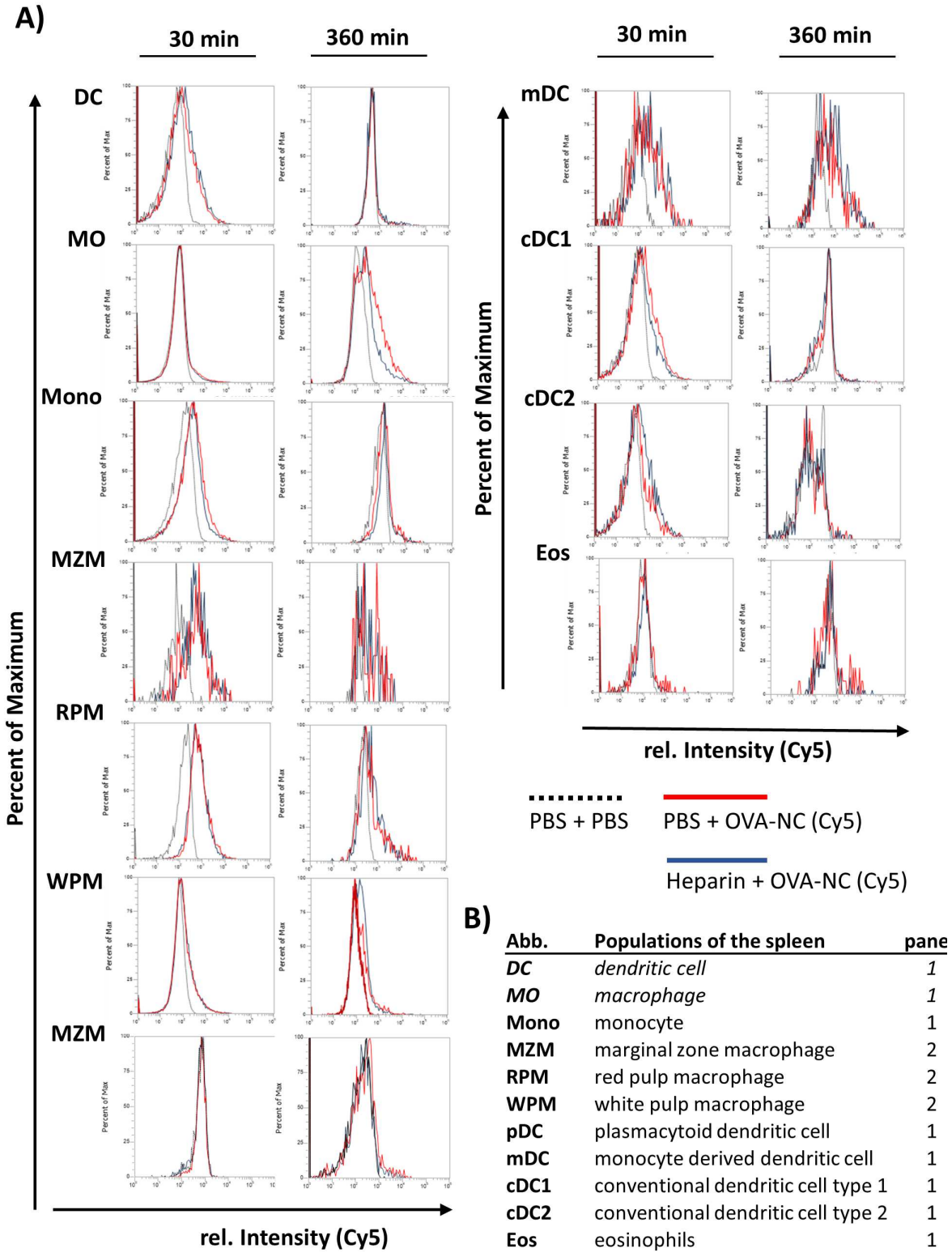

B)

Abb.	Populations of the spleen	pane
DC	*dendritic cell*	*1*
MO	*macrophage*	*1*
Mono	monocyte	1
MZM	marginal zone macrophage	2
RPM	red pulp macrophage	2
WPM	white pulp macrophage	2
pDC	plasmacytoid dendritic cell	1
mDC	monocyte derived dendritic cell	1
cDC1	conventional dendritic cell type 1	1
cDC2	conventional dendritic cell type 2	1
Eos	eosinophils	1

Supplement 28: Uptake of OVA-NC (Cy5) into spleen cell populations in heparinized animal.

A: Relative Cy5 intensity distribution for defined liver cell populations (abbreviation see B). The overlay represents the normalized intensity distribution curve measured with the channel 'RL1-H' for representative samples of 'PBS + OVA-NC (Cy5)' (red), 'heparin + OVA-NC (Cy5)' (blue) and an untreated control (black). For each condition (0 and 4 U/ml), a representative sample was selected. **B:** The table lists the names and abbreviations (abb.) of populations investigated by flow cytometry.

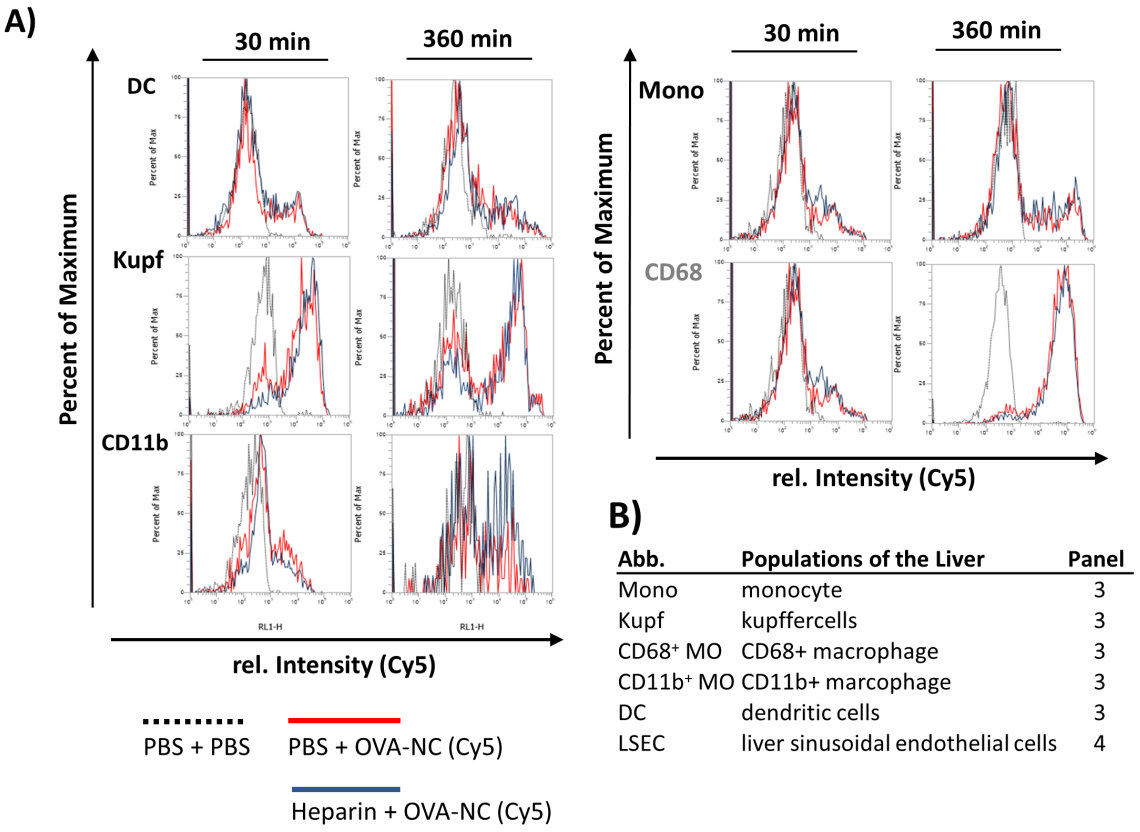

B)

Abb.	Populations of the Liver	Panel
Mono	monocyte	3
Kupf	kupffercells	3
CD68⁺ MO	CD68+ macrophage	3
CD11b⁺ MO	CD11b+ marcophage	3
DC	dendritic cells	3
LSEC	liver sinusoidal endothelial cells	4

Supplement 29: Uptake of OVA-NC (Cy5) in liver cell populations in heparinized animal.

A: Relative Cy5 intensity distribution for defined liver populations (abbreviation see B). The overlay represents the normalized intensity distribution curve measured with the channel 'RL1-H' for representative samples of 'PBS + OVA-NC (Cy5)' (red), 'heparin + OVA-NC (Cy5)' (blue) and an untreated control (black). For each condition (0 and 4 U/ml), a representative sample was selected. **B:** The table lists the names and abbreviations (abb.) of populations investigated by flow cytometry.

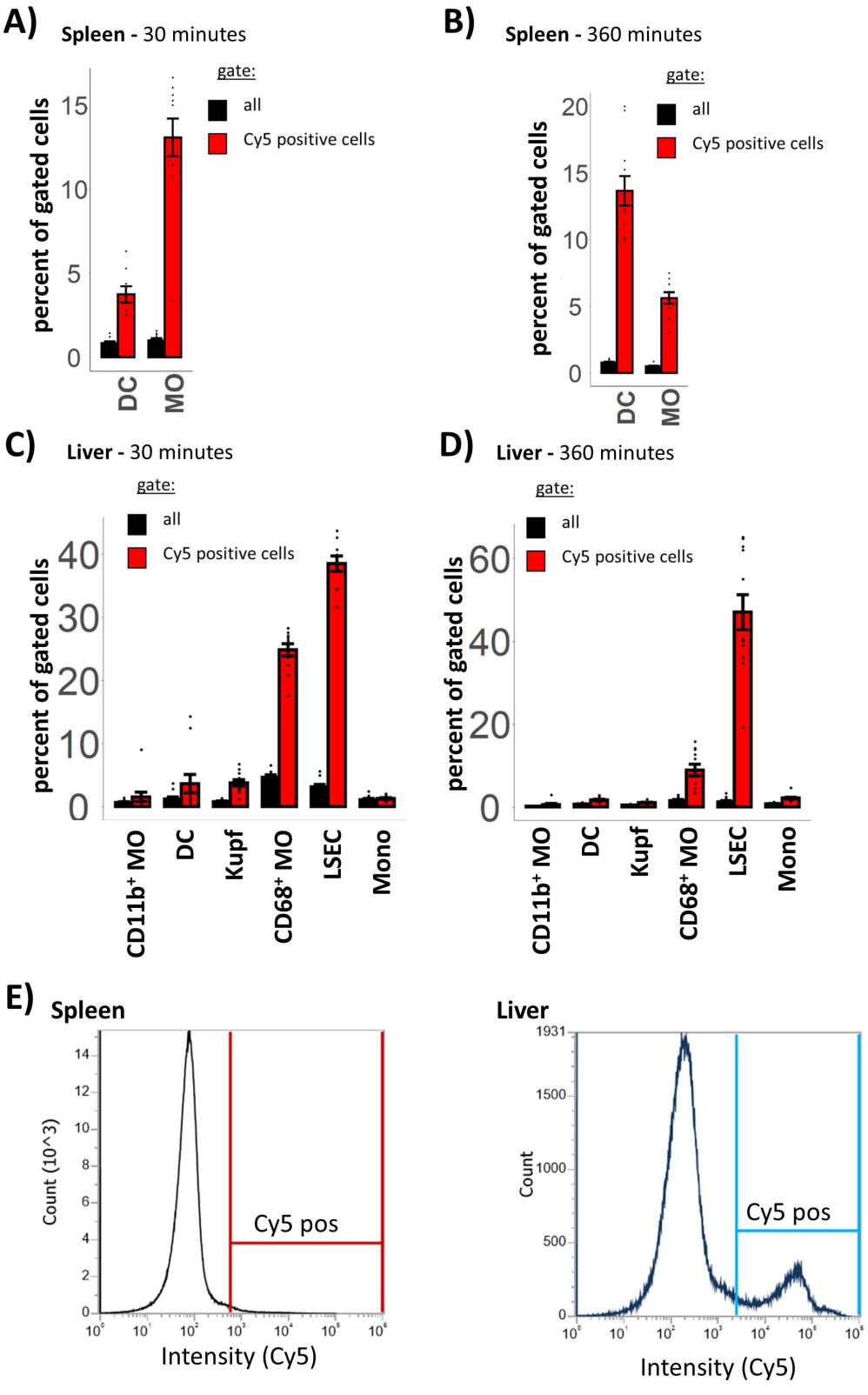

Supplement 30: Identification of the most relevant cells for the uptake of OVA-NC (Cy5) in liver and spleen.

A/B: The graph represents the mean +/- SEM of the percent of the population DC and MO contributing to the group of all Cy5 positive cells / all cells in the spleen at A) 30 minutes (n = 11) and B) 360 minutes (n = 11). **C/D:** The graph represents the mean +/- SEM of the percent of the liver cell populations contributing to the group of all Cy5 positive cells at C) 30 minutes (n = 11) and D) 360 minutes (n = 11). **E:** Relative Cy5 intensity distribution for all spleen cells (left) and liver cells (right). The gate 'Cy5 pos' was placed at a representative untreated control sample.

9.3 Supplements Chapter 3

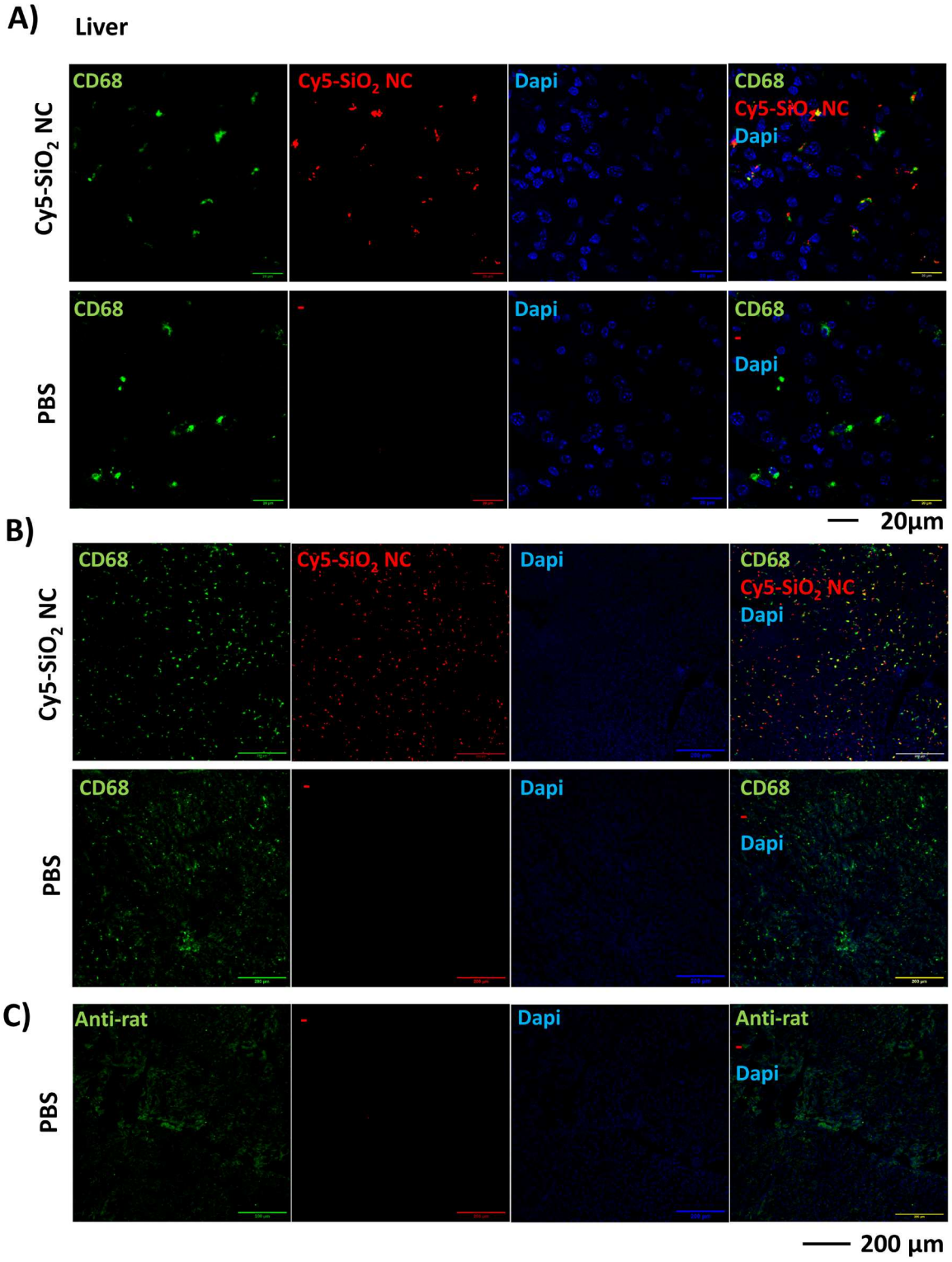

Supplement 31: Confocal microscopy of Cy5-SiO_2 NC and CD68 on liver sections.

A/B/C: Presented are two magnifications of liver sections of a Cy5-SiO_2 NC treated animal as well as a PBS treated one (**A:** 63x oil, **B/C:** 10x, at different spots). The combination shows the image of an immune fluorescent staining of CD68 (green), the tissue distribution of Cy5-SiO_2 NC (red), Dapi (blue) as well the overlay of all named channels. Cy5-SiO2 NC – CD68. Colocalization appears in yellow on the merged image. **C:** The unspecific binding of the secondary antibody was evaluated in the control staining.

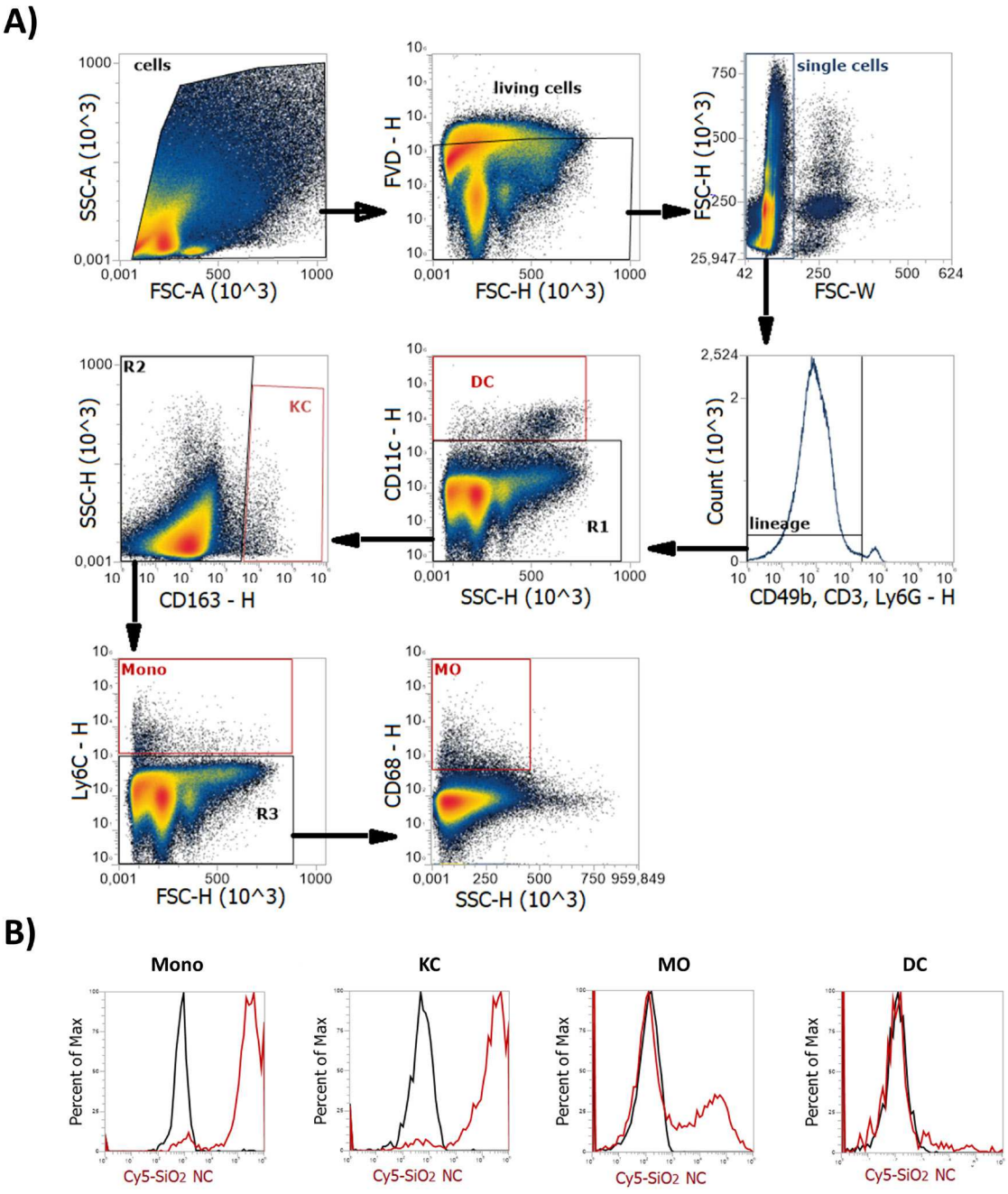

Supplement 32: Flow cytometry of the liver of Cy5-SiO_2-NC treated mice.

A: Gating scheme. Dead cells were excluded by live/dead staining. Doublets were excluded upon a high FSC-W. For all following gates, the region of interest was chosen according to the FMO (fluorescence minus one) control. Lineage negative cells were gated for CD11c and defined as dendritic cells (DCs). The CD11c negative population was gated for CD163, which is a marker expressed on Kupffer cells (KC) [146]. The negative population was gated for Ly6C, a marker for monocytes (Mono). The pan-macrophage marker CD68 was used to determine a further macrophage population (MO). **B:** Cy5-SiO_2NC uptake into NPC population. The histogram represents the distribution of Cy5 intensity of the defined cell populations (in a) for a representative Cy5-SiO2 NC treated (red) and PBS treated mouse (black).

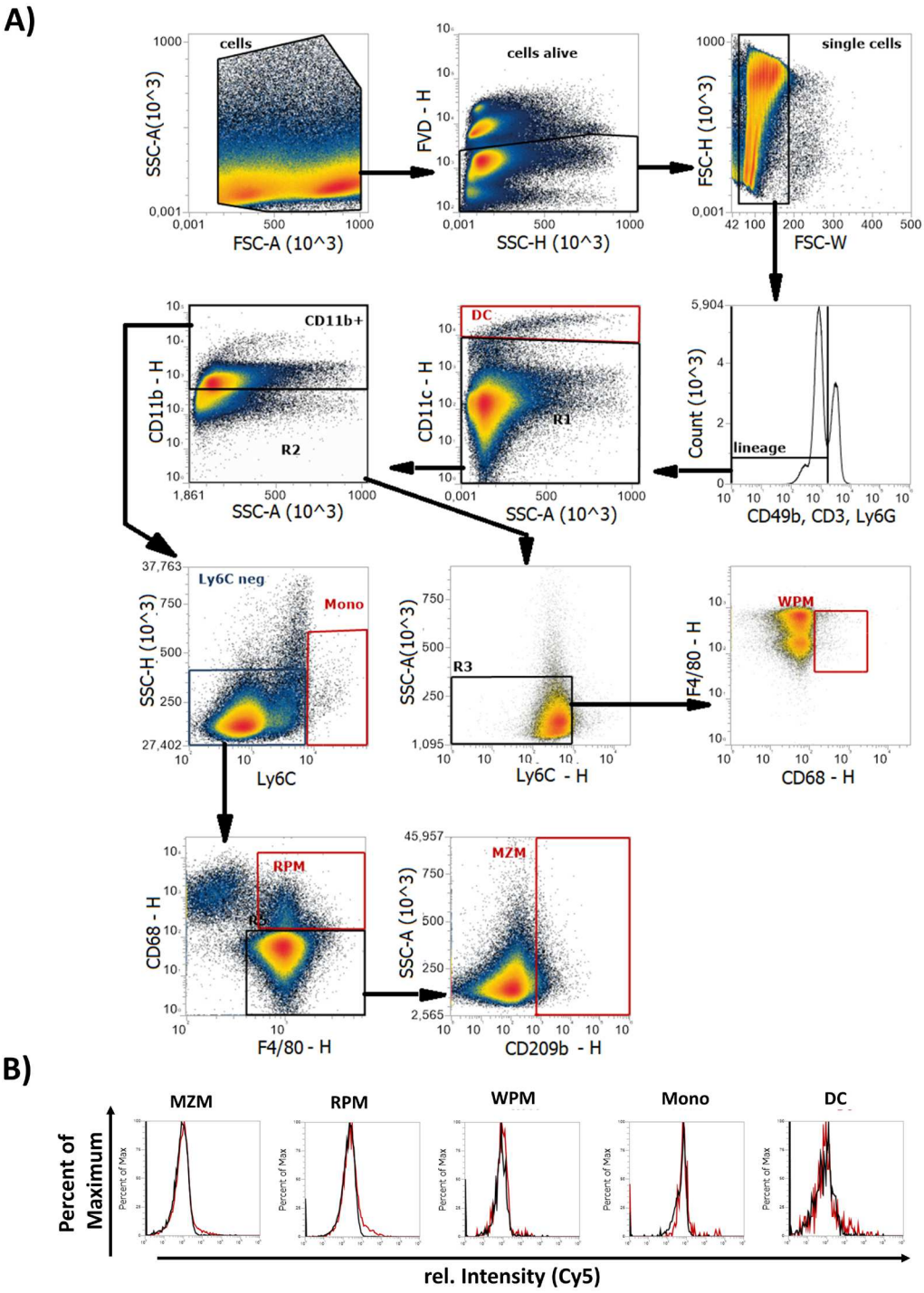

Supplement 33: Flow cytometry of the spleen of Cy5-SiO_2-NC treated mice.

A: Gating scheme. Dead cells were excluded by live/dead staining. For following gates, the region of interest was adapted to the FMO (fluorescence minus one) control. Doublets were excluded upon a high FSC-W. CD11c high expressing cells were defined as the dendritic cells (DC) population. CD11c low/negative cells were separated into CD11b positive and CD11b negative cells. CD11b positive cells were gated for Ly6C, determining a monocyte (Mono) population. The Ly6C negative cells, were gated for co-expression of CD68 and F4/80 and classified as RPM. The CD68 negative / F4/80 positive population was gated for expression of CD209b and assigned as MZM. In order to obtain the population of WPM, the CD11b negative population was gated for Ly6C negative and following gated for CD68 positive and F4/80 negative cells. The gating strategy based on Borges da Silva et al. and Shawn Rose et al.[67, 191] **B:** Cy5-SiO_2 NC uptake into spleen cell populations. The histogram represents the distribution of Cy5 intensity of the defined cell populations (in a) for a representative Cy5-SiO_2 NC treated (red) and PBS treated mouse (black).

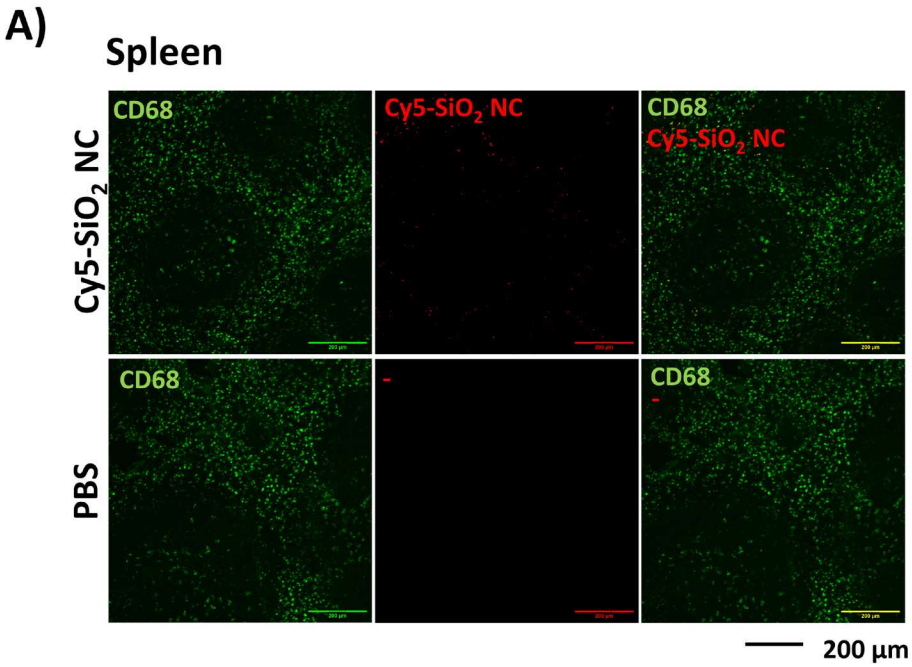

Supplement 34: Confocal microscopy of Cy5-SiO2 NC and CD68 on spleen sections.

A: Depicted is a confocal image (10x) of a representative section of the spleen of a Cy5-SiO_2 NC treated and PBS-treated animal, stained for CD68. The images show: CD68 (green, left column), Cy5-SiO_2 NC (red, middle column) and the overlaid channels (right column). Using the same laser settings for the Cy5 channel as for the liver-staining (Supplement 31), the distribution of Cy5-SiO_2 NC in the spleen is by this image representatively depicted and appears significantly lower than on the liver section (Supplement 31).

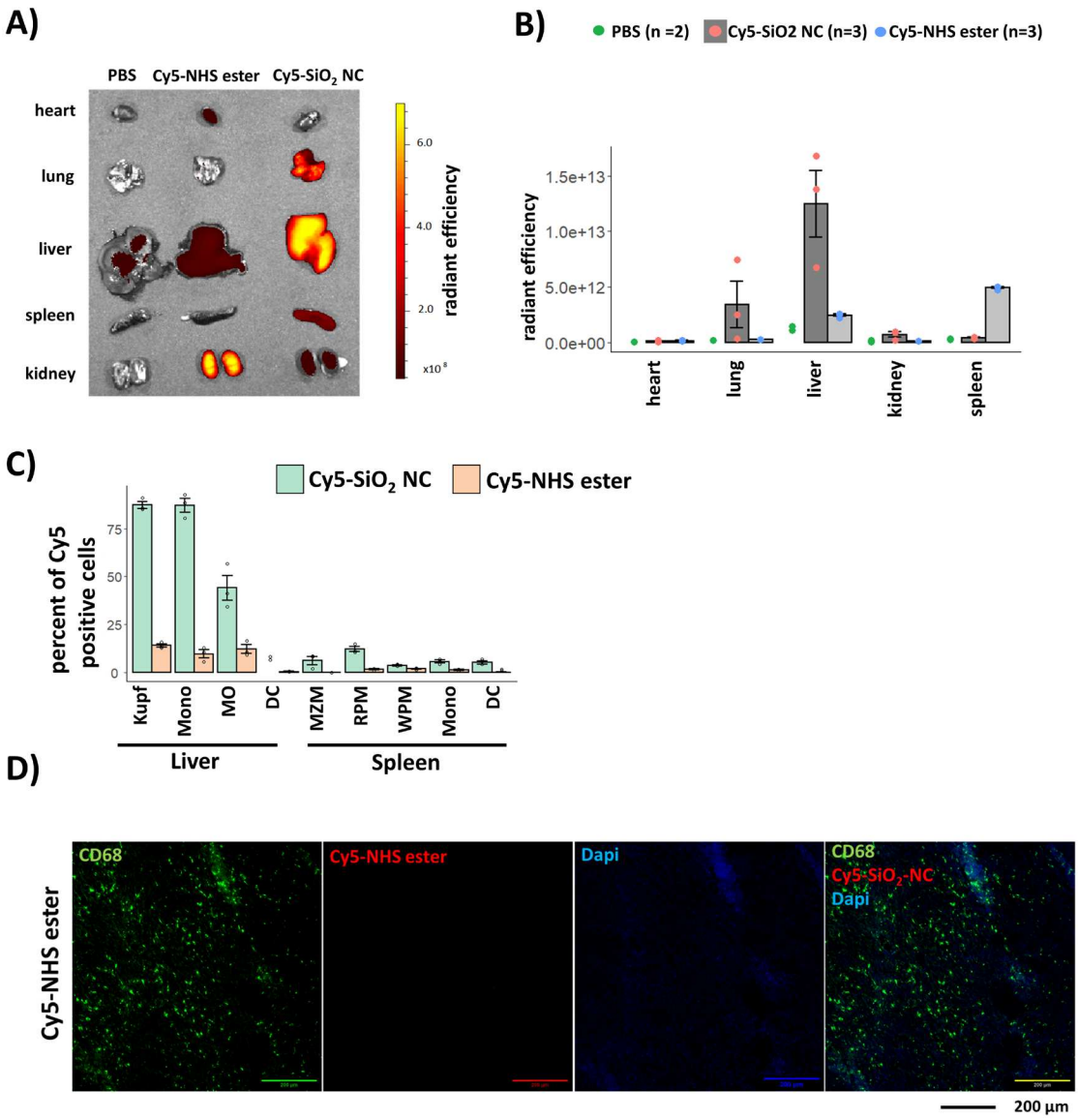

Supplement 35: *In vivo* biodistribution of Cy5-NHS ester and Cy5-SiO_2 NCs in organs and cell populations.

A: *Ex vivo* fluorescence images of organs after intravenous injection of Cy5-NHS ester (free dye, 9.7 µg/ml) and Cy5-SiO_2 NCs at a blood concentration of 300 µg/ml for 2 h. The same fluorescence intensity of Cy5 for the free and conjugated formulation was used. Parts of the figure are presented in Figure 26. **B:** Radiant efficiency of organs from the mice sacrificed at 2 h post injection. Data are partly presented in Figure 26 for the conditions "PBS" and "Cy5-SiO_2 NC". **C:** Percentage of Cy5-NHS ester positive cells compared to the Cy5-SiO_2 NC positive ones. The graph shows mean (+/- SEM) of the percentage of Cy5 positive gated cells of the populations of interest (described in Figure 26 E, Supplement 32 and Supplement 33). If the population included less than 50 cells, the value was excluded to reduce susceptibility to errors (data also presented in Figure 26 F). Three animals were analyzed (liver DC: 2). **D:** Confocal microscopy of Cy5-NHS ester and CD68 on liver sections. The image shows the overlay of Cy5-NHS ester (red) and CD68 (green), as well Dapi (blue). For the acquisitions the same laser settings as for the liver sections (Figure 26 D, Supplement 31) has been used.

9.4 Supplements Chapter 4

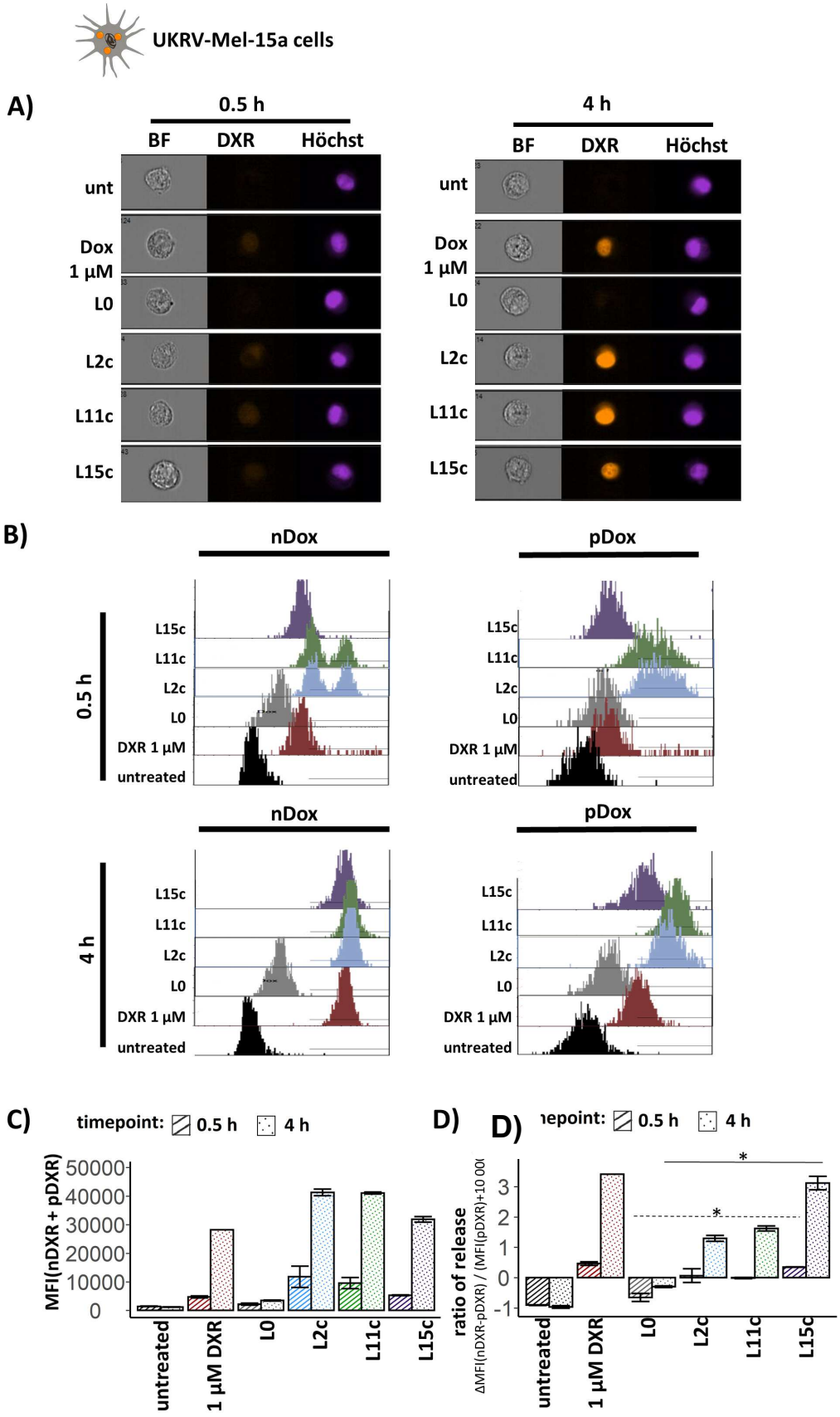

Supplement 36: Amnis® ImageStream® XMarkII analysis on the intracellular release of DXR from L0, L2c, L11c and L15c in UKRV-Mel-15a cells.

A: Representative images of UKRV-Mel-15a cells (gating see Figure 30A) for each condition and time point. Shown are the images of Ch1 (BF), Ch4 (DXR) and Ch7 (Höchst). **B:** Representative histograms of the features nDXR and pDXR (description of features see Figure 30 B, C) for each condition and time point. **C:** 'Total uptake' of DXR-liposomes into the cell. The graph represents the sum of the means of MFI(nDXR) and MFI(pDXR) +/- sqrt(SEM_{pDXR} + SEM_{nDXR}). The parameter was calculated according to Table 9. n = 3, except for '1 µM DXR' t_4 n = 1, 'L0' t_4 n = 2, for 'L11c' t_4 n = 2**. D:** The 'release ratio' (mean +/- SEM) of DXR. The parameter was calculated according to Table 9. Values were compared with each other by a Dunn Test (package R, method = "none") following a Kruskal-Wallis test. $p < 0.05$ = *, $p < 0.005$ = **. n = 3, except for '1 µM DXR' t_4 n = 1, 'L0' t_4 n=2, for 'L11c' t_4 n = 2.

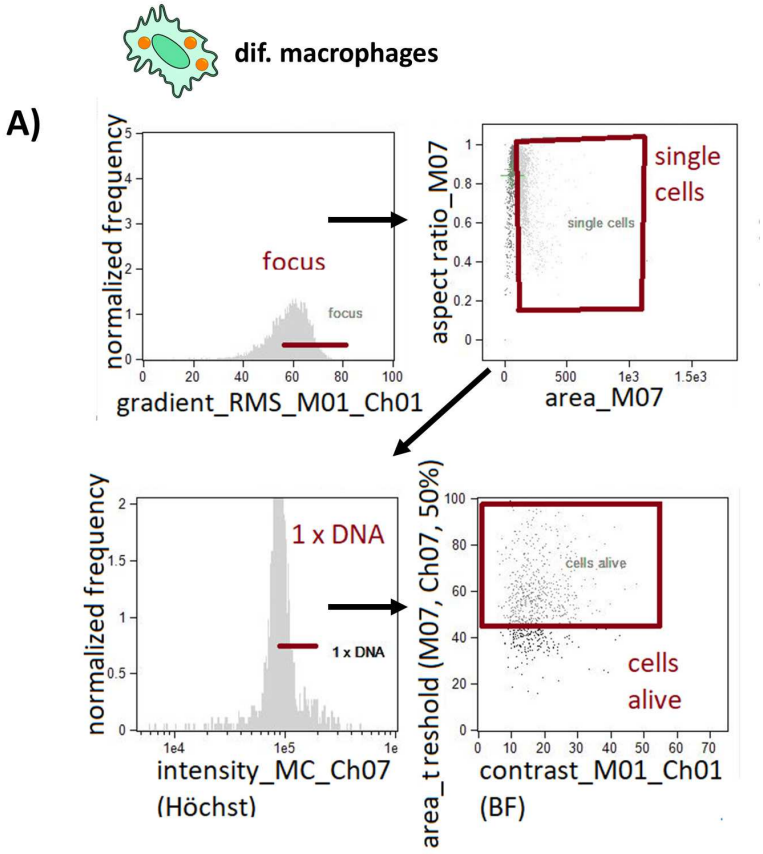

Supplement 37: Adapted gating strategy on primary dif. macrophages for Amnis® ImageStream®XMark II evaluations.

A: Preliminary gating strategy on primary dif. macrophages for selection of the images undergoing further analysis. Predefined wizards were applied for defining cells of 'focus', 'single cells', 'mononuclear cells' (exclusion of mitotic cells) and 'alive cells'. Further evaluations on parameters (Table 9) were performed on 'alive cells'.

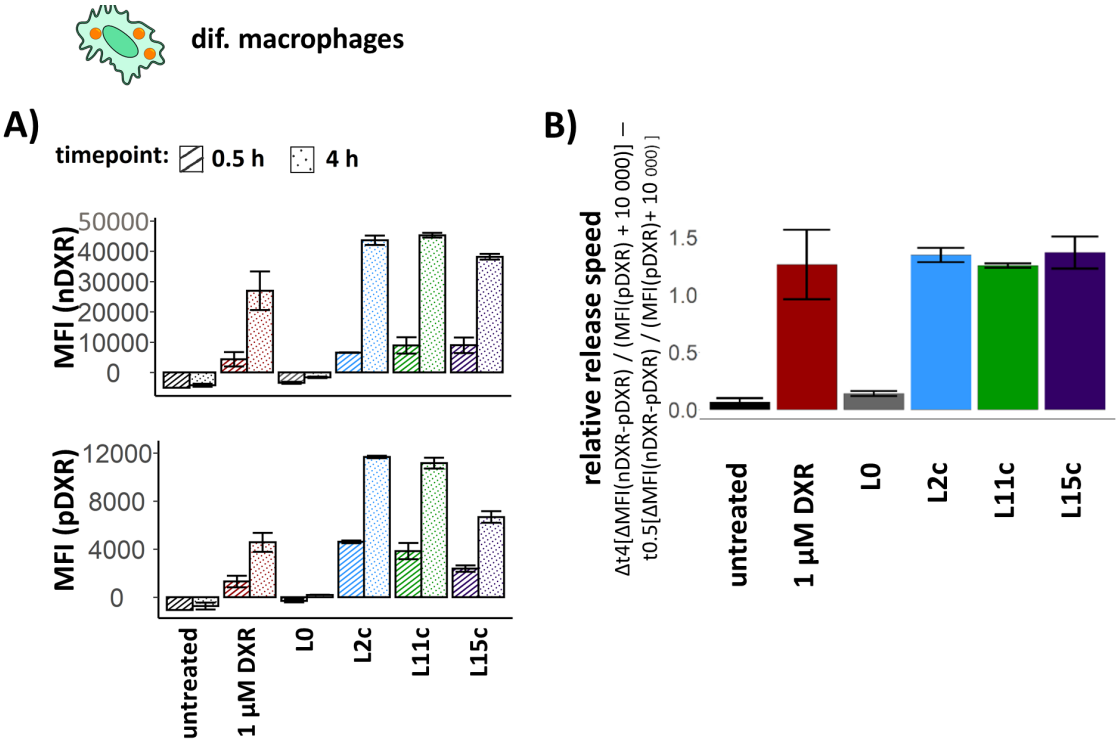

Supplement 38: Intracellular release of DXR from L0, L2c, L11c and L15c into human dif. macrophages.

A: DXR accumulation in nucleus and cytoplasm of human primary dif. macrophages. *Top:* The MFI of DXR in nuclei (MFI(nDXR)) (mean +/- SEM). *Bottom:* The MFI of DXR (mean +/- SEM) in cytoplasm (MFI(pDXR)). n = 2, except for 'L2c' $t_{0.5}$ n = 1. **B:** The relative release speed of DXR in primary dif. macrophages. Represented is (mean +/- SEM). The parameter was calculated according to Table 9. n = 2, except for 'L2c' $t_{0.5}$ n = 1.

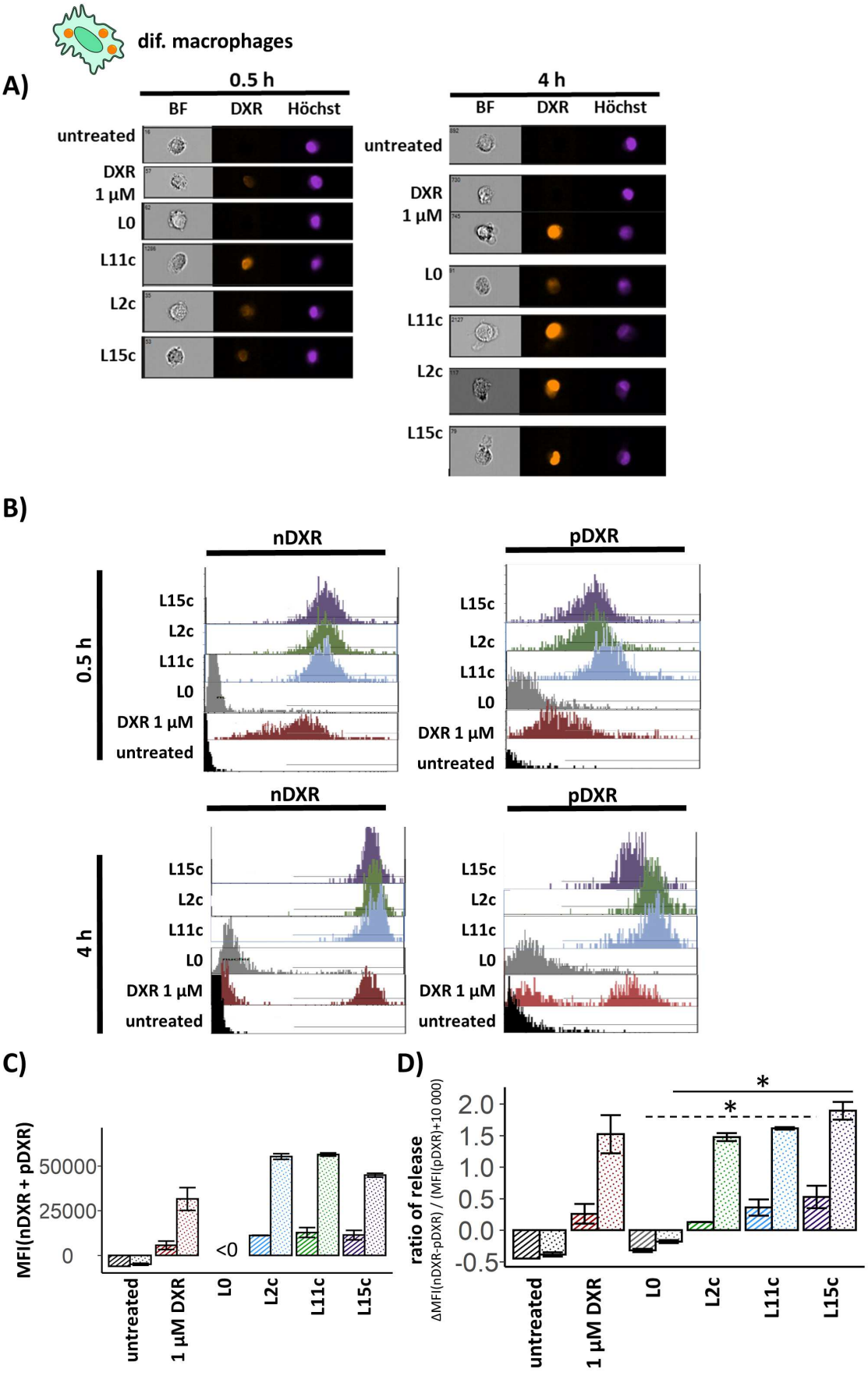

Supplement 39: Amnis® ImageStream® XMarkII analysis on release of DXR from L0, L2c, L11c and L15c in primary dif. macrophages.

A: Representative images of primary dif. macrophages (gating see Supplement 37) for each condition and time point. Shown are the images of Ch1 (BF), Ch4 (DXR) and Ch7 (Höchst). **B:** The graphs show representative histograms of the features nDXR and pDXR (description of features see Figure 30 B, C) of both timepoints ($t_{0.5}$ and t_4) for each condition. **C:** 'Total uptake' of DXR. The graph represents the sum of the means of MFI(nDXR) and MFI(pDXR) +/- sqrt(SEM_{pDXR} + SEM_{nDXR}). The parameter was calculated according to Table 9. n=2, except for 'L2c' $t_{0.5}$ n = 1. **E:** The 'release ratio' (mean +/- SEM) of DXR. The parameter was calculated according to Table 9. n=2, except for 'L2c' $t_{0.5}$ n = 1.

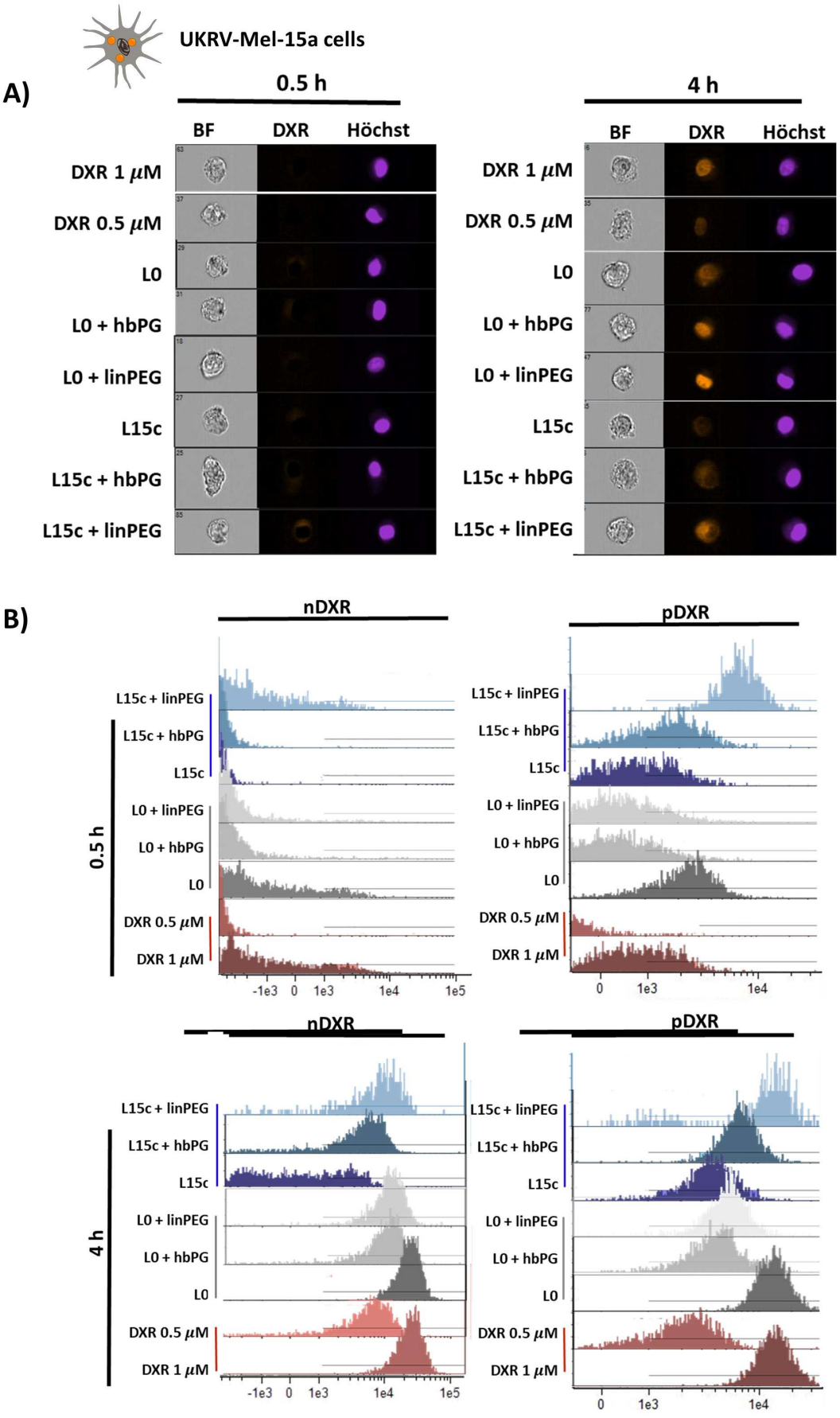

- the figure proceeds on the next page -

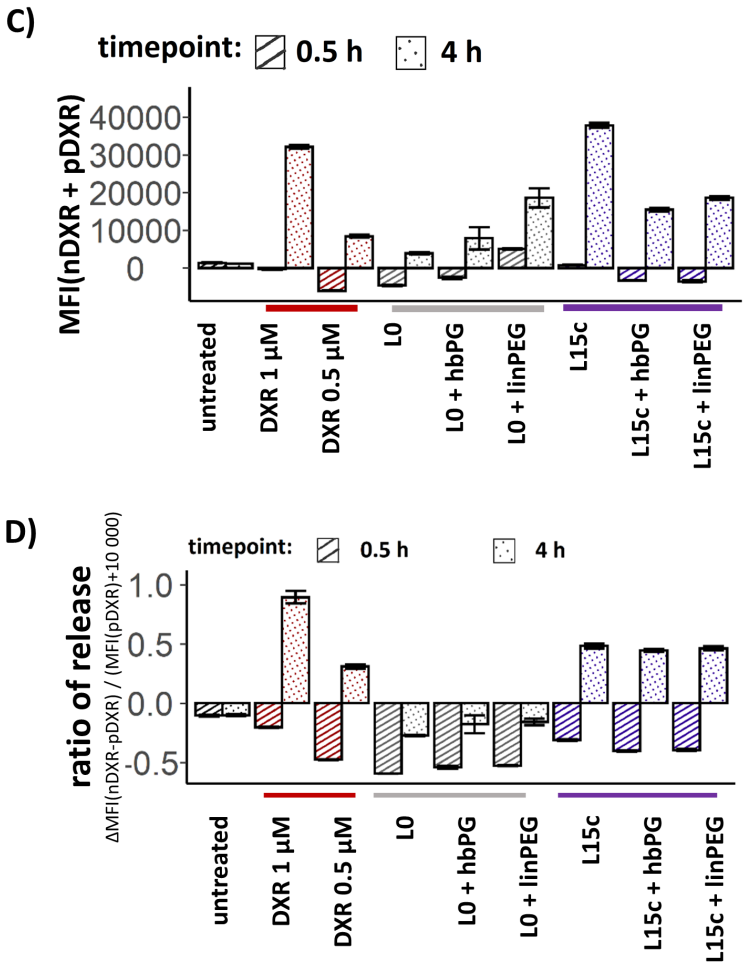

Supplement 40: Effect of surface modification with hbPG and linPEG on intracellular release of DXR from liposomes.

A: Representative images of UKRV-Mel-15a cells (gating see Figure 30A) for each condition and time point. Shown are the images of Ch1 (BF), Ch4 (DXR) and Ch7 (Höchst). **B:** Representative histograms of the features nDXR and pDXR (description of features see Figure 30 B, C) for each condition and time point. **C: '**Total uptake' of DXR-liposomes into the cell. The graph represents the sum of the means of MFI(nDXR) and MFI(pDXR) +/- sqrt(SEM_{pDXR} + SEM_{nDXR}). The parameter was calculated according to Table 9. n = 3. **D:** The 'release ratio' (mean +/- SEM) of DXR. The parameter was calculated according to Table 9. Values of the groups 'L0' and 'L15c' were compared with each other for each time point by a Dunn Tests (package R, method = "none") following a Kruskal-Wallis test. No significant differences were detected. n = 3.

10 Appendix

i. List of abbreviations

Abbreviation	Meaning of the Abbreviation
AEMH	2-aminoethyl methacrylate hydrochloride
Abb.	Abbreviation (sometimes used abbreviation)
Amph	Amphotericin B
ATIII	antithrombin III
B-Cells	B-cells
BMDC	Bone marrow derived dendritic cells
BMM	Bone marrow derived macrophages
BP	Bodipy (630 nm/650 nm)
CD	Cluster of differentiation
$CD11b^+$ MO	Macrophages (CD11b expressing)
$CD68^+$ MO	Macrophages (CD68 expressing)
cDC1	Conventional dendritic cells type 1
cDC2	Conventional dendritic cells type 2
Ch	Channel (sometimes used abbreviation)
CHEMS	Cholesteryl-hemisuccinate
CHOL	Cholesterol
COPD	chronic obstructive pulmonary disease
CTMA-Cl	Cetyltrimethylammonium hydrochlorid
Cy5	Cyanine 5
Cy5-oligo	Cyanine 5-5'-CCA CTC CTT TCC AGA AAA CT (0.1 nmol μL^{-1} in PBS buffer)
DC	Dendritic cell
DiD	1,1'-Dioctadecyl-3,3,3',3'-tetramethylindodicarbocyanine, 4-chlorobenzenesulfonate salt
dif.	Differentiated (sometimes used abbreviation)
DiR	1,1'-Dioctadecyl-3,3,3',3'-tetramethylindotricarbocyanine iodide
DMEM	Dulbecco's Modified Eagle's Medium
DMPC	1,2-Dimyristoyl-sn-glycero-3-phosphocholine
DODAP	1,2-Dioleoyl-3-dimethylammonium-propane
DOPC	1,2-Dioleoyl-sn-glycero-3-phospho-ethanolamine
DOPG	1,2-Dioleoyl-sn-glycero-3-phospho-rac-(1-glycerol) sodium salt
DOTAP	N-[1-(2,3-dioleoyloxy)propyl]-N,N,N-trimethylammonium chloride
DPPC	1,2-Dipalmitoyl-sn-glycero-3-phsopho-rac-(1-glycerol) sodium salt
DSPE	Distearoyl-sn-glycero-phosphoethanolamine
DSPE-PEG(2000)	1,2-Distearoyl-sn-glycero-3-phosphoethanolamine-N-[amino(polyethylene glycol)-2000]
DSPG	1,2-Distearoyl-sn-glycero-3-phospho-rac-(1-glycerol)
DXM	Dexamethasone
DXR	Doxorubicin
EDTA	Ethylenediaminetetraacetic acid
EMEM	Eagle's Minimum Essential Medium
Eos	Eosinophils
EPC	Egg phosphatidyl choline
EPR	Enhanced permeability and retention
EU	Endotoxin units
FCS	Fetal bovine serum
FDA	Food and Drug Administration
FVD	Fixable viability dye
Gln	Glutamin
GM-CSF	Granulocyte-macrophage colony-stimulating factor
h	Hours (sometimes used abbreviation)
hbPG	Hyperbranched Polyglycol
HBSS	Hank's balanced salt solution
HD	Hexadecane
HeLa	(name cell line)
hep	heparin (sometimes used abbreviation)
hPc	human citrate plasm

HPLC	High Performance Liquid Chromatography
HS	Horse serum
HSA	Human serum albumine
HSPC	Hydrogenated soy phosphatidylcholine
i.v.	Intravenous
IL-6	Interleukine 6
IMDM	Iscove's Modified Dulbecco's Medium
Inj.	Injection (sometimes used abbreviation)
IUPAC	International Union of Pure and Applied Chemistry
KC	Kupffer cells
KCL	Kaliumchloride
KH_2PO_4	Potassium dihydrogen phosphate
$KHCO_3$	Kaliumhydrogencarbonat
linPEG	linear polyethyleneglycole
Lip-Amb	Ambisome ®-like liposomes
Lip-Dox	Doxil®-like liposomes
Lip-Myo	Myocet®-like liposomes
Lip-Myo-PEG	PEGylated Myocet®-like liposomes
LMWH	Low molecular weight heparin
LPS	Lipopolysaccharides
LSEC	Liver sinusoidal cells
M-700 CSF	M-700 colony-stimulating factor
M-CSF	Macrophage colony-stimulating factor
mDC	Macrophage derived dendritic cells
MEM	Minimal essential medium
MFI	Median flourescence intensity
MHC-II	Major histocompatibility complex II
min	Minutes (sometimes used abbreviation)
MMM	Marginal metallophilic macrophage
MO	Macrophages
Mono	Monocytes
MS	Balb/c mouse serum (sometimes used abbreviation)
MZM	Marginal zone macrophage
NaCl	Natriumchloride
NaH_2PO	Monosodium phosphate
NC	Nanocapsule
NF-κB	Nuclear factor kappa-light-chain-enhancer
NH_4Cl	Ammonium chloride
NPC	Non-parenchymal liver cells
OVA	Ovalbumine
P((E/B)-b-EO)	Poly((ethylene-co-butylene)-block-(ethylene oxide)
PBS	Dulbecco's phosphate buffered saline
pDC	Plasmacytoid dendritic cells
PdI	Polydispersity index
PDXM	Polydexamethasone
PEG	Polyethyleneglycole
PEG2000-DSPE	N-(carbonyl-methoxypolyethylene glycol 2000)-1,2-distearoyl-sn-glycero-3-phosphoethanolamine sodium salt
$PEG5k_{0.2}$	Isocyanate-mPEG molecular weight = 5 kDa
Pen-Strep	Penicillin-streptomycin
PFA	Paraformaldehyde
PF-4	Platelet factor 4
RAW 264.7	(name cell line)
RES	Reticuloendothelial system
RPM	Red pulp macrophages
RPMI-1640	(name culture medium)
s	Seconds (sometimes used abbreviation)
SD	Standard deviation
SDS	Sodium dodecyl sulfate (99%)
SEM	Standard error of the mean
Siglec/ SIGLEC	Sialic acid-binding immunoglobulin
SiO_2	Silica

ß-Me	ß-Mercaptoethanol
T-Cells	T-cells
TDI	2,4-Toluene diisocyanate (99%)
α-Toc	Alpha-Tocopherol
U.S. Food and Drug Administration	FDA
UFH	Unfractionated heparin
UKRV-Mel-15a	(name cell line)
WPM	White pulp macrophage

ii. List of cell surface markers

Cell surface marker	Description
CD11b	Integrin α-M
CD11c	Complement component 3 receptor 4 subunit
CD146	Melanoma cell adhesion molecule
CD163	(Transmembrane scavenger receptor that is expressed on monocytes and macrophages)
CD209b	DC-SIGN-related protein 1
CD3	(Protein complex and T cell co-receptor)
CD31	Platelet endothelial cell adhesion molecule
CD45	Protein tyrosine phosphatase receptor type C
CD45R	(Member of the protein tyrosine phosphatase family)
CD49b	Integrin α-2
CD68(a)	Macrosialin
CD8a	(Co-receptor for the T-cell receptor)
F4/80	EGF-like module-containing mucin-like hormone receptor-like 1
Ly6C	(GPI-linked surface protein)
Ly6G	Lymphocyte antigen 6 complex locus G6D
MHCII	Major Histocompatibility Complex
Siglec-F	Sialic acid-binding immunoglobulin-type lectin F
Siglec-H	Sialic acid-binding immunoglobulin-type lectin 1

iii. List of figures

iv. List of supplements

v. License numbers of requested permissions

	Description	License Number/ other permissions
Table 1	Overview on clinical relevant liposomal formulations.	Open access article distributed under the Creative Commons Attribution License
Figure 1	“Total doxorubicin concentration to time profile in tissues and blood” [5]	4940880968003 (Copyright Clearance Centre)
Figure 4	“Schematic of nanoparticle clearance pathways” [37]	5037110270440 (Copyright Clearance Centre)
Figure 7	Structure of the spleen (A)	4941020241778 (Copyright Clearance Centre)
Figure 7	The follicular versus marginal zone (B)	4941020522684 (Copyright Clearance Centre)
Figure 9	Schematic illustration oft the blood clearance of nanoparticles by the liver.	Permission requested at Copyright Clearance Centre
Figure 10	Heparin and heparan sulfate: structure and function.	Permission received from Chloe Szebrat Contracts and Copyright Executive Royal Society of Chemistry
Figure 11	Schematic representation of heparin clearnce after i.v. injection.	5007821279682 (Copyright Clearance Centre)
Figure 12	Adding of heparin into the process of corona formation of nanocarriers causes changes of uptake.	open access article distributed under the Creative Commons Attribution License
Figure 29	DXR intercalating with DNA base pairs. (A)	Creative Commons Attribution-NonCommercial_ShareAlike License
Figure 29	DXR intercalating with DNA base pairs. (B)	Creative Commons Attribution-NonCommercial_ShareAlike License
Figure 29	DXR intercalating with DNA base pairs. (C)	5051310722424 (Copyright Clearance Centre)

vi. List of tables

11 References

1. Weissig, V., T.K. Pettinger, and N. Murdock, *Nanopharmaceuticals (part 1): products on the market.* Int J Nanomedicine, 2014. **9**: p. 4357-73.
2. Duffus, J.H., M. Nordberg, and D.M. Templeton, *Glossary of terms used in toxicology, (IUPAC Recommendations 2007).* Pure and Applied Chemistry, 2007. **79**(7): p. 1153-1344.
3. US FDA, A., *Report of the US Food and Drug Administration Nanotechnology Task Force.* US Food and Drug Administration, Washignton DC, 2007.
4. James, J., *DOXIL approved for KS.* AIDS treatment news, 1995(236): p. 6.
5. Luo, R., et al., *Distinct biodistribution of doxorubicin and the altered dispositions mediated by different liposomal formulations.* International journal of pharmaceutics, 2017. **519**(1-2): p. 1-10.
6. Shin, M.D., et al., *COVID-19 vaccine development and a potential nanomaterial path forward.* Nature nanotechnology, 2020. **15**(8): p. 646-655.
7. Bulbake, U., et al., *Liposomal formulations in clinical use: an updated review.* Pharmaceutics, 2017. **9**(2): p. 12.
8. Torchilin, P.V., et al., *Liposomes: a practical approach*. 2003: Oxford University Press.
9. Barenholz, Y.C., *Doxil®—the first FDA-approved nano-drug: lessons learned.* Journal of controlled release, 2012. **160**(2): p. 117-134.
10. Batist, G., *Cardiac safety of liposomal anthracyclines.* Cardiovascular toxicology, 2007. **7**(2): p. 72-74.
11. Duggan, S.T. and G.M. Keating, *Pegylated liposomal doxorubicin.* Drugs, 2011. **71**(18): p. 2531-2558.
12. Gabizon, A., et al., *Prolonged circulation time and enhanced accumulation in malignant exudates of doxorubicin encapsulated in polyethylene-glycol coated liposomes.* Cancer research, 1994. **54**(4): p. 987-992.
13. Torchilin, V., *Tumor delivery of macromolecular drugs based on the EPR effect.* Advanced drug delivery reviews, 2011. **63**(3): p. 131-135.
14. Williams, T. and J. Morley, *Prostaglandins as potentiators of increased vascular permeability in inflammation.* Nature, 1973. **246**(5430): p. 215-217.
15. Kanwal, U., et al., *Advances in nano-delivery systems for doxorubicin: an updated insight.* Journal of Drug Targeting, 2018. **26**(4): p. 296-310.
16. Harris, L., et al., *Liposome-encapsulated doxorubicin compared with conventional doxorubicin in a randomized multicenter trial as first-line therapy of metastatic breast carcinoma.* Cancer, 2002. **94**(1): p. 25-36.
17. Adler-moore, J.P. and R.T. Proffitt, *Development, Characterization, Efficacy and Mode of Action of Ambisome, A Unilamellar Liposomal Formulation of Amphotericin B.* Journal of Liposome Research, 1993. **3**(3): p. 429-450.
18. Adler-Moore, J. and R.T. Proffitt, *AmBisome: liposomal formulation, structure, mechanism of action and pre-clinical experience.* Journal of Antimicrobial Chemotherapy, 2002. **49**(suppl_1): p. 21-30.
19. Lopez-Berestein, G., et al., *Treatment of hepatosplenic candidiasis with liposomal-amphotericin B.* Journal of Clinical Oncology, 1987. **5**(2): p. 310-317.
20. van Etten, E.W., et al., *Biodistribution of liposomal amphotericin B (AmBisome) and amphotericin B-desoxycholate (Fungizone) in uninfected immunocompetent mice and leucopenic mice infected with Candida albicans.* Journal of Antimicrobial Chemotherapy, 1995. **35**(4): p. 509-519.
21. Grabbe, S., et al., *Translating nanoparticulate-personalized cancer vaccines into clinical applications: case study with RNA-lipoplexes for the treatment of melanoma.* Nanomedicine, 2016. **11**(20): p. 2723-2734.
22. Till, U. *Biontech Corona-Impfstoff offenbar sehr wirksam*. SWR >>Wissen 2020 09.11.2020 15:34.

23. Gheibi Hayat, S.M. and M. Darroudi, *Nanovaccine: A novel approach in immunization.* J Cell Physiol, 2019. **234**(8): p. 12530-12536.
24. Banchereau, J., et al., *Immunobiology of dendritic cells.* Annual review of immunology, 2000. **18**(1): p. 767-811.
25. Bhardwaj, N., *Processing and presentation of antigens by dendritic cells: implications for vaccines.* Trends in molecular medicine, 2001. **7**(9): p. 388-394.
26. Elamanchili, P., et al., *"Pathogen-mimicking" nanoparticles for vaccine delivery to dendritic cells.* Journal of immunotherapy, 2007. **30**(4): p. 378-395.
27. Dubensky, T.W. and S.G. Reed, *Adjuvants for cancer vaccines.* Seminars in Immunology, 2010. **22**(3): p. 155-161.
28. Allison, A.C. and N.E. Byars, *Immunological adjuvants: Desirable properties and side-effects.* Molecular Immunology, 1991. **28**(3): p. 279-284.
29. Piradashvili, K., et al., *Biodegradable protein nanocontainers.* Biomacromolecules, 2015. **16**(3): p. 815-821.
30. Paßlick, D., et al., *Delivering all in one: Antigen-nanocapsule loaded with dual adjuvant yields superadditive effects by DC-directed T cell stimulation.* Journal of Controlled Release, 2018. **289**: p. 23-34.
31. Didierlaurent, A.M., et al., *Enhancement of adaptive immunity by the human vaccine adjuvant AS01 depends on activated dendritic cells.* The Journal of Immunology, 2014. **193**(4): p. 1920-1930.
32. Dölen, Y., et al., *Nanovaccine administration route is critical to obtain pertinent iNKt cell help for robust anti-tumor T and B cell responses.* OncoImmunology, 2020. **9**(1): p. 1738813.
33. Zhu, G., et al., *Albumin/vaccine nanocomplexes that assemble in vivo for combination cancer immunotherapy.* Nature Communications, 2017. **8**(1): p. 1954.
34. Aktories, K., et al., *Allgemeine und spezielle Pharmakologie und Toxikologie: Begründet von W. Forth, D. Henschler, W. Rummel*. 2017: Elsevier Health Sciences.
35. Lüllmann, H., K. Mohr, and L. Hein, *Pharmakologie und Toxikologie. 16.* Auflage. sl: Georg Thieme Verlag. S, 1999. **190**.
36. Yu, M. and J. Zheng, *Clearance Pathways and Tumor Targeting of Imaging Nanoparticles.* ACS nano, 2015. **9**(7): p. 6655-6674.
37. Sun, T., et al., *Engineered nanoparticles for drug delivery in cancer therapy.* Angewandte Chemie International Edition, 2014. **53**(46): p. 12320-12364.
38. Longmire, M., P.L. Choyke, and H. Kobayashi, *Clearance properties of nano-sized particles and molecules as imaging agents: considerations and caveats.* Nanomedicine (Lond), 2008. **3**(5): p. 703-17.
39. Zhang, Y.-N., et al., *Nanoparticle–liver interactions: cellular uptake and hepatobiliary elimination.* Journal of controlled release, 2016. **240**: p. 332-348.
40. Liu, T., et al., *RES blockade: A strategy for boosting efficiency of nanoparticle drug.* Nano Today, 2015. **10**(1): p. 11-21.
41. Sun, X., et al., *Improved tumor uptake by optimizing liposome based RES blockade strategy.* Theranostics, 2017. **7**(2): p. 319.
42. Chonn, A., S. Semple, and P. Cullis, *Association of blood proteins with large unilamellar liposomes in vivo. Relation to circulation lifetimes.* Journal of Biological Chemistry, 1992. **267**(26): p. 18759-18765.
43. Madathiparambil Visalakshan, R., et al., *The influence of nanoparticle shape on protein corona formation.* Small, 2020: p. 2000285.
44. Sakulkhu, U., et al., *Significance of surface charge and shell material of superparamagnetic iron oxide nanoparticle (SPION) based core/shell nanoparticles on the composition of the protein corona.* Biomaterials science, 2015. **3**(2): p. 265-278.
45. Schöttler, S., et al., *Protein source and choice of anticoagulant decisively affect nanoparticle protein corona and cellular uptake.* Nanoscale, 2016. **8**(10): p. 5526-5536.
46. Hajipour, M.J., et al., *Personalized disease-specific protein corona influences the therapeutic impact of graphene oxide.* Nanoscale, 2015. **7**(19): p. 8978-8994.

47. Corbo, C., et al., *Personalized protein corona on nanoparticles and its clinical implications.* Biomaterials Science, 2017. **5**(3): p. 378-387.
48. Ritz, S., et al., *Protein corona of nanoparticles: distinct proteins regulate the cellular uptake.* Biomacromolecules, 2015. **16**(4): p. 1311-1321.
49. Aggarwal, P., et al., *Nanoparticle interaction with plasma proteins as it relates to particle biodistribution, biocompatibility and therapeutic efficacy.* Advanced drug delivery reviews, 2009. **61**(6): p. 428-437.
50. Owens, D.E. and N.A. Peppas, *Opsonization, biodistribution, and pharmacokinetics of polymeric nanoparticles.* International Journal of Pharmaceutics, 2006. **307**(1): p. 93-102.
51. Wani, T.U., S.N. Raza, and N.A. Khan, *Nanoparticle opsonization: forces involved and protection by long chain polymers.* Polymer Bulletin, 2020. **77**(7): p. 3865-3889.
52. Schöttler, S., et al., *Protein adsorption is required for stealth effect of poly(ethylene glycol)- and poly(phosphoester)-coated nanocarriers.* Nat Nanotechnol, 2016. **11**(4): p. 372-7.
53. Lynch, I. and K.A. Dawson, *Protein-nanoparticle interactions.* Nano today, 2008. **3**(1-2): p. 40-47.
54. Moghimi, S.M., A.C. Hunter, and J.C. Murray, *Long-circulating and target-specific nanoparticles: theory to practice.* Pharmacological reviews, 2001. **53**(2): p. 283-318.
55. Moghimi, S.M., A. Hunter, and T. Andresen, *Factors controlling nanoparticle pharmacokinetics: an integrated analysis and perspective.* Annual review of pharmacology and toxicology, 2012. **52**: p. 481-503.
56. Samuelsson, E., et al., *Contribution of Kupffer cells to liposome accumulation in the liver.* Colloids and Surfaces B: Biointerfaces, 2017. **158**: p. 356-362.
57. Demoy, M., et al., *In vitro evaluation of nanoparticles spleen capture.* Life Sci, 1999. **64**(15): p. 1329-37.
58. Crean, P.A., et al., *The fractional distribution of the cardiac output in man using microspheres labelled with technetium 99m.* The British Journal of Radiology, 1986. **59**(699): p. 209-215.
59. MacDonald, I., et al., *Kinetics of red blood cell passage through interendothelial slits into venous sinuses in rat spleen, analyzed by in vivo microscopy.* Microvascular research, 1987. **33**(1): p. 118-134.
60. Kraal, G., *Cells in the marginal zone of the spleen*, in *International review of cytology*. 1992, Elsevier. p. 31-74.
61. Cataldi, M., et al., *Emerging role of the spleen in the pharmacokinetics of monoclonal antibodies, nanoparticles and exosomes.* International journal of molecular sciences, 2017. **18**(6): p. 1249.
62. Den Haan, J.M. and G. Kraal, *Innate immune functions of macrophage subpopulations in the spleen.* Journal of innate immunity, 2012. **4**(5-6): p. 437-445.
63. Mebius, R.E. and G. Kraal, *Structure and function of the spleen.* Nature reviews immunology, 2005. **5**(8): p. 606-616.
64. Mebius, R.E. and G. Kraal, *Structure and function of the spleen.* Nature Reviews Immunology, 2005. **5**: p. 606.
65. Moghimi, S.M., et al., *An investigation of the filtration capacity and the fate of large filtered sterically-stabilized microspheres in rat spleen.* Biochimica et Biophysica Acta (BBA)-General Subjects, 1993. **1157**(2): p. 233-240.
66. Pillai, S. and A. Cariappa, *The follicular versus marginal zone B lymphocyte cell fate decision.* Nature Reviews Immunology, 2009. **9**(11): p. 767-777.
67. Borges da Silva, H., et al., *Splenic macrophage subsets and their function during blood-borne infections.* Frontiers in immunology, 2015. **6**: p. 480.
68. Noel, G., et al., *Postburn monocytes are the major producers of TNF-α in the heterogeneous splenic macrophage population.* Shock, 2007. **27**(3): p. 312-319.
69. Hey, Y.Y. and H.C. O'Neill, *Murine spleen contains a diversity of myeloid and dendritic cells distinct in antigen presenting function.* J Cell Mol Med, 2012. **16**(11): p. 2611-9.
70. Dölen, Y., et al., *Nanovaccine administration route is critical to obtain pertinent iNKt cell help for robust anti-tumor T and B cell responses.* OncoImmunology, 2020. **9**(1): p. 1738813.

71. Kim, J., et al., *Injectable, spontaneously assembling, inorganic scaffolds modulate immune cells in vivo and increase vaccine efficacy.* Nature biotechnology, 2015. **33**(1): p. 64-72.
72. Gasser, O., et al., *A phase I vaccination study with dendritic cells loaded with NY-ESO-1 and α-galactosylceramide: induction of polyfunctional T cells in high-risk melanoma patients.* Cancer Immunology, Immunotherapy, 2018. **67**(2): p. 285-298.
73. Guilliams, M., et al., *Dendritic cells, monocytes and macrophages: a unified nomenclature based on ontogeny.* Nature Reviews Immunology, 2014. **14**(8): p. 571-578.
74. Dong, M.B., M.J. Rahman, and K.V. Tarbell, *Flow cytometric gating for spleen monocyte and DC subsets: differences in autoimmune NOD mice and with acute inflammation.* Journal of immunological methods, 2016. **432**: p. 4-12.
75. Shortman, K. and W.R. Heath, *The CD8+ dendritic cell subset.* Immunological reviews, 2010. **234**(1): p. 18-31.
76. Binnewies, M., et al., *Unleashing type-2 dendritic cells to drive protective antitumor CD4+ T cell immunity.* Cell, 2019. **177**(3): p. 556-571. e16.
77. Tacke, F., et al., *Immature monocytes acquire antigens from other cells in the bone marrow and present them to T cells after maturing in the periphery.* The Journal of experimental medicine, 2006. **203**(3): p. 583-597.
78. Jakubzick, C., et al., *Minimal differentiation of classical monocytes as they survey steady-state tissues and transport antigen to lymph nodes.* Immunity, 2013. **39**(3): p. 599-610.
79. de Graaff, P.M., et al., *Respiratory syncytial virus infection of monocyte-derived dendritic cells decreases their capacity to activate CD4 T cells.* The Journal of Immunology, 2005. **175**(9): p. 5904-5911.
80. Noubade, R., S. Majri-Morrison, and K.V. Tarbell, *Beyond cDC1: Emerging Roles of DC Crosstalk in Cancer Immunity.* Frontiers in Immunology, 2019. **10**(1014).
81. Swiecki, M., et al., *Plasmacytoid dendritic cell ablation impacts early interferon responses and antiviral NK and CD8+ T cell accrual.* Immunity, 2010. **33**(6): p. 955-966.
82. Ghibellini, G., E.M. Leslie, and K.L. Brouwer, *Methods to evaluate biliary excretion of drugs in humans: an updated review.* Molecular pharmaceutics, 2006. **3**(3): p. 198-211.
83. Willekens, F.L., et al., *Liver Kupffer cells rapidly remove red blood cell–derived vesicles from the circulation by scavenger receptors.* Blood, 2005. **105**(5): p. 2141-2145.
84. Racanelli, V. and B. Rehermann, *The liver as an immunological organ.* Hepatology, 2006. **43**(S1): p. S54-S62.
85. Zheng, M. and Z. Tian, *Liver-Mediated Adaptive Immune Tolerance.* Frontiers in Immunology, 2019. **10**(2525).
86. Knook, D. and E.C. Sleyster, *Separation of Kupffer and endothelial cells of the rat liver by centrifugal elutriation.* Experimental cell research, 1976. **99**(2): p. 444-449.
87. Scherphof, G., et al., *Targeting liposomes and lipoplexes to cells in the liver.* Cellular and Molecular Biology Letters, 2002. **7**(2): p. 251-254.
88. Malik, R., C. Selden, and H. Hodgson. *The role of non-parenchymal cells in liver growth*. in *Seminars in cell & developmental biology*. 2002. Elsevier.
89. Poon, W., et al., *Elimination pathways of nanoparticles.* Acs Nano, 2019. **13**(5): p. 5785-5798.
90. Abdel-Misih, S.R. and M. Bloomston, *Liver anatomy.* Surgical Clinics, 2010. **90**(4): p. 643-653.
91. Widmann, J.-J., R.S. Cotran, and H.D. Fahimi, *Mononuclear phagocytes (Kupffer cells) and endothelial cells: identification of two functional cell types in rat liver sinusoids by endogenous peroxidase activity.* The journal of cell biology, 1972. **52**(1): p. 159-170.
92. Gaumet, M., et al., *Nanoparticles for drug delivery: the need for precision in reporting particle size parameters.* European journal of pharmaceutics and biopharmaceutics, 2008. **69**(1): p. 1-9.
93. Wang, H., et al., *Diagnostic imaging and therapeutic application of nanoparticles targeting the liver.* Journal of Materials Chemistry B, 2015. **3**(6): p. 939-958.
94. Bilzer, M., F. Roggel, and A.L. Gerbes, *Role of Kupffer cells in host defense and liver disease.* Liver International, 2006. **26**(10): p. 1175-1186.

95. Dobrovolskaia, M.A. and S.E. McNeil, *Immunological properties of engineered nanomaterials.* Nature nanotechnology, 2007. **2**(8): p. 469.
96. Sadauskas, E., et al., *Kupffer cells are central in the removal of nanoparticles from the organism.* Particle and fibre toxicology, 2007. **4**(1): p. 1-7.
97. Boltjes, A., et al., *The role of Kupffer cells in hepatitis B and hepatitis C virus infections.* Journal of hepatology, 2014. **61**(3): p. 660-671.
98. Charles, A. and D. Scott, *Studies on heparin II. Heparin in various tissues.* Journal of Biological Chemistry, 1933. **102**(2): p. 431-435.
99. Fulton, G.P., et al., *Humoral aspects of tissue mast cells.* Physiological Reviews, 1957. **37**(2): p. 221-232.
100. Rabenstein, D.L., *Heparin and heparan sulfate: structure and function.* Natural product reports, 2002. **19**(3): p. 312-331.
101. Mulloy, B., E. Gray, and T.W. Barrowcliffe, *Characterization of unfractionated heparin: comparison of materials from the last 50 years.* THROMBOSIS AND HAEMOSTASIS-STUTTGART-, 2000. **84**(6): p. 1052-1056.
102. McLean, J., *The thromboplastic action of cephalin.* American Journal of Physiology-Legacy Content, 1916. **41**(2): p. 250-257.
103. Howell, W.H. and E. Holt, *Two new factors in blood coagulation—heparin and pro-antithrombin.* American Journal of Physiology-Legacy Content, 1918. **47**(3): p. 328-341.
104. Howell, W., *The purification of heparin and its presence in blood.* American Journal of Physiology-Legacy Content, 1925. **71**(3): p. 553-562.
105. Lindahl, U., et al., *Evidence for a 3-O-sulfated D-glucosamine residue in the antithrombin-binding sequence of heparin.* Proceedings of the National Academy of Sciences, 1980. **77**(11): p. 6551-6555.
106. Jin, L., et al., *The anticoagulant activation of antithrombin by heparin.* Proceedings of the National Academy of Sciences, 1997. **94**(26): p. 14683-14688.
107. Hirsh, J., et al., *Heparin and low-molecular-weight heparin: mechanisms of action, pharmacokinetics, dosing, monitoring, efficacy, and safety.* Chest, 2001. **119**(1 Suppl): p. 64s-94s.
108. Björk, I. and U. Lindahl, *Mechanism of the anticoagulant action of heparin.* Molecular and cellular biochemistry, 1982. **48**(3): p. 161-182.
109. Brandjes, D.P., et al., *Acenocoumarol and heparin compared with acenocoumarol alone in the initial treatment of proximal-vein thrombosis.* New England Journal of Medicine, 1992. **327**(21): p. 1485-1489.
110. Hoffman, M., *Heparins: clinical use and laboratory monitoring.* Laboratory Medicine, 2010. **41**(10): p. 621-626.
111. Boneu, B., et al., *Evidence for a saturable mechanism of disappearance of standard heparin in rabbits.* Thrombosis research, 1987. **46**(6): p. 835-844.
112. Maurer, J.r., et al., *Analysis of the complex formation of heparin with protamine by light scattering and analytical ultracentrifugation: implications for blood coagulation management.* Journal of the American Chemical Society, 2011. **133**(4): p. 1134-1140.
113. Hattersley, P.G., *Activated coagulation time of whole blood.* Jama, 1966. **196**(5): p. 436-440.
114. Boneu, B., C. Caranobe, and P. Sie, *3 Pharmacokinetics of heparin and low molecular weight heparin.* Bailliere's clinical haematology, 1990. **3**(3): p. 531-544.
115. Dawes, J. and D.S. Pepper, *Catabolism of low-dose heparin in man.* Thrombosis Research, 1979. **14**(6): p. 845-860.
116. Hiebert, L.M. and L.B. Jaques, *The observation of heparin on endothelium after injection.* Thrombosis research, 1976. **8**(2): p. 195-204.
117. Jaques, L., J. Mahadoo, and J. Riley, *The mast cell/heparin paradox.* The Lancet, 1977. **309**(8008): p. 411-413.
118. Palm, M. and C. Mattsson, *Pharmacokinetics of heparin and low molecular weight heparin fragment (Fragmin®) in rabbits with impaired renal or metabolic clearance.* Thrombosis and haemostasis, 1987. **57**(03): p. 932-935.

119. Glimelius, B., C. Busch, and M. Höök, *Binding of heparin on the surface of cultured human endothelial cells.* Thrombosis research, 1978. **12**(5): p. 773-782.
120. Barzu, T., et al., *Endothelial binding sites for heparin. Specificity and role in heparin neutralization.* Biochemical Journal, 1986. **238**(3): p. 847-854.
121. De Swart, C., et al., *Kinetics of intravenously administered heparin in normal humans.* 1982.
122. Jia, Z., et al., *Pharmacokinetic model of unfractionated heparin during and after cardiopulmonary bypass in cardiac surgery.* J Transl Med, 2015. **13**: p. 45.
123. Delavenne, X., et al., *Pharmacokinetic/pharmacodynamic model for unfractionated heparin dosing during cardiopulmonary bypass.* BJA: British Journal of Anaesthesia, 2017. **118**(5): p. 705-712.
124. Leentjens, J., et al., *Initial anticoagulation in patients with pulmonary embolism: thrombolysis, unfractionated heparin, LMWH, fondaparinux, or DOACs?* British journal of clinical pharmacology, 2017. **83**(11): p. 2356-2366.
125. Hirsh, J. and M.N. Levine, *Low molecular weight heparin.* Blood, 1992. **79**(1): p. 1-17.
126. Donat, F., et al., *The pharmacokinetics of fondaparinux sodium in healthy volunteers.* Clin Pharmacokinet, 2002. **41 Suppl 2**: p. 1-9.
127. *Heparin Market By Product (Unfragmented Heparin, Low Molecular Weight Heparin and Ultra-Low Molecular Weight Heparin), By Route of Administration (Subcutaneous and Intravenous) - Growth, Future Prospects & Competitive Analysis 2017 - 2025*. 2018: https://www.credenceresearch.com/report/heparin-market.
128. Merli, G.J. and J.B. Groce, *Pharmacological and clinical differences between low-molecular-weight heparins: implications for prescribing practice and therapeutic interchange.* Pharmacy and Therapeutics, 2010. **35**(2): p. 95.
129. Champanhac, C., et al., *Timing of Heparin Addition to the Biomolecular Corona Influences the Cellular Uptake of Nanocarriers.* Biomacromolecules, 2019. **20**(10): p. 3724-3732.
130. Hevonoja, T., et al., *Structure of low density lipoprotein (LDL) particles: basis for understanding molecular changes in modified LDL.* Biochimica et Biophysica Acta (BBA)-Molecular and cell biology of lipids, 2000. **1488**(3): p. 189-210.
131. Srinivasan, S.R., et al., *Low density lipoprotein retention by aortic tissue: contribution of extracellular matrix.* Atherosclerosis, 1986. **62**(3): p. 201-208.
132. Joshi, M.D., et al., *Targeting tumor antigens to dendritic cells using particulate carriers.* Journal of controlled release, 2012. **161**(1): p. 25-37.
133. Balazsovits, J., et al., *Analysis of the effect of liposome encapsulation on the vesicant properties, acute and cardiac toxicities, and antitumor efficacy of doxorubicin.* Cancer chemotherapy and pharmacology, 1989. **23**(2): p. 81-86.
134. Working, P. and A. Dayan, *Pharmacological-toxicological expert report CAELYXTM:(stealth® liposomal doxorubicin HCl).* Human & experimental toxicology, 1996. **15**(9): p. 751-785.
135. Rosenecker, J., et al., *Increased liposome extravasation in selected tissues: effect of substance P.* Proceedings of the National Academy of Sciences, 1996. **93**(14): p. 7236-7241.
136. Yan, Y., et al., *Non-anticoagulant effects of low molecular weight heparins in inflammatory disorders: A review.* Carbohydrate polymers, 2017. **160**: p. 71-81.
137. Kevane, B., et al., *Endothelial barrier protective properties of low molecular weight heparin: A novel potential tool in the prevention of cancer metastasis?* Research and practice in thrombosis and haemostasis, 2017. **1**(1): p. 23-32.
138. Tonigold, M., et al., *Pre-adsorption of antibodies enables targeting of nanocarriers despite a biomolecular corona.* Nature nanotechnology, 2018. **13**(9): p. 862-869.
139. Mousa, S.A., *Low-Molecular-Weight Heparins in Thrombosis and Cancer: Emerging Links.* Cardiovascular drug reviews, 2004. **22**(2): p. 121-134.
140. Faghfuri, E., et al., *Recent developments of RNA-based vaccines in cancer immunotherapy.* Expert Opinion on Biological Therapy, 2020: p. 1-18.
141. Huntington, J.A. and P.E. Stein, *Structure and properties of ovalbumin.* Journal of Chromatography B: Biomedical Sciences and Applications, 2001. **756**(1-2): p. 189-198.

142. Krumb, M., et al., *Multivalency Beats Complexity: A Study on the Cell Uptake of Carbohydrate Functionalized Nanocarriers to Dendritic Cells.* Cells, 2020. **9**(9): p. 2087.
143. Rezaeipoor, R., et al., *Fc-DIRECTED ANTIBODY CONJUGATION OF MAGNETIC NANOPARTICLES FOR ENHANCED MOLECULAR TARGETING.* Journal of innovative optical health sciences, 2009. **2**(4): p. 387-396.
144. Capila, I. and R.J. Linhardt, *Heparin–protein interactions.* Angewandte Chemie International Edition, 2002. **41**(3): p. 390-412.
145. Wei, D., et al., *Noninvasive monitoring of nanoparticle clearance and aggregation in blood circulation by in vivo flow cytometry.* J Control Release, 2018. **278**: p. 66-73.
146. Zigmond, E., et al., *Infiltrating monocyte-derived macrophages and resident kupffer cells display different ontogeny and functions in acute liver injury.* The Journal of Immunology, 2014. **193**(1): p. 344-353.
147. Autengruber, A., et al., *Impact of enzymatic tissue disintegration on the level of surface molecule expression and immune cell function.* European Journal of Microbiology and Immunology, 2012. **2**(2): p. 112-120.
148. van Dinther, D., et al., *Functional CD169 on macrophages mediates interaction with dendritic cells for CD8+ T cell cross-priming.* Cell reports, 2018. **22**(6): p. 1484-1495.
149. Mousavi, S., et al., *Anti-Inflammatory Effects of Heparin and Its Derivatives: A Systematic Review.* Advances in Pharmacological Sciences, 2015. **2015**: p. 507151.
150. Chimenti, L., et al., *Nebulized heparin attenuates pulmonary coagulopathy and inflammation through alveolar macrophages in a rat model of acute lung injury.* Thrombosis and haemostasis, 2017. **117**(11): p. 2125.
151. Baeuerle, P.A. and T. Henkel, *Function and activation of NF-kappaB in the immune system.* Annual review of immunology, 1994. **12**(1): p. 141-179.
152. Li, Q. and I.M. Verma, *NF-κB regulation in the immune system.* Nature Reviews Immunology, 2002. **2**(10): p. 725-734.
153. Moser, B., et al., *Increased vaccine tolerability and protection via NF-κB modulation.* Science Advances, 2020. **6**(37): p. eaaz8700.
154. Thiele, L., et al., *Evaluation of particle uptake in human blood monocyte-derived cells in vitro. Does phagocytosis activity of dendritic cells measure up with macrophages?* Journal of Controlled Release, 2001. **76**(1-2): p. 59-71.
155. Li Mengyi, et al., *Encapsulation of Polyprodrugs enables an Efficient and Controlled Release of Dexamethasone*. 2021: About to submit.
156. Matsusaka, T., et al., *Transcription factors NF-IL6 and NF-kappa B synergistically activate transcription of the inflammatory cytokines, interleukin 6 and interleukin 8.* Proceedings of the National Academy of Sciences, 1993. **90**(21): p. 10193-10197.
157. Baeuerle, P.A. and V.R. Baichwal, *NF-kB as a frequent target for immunosuppressive and anti-inflammatory molecules.* Advances in immunology, 1997. **65**: p. 111-138.
158. Luedde, T., et al., *Losing balance: cytokine signaling and cell death in the context of hepatocyte injury and hepatic failure.* European cytokine network, 2003. **13**(4): p. 377-83.
159. Crinelli, R., et al., *Selective inhibition of NF-kB activation and TNF-α production in macrophages by red blood cell-mediated delivery of dexamethasone.* Blood Cells, Molecules, and Diseases, 2000. **26**(3): p. 211-222.
160. Bae, Y., et al., *Multifunctional polymeric micelles with folate-mediated cancer cell targeting and pH-triggered drug releasing properties for active intracellular drug delivery.* Molecular BioSystems, 2005. **1**(3): p. 242-250.
161. Quan, L., et al., *Nanomedicines for inflammatory arthritis: head-to-head comparison of glucocorticoid-containing polymers, micelles, and liposomes.* ACS nano, 2013. **8**(1): p. 458-466.
162. Scheschowitsch, K., J.A. Leite, and J. Assreuy, *New insights in glucocorticoid receptor signaling–more than just a ligand binding receptor.* Frontiers in endocrinology, 2017. **8**: p. 16.
163. Kadmiel, M. and J.A. Cidlowski, *Glucocorticoid receptor signaling in health and disease.* Trends in pharmacological sciences, 2013. **34**(9): p. 518-530.

164. Zen, M., et al., *The kaleidoscope of glucorticoid effects on immune system.* Autoimmunity reviews, 2011. **10**(6): p. 305-310.
165. Ulrich, S., et al., *Modifying the Adsorption Characteristic of Inert Silica Films by Inserting Anchoring Sites.* Physical Review Letters, 2009. **102**(1): p. 016102.
166. Skrastina, D., et al., *Silica nanoparticles as the adjuvant for the immunisation of mice using hepatitis B core virus-like particles.* PloS one, 2014. **9**(12): p. e114006.
167. Davis, G.F., *Adverse effects of corticosteroids: II. Systemic.* Clinics in dermatology, 1986. **4**(1): p. 161-169.
168. Yu, Y., et al., *Silica nanoparticles induce liver fibrosis via TGF-β1/Smad3 pathway in ICR mice.* International journal of nanomedicine, 2017. **12**: p. 6045.
169. Sawhney, S., P. Woo, and K. Murray, *Macrophage activation syndrome: a potentially fatal complication of rheumatic disorders.* Archives of disease in childhood, 2001. **85**(5): p. 421-426.
170. Janka, G.E., *Hemophagocytic syndromes.* Blood reviews, 2007. **21**(5): p. 245-253.
171. Gaies, E., et al., *Methotrexate side effects: review article.* J Drug Metab Toxicol, 2012. **3**(4): p. 1-5.
172. Matthews, D., et al., *Dihydrofolate reductase: X-ray structure of the binary complex with methotrexate.* Science, 1977. **197**(4302): p. 452-455.
173. Zuba-Surma, E.K., et al., *The ImageStream System: a key step to a new era in imaging.* Folia Histochemica et Cytobiologica, 2007. **45**(4): p. 279-290.
174. Matthias Voigt, J.S., Lukas Kleue, Andrea Tüttenberg, Mark Helm, *Systematic screening approach to identify liposomes at the edge of stability*. 2020: unpublished manuskript.
175. Laginha, K.M., et al., *Determination of doxorubicin levels in whole tumor and tumor nuclei in murine breast cancer tumors.* Clinical cancer research, 2005. **11**(19): p. 6944-6949.
176. *HIGHLIGHTS OF PRESCRIBING INFORMATION DOXORUBICIN HYDROCHLORIDE* in *3399075*, U.S.F.a.D. Administration, Editor. 2013: https://www.accessdata.fda.gov/drugsatfda_docs/label/2013/050467s073lbl.pdf.
177. Cheng, L., et al., *Multifunctional nanoparticles for upconversion luminescence/MR multimodal imaging and magnetically targeted photothermal therapy.* Biomaterials, 2012. **33**(7): p. 2215-2222.
178. Zhang, S., et al., *Identification of the molecular basis of doxorubicin-induced cardiotoxicity.* Nature medicine, 2012. **18**(11): p. 1639-1642.
179. Kumar, P., S. Agnihotri, and I. Roy, *Synthesis of dox drug conjugation and citric acid stabilized superparamagnetic iron-oxide nanoparticles for drug delivery.* Biochem. Physiol, 2016. **5**(194): p. 2.
180. Gigli, M., et al., *Quantitative study of doxorubicin in living cell nuclei by microspectrofluorometry.* Biochimica et Biophysica Acta (BBA) - Gene Structure and Expression, 1988. **950**(1): p. 13-20.
181. Arora, H.C., et al., *Nanocarriers Enhance Doxorubicin Uptake in Drug-Resistant Ovarian Cancer Cells.* Cancer Research, 2012. **72**(3): p. 769.
182. Dai, X., et al., *Fluorescence intensity and lifetime imaging of free and micellar-encapsulated doxorubicin in living cells.* Nanomedicine: Nanotechnology, Biology and Medicine, 2008. **4**(1): p. 49-56.
183. Yang, F., et al., *Doxorubicin, DNA torsion, and chromatin dynamics.* Biochimica et Biophysica Acta (BBA) - Reviews on Cancer, 2014. **1845**(1): p. 84-89.
184. *INSPIRE™ ImageStreamX MKII Software User's Manual*. 2018, Amnis Corporation: www.amnis.com.
185. Schlaad, H., et al., *Synthesis of α, ω-heterobifunctional poly (ethylene glycol) s by metal-free anionic ring-opening polymerization.* Macromolecules, 2001. **34**(13): p. 4302-4304.
186. Pansare, V.J., et al., *Review of Long-Wavelength Optical and NIR Imaging Materials: Contrast Agents, Fluorophores, and Multifunctional Nano Carriers.* Chemistry of Materials, 2012. **24**(5): p. 812-827.
187. Rigler, R. and E.S. Elson, *Fluorescence correlation spectroscopy: theory and applications*. Vol. 65. 2012: Springer Science & Business Media.

188. Health, U.D.o. and H. Services, *Guidance for Industry Pyrogen and Endotoxins Testing: Questions and Answers.* Washington, DC: US Food and Drug Administration, 2012.
189. Gehring, S., et al., *Kupffer cells abrogate cholestatic liver injury in mice.* Gastroenterology, 2006. **130**(3): p. 810-822.
190. Fichter, M., et al., *Nanocapsules generated out of a polymeric dexamethasone shell suppress the inflammatory response of liver macrophages.* Nanomedicine: Nanotechnology, Biology and Medicine, 2013. **9**(8): p. 1223-1234.
191. Rose, S., A. Misharin, and H. Perlman, *A novel Ly6C/Ly6G-based strategy to analyze the mouse splenic myeloid compartment.* Cytometry Part A, 2012. **81**(4): p. 343-350.
192. O'Neill, A.S., T.K. van den Berg, and G.E. Mullen, *Sialoadhesin–a macrophage-restricted marker of immunoregulation and inflammation.* Immunology, 2013. **138**(3): p. 198-207.
193. Nascimento, M., et al., *Ly6C hi monocyte recruitment is responsible for Th2 associated host-protective macrophage accumulation in liver inflammation due to schistosomiasis.* PLoS Pathog, 2014. **10**(8): p. e1004282.
194. Lukacs-Kornek, V. and D. Schuppan, *Dendritic cells in liver injury and fibrosis: Shortcomings and promises.* Journal of Hepatology, 2013. **59**(5): p. 1124-1126.
195. Seckert, C.K., et al., *Liver sinusoidal endothelial cells are a site of murine cytomegalovirus latency and reactivation.* Journal of virology, 2009. **83**(17): p. 8869-8884.

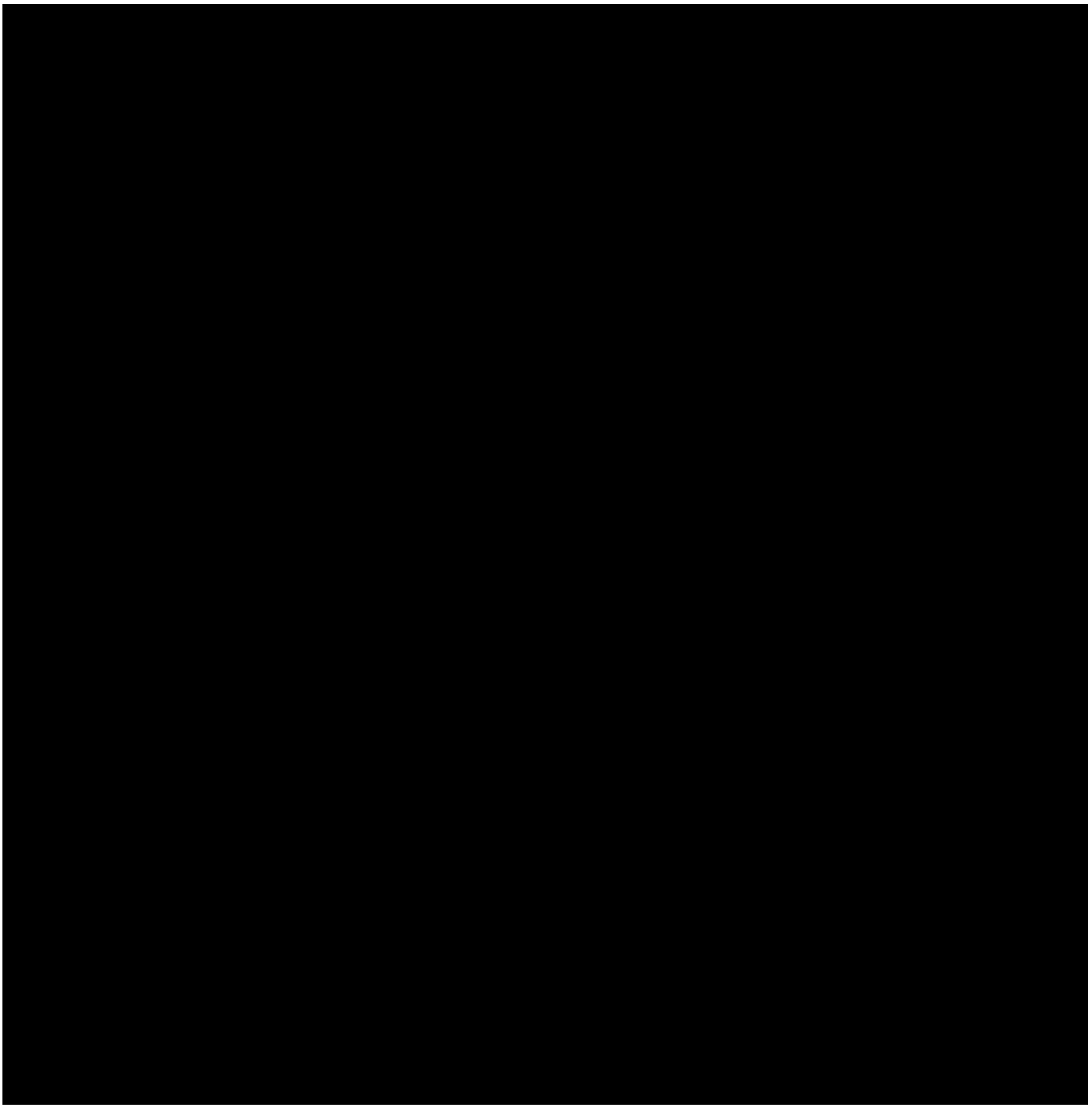

VI. Achievments

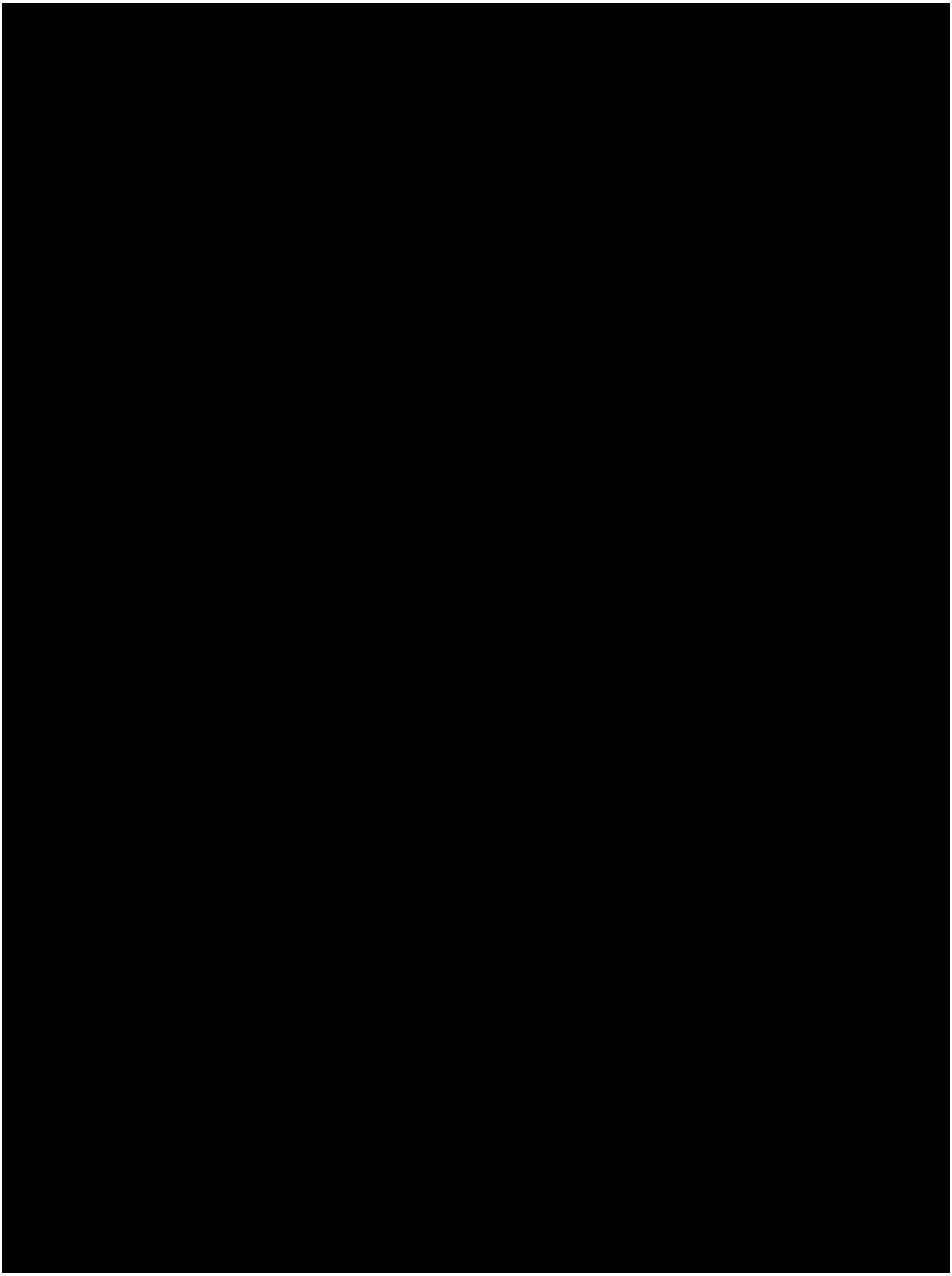

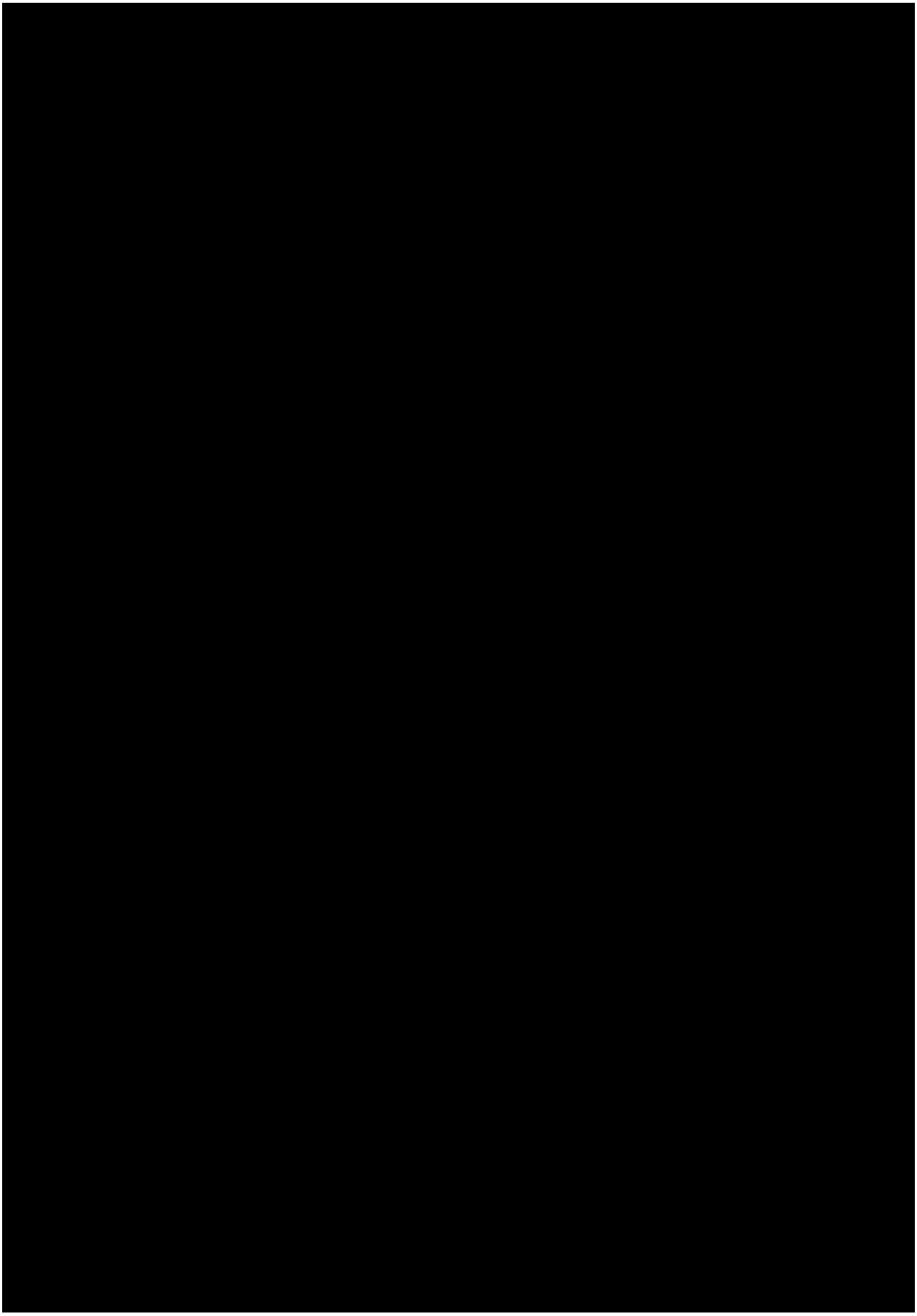

Errata

#	Entry
1	5.8.2021 Page: 35 The reference to institution for Co-author Mark Helm is (c)
2	5.8.2021 Page: 37-38 (section 3.2 introduction) In section - *3.2 introduction* - numbers of references do not correspond with the reference directory (section 11). This is due to an unintentional technical error. Find the references of the section on page 37-38 here: 1. McLean, J., *The thromboplastic action of cephalin.* American Journal of Physiology-Legacy Content, 1916. **41**(2): p. 250-257. 2. Murray, G.D. and C.H. Best, *THE USE OF HEPARIN IN THROMBOSIS.* Ann Surg, 1938. **108**(2): p. 163-77. 3. Hoffman, M., *Heparins: clinical use and laboratory monitoring.* Laboratory Medicine, 2010. **41**(10): p. 621-626. 4. Barenholz, Y.C., *Doxil®—the first FDA-approved nano-drug: lessons learned.* Journal of controlled release, 2012. **160**(2): p. 117-134. 5. James, J., *DOXIL approved for KS.* AIDS treatment news, 1995(236): p. 6. 6. Bulbake, U., et al., *Liposomal formulations in clinical use: an updated review.* Pharmaceutics, 2017. **9**(2): p. 12. 7. Torchilin, P.V., et al., *Liposomes: a practical approach*. 2003: Oxford University Press. 8. Working, P. and A. Dayan, *Pharmacological-toxicological expert report CAELYXTM:(stealth® liposomal doxorubicin HCl).* Human & experimental toxicology, 1996. **15**(9): p. 751-785. 9. Adler-Moore, J. and R.T. Proffitt, *AmBisome: liposomal formulation, structure, mechanism of action and pre-clinical experience.* Journal of Antimicrobial Chemotherapy, 2002. **49**(suppl_1): p. 21-30. 10. Luo, R., et al., *Distinct biodistribution of doxorubicin and the altered dispositions mediated by different liposomal formulations.* International journal of pharmaceutics, 2017. **519**(1-2): p. 1-10.

11. Schöttler, S., et al., *Protein source and choice of anticoagulant decisively affect nanoparticle protein corona and cellular uptake.* Nanoscale, 2016. **8**(10): p. 5526-5536.

12. Champanhac, C., et al., *Timing of Heparin Addition to the Biomolecular Corona Influences the Cellular Uptake of Nanocarriers.* Biomacromolecules, 2019. **20**(10): p. 3724-3732.

13. Liu, T., et al., *RES blockade: A strategy for boosting efficiency of nanoparticle drug.* Nano Today, 2015. **10**(1): p. 11-21.

14. Sun, X., et al., *Improved tumor uptake by optimizing liposome based RES blockade strategy.* Theranostics, 2017. **7**(2): p. 319.

15. Zhang, Y.-N., et al., *Nanoparticle–liver interactions: cellular uptake and hepatobiliary elimination.* Journal of controlled release, 2016. **240**: p. 332-348.

16. Cataldi, M., et al., *Emerging role of the spleen in the pharmacokinetics of monoclonal antibodies, nanoparticles and exosomes.* International journal of molecular sciences, 2017. **18**(6): p. 1249.

~~17.~~

18. Moghimi, S.M., et al., *An investigation of the filtration capacity and the fate of large filtered sterically-stabilized microspheres in rat spleen.* Biochimica et Biophysica Acta (BBA)-General Subjects, 1993. **1157**(2): p. 233-240.

19. Borges da Silva, H., et al., *Splenic macrophage subsets and their function during blood-borne infections.* Frontiers in immunology, 2015. **6**: p. 480.

20. Hey, Y.Y. and H.C. O'Neill, *Murine spleen contains a diversity of myeloid and dendritic cells distinct in antigen presenting function.* J Cell Mol Med, 2012. **16**(11): p. 2611-9.

21. Davies, L.C., et al., *Tissue-resident macrophages.* Nature immunology, 2013. **14**(10): p. 986.

22. Kao, Y. and R. Juliano, *Interactions of liposomes with the reticuloendothelial system effects of reticuloendothelial blockade on the clearance of large unilamellar vesicles.* Biochimica et Biophysica Acta (BBA)-General Subjects, 1981. **677**(3-4): p. 453-461.

23. Gustafson, H.H., et al., *Nanoparticle uptake: the phagocyte problem.* Nano today, 2015. **10**(4): p. 487-510.

24. Mebius, R.E. and G. Kraal, *Structure and function of the spleen.* Nature Reviews Immunology, 2005. **5**: p. 606.

25. Poon, W., et al., *Elimination pathways of nanoparticles.* Acs Nano, 2019. **13**(5): p. 5785-5798.

26. van Etten, E.W., et al., *Biodistribution of liposomal amphotericin B (AmBisome) and amphotericin B-desoxycholate (Fungizone) in uninfected immunocompetent mice and leucopenic mice infected with Candida albicans.* Journal of Antimicrobial Chemotherapy, 1995. **35**(4): p. 509-519.

27. Balazsovits, J., et al., *Analysis of the effect of liposome encapsulation on the vesicant properties, acute and cardiac toxicities, and antitumor efficacy of doxorubicin.* Cancer chemotherapy and pharmacology, 1989. **23**(2): p. 81-86.